

Photoemission studies of the light actinides

Paul Nevitt

UMI Number: U584870

All rights reserved

INFORMATION TO ALL USERS

The quality of this reproduction is dependent upon the quality of the copy submitted.

In the unlikely event that the author did not send a complete manuscript and there are missing pages, these will be noted. Also, if material had to be removed, a note will indicate the deletion.



UMI U584870

Published by ProQuest LLC 2013. Copyright in the Dissertation held by the Author.
Microform Edition © ProQuest LLC.

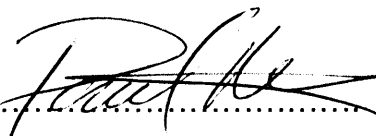
All rights reserved. This work is protected against
unauthorized copying under Title 17, United States Code.

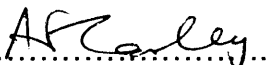


ProQuest LLC
789 East Eisenhower Parkway
P.O. Box 1346
Ann Arbor, MI 48106-1346

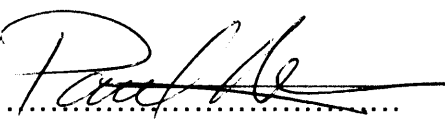
Declaration

I hereby declare that the work contained within this thesis is solely the result of my own personal investigations, except where otherwise stated. This thesis has not previously been accepted in substance for any degree, and is not being concurrently submitted in candidature for any degree.

Signed 
P. Nevitt (Candidate)

Witnessed 
Dr. A.F. Carley (Supervisor)

I hereby give consent for my thesis, if accepted, to be available for photocopying and for inter-library loan, and that the title and abstract may be made available to outside organisations.

Signed 
P. Nevitt (Candidate)

Abstract

The surface reactivity of thorium, uranium, neptunium and americium has been investigated under UHV conditions using X-ray photoelectron spectroscopy (XPS) and ultra violet photoelectron spectroscopy (UPS). Oxygen, nitric oxide, nitrogen dioxide and nitrous oxide adsorption on a polycrystalline thorium surface has been investigated at 298 K. O₂ dissociatively adsorbs on the surface resulting in the growth of ThO₂. All three of the nitrogen oxides adsorb dissociatively with both oxygen and nitrogen adsorbed on the thorium surface. The formation of thorium oxynitride (ThO_xN_y) is proposed. Reaction of NO, NO₂ and N₂O with a polycrystalline uranium surface has also been investigated at 298 K. N₂O adsorbs dissociatively leaving only oxygen adsorbed on the uranium surface. NO and N₂O also adsorb dissociatively but in these cases both oxygen and nitrogen remain on the surface. The formation of uranium oxynitride (UO_xN_y) is proposed. For exposures >350 L the rate of reaction of NO with the oxynitride surface decreases significantly. In contrast, NO₂ continues to react with the surface and a further increase in surface oxygen concentration is observed. Adsorption of O₂, NO and CO on thin films of neptunium metal has been studied at 80 and 300K. Following exposure to O₂ at 80 and 300K, an intermediate surface oxide of Np is formed which is unstable with respect to the formation of NpO₂. This intermediate oxide is proposed to be associated with the chemisorption phase, NpO_(Chem). Dissociative adsorption of CO and NO is observed at 80 and 300K. A surface oxidic compound is formed which is not a simple neptunium oxide. NpO_(Chem) states are proposed to be stabilized by the presence of carbon/nitrogen as neptunium oxycarbide and oxynitride respectively. The interaction of O₂ and NO with americium thin films has also been investigated. The formation of Am₂O₃ is proposed and it was found that it is not thermodynamically viable to produce a higher oxidation state of americium via gas dosing (at 300 K under UHV). Adsorption of NO on the surface results in the dissociative adsorption of N and O, and in the formation of a surface compound.

ACKNOWLEDGEMENTS

I would like to sincerely acknowledge the following people:

Firstly thanks go to Dr. Albert Carley for allowing me to undertake such an interesting Ph.D and for his continued support and technical knowledge during the past three years.

To Dr Paul Roussel I will be forever grateful for the huge amount of time and effort you have given me over the past three years. You were a great supervisor with vast knowledge, unrivalled enthusiasm and a constant source of inspiration.

The AWE for their financial support and providing me with the chance to undertake this project.

To the guys in the lab who made working a whole lot easier and more fun. In particular my thanks must go to Dr Dave with whom I spent a lot of time learning and trying to make things work. You made my three years a whole lot easier, more interesting, and a lot of fun.

Andy, Ian and Jim I don't say thanks very often so I thought I'd take this chance. My university life has been whole lot better for knowing you guys. Thanks for the past six years, the laughs, the beers, the European cities, its all made this PhD a whole lot more fun and a lot less stressful.

Finally I'd like to thank those closest to me. Meryl, your love and support means everything to me. You've seen the highs and the lows over the past three years and put up with them all. To my family and in particular my mom and dad, my everlasting thanks. You have supported me always in whatever I have chosen to do. My student years are finally over, and they were the best years of my life because of your support. I couldn't have done it without you.

Contents

Chapter 1

Introduction: Reactions at Actinide Surfaces

1.1	Introduction	1
1.2	Actinide Surface Chemistry	3
1.3	Studies of Actinide Clean Surfaces	4
1.4	Oxidation and Interaction of Small Molecules with Actinide Surfaces	8
	1.4.1 Oxidation	
	1.4.2 Oxycarbide and Oxynitride	
	1.4.3 Reaction with Small Molecules	
	1.4.4 Nitrides	
	1.4.5 Sulphur Containing molecules	
1.5	Adsorption of Organic Molecules on Actinide Surfaces	24
1.6	Summary	30
1.7	References	31

Chapter 2

Experimental

2.1	Experimental	39
2.2	Data Analysis	40
	2.2.1 Inelastic Background – Background types	
	2.2.2 Complication for Actinides: Asymmetric Tail	
	2.2.3 Spectral Smoothing	
	2.2.4 Spike removal	

2.2.5	Spectral subtraction	
2.2.6	Curve Fitting	
2.2.7	Quantification	
2.2.8	Inelastic mean free path and Depth Calculations	
2.3	References	52

Chapter 3

Photoemission Studies of the Surface Reactivity of Thorium: O₂, NO, NO₂ and N₂O adsorption studies

3.1	Introduction	53
3.2	Results	53
3.2.1	Oxygen Adsorption	
3.2.2	Nitric Oxide Adsorption	
3.2.3	Nitrogen Dioxide Adsorption	
3.2.4	Nitrous Oxide Adsorption	
3.3	Quantification	76
3.4	Discussion	81
3.5	Conclusion	85
3.6	References	87

Chapter 4

The interaction of uranium metal with nitrogen oxides: the formation of an oxynitride

4.1	Introduction	89
4.2	Results	89
4.2.1	Adsorption of Nitrous Oxide	
4.2.2	Adsorption of Nitric Oxide	

4.2.3	Adsorption of Nitrogen Dioxide	
4.3	Discussion	105
4.4	Conclusion	118
4.5	References	120

Chapter 5

Gas adsorption Studies on Np metal by photoemission spectroscopy

5.1	Introduction	122
5.2	Results	122
5.2.1	Adsorption of Oxygen	
5.2.2	Adsorption of CO	
5.2.3	Adsorption of NO	
5.3	Discussion	137
5.4	Conclusion	147
5.5	References	149

Chapter 6

Gas adsorption Studies on Am metal by photoemission Spectroscopy

6.1	Introduction	151
6.2	Results	151
6.2.1	Adsorption of Oxygen	
6.2.2	Adsorption of NO	
6.3	Discussion	160
6.4	Conclusion	163

6.5	References	164
-----	------------	-----

Chapter 7

Conclusion

7.1	Introduction	165
7.2	Actinide Oxidation	165
7.3	Reaction with NO	169
7.4	Conclusion	174
7.5	References	175

Appendix 1

Photoelectron Spectroscopy (PES)

A1.1	Basics of Photoelectron Spectroscopy	I
A1.1.1	X-ray Photoelectron Spectroscopy (XPS)	
A1.1.2	Ultraviolet Photoelectron Spectroscopy (UPS)	
A1.2	Core levels and Final States	VII
A1.2.1	Koopmans Theorem	
A1.2.2	Spin Orbit Coupling, Relative Intensities and Peak Widths	
A1.2.3	Fate of the Core hole	
A1.2.4	Chemical Shift	
A1.2.4.1	Actinides - An alternative view of chemical shifts	
A1.2.5	Surface Sensitivity in XPS	
A1.2.6	Angle Resolved XPS	
A1.2.7	The Reference Level	
A1.3	Secondary Structure	XXI
A1.3.1	X-ray satellites	
A1.3.2	Multiplet splitting	
A1.4	References	XXV

Appendix 2

Instrumentation

A2.1	Introduction	XXVI
A2.2	Requirements for Surface Studies	XXVI
A2.2.1	Ultra High Vacuum Requirements	
A2.2.1.1	Achieving UHV	
A2.2.1.2	Pressure Measurement	
A2.3	The Spectrometers	XXX
A2.3.1	Sample and Gas Handling	
A2.3.1.1	Sample Preparation	
A2.3.1.2	Sample Cleaning	
A2.3.1.3	The gas-handling line	
A2.3.2	Radiation Sources	
A2.3.2.1	The X-ray Source	
A2.3.2.2	X-ray source: Design	
A2.3.2.3	Ultra Violet source	
A2.3.3	The Electron Energy Analyser	
A2.3.4	The Electron multiplier	
A2.4	References	XL

CHAPTER 1**Introduction: Reactions at Actinide Surfaces**

Actinide surface science has previously been reviewed in great detail [1], therefore predominantly recent data will be covered within this literature review. For a description of the techniques used in surface science the reader is referred to references [2-4]. Appendices 1 and 2 give a more detailed description of the spectroscopies and instrumentation used in the work reported in this thesis.

The study of actinide surface chemistry provides a great challenge to both experimental and theoretical chemists. The aim of this review is to provide an introduction to the background of actinide chemical research and an overview of the reactions undertaken with thorium, uranium, neptunium, plutonium, and americium surfaces. A general introduction to the research carried out in actinide surface chemistry is followed by a description of the studies of actinide clean surfaces, oxidation and interaction of small molecules, and the adsorption of organic molecules on actinide surfaces.

1.1 Introduction

Actinide science deals with the chemical, physical, and nuclear properties of a large group of elements ranging from thorium through lawrencium (the actinides). This group of elements, which comprises about 21% of the elements in the periodic table, are unique because most of these elements are man-made (with the exception of the first three members-thorium, protactinium, and uranium). Another common characteristic of these elements is that they are all radioactive, which makes their study a particularly difficult and highly specialized field of science. To perform measurements on highly radioactive materials requires special facilities, instrumentation, and training for their safe handling. These characteristics distinguish actinide science from other research fields.

The chemistry of the lanthanide ($[\text{Xe}] 6s^2 5d^1 4f^n$) series of elements (Ce–Lu) is dominated by the trivalent state arising from the $6s^2$ and $5d^1$ electrons. The $4f$ electrons of these elements lie somewhat lower in energy (with respect to the Fermi level (E_F)) than the $6s^2$ and $5d^1$ levels and hence are considered non-interacting. In strong contrast to this, the first half of the actinide ($[\text{Rn}] 7s^2 6d^1 5f^n$) series of elements (the light actinides) display a multitude of oxidation states. Compared to the lanthanide $4f$ electrons the $5f$ electrons

Th	Pa	U	Np	Pu	Am
					2
3	3	3	3	3	3
4	4	4	4	4	4
	5	5	5	5	
		6	6	6	
			7	7	

Table 1.1. The Available valencies of the light actinides (bold signifies the most stable valencies)[5]

have a greater radial extension and thus become interacting/bonding. The core $4f$ electrons in the light actinides partially screen the nuclear charge allowing just enough extension of the $5f$ wave function so that interaction with the valence electrons can occur. This affords multiple oxidation states (Table 1.1).

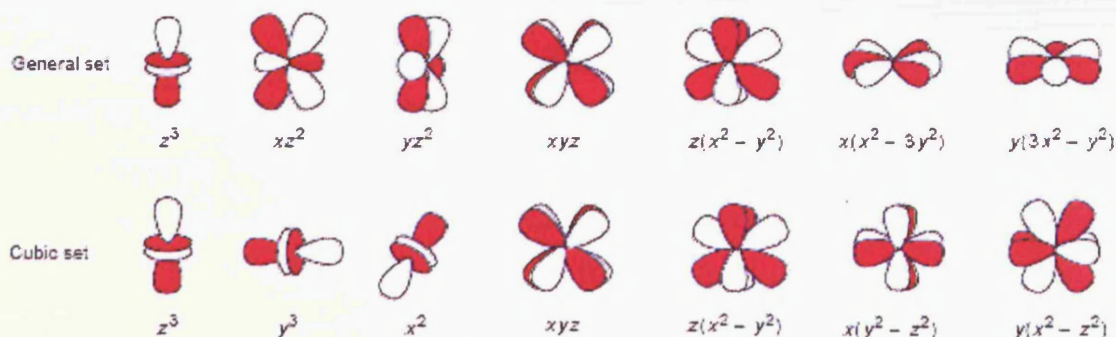


Figure 1.1. Shapes of the f orbitals [6].

The high directionality and unusual shape of the 5f wave function (figure 1.1) affords the unusual metallic ground state structures observed in the actinide metals. Hence the involvement of the 5f electrons gives rise to the much varied and interesting chemistry of these elements.

The latter half of the actinide series, Am onwards, exhibit similar chemistry to the lanthanide elements. The delocalised 5f system of the early actinides is affected by an *actinide contraction*, where an increase in the nuclear charge across the actinide series causes the atomic radii to contract, resulting in the 5f wave function gradually being pulled in more closely to the atomic core. Like lanthanide contraction, the actinide contraction affects both the actinide ions and metals. Since the 5f wave functions only barely overlap to bond in the early actinides this slight contraction pulls the 5f wave function into the core, so for americium the 5f electrons becomes localised, not participating in chemical bonding. The effects are dramatic: the s- and d- electron bands dominate, atomic volumes increase enormously and high symmetry crystal structures are favoured.

1.2 Actinide Surface Chemistry

The unique electronic structure of the actinides has led to a great deal of research into this area [7, 8]. Over the past 30 years there have been many electronic structure determinations of the light actinide metals (Th to Pu) by both photoemission studies [8, 9] and by theoretical calculations [7, 10-12]. It has been generally accepted that high resolution valance-band photoelectron spectra of actinide metals exhibit a gradually increasing 5f spectral intensity in the sequence Th, U, Np, Pu [8]. It is broad, has no distinct sharp features, reaches a maximum at E_F , and indicates the itinerant character of the 5f states. The 5f localization in Am leads to a shift of the 5f photoelectron emission from E_F and the appearance of a multiplet structure [13]. Thus photoelectron spectroscopy has proved to be a very convenient tool to distinguish between band and localized character.

A greater understanding of the interaction of actinide metals/oxide surface with gaseous molecules is also an important area of actinide chemistry. For example, the oxidation and corrosion of uranium as studied by surface techniques is well reported [14-21]. The electronic [22-25], surface [26-29], and defect structure [30, 31], and physical properties [32] of uranium have been extensively investigated for the past 40 years. More recently there has been a growing interest in the investigation of the interactions of small molecules on both poly- and single-crystalline uranium dioxide surfaces [28, 33-42]. These include the interactions of water [36, 39, 43-48], methyl iodide [40], formic acid [37], and methanol [38] with polycrystalline samples.

The most widely reported chemistry of the actinides involves oxides. The large size and electropositivity of the light actinide elements means they are found in nature as oxides and any exposed metal oxidises even in the controlled environment of a high quality inert atmosphere glove box. For example, cations in uranium oxides, the most complicated oxide system known [5], exhibit changes in oxidation states from U^{+4} to U^{+6} , with comparable stability; however several uranium oxide phases, such as UO_2 , the main product of oxidation of uranium metal, U_4O_7 , U_3O_8 , U_4O_9 , and UO_3 , can be easily isolated using moderate conditions.

1.3 Studies of Actinide Clean Surfaces

To understand the electronic interactions of the 5f band, photoemission spectra of the actinide metals has been extensively studied. However, the highly reactive nature of these elements towards electronegative ligands requires samples to be prepared under UHV conditions immediately prior to study. The most common method of cleaning surface contaminants has been by ion sputtering and annealing cycles [49]. More recently in situ sputtering of an actinide target has been used to generate pure samples [50]. Extra attention must be given in preparing a well annealed surface free of carbon and oxygen [51]: high purity metal and clean vacuum conditions are equally essential. For example, impurities on the uranium surface have a profound effect on the hydriding rate [52] and on the adsorption properties of hydrogen

on the surface [53]. Also oxygen is known to reduce the interaction of water with uranium [54]. Previous studies of the initial oxidation of Pu [50, 55-60], have found varying degrees of success in obtaining clean, contamination free, sample surfaces as a starting point. Thin plutonium films [50, 57-59] have successfully provided reasonably clean surfaces but the cleaning of bulk samples has proven much more difficult. Initial contamination at the surface can result in the superposition of photoemission features or even features related to the sample being obscured by those of surface contaminants.

Metallic thorium shows a broad peak between 0 and 2 eV BE in the valence band photoelectron spectra, which is attributed to 6d7s conduction band [8]. Th is the only actinide without 5f-electrons, and can serve as a reference material showing the influence of the 6d7s electrons. The core level photoelectron spectra show Th (4f) metal peaks are located at 342 and 333 eV for $4f_{5/2}$ and $4f_{7/2}$ respectively [8]. The satellites which are located at about 2.2 eV higher binding energy, are understood to be due to the screening of the 4f core hole by the 6d electrons, whereas the main lines reflect the screening by the 5f states, which are above E_F in the ground state, but become populated in the presence of the 4f hole [61].

All the accessible core and valence electron levels of uranium have been comprehensively investigated by recording the X-ray photoelectron spectra (XPS) spectrum of a freshly evaporated, uncontaminated film of the metal [16]. As well as uranium, an intensive investigation of the XPS spectrum characteristic of stoichiometric UO_2 has been reported [19]. Valence band photoemission spectra of U metal [16, 19, 62] provide clear evidence for the itinerant character of the 5f electrons, which were identified to be at E_F . XPS and Bremsstrahlung Isochromat Spectroscopy (BIS) spectra of Th and U metals have been reported in the range of interest for the 5f electrons, below as well as above the E_F [62].

As part of the investigation to study the electronic structure and surface properties of actinide metals and their compounds, photoemission data for clean Np metal and its surface oxidation behaviour have been reported [63].

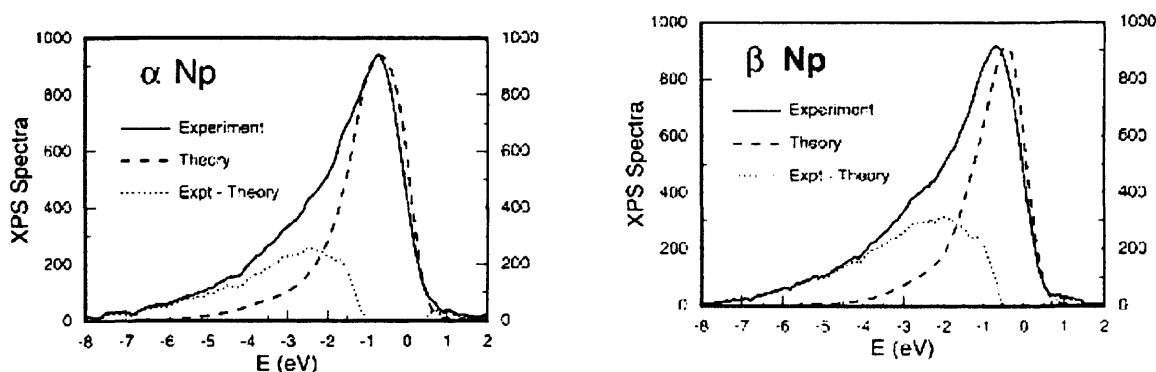


Figure. 1.2. Comparison of the experimental (solid line) and theoretical (dashed line) XPS spectra for α and β Np in arbitrary units. The two curves were scaled to have equal peak heights. Difference spectra are shown as a dotted curve[64].

The electronic structure, density of states, and XPS intensities of the α , β , and γ phases of Np have been theoretically determined [64]. Experimentally, α and β XPS valence band intensities are found to be almost identical and show no evidence for theoretically predicted f-band narrowing (figure 1.2). In addition there is a large additional experimental intensity at higher BE that is not present in the calculations [64].

Plutonium metal has 6 temperature induced allotropes. Of these the most and least dense phases have been studied by PES (alpha and delta respectively). The δ -phase is of particular interest because of the high symmetry crystal structure and the stability of the phase to low temperatures by alloying with small amounts of trivalent elements. Consequently much of the recent experimental and theoretical work has focused on this allotrope. The valence band, of both the alpha and delta phases, show similar features i.e. a sharp feature at E_F accompanied by a broad shoulder at approximately 0.8 eV [59, 65]. The Pu (4f) XP spectra may indicate different peak shifts for these two phases according to different screening mechanisms; well and poorly screened. Further more it has been suggested that the surface of alpha Pu reconstructs to the delta phase [50]. From an experimental point of

view, the reactivity and radioactivity of Pu, and the complexity of the phase diagram, makes it exceedingly complicated to collect high-quality data. Photoemission data for the Ga stabilised δ -phase of plutonium [66] has been reported in which a very clean δ -Pu sample surface was obtained using laser ablation. Gas dosing studies obtained from the same samples have been reported [67].

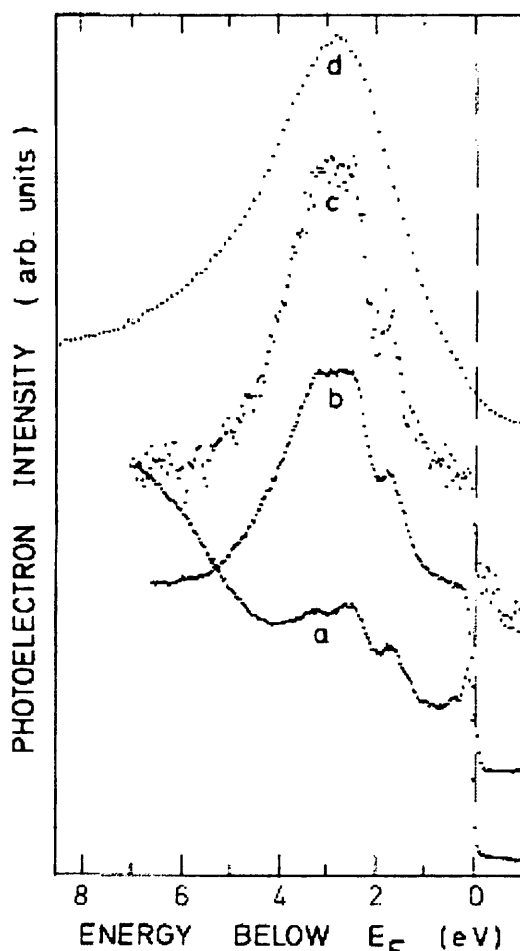


Figure. 1.3. UPS/XPS conduction band spectra of Am metal for (a) 21.1, (b) 40.8 (c) 48.4, and (d) 1253.6eV excitation energy [13]

The solid state properties of Am indicate that Am is the first rare-earth-like metal in the actinide series [10]. Photoemission spectra of the 4f core levels (XPS) and of the conduction band (XPS, UPS) of Am metal have been presented (figure 1.3) [13]. The conduction band spectra of Am metal show that for increasing photon energy the emission at E_F becomes less intense relative to that of a peak around 2.8 eV. The photon energy dependant

excitation probability for f electrons in the UPS regime [68] and the order of magnitude higher probability for 5f electron excitation compared to that for 6d and 7s electrons in the XPS regime [69] give unambiguous evidence of the 5f character of the emission around 2.8 eV; i.e. the 5f electrons are drawn away from E_F . This is an indication of 5f electron localization in Am, and confirms that Am metal is indeed the first rare-earth like metal in the actinide series. The 4f core levels also reflect the degree of 5f electron localization in their shape arising from the photoionisation core hole screening mechanism (an explanation of screening mechanisms can be found in references [70, 71] or there is a brief introduction in appendix 1). The 4f core potential pulls screening levels, that are not occupied in the ground state (i.e. above E_F), down below E_F into the occupied part of the conduction band. The occupation of these levels, either by 5f or by 6d,7s electrons, lowers the total energy of the final state characteristically; the occupation probability depends critically on the hybridization with the conduction states in the initial state (5f states delocalized, final state: "well screened" peak at low binding energy; 5f states localized, final state: "poorly screened" peak at higher binding energy). The 4f core level spectra are dominated by nearly symmetric $4f_{5/2}$ and $4f_{7/2}$ lines, each line being accompanied by a satellite at 4eV lower binding energy. The main peak is attributed to "poor screening" by (6d7s) conduction electrons. The satellite is due to "good screening" by 5f electrons; its intensity is weak since the 5f hybridisation is poor, i.e. the 5f states are almost completely localized.

1.4 Oxidation and Interaction of Small Molecules with Actinide Surfaces

The interaction of the actinide metals with reactive gases permits the investigation of the role of the 5f electrons in chemical reactions [14, 49, 61, 62, 72, 73]. Thorium ($5f^0 6d^2 7s^2$) has unoccupied 5f levels and provides an interesting comparison with uranium ($5f^3 6d^1 7s^2$), neptunium ($5f^4 6d^1 7s^2$), plutonium ($5f^6 7s^2$) etc. which have occupied 5f levels, regarding the role of the 5f electrons in reactions and bonding. Also the elements Pu and Am are in the transition region between delocalized (itinerant) and localized behavior of the 5f states, hence it is interesting to speculate on the role of the 5f

electrons in surface reactions and bonding. For example, the difference in the valance band photoelectron spectra of uranium and thorium dioxides is attributable to uranium having 5f electrons (see Figure 1.4).

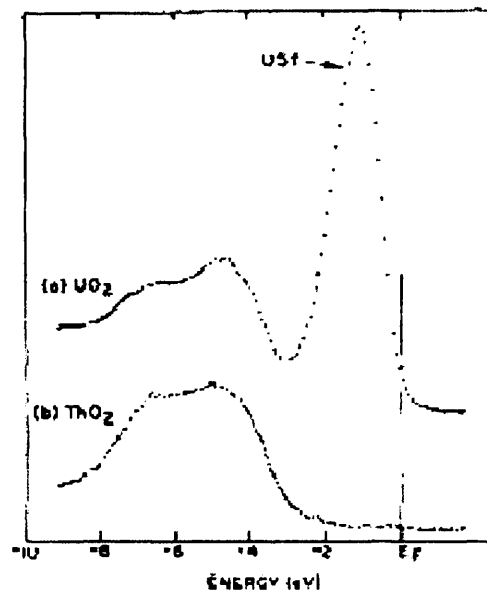


Figure. 1.4. X-ray Photoelectron valance spectra of UO_2 and ThO_2 , clearly highlighting the U (5f) band of UO_2 close in energy to the Fermi edge. [16]

1.4.1 Oxidation

The initial reaction of a clean uranium surface with O_2 has been studied by XPS [49, 74] and Auger electron spectroscopy (AES) [74]. During an early reaction stage for exposures up to 60 Langmuirs (L) (1 Langmuir 1×10^{-6} Torr s^{-1}) U metal and an oxide phase coexist; for higher exposures stage 100L the surface is covered exclusively by oxides. The boundary between the two regimes is strongly temperature dependant; at low temperatures a smaller O_2 exposure is needed for complete oxidation of the surface than at higher temperatures. Whereas a high surface coverage leads to stoichiometric UO_2 or hyperstoichiometric UO_{2+x} [19], low O_2 exposures produce surfaces composed either of substiochiometric UO_{2-x} or islands of UO_2 on U metal [49]. Differing results were obtained earlier by Nornes et al. [48] who exposed a sputtered U surface to 20 L O_2 at 120 K. Measurements of the U (4f) levels using XPS showed the almost complete oxidation of U, as indicated by the shift of the U (4f) photoemission lines to higher energy. The

O (1s) peak had a shoulder on the high BE (binding energy) side. This was ascribed to multiple surface bonding binding states, i.e. chemisorbed O. On the other hand, Allen et al. [17] produced stoichiometric $\text{UO}_{2.0}$ by exposing a clean U surface to 27000 L O_2 at 300 K, while Winer et al. [74] studied the interaction of U with lower oxygen dosages of 40 L and 1200 L at 298 K. The latter found that the binding energies from the photoemission of the O (1s) and the U (4f) levels both shifted to lower values after 1200 L exposure but not for 40 L exposure to O_2 . They attributed this to the change of the work function of the UO_2 semiconductor, when transforming from an n-type (UO_{2-x}) to a p-type (UO_{2+x}). This interpretation is in agreement with the work of Veal et al. [15] who noted that the reduction of $\text{UO}_{2.001}$ by argon ion sputtering resulted in a collective shift of the photoemission lines to higher binding energies (figure 1.5).

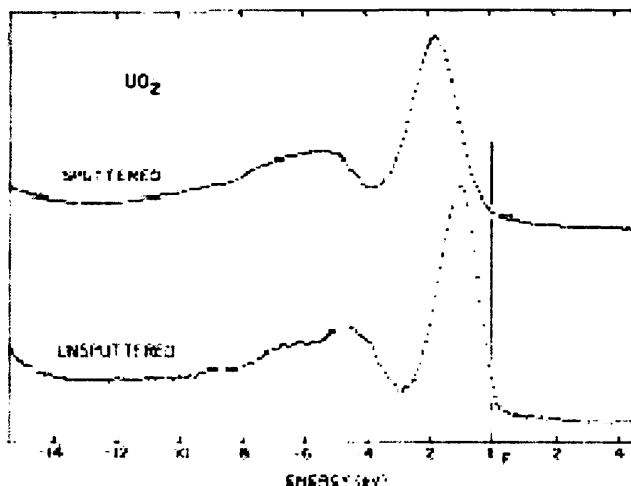


Figure. 1.5. Comparison of the sputtered and un-sputtered UO_2 by XPS [16]

Adsorption of O_2 on U has also been followed by Ultraviolet Photoelectron Spectroscopy (UPS) to help provide clarification of some of the conflicting reports in the literature [75]. The surface oxidation of U at 73 K, 300 K and 573 K was studied, and evidence for the existence of O chemisorbed on the metal at low temperature and low surface exposure was found. Subsequently, substoichiometric UO_{2-x} is formed as long as there is U metal at or near the surface. Finally, at 73 K, UO_{2-x} oxidizes further to UO_2 and

UO_{2+x} while at higher temperatures only substoichiometric UO_{2-x} is formed. The change in oxide stoichiometries results in a decrease in BE of all oxide emission lines, which is attributed to a change of the position of the Fermi energy in uranium oxides. The O (2p)/U (5f) intensity ratio also varies with the surface oxidation due to a transfer of U (5f) electrons into the O (2p) band, which Allen et al. has used to estimate the stoichiometry of the oxides. The initial investigation by Allen et al. [76] into this surface reaction compared oxidation of (111), (110) and (100) planar slices of single crystalline UO_2 , with a polycrystalline sample, in 1 Torr of oxygen at 25 °C, 225 °C and 300 °C using XPS. The rate and extent of oxidation from U_3O_7 to U_3O_8 at 225 and 300 °C varied with the choice crystal face, decreasing along the series: (111) > (110) > (100) > (polycrystalline). Subsequent studies by Allen and co-workers [77] observed changes in the bulk oxide structure and oxide morphology occurring within the top 3 μm of the surface as studied using XRD and scanning electron microscopy (SEM). The oxidation kinetics of unirradiated UO_2 fuel pellets may be described in terms of an initial induction period (during which a linear but small weight gain is observed), followed by a period of bulk oxidation to U_3O_8 . As oxidation nears completion the rate slows, producing an overall weight-gain vs. time curve of sigmoid shape. Various authors have postulated that the induction period represents the growth and formation of a surface layer of U_3O_7 [78, 79]. The eventual disruption of this surface and ultimate spallation of particulates may be due to the lattice contraction which would occur during the formation of a U_3O_7 layer or the production of U_3O_8 , which has an entirely different crystal structure.

There has been no adsorption studies carried out on a neptunium surface to the best of our knowledge. The only previous XPS study of Np was of the formation of surface oxides caused by the slow segregation of residual bulk impurities, and contamination from within the experimental chamber [63]. Phase diagram studies for the system Np-O [80] excluded the existence of bulk NpO and Np_2O_3 , but it has been shown that the deviation of the electronic structure of the surface from that of the bulk may stabilize surface phases that are not formed as bulk materials. Analysis of UPS conduction band spectra of Am metal [81] indicates a contribution of divalent Am atoms

on the surface of bulk trivalent Am metal. It has been shown that in contrast to oxide formation on U and Pu metal surfaces, where surface and bulk oxides are the same, Np forms a lower oxide in addition to NpO_2 . This oxide is identified as Np_2O_3 and is only stable as a surface layer in the presence of Np metal [63].

Room temperature adsorption of oxygen at plutonium metal surfaces studied by XPS and AES has been reported by Larson [60]. At low oxygen exposures (10 L) the plutonium sub-oxide, Pu_2O_3 was produced. The binding energies for the Pu $4f_{7/2}$ and $4f_{5/2}$ peaks for the sesquioxide occur at 424.4 eV and 437.1 eV. Higher oxygen exposures (160 L) transforms the sesquioxide surface layer into PuO_2 with characteristic binding energies for the Pu $4f_{7/2}$ and $4f_{5/2}$ peaks at 426.0 eV and 438.7 eV. The oxide thickness for an exposure of 1.8×10^8 L was 200 Å. On oxidation of plutonium metal to form an outer layer of PuO_2 , there is always a thin layer of Pu_2O_3 , which exists next to the metal. Additional oxidation studies on plutonium metal by UPS [82] at 77 K and 296 K showed that at both temperatures low exposures produced Pu_2O_3 . PuO_2 formation was seen to occur after 60 L exposure at 296 K, and 8L at 77 K. The XPS spectra of trivalent Pu_2O_3 [60] shows the Pu $4f_{7/2}$ and $4f_{5/2}$ peaks at 425.1 and 437.9 eV binding energy respectively; of particular interest is the absence of shake up satellites accompanying the main Pu (4f) peaks. The absence of satellite structure is not unique to plutonium [83], but is also observed for the sesquioxides of neptunium [63], americium [8], and is attributed to various screening mechanisms occurring within these actinide compounds.

1.4.2 Oxycarbide and Oxynitride

The interaction of O_2 with clean uranium produces a UO_2 phase when surfaces are free of carbon contamination [48]. The adsorption of O_2 on a surface contaminated with carbon leads to a UO_xC_y phase [18] which is difficult to characterise chemically. Oxycarbide layers [51] are common on actinide metals and an anomalous temperature dependence for the oxidation

kinetics of the outermost oxycarbide layers on polycrystalline uranium metal has been observed. Normally, oxidation or corrosion reactions are expected to proceed more rapidly as the temperature is elevated. However it was observed that the oxidation reaction reproducibly proceeds at a much faster rate at 25°C than at 280°C [51]. Thin films of UN_xO_y and UC_xO_y have been prepared by reactive sputtering of U in an Ar atmosphere containing O_2 and N_2 admixtures, and sputtering of U and C in an Ar/ O_2 atmosphere (figure 1.6) [84]. The metallic nature of uranium oxycarbides and oxynitrides (at low oxygen content) and the itinerant character of their 5f electrons has been demonstrated [84].

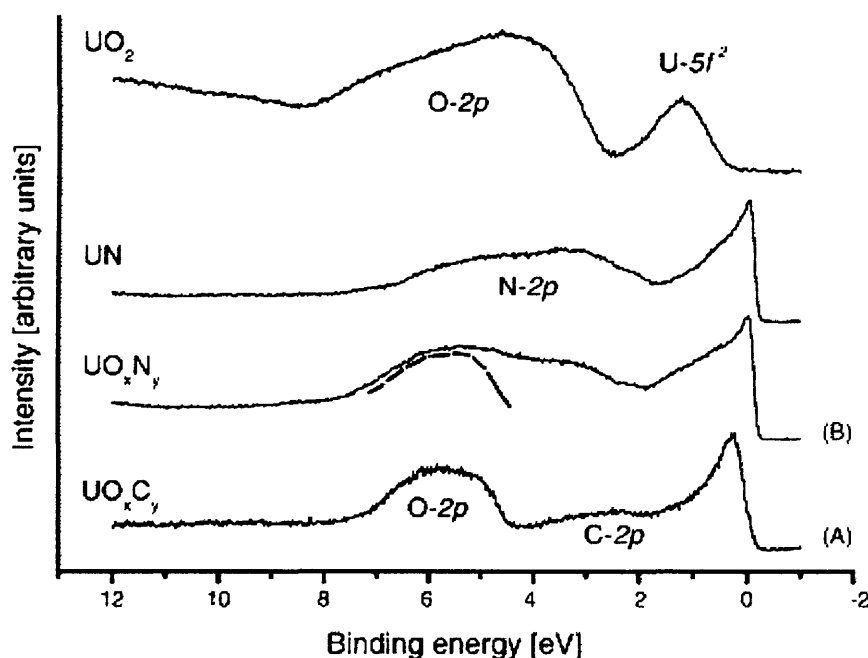


Figure. 1.6. He(II) valence band spectra of: UO_xC_y , UO_xN_y , UN and UO_2 [84]

In addition to the two stable oxides of plutonium, PuO_2 and Pu_2O_3 discussed earlier, Zachariasen [85] was the first to discover the existence of plutonium monoxide film as an impurity on plutonium metal. High temperature XRD studies by Terada et al [86] confirmed the existence of PuO . The failure to prepare bulk quantities of the PuO phase by Mulford [87] led to the suggestion that small amounts of an impurity species such as carbon were required to stabilise the monoxide phase, so producing a plutonium

oxycarbide (PuO_xC_y). The possible existence of Pu monoxide has fuelled much debate over the last 30 years. The subsequent investigation by XPS and AES of the surface phases formed when PuO_2 coated plutonium was heated have since confirmed the existence of the oxycarbide. The thin layer of oxycarbide ($1\mu\text{m}$) formed at 400°C had a composition determined by AES and XPS of $\text{PuO}_{0.65\pm 0.15}\text{C}_{0.45\pm 0.15}$ [87]. The oxycarbide formed was seen to maintain its metallic lustre and integrity after extended air exposure, with the oxycarbide layer formed acting as an effective diffusion barrier against extensive reaction.

1.4.3 Reaction with Small Molecules

McLean et al. examined the chemisorption and initial stages of reaction of O_2 , CO and CO_2 on clean thorium and uranium metals [49]. Low-energy electron diffraction (LEED) studies on single crystals of thorium indicated that adsorption of these gases at room temperature proceeded in a disordered manner [78, 88]. XPS was used to probe the adsorbed species [49] in a study of the chemisorption of O_2 , CO, and CO_2 on thorium and uranium from submonolayer to monolayer coverage at room temperature. AES and secondary-ion mass spectrometry (SIMS) were also used to clarify and confirm the behaviour observed in the XPS studies. Exposure of thorium and uranium metal to oxygen was observed to produce only metal dioxide in both cases. Carbon monoxide and carbon dioxide dissociated on the surface of Th (111) at low coverage to produce carbon and oxygen [49]. The former diffused into the metal to produce a carbide, while the latter remained on the surface as an oxide. "Graphitic" carbon and bound molecular CO were observed at high CO and CO_2 coverage, while a second molecular species, tentatively identified as a monodentate carbonate, was detected at saturation CO_2 coverage. The adsorption of CO and CO_2 on uranium was much simpler since each gas dissociated to produce carbon as carbide below the surface and an oxide on the surface [49].

The adsorption of CO₂, CO and C₂H₄ on Pu metal has been studied at 77 and 296 K by UPS and XPS [82]. At 77 K, CO₂ is dissociated for low dosages (2 L). For higher dosages (> 20 L) CO₂ physisorbs. At 296 K, the behavior is similar to that at 77 K with the exception that physisorbed CO₂ is not observed. Low dosages (4 L) of CO at 77 K results in dissociation of the molecule. At higher dosages (> 6 L) chemisorbed CO is detected. At 296 K, CO behaves in the same way as CO₂ at this temperature. For both CO₂ and CO, the dissociation of the gases is always followed by the formation of some amount of Pu₂O₃. For C₂H₄ at 77 and 296 K, dissociation of the gas is followed either by formation of PuC or chemisorbed C. The formation of some PuH₂ is also observed. At 77 K, and high dosages (100 L), a very weak physisorbed phase of C₂H₄ can be observed. These results are quite different from those for U metal, for which dissociation of the gases is observed at all temperatures, and additionally at low temperatures CO₂, CO and C₂H₄ are physisorbed at exposures higher than 6 L. It is not yet, however, clear, how this large variety of surface reactivity in the actinide series is related to the gradual localization of 5f electrons.

Water is regarded as one of the corrosive gases found in nuclear storage facilities, and it is also known to adsorb easily on uranium surfaces. Several investigations have shown that the adlayer of water has an effect on the kinetics of gas-phase corrosion reactions and also on the coadsorption of other gas species such as hydrogen [89]. Furthermore, radiolytic processes will reduce water to H₂ and O₂, and the build-up of these potentially explosive gases would be detrimental to the storage infrastructure [36]. The interactions of water have been studied under both atmospheric pressure and UHV conditions [36, 89]. The former was carried out on the (001) face of a uranium dioxide single crystal [36], while the latter was investigated using both heavily and slightly oxidised polycrystalline uranium samples [89]. Hydrogen gas formed on all the oxidised uranium samples, and in addition surface hydroxide and oxygen anions readily diffused through the oxide layer to the oxide-metal interface, further oxidising the uranium and forming uranium hydride (UH₃) [89]. The use of electron-stimulated desorption (ESD) and low-energy ion scattering (LEIS) in the single crystal work confirmed the

dissociation of water on the surface of UO_2 and that oxygen diffused into the bulk [36].

Previous studies, using XPS, of water and oxygen adsorbed on uranium have exhibited O (1s) binding energies of ~ 532.4 eV and 530.9 eV for surface-bound hydroxyl and oxygen respectively [48, 49, 54, 90]. Similarly, surface-bound water also undergoes dissociation below 200 K to produce a mixture of OH, O, and H species on uranium [43]. Nornes and Meisenheimer [48] exposed clean, high-purity uranium surfaces to O_2 and $\text{H}_2\text{O}_{(v)}$ at 120 K and followed the reaction with XPS. Their results with oxygen are in good agreement with similar work by Allen et al. [90], McLean et al. [49], and Teterin et al. [20]. Allen et al. studied the reaction of clean uranium with $\text{H}_2\text{O}_{(v)}$ and $\text{H}_2\text{O}_{(v)}/\text{O}_2$ mixtures with XPS [46]. They determined that $\text{H}_2\text{O}_{(v)}$ reacted more rapidly with clean uranium than $\text{H}_2\text{O}_{(v)}/\text{O}_2$ contrary to the findings of Nornes and Meisenheimer [48]; they also determined that the presence of oxygen retarded the $\text{H}_2\text{O}_{(v)}/\text{U}$ reaction, and they suggested that oxygen controlled the transport of OH anion interstitials. However, they did not observe the structure in the U (4f) core-level satellite peaks characteristic of defect cluster formation [20, 46, 90]. They postulated that this is due to the involvement of OH anion in the growth of the surface oxide and the presence of hydrogen in the surface film.

There have been many studies of the interaction of hydrogen [52, 53, 91] and water vapour [54, 92] with clean and oxidised uranium metal. While the overall hydriding reaction of uranium is known empirically [52], the elementary reaction steps or mechanism are yet to be determined. In an effort to begin to elucidate the reaction steps Balooch and Hamza [45] measured the initial sticking probability and dissociative adsorption of dihydrogen on uranium and the reaction probability for the formation of uranium hydride. The high reactivity of uranium metal towards water vapor and oxygen dictate that clean metal surfaces are not found in technical situations. Thus, the changes in the hydrogen adsorption and recombination properties on oxidized and water-covered surfaces were also studied [45]. In the work reported by Balooch and Hamza [45], the fundamental interactions

of hydrogen and water on uranium metal were examined using the combined techniques of molecular beam scattering, thermal desorption mass spectroscopy (TDMS) and atomic force microscopy (AFM). Hydrogen was observed to desorb in three states from uranium following H₂O exposure. Manner et al. [43] have used UPS, XPS and static secondary ion mass spectroscopy (SSIMS) to follow the interfacial growth of surface hydroxyls following exposure of UNb alloys to water. Furthermore, the thermal conversion of surface hydroxyls to oxide with concomitant release of H₂ (or D₂) was also monitored and appeared to contrast with the inferences made by Balooch and Hamza [45].

In the light of this inconsistency, the fundamental interaction of water at uranium metal surfaces was re-examined [43], using the combined techniques of TDMS, SSIMS, UPS and XPS, and a different interpretation for hydrogen desorption following water exposure at uranium surfaces was suggested. These studies provide an additional insight into the reactivity of D₂O on clean uranium and the adsorbed species present as a function of temperature and exposure, and conclude that the combined data [45, 48, 54] previously reported were not complete, thereby preventing an adequate description of the uranium-D₂O interaction. At low temperatures (85 K), D₂O adsorbs dissociatively at low exposures (≤ 1.2 L) forming a mixture of surface-bound OD, O and D species while at higher exposures both molecular and dissociative adsorption is observed. The OD species are relatively stable up to ~ 200 K; above this temperature their concentration rapidly decreases (undetectable at $T \geq 400$ K). Three D₂ desorption stages were observed upon annealing a D₂O layer(s) on a uranium surface prepared at 85 K. First, deuterium atoms recombining directly from dissociating OD/D₂O groups between 120 and 300 K; secondly, recombination of deuterium adsorbed directly on the metal surface at ~ 395 K (≤ 1.2 L), and finally deuterium atoms that interact with the metal and recombine and desorb in the presence of an oxygen layer at ~ 435 K (≥ 1.2 L). At 300 K, adsorption is primarily dissociative with the formation of OD groups at high exposures (≥ 3.0 L). Similar to adsorption at 85 K, three D₂ desorption states are observed in the TDMS spectra when D₂O is adsorbed at 300 K. The

origin of these peaks is the same as for the 85 K experiment except that the desorption temperature for the last peak is notably higher. This difference in T_{\max} for the high-temperature peak when dosing at 300 K is attributed to the thicker oxide/oxygen layer obtained when exposing the surface to D_2O at 300 K.

The presence of moisture in air accelerates the oxidation rate of plutonium at room temperature by 200 times; the rate is increased by five orders of magnitude at 100°C . A mechanism for this water-catalysed reaction has recently been proposed [93] to occur by the formation of hyperstoichiometric plutonium oxide (PuO_{2+x}) and hydrogen. In the hyperstoichiometric oxide Pu (IV) cations of PuO_2 are replaced by Pu (VI) and an equal number of O^{2-} ions occupy octahedral interstices. Hydrogen produced from the reaction combines with surface oxygen atoms to reform water on the surface.

Thermal dehydration experiments of Pu oxides prepared and treated under a variety of conditions, coupled with analysis of standard compounds has led to a better understanding of the PuO_2 surface [94]. Surface hydroxylation occurred rapidly at very low H_2O vapour exposure. At room temperature, the hydroxylated layer was about 3 nm thick. The surface hydroxides resist thermal decomposition up to 590°C . Important factors influencing surface chemistry are processing conditions (thermal treatment, in particular) and specific activity. Active sites for the reaction of H_2O and other small molecules can be renewed by thermal energy or by effects of radiation. Other properties such as surface area, particle size and particle morphology, although not specifically addressed in this study, are also expected to be important.

PuO_{2+x} showed evidence of extensive hydroxylation and spectroscopic features that are consistent with higher Pu oxidation states, and suggestive of Pu(V) [94]. Curve fitting of the Pu (4f) levels indicated that about 10% of the Pu could be in this higher oxidation state. Pu oxide exposed to air will display the complex surface chemistry demonstrated by the hyperstoichiometric Pu oxide, including a small fraction of Pu in oxidation

states greater than (IV). High-fired PuO_2 (heated at 900 °C or higher for hours or longer) has been shown to be more highly ordered and more stoichiometric (purely Pu(IV)), thus more difficult to dissolve than low-fired material [95]. The higher degree of surface hydroxylation observed for PuO_{2+x} powders may effectively increase apparent Pu solubility because hydrated PuO_2 ($\text{PuO}_2 \cdot \text{H}_2\text{O}$ or $\text{Pu}(\text{OH})_4$) has a higher free energy than stoichiometric high-fired PuO_2 and is therefore more soluble and prone to surface corrosion. A review of the solubility of tetravalent actinides found greater solubility for amorphous PuO_2 than for crystalline PuO_2 in acidic solutions [96].

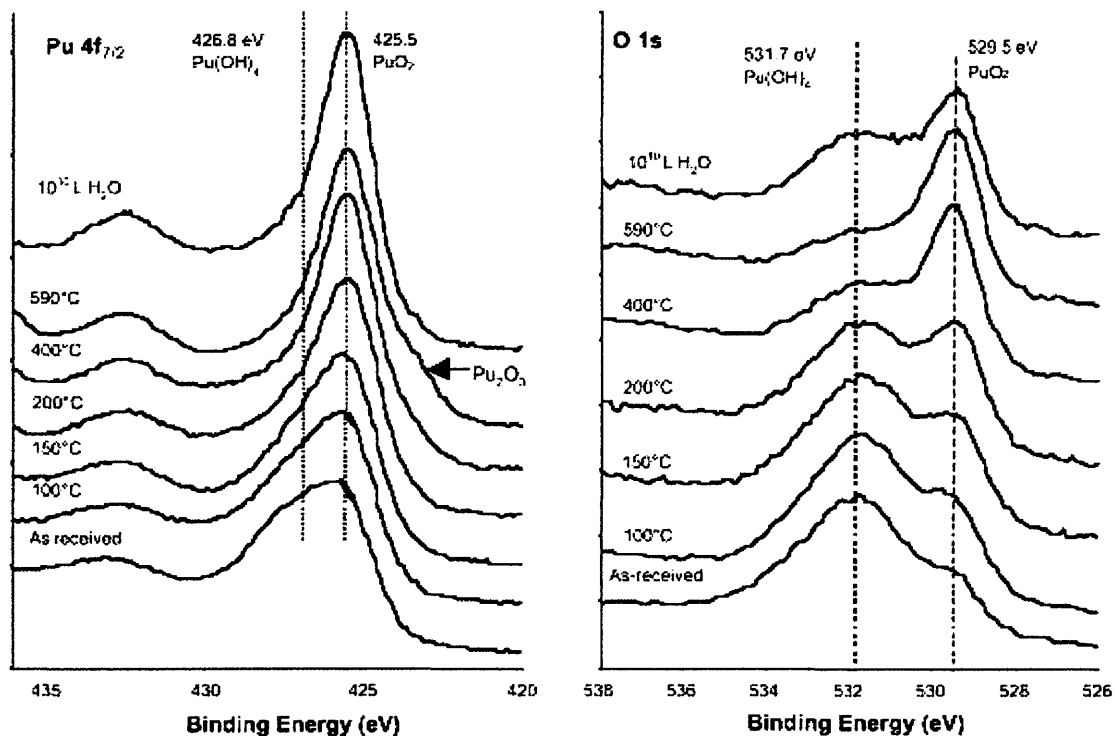


Figure 1.7. $^{239}\text{PuO}_2$ thermal dehydration. Pu $4f_{7/2}$ and O $1s$ core levels for a $^{239}\text{PuO}_2$ powder in the as-received condition, through a series of thermal treatments, then followed by exposure to 10^{10} L H_2O . Pu $4f$ peaks narrow and become more bulk dioxide-like as the O $1s$ dioxide peak grows with respect to the hydroxide intensity. Exposure to H_2O vapor restores some surface hydroxides and eliminates the reduced Pu oxide [94].

Pu adsorbed from water on mineral surfaces is often observed by XPS in the +4 state with peak positions and line shapes corresponding to those observed for the humid-air-exposed PuO_2 and $\text{Pu}(\text{OH})_4$ samples [97]. XPS spectra observed on air-exposed Pu metal also share many of the same

features – shake-up satellites characteristic of Pu (IV) and broad peaks that indicate multiple chemical states for both Pu and O [94] (figure 1.7).

Plutonium readily reacts with hydrogen forming PuH_x , where x varies from 1.9 to 3.0. Plutonium hydrides have been shown [98] to form in the fluorite structure similar to PuO_2 . The ever-present layer of oxide on the surface further complicates the reaction of metallic plutonium with hydrogen. Hydrogen can only react at the metal surface by penetration at cracks and spallation sites on the plutonium oxide, and the hydriding rate increases exponentially as nucleation sites grow. Once the entire metal surface is covered with hydride, the reaction rate is extremely rapid, the reaction rate of H_2 with the plutonium surface being 10^{11} times faster compared to the reaction with dry air. The rapid enhancement in the reaction rate is due to the rapid dissociation of adsorbed H_2 . Although the mechanism for this dissociation is still unclear, two mechanisms have been proposed by Haschke [99]. The first suggests that the formation of PuH_x catalyses the dissociation reaction and promotes the transport of atomic hydrogen to the hydride metal interface. Alternatively cubic Pu_2O_3 on the metal surface is the catalyst for the reaction. Whichever proposed mechanism is correct both anion deficient fluorite structures of PuH_x and cubic Pu_2O_3 have vacant tetrahedral and octahedral sites, able to transport anions such as hydrogen and oxygen.

Surface plutonium hydride (PuH_x) is seen to catalyse the corrosion reaction with oxygen [100]. The reaction between oxygen and the pyrophoric plutonium hydride produces heat and an oxide layer, and the rise in temperature from the reaction is sufficient to produce the cubic sesquioxide. The hydrogen produced at the oxide-hydride interface moves through the PuH_x layer increasing the stoichiometry of the hydride. Excess hydrogen is continuously produced at the oxide-hydride interface and consumed at the hydride-metal interface. This hydride-catalysed reaction continues until all the metal is consumed.

1.4.4 Nitrides

In an attempt to elucidate the nature of the 5f electrons in actinide compounds, Norton et al. report a detailed photoemission study of Th, ThN, U, UN, and UO₂ [14]. The measurements provide convincing evidence that the 5f electrons of UN are located in a narrow band at the Fermi level. An XPS study of ThN prepared by N₂ exposure of the Th surface at high temperatures led to the conclusion that emission intensity has been completely removed in the energy range down to 1.3 eV below the E_F [14]. Reactive sputtering of U in nitrogen containing Ar has been demonstrated to be a convenient method for preparation of high purity films of U nitrides [101] (figure 1.8). This work showed how the variable concentration of the highly reactive atomic nitrogen can determine the stoichiometry of deposited nitrides. This opened up the possibility of the preparation of actinide nitrides with greater nitrogen content and their study under UHV conditions.

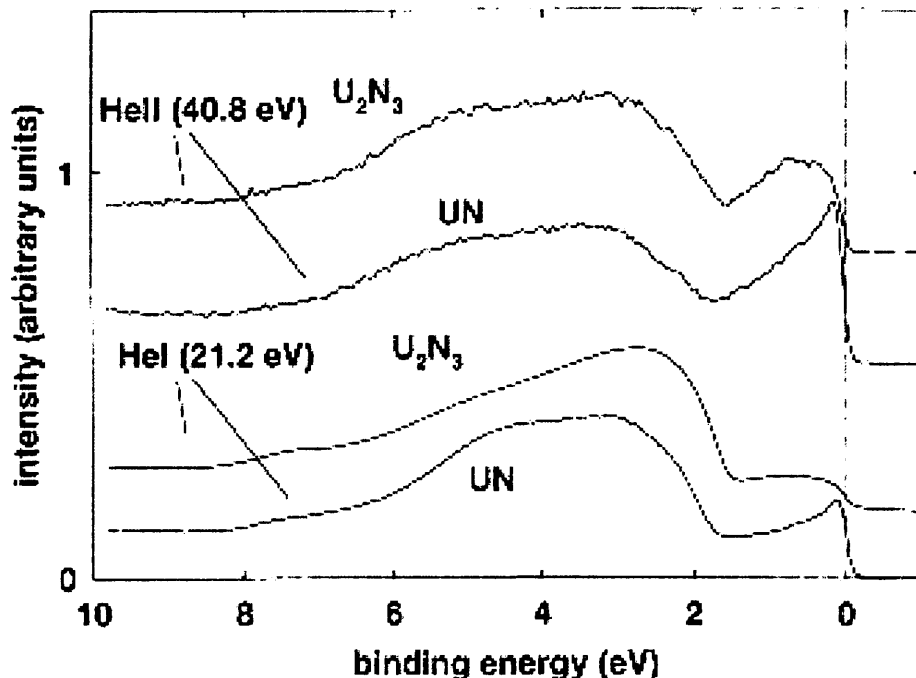


Figure. 1.8. Comparison of HeI ($h\nu=21.2$ eV) and HeII (40.8 eV) valence band spectra of UN and U₂N₃ [101].

Three stable U–N phases were reported: UN (fcc), hexagonal sesquinitride (β -U₂N_{3-x}) existing at higher temperatures, and bcc sesquinitride (α -U₂N_{3+x}).

In addition, fcc UN_{2-x} has been reported [101], but it is not clear whether it exists as a separate phase or forms in a homogeneous transition from α - U_2N_{3+x} by filling holes in the defective lattice (interstitial nitrogen). UN is the lowest nitride and coexists with U metal at low N content. Compared to U nitrides, the nitrides of Th are known to be much less stable. However Gouder and coworkers have reported the synthesis of oxygen-free thin layers of Th, ThN [61].

Allen and Holmes reported a similar method used to produce UN surfaces [102], by bombarding a U metal surface with activated N. XPS spectra revealed sharp U (4f) photoemission lines, leading them to infer the formation of one well-defined U phase. After exposure to air, the N (1s) peak shifted to lower BE and a second component appeared at higher BE (399.4 eV), which was tentatively attributed to an oxidised nitride species. The XPS valence-band study showed, after nitriding of the metal surface, a decrease in the intensity at E_F and the appearance of the U–N band at 3 eV. This result appears to contradict with UPS data reported in the previous studies, which showed a high intensity peak at E_F and a weaker intensity peak at 3 eV. The discrepancies discussed above suggest that two different uranium nitrides can be synthesised by varying the preparation conditions. The discrepancies in these results have been addressed by Black et al. [101]. Reactive sputtering of U and Th in Ar gas containing N has proved to be a convenient method for preparation of high-purity films of actinide nitrides [61, 101].

Unlike Th and U, the Pu-N phase diagram exhibits only one known phase, namely, PuN [103], analogous to ThN and UN. In situ preparation of Pu-N enabled the study of its electronic structure by XPS and UPS. Sputter-deposition synthesis in the presence of N plasma proves that no higher nitride analogous to U_2N_3 or Th_3N_4 exists for Pu, and PuN is the only known nitride [104]. The large scale features of its electronic structure are similar to ThN and UN regarding the position of the N (2p) states. The 5f states appear in the vicinity of the Fermi level, exhibiting the same type of features at 0.85 eV, 0.50 eV, and E_F , observed in the majority of Pu systems studied.

1.4.5 Sulphur containing molecules

New interest has arisen recently in the possibility of using depleted uranium in catalysts for various applications. Uranium oxides (e.g., UO_2) display catalytic activity for the oxidative destruction of volatile organic compounds (VOCs) such as butane, benzene, chlorobenzene, and other chlorine containing molecules [105, 106]; UO_2 has also been used as a catalytic support for steam reforming of methane [107]. Surface defects on single crystals of UO_2 have been shown to influence the surface chemistry [33, 34]. Recently, the adsorption of H_2S on a single crystal of UO_2 [108] (figure 1.9) and polycrystalline UO_2 has been studied. It is found that hydrogen sulfide (H_2S) dissociates on both surfaces and atomic sulfur is accumulated on the surface. Recently adsorption and desorption of thiophene on polycrystalline UO_2 has been investigated by means of X-ray photoelectron spectroscopy (XPS), temperature programmed desorption (TPD) and electron stimulated desorption (ESD) at variable exposures and temperatures [109].

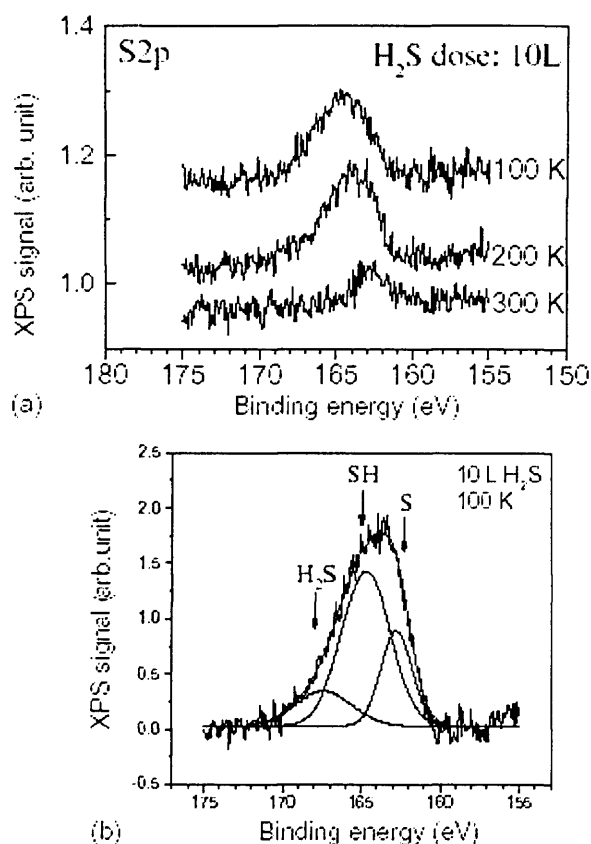


Figure 1.9. (a) Grazing angle S (2p) XPS spectra at different temperatures (100, 200, and 300 K) after 10 L H_2S dose, (b) curve fitting of the S 2p XPS after 10 L dose at 100 K.[108]

The effects of X-ray, UV, and electron irradiation on a thiophene film have also been explored. In brief, it was found that thiophene adsorbs on stoichiometric polycrystalline UO_2 and desorbs reversibly in molecular form, with no evidence of dissociation. However, exposure of adsorbed thiophene to X-rays, UV radiation or an electron beam leads to oligomerization, polymerization and dissociation. It was found also that the reactivity of polycrystalline UO_2 increases when the surface is oxygen-deficient; thiophene dissociates at temperatures as low as 100 K on defective UO_2 surfaces.

1.5 Adsorption of Organic Molecules on Actinide Surfaces

The thermal chemistry of formic acid [37] and methanol [38] on the surfaces of polycrystalline uranium and uranium dioxide under UHV conditions have been investigated. TPD studies of formic acid reported the production of hydrogen from surfaces of both uranium and uranium dioxide [37]. In addition, water and methane were also desorbed from the uranium surface, with carbon monoxide, water, and formaldehyde being the other products. Unlike formic acid, reactions of methanol on both uranium and uranium dioxide yield nearly the same products in the form of hydrogen and methane, with CO as the additional product from uranium dioxide [38].

The direct oxidative coupling of two molecules of acetylene to furan ($\text{C}_4\text{H}_4\text{O}$) over the surface of pure polycrystalline $\beta\text{-UO}_3$ has been reported [110]. In contrast, only traces of furan are formed over $\alpha\text{-U}_3\text{O}_8$ and none on UO_2 surfaces. A comparison with the reactions of other C_2 compounds (ethanol [111], acetaldehyde [112], and ethylene [113, 114]) over $\beta\text{-UO}_3$ indicates the presence of two mechanisms for the synthesis of furan from C_2 compounds: one via aldolization and the other by oxidative coupling. Although the previous highest yield for furan over beta- UO_3 [110] was reported from acetaldehyde [112], considerable formation of crotonaldehyde (formed by β -aldolization of two molecules of acetaldehyde) was also reported. Furan is easily formed from crotonaldehyde. Moreover, acetaldehyde was formed from ethylene as well as from ethanol adding a further complication to the

scheme. The absence of acetaldehyde and crotonaldehyde during acetylene-TPD, clearly suggests the presence of a direct route for making furan from acetylene. Uranium oxide is considered to be a very good catalyst for oxidation reactions [105], and U atoms are very active for carbon-carbon coupling reactions [115]. This is demonstrated by the fact that both routes can be successfully combined on β - UO_3 as evidenced by the direct synthesis of furan ($\text{C}_4\text{H}_4\text{O}$) from acetylene (C_2H_2) [116].

The chemistry of formic acid adsorption on uranium metal and uranium oxide overlayers [37] serves as a basis for studies involving more complex hydrocarbons. Small concentrations of carbon or oxygen containing products were reported to desorb from a clean uranium surface exposed to formic acid. The fact that CO and CO_2 do not desorb from a clean uranium surface is not surprising. Only H_2 , HD, and D_2 desorb in large quantities after exposing a uranium surface to DCOOH or HCOOD [37]. The ratio of the desorption products was dependant on the hydrogen isotope adsorbed on the surface. Surprisingly, the acyl proton contributed much more intensity in these three channels of desorption (H_2 , HD, and D_2) than the acidic proton. A possible explanation could be desorption of the acidic proton as water or an isotope of methane. The desorption temperatures T_{max} for H_2 , HD, and D_2 were somewhat higher than those expected for hydrogen and deuterium on a clean uranium surface [37]. In a study of the adsorption and reactivity of methanol (CH_3OD) at uranium and $\text{UO}_{2.0}$ surfaces [38] the low-temperature adsorption of CH_3OD resulted in the cleavage of the O-D bond to form an adsorbed methoxy species. Unlike formic acid, however, the adsorbed methoxy was stable over a larger temperature range, it being detected in significant quantities at 300 K (decomposition resulted after annealing to 400 K). Approximately 90% of the methoxy species completely decomposes to form a uranium oxy-carbide overlayer. Similarly, formic acid interacts directly with the uranium surface and undergoes complete dissociation to leave surface bound carbon and oxygen with H_2 , HD, and D_2 desorbing at higher temperatures.

Acetone reactions have been reported on the surfaces of U_3O_8 and H_2 reduced U_3O_8 using TPD, while the surface and bulk characteristics were followed by XPS and XRD [117]. A considerable difference between the reactivity of the surfaces of U_3O_8 and UO_2 to acetone are reported. On U_3O_8 a carbon-carbon bond formation reaction producing isobutene and an acetate species during TPD is observed. Isobutene from acetone was not observed on the surfaces of UO_2 . However, on UO_2 , acetone reacted to give mainly propene. Propene is most likely formed due to the capacity of the UO_2 surface to accommodate large quantities of atomic oxygen in interstitial positions whilst maintaining the fluorite structure.

The first study of the surface reactions of an organic molecule over a UO_x single crystal was reported by Chong et al. [33]. The attenuation of the U ($O_3P_1P_1$) Auger line was successfully used to calibrate the surface coverage and determine the sticking coefficient of ethanol over stoichiometric UO_2 (111). The sticking coefficient of ethanol at room temperature is coverage dependant, and is ca. 10^{-2} near saturation. TPD results have shown the ability of UO_2 (111) to dehydrogenate and dehydrate ethanol to form acetaldehyde and ethylene, respectively, with a ratio of ca. 0.8. The reaction selectivity is not sensitive to either ethanol coverage and O_2 dosing. The comparison with other single crystals of oxide materials indicates that overall, UO_2 (111) behaves like the faceted TiO_2 (001) single crystal and unlike TiO_2 (110) single crystal [42]. The reason for this is most likely the coordinative unsaturation of U^{4+} cations (like Ti^{4+} in faceted TiO_2 (001) and unlike the TiO_2 (110) where half of the surface Ti^{4+} cations are fully saturated). Moreover, although ZnO (0001)-O does not adsorb primary alcohols dissociatively, UO_2 (111) does. This might be explained by a larger interstitial area in the case of UO_2 (about twice that of ZnO) which allows electronic interaction between the adsorbate and U^{4+} cations in the second layer. An inverse linear relationship between the dielectric constant of five oxides and the dehydrogenation/dehydration reaction selectivity during ROH-TPD is observed. Equally important, it appears that large negative values of the Madelung potential of the metal cation orient towards dehydration reactions while negative values orient towards dehydrogenation reactions.

The interaction of formic acid with UO_2 (111) single crystal surfaces studied through dynamic-LEED, and TPD experiments, has recently been reported [41]. The sticking probability of formic acid, acetic and propionic acids was found to track the gas-phase acidity of these molecules. Two states for formate decomposition were observed over the stoichiometric surface. The first is through the dehydration pathway, to give CO and H_2O (α -state) and is independent of initial surface coverage. The second pathway is dehydrogenation to CO_2 (β -state) and is coverage dependant. Surfaces modified by argon ion bombardment, exclusively afford CO_2 desorption by dehydrogenation. Moreover, high coverages of formaldehyde (formed on the reduced surface) react to give ethylene, via reductive coupling. The increase in formaldehyde production on the reduced surface is ascribed to the presence of two types of reduction site. The population of the first type decreases with increasing sputtering time, while that of the second type increases. It is thus reasonable to consider this first type as resulting from reactions on oxygen defected but ordered surfaces. Previously, the reactions of ethanol [33, 34] and acetic acid [35] on stoichiometric, electron-bombarded, and argon ion-sputtered UO_2 (111) surfaces have been reported. The reactions of these C_2 molecules exhibit similar chemistry to those observed on other transition metal oxide surfaces such as TiO_2 , in which dehydration and dehydrogenation reactions were reported. Reductive coupling and aldol condensation reactions have also been reported for the reaction of acetic acid on a UO_2 (111) which had been made defective by electron irradiation [35].

The reactions of acetaldehyde have been studied on the stoichiometric, electron-irradiated, H_2 -reduced, and argon ion bombarded surfaces of UO_2 (111) using TPD [42], in order to explore how the chemistry would change with respect to surface structure and oxidation states. Several reactions have been observed: oxidation (dehydrogenation) to ketene, reduction (hydrogenation) to ethanol, aldol condensation to crotonaldehyde, and cyclization to benzene. While only traces of benzene were observed on the stoichiometric surface, oxidation to ketene as well as aldol condensation to crotonaldehyde was also observed (in addition to benzene) on the H_2 -

reduced surface. The electron and argon ion sputtered surfaces were both able to reduce and oxidize acetaldehyde to ethanol and ketene, respectively. The production of benzene was also found to be favoured on more reduced and defective surfaces, the argon ion-sputtered surface giving the highest benzene yield.

For the reaction of ethanol on a UO_2 (111) single crystal surface [33], two reaction pathways were observed on the stoichiometric surface. These are dehydration to ethylene and dehydrogenation to acetaldehyde, forming with a product ratio of near unity. Pre-dosing the surface with oxygen was found to alter neither the selectivity nor the yield of the dehydrogenation/dehydration reactions. The absence of an effect due to pre-dosing the surface with oxygen (>100 L) at room temperature was attributed to the fact that the surface of UO_2 (111) is oxygen terminated [26, 27]. Furthermore, scanning tunnelling microscopy (STM) studies [118] have indicated that additional adsorbed oxygen atoms are positioned at the interstitial sites of the surface. Taking into account these two factors it has been proposed that adsorbed oxygen is easily displaced from the surface by ethanol, and thus is not present to influence the reaction pathways for ethanol in TPD experiments [33]. The reaction of ethanol on the argon ion bombarded surface of UO_2 (111) single crystal was studied by XPS and TPD [34]. TPD results show that, in addition to products obtained via dehydrogenation and dehydration pathways, products formed via reductive coupling and ketonisation were observed. The operation of these pathways is supported by the presence of surface acetate, acetaldehyde and ethoxide species, identified from XPS measurements on this reduced surface. In addition to dehydrogenation and dehydration pathways, several minor reactions were reported. These were: (1) oxidation to acetates followed by dehydration (ketene) and ketonisation (acetone), and (2) reduction to acetaldehyde followed by coupling to butene. XPS of the O (1s) region showed no significant changes before and after sputtering. However, the C (1s) spectra showed the existence of traces of carbon-containing species around 282.3-282.7 eV on both the sputtered and non sputtered surfaces, which might be attributed to UC. The formation of uranium carbide has been

reported on the surface of uranium metal after vacuum annealing [18, 119], as well as after the reaction of methanol [38].

The conditions for the formation of uranium iodides have been documented and the physical properties of uranium halides have been reported [5]. One approach for investigating the reactions of uranium-containing material with iodides has been taken [40]. The approach was to prepare well characterized clean uranium metal and uranium dioxide surfaces under ultra high vacuum conditions and to investigate quantitative and chemical characteristics of the surfaces following the adsorption and reaction with gaseous methyl iodide using XPS and AES techniques. The surface chemical reactions differ in that UC and $U\text{I}_3$ are formed on uranium while CH_3I adsorption on UO_2 could yield UOCH_3 and UOI , H_3CUO and IUO or IUOCH_3 and H_3CUOI surface species. The identification of the surface species on uranium was accomplished by a detailed examination of the XP spectra. For uranium metal it was shown that CH_3I adsorption could be fitted to a precursor kinetic model. The implication of this finding led to the suggestion that the adsorption of CH_3I via a uranium-iodine bond is the rate determining step.

It has been shown previously that the complete oxidation of VOCs by uranium oxide catalysts takes place by a redox mechanism with lattice oxygen, probably at defect sites, as oxidant [120]. The rate determining step of this reaction has not been unequivocally determined. However, it is feasible that the rate determining step may be the reoxidation of the reduced catalyst, and this has also been proposed for other redox oxidation catalysts [121]. The presence of water vapour is known to promote the oxidation of uranium oxides when compared to oxidation rates under dry conditions [92]. It is therefore feasible that the oxidation rate for VOCs is promoted by water as the catalyst reoxidation rate is enhanced. The reoxidation of the catalysts may also aid desorption of CO_2 , although the higher rates of benzene oxidation compared to propane indicates that desorption of CO_2 may not be rate limiting. The role of water may also have an effect on the initial activation of the hydrocarbons, indeed, co-feeding 2.6% water reduced the light off temperature for propane by 100°C [122]. This effect may be due to

modification of the uranium oxide surface by hydroxylation which effectively aids hydrocarbon activation. Uranium oxide based catalysts are active for the oxidation of benzene and propane to carbon oxide in the absence of co-fed water. However the addition of low levels of water (2.6%) has a marked effect on oxidation activity, promoting the rate of complete oxidation. The addition of higher concentrations of water (12.1%) has a detrimental effect on oxidation activity. The addition of water also increases selectivity towards CO_2 and this may be due to the water gas shift reaction [122]. The origin of the increased activity is not clear but may be due to modification of the U_3O_8 catalyst surface by hydroxylation, and the contribution from new reaction pathways, such as steam reforming, cannot be discounted.

1.6 Summary

This literature review has covered a general introduction to actinide science, followed by the surface science measurements of thorium, uranium, neptunium, plutonium and americium metals and reactions with reactive gases. It is quite clear from the literature that there has been a great deal more interest in actinide oxide chemistry, in particular uranium oxide in relation to possible catalytic properties. Also the surface chemistry of uranium and plutonium have received greater attention than the other light actinides (and americium) as these are the two most amenable elements i.e. amounts available. Notwithstanding the uranium and plutonium research there is significantly less research published with regard to clean metal studies. However, if one wants to investigate the interaction and role of the 5f electrons then it is comparison of reactions with a range of actinide metals (in particular the light actinides) that will afford this information. Nevertheless, obtaining the metal surface free of contamination can be problematic and hence makes such a study difficult. The majority of reactions reported in this area are of the reaction of actinide metals with gases found in natural environment (e.g. CO , CO_2 , H_2 , H_2O , O_2 , and N_2). This leaves a wide scope of investigation into more molecules and the role of 5f electrons in surface reactions and bonding.

1.7 References

1. J.M.Fournier, Actinides - chemistry and physical properties, Structure and Bonding, 1985. **59/60**. 127 - 196.
2. M.P.Seah, Practical Surface Analysis, ed. D.Briggs and M.P.Seah. 1990, Chichester: John Wiley and Sons.
3. D.P.Woodruff and T.A.Delchar, Modern Techniques of Surface Science. Second ed. Cambridge Solid State Science Series. 1999, Cambridge: The Press Syndicate of the University of Cambridge. 586.
4. S.Hufner, Photoelectron Spectroscopy. Third ed. 2003, Berlin Heidelberg: Springer. 662.
5. F.A.Cotton and G.Wilkinson, Advanced Inorganic Chemistry. fifth ed, New York: Wiley.
6. D.L.Clark, Los Alamos Science, 2000. **26**.
7. M.S.S.Brooks, B.Johansson, and H.L.Skriver, Chap. 3, in Handbook on the Physics and Chemistry of the Actinides, A. J. Freeman and G. Lander, Editors. 1984, Elsevier: Amsterdam.
8. J.R.Naegele, J.Ghijsen, and L.Manes, Structure and Bonding, 1985. **59-60**. 197-262.
9. Y.Baer, Chap 4, in Handbook on the Physics and Chemistry of the Actinides.
10. H.L.Skriver, O.K.Andersen, and B.Johansson, Physical Review Letters, 1978. **41**. 42.
11. H.L.Skriver, Physical Review B, 1985. **31**. 1909.
12. L.E.Cox, O.Eriksson, and B.R.Cooper, Physical Review B, 1992. **46**. 13571.
13. J.R.Naegele, L.Manes, J.C.Spirlet, and W.Muller, Physical Review Letters, 1984. **52(20)**. 1834.
14. P.R.Norton, R.L.Tapping, D.K.Creber, and W.J.L.Buyers, Physical Review B, 1980. **21**. 2572-2577.
15. B.W.Veal and D.J.Lam, Physical Review B, 1974. **10**. 4902.
16. J.C.Fuggle, A.F.Burr, L.M.Watson, D.J.Fabian, and W.Lang, Journal of Physics F (Metal Phys.), 1974(4). 335.

17. G.C.Allen, J.A. Crofts, M.T. Curtis, P.M. Tucker, D. Chadwick, and P.J. Hampson, *Journal of the Chemistry Society Dalton Transactions*, 1974. 1296.
18. G.C.Allen and P.M.Tucker, *Journal of the Chemical Society-Chemical Communications*, 1973(Dalton Trans). 470.
19. G.C.Allen, P.M.Tucker, and I.R.Trickle, *Philosophical Magazine B-Physics of Condensed Matter Statistical Mechanics Electronic Optical and Magnetic Properties*, 1981. **43**(4). 689-703.
20. Y.A.Teterin, V.M.Kulakov, A.S.Baev, N.B.Nevzorov, I.V.Melnikov, V.A.Streltsov, L.G.Mashirov, D.N.Suglobov, and A.G.Zelenkov, *Physics and Chemistry of Minerals*, 1981. **7**(4). 151-158.
21. L.E.Cox, *Journal of Electron Spectroscopy and Related Phenomena*, 1982. **26**(2). 167-171.
22. L.E.Cox, W.P.Ellis, R.D.Cowan, J.W.Allen, and S.J.Oh, *Physical Review B*, 1985. **31**(4). 2467-2471.
23. K.Winer, F.Wooton, C.A.Colmenares, and R.L.Smith, *Journal of Luminescence*, 1986. **35**(6). 311-319.
24. L.E.Cox and W.P.Ellis, *Solid State Communications*, 1991. **78**(12). 1033-1037.
25. F.Jollet, T.Petit, S.Gota, N.Thromat, M.GautierSoyer, and A.Pasturel, *Journal of Physics-Condensed Matter*, 1997. **9**(43). 9393-9401.
26. K.A.Thompson, W.P.Ellis, T.N.Taylor, S.M.Valone, and C.J.Maggiore, *Nuclear Instruments & Methods in Physics Research*, 1983. **218**(1-3). 475-479.
27. W.P.Ellis and T.N.Taylor, *Surface Science*, 1978. **75**(2). 279-286.
28. W.P.Ellis, *Journal of Chemical Physics*, 1968(48). 5695.
29. M.R.Castell, C.Muggelberg, G.A.D.Briggs, and D.T.Goddard, *Journal of Vacuum Science & Technology B*, 1996. **14**(2). 966-969.
30. P.R.Graves, *Applied Spectroscopy*, 1990. **44**(10). 1665-1667.
31. T.Petit, C.Lemaignan, F.Jollet, B.Bigot, and A.Pasturel, *Philosophical Magazine B-Physics of Condensed Matter Statistical Mechanics Electronic Optical and Magnetic Properties*, 1998. **77**(3). 779-786.

32. C.A.Colmenares, The Oxidation of thorium, uranium and plutonium, in Progress in Solid State Chemistry, G. S. E. J.O. McCaldin, Editor. 1975, Pergamon Press: Oxford. p. 139.
33. S.V.Chong, T.R.Griffiths, and H.Idriss, Surface Science, 2000. **444**(1-3). 187-198.
34. S.V.Chong, M.A.Barteau, and H.Idriss, Catalysis Today, 2000. **63**(2-4). 283-289.
35. S.V.Chong and H.Idriss, Journal of Vacuum Science & Technology a- Vacuum Surfaces and Films, 2000. **18**(4). 1900-1905.
36. M.N.Hedhili, B.V.Yakshinskiy, and T.E.Madey, Surface Science, 2000. **445**(2-3). 512-525.
37. W.L.Manner, J.A.Lloyd, and M.T.Paffett, Surface Science, 1999. **441**(1). 117-132.
38. J.A.Lloyd, W.L.Manner, and M.T.Paffett, Surface Science, 1999. **423**(2-3). 265-275.
39. L.Nowicki, A.Turos, F.Garrido, C.Choffel, L.Thome, J.Jagielski, and H.Matzke, Nuclear Instruments & Methods in Physics Research Section B- Beam Interactions with Materials and Atoms, 1998. **138**. 447-452.
40. J.G.Dillard, H.Moers, H.Klewenebenius, G.Kirch, G.Pfennig, and H.J.Ache, Surface Science, 1984. **145**(1). 62-86.
41. S.V.Chong and H.Idriss, Surface Science, 2002. **504**(1-3). 145-158.
42. S.V.Chong and H.Idriss, Journal of Vacuum Science & Technology a- Vacuum Surfaces and Films, 2001. **19**(4). 1933-1937.
43. W.L.Manner, J.A.Lloyd, and M.T.Paffett, Journal of Nuclear Materials, 1999. **275**(1). 37-46.
44. J.A.Lloyd, W.L.Manner, and M.T.Paffett, Abstracts of Papers of the American Chemical Society, 1999. **217**. 137-COLL.
45. M.Balooch and A.V.Hamza, Journal of Nuclear Materials, 1996. **230**(3). 259-270.
46. G.C.Allen, P.M.Tucker, and R.A.Lewis, Journal of the Chemical Society-Faraday Transactions II, 1984. **80**. 991-1000.
47. A.G.Ritchie, Journal of Nuclear Materials, 1981. **102**(1-2). 170-182.

48. S.B.Nornes and R.G.Meisenheimer, *Surface Science*, 1979. **88**(1). 191-203.
49. W.McLean, C.A.Colmenares, R.L.Smith, and G.A.Somorjai, *Physical Review B*, 1982. **25**(1). 8-24.
50. T.Gouder, L.Havela, F.Wastin, and J.Rebizant, *Europhysics Letters*, 2001. **55**(5). 705-711.
51. W.P.Ellis, *Surface Science*, 1981. **109**(3). L567-L570.
52. G.L.Powell, W.L.Harper, and J.R.Kirkpatrick, *Journal of the Less-Common Metals*, 1991. **172**. 116-123.
53. E.Swissa, I.Jacob, U.Atzmony, N.Shamir, and M.H.Mintz, *Surface Science*, 1989. **223**(3). 607-620.
54. K.Winer, F.Wooton, C.A.Colmenares, and R.L.Smith, *Surface Science*, 1987. **183**(1-2). 67-99.
55. J.G.Tobin, B.W.Chung, R.K.Schulze, J.Terry, J.D.Farr, D.K.Shuh, K.Heinzelman, E.Rotenberg, G.D.Waddill, and G.v.d. Laan, *Physical Review B*, 2003. **68**. 155109.
56. J.Terry, R.K.Shulze, J.D.Farr, T.Zocco, K.Heinzelman, E.Rotenberg, D.K.Shuh, G.v.d. Laan, D.C.Arena, and J.G.Tobin, *Surface Science*, 2002. **499**. L141.
57. T.Gouder, *Journal of Electron Spectroscopy and Related Phenomena*, 1999. **101-103**. 419-422.
58. T.Gouder, *Journal of Alloys and Compounds*, 1998. **271-273**. 841.
59. L.Havela, T.Gouder, F.Wastin, and J.Rebizant, *Physical Review B*, 2002. **65**. 235118.
60. D.T.Larson, *Journal of Vacuum Science & Technology a-Vacuum Surfaces and Films*, 1980. **17**. 55.
61. T.Gouder, L.Havela, L.Black, F.Wastin, J.Rebizant, P.Boulet, D.Bouexiere, S.Heathman, and M.Idiri, *Journal of Alloys and Compounds*, 2002. **336**(1-2). 73-76.
62. Y.Baer and J.K.Lang, *Physical Review B*, 1980. **21**(6). 2060 - 2062.
63. J.R.Naegele and L.E.Cox, *Inorganica Chimica Acta*, 1987. **139**(327-329).
64. R.C.Albers, A.M.Boring, J.M.Wills, L.E.Cox, O.E.Eriksson, and N.E.Christensen, *Physical Review B*, 1996. **54**(20). 14405.

65. J.Naegele, Numerical Data and Functional Relationships in Science and Technology. Landolt-Bornstein, New Series, Group III. Vol. 23. 1994, Berlin: Springer-Verlag. 300.
66. J.M.Wills, O.Eriksson, A.Delin, P.H.Andersson, J.J.Joyce, T.Durakiewicz, M.T.Butterfield, A.J.Arko, D.P.Moore, and L.A.Morales, Journal of Electron Spectroscopy and Related Phenomena, 2004. **135**. 163-166.
67. M.T.Butterfield, T.Durakiewicz, E.Guziewicz, J.J.Joyce, A.J.Arko, K.S.Graham, D.P.Moore, and L.A.Morales, Surface Science, 2004. **571(1-3)**. 74-82.
68. D.E.Eastman and M.Kuznietz, Physical Review Letters, 1971. **26**. 846.
69. J.H.Scofield, Journal of Electron Spectroscopy and Related Phenomena, 1976. **8**. 129.
70. J.C.Fuggle, M.Campagna, Z.Zolnierek, R.Lasser, and A.Platau, Physical Review Letters, 1980. **45**. 1597.
71. F.U.Hillebrecht and J.C.Fuggle, Physical Review B, 1982. **25**. 3350.
72. L.E.Cox and J.D.Farr, Physical Review B, 1989. **39**. 11142-11145.
73. G.M.Bancroft, T.K.Sham, J.L.Esquivel, and S.Larsson, Chemical Physics Letters, 1977. **51(1)**. 105-110.
74. K.Winer, F.Wooton, C.A.Colmenares, and R.L.Smith, Surface Science, 1986. **177(3)**. 484-492.
75. T.Gouder, C.Colmenares, J.R.Naegele, and J.Verbist, Surface Science, 1990. **235(2-3)**. 280-286.
76. G.C.Allen, P.A.Tempest, and J.W.Tyler, Journal of the Chemical Society-Faraday Transactions I, 1987. **83**. 925-&.
77. G.C.Allen, P.A.Tempest, and J.W.Tyler, Journal of the Chemical Society-Faraday Transactions I, 1988. **84**. 4049-4059.
78. P.Taylor, E.A.Burgess, and D.G.Owen, Journal of Nuclear Materials, 1980(88). 153.
79. P.Wood, M.J.Bennett, M.R.Houlton, and J.B.Price. in BNES. 1985. Stratford.
80. K.Richter and C.Sari, Journal of Nuclear Materials, 1987. **148**. 266.
81. N.Martensson, B.Johansson, and J.R.Naegele, Physical Review B, 1987. **35**. 1437.

82. T.Almeida, L.E.Cox, J.W.Ward, and J.R.Naegele, *Surface Science*, 1993. **287/288**(141).
83. D.Courteix, J.Chayrouse, L.Heintz, and R.Babtist, *Solid State Communications*, 1981. **39**. 209.
84. M.Eckle and T.Gouder, *Journal of Alloys and Compounds*, 2004. **374**(1-2). 261-264.
85. J.T.Waber, American Nuclear Society, La Grange Park, IL, 1980. 145 - 189.
86. Terada, K.Meisel, and R.L.Dringman, *Journal of Nuclear Materials*, 1969. **30**. 340.
87. R.N.R.Mulford, F.H.Ellinger, and K.A.Johnson, *Journal of Nuclear Materials*, 1965. **17**. 324.
88. R.Bastasz, C.A.Colmenares, R.L.Smith, and G.A.Somorjai, *Surface Science*, 1977. **67**(1). 45-60.
89. A.Danon, J.E.Koresh, and M.H.Mintz, *Langmuir*, 1999. **15**(18). 5913-5920.
90. G.C.Allen, P.M.Tucker, and J.W.Tyler, *Journal of Physical Chemistry*, 1982. **86**(2). 224-228.
91. J.R.Kirkpatrick and J.B.Condon, *Journal of the Less-Common Metals*, 1991. **172**. 124-135.
92. C.A.Colmenares, *Progress in Solid State Chemistry*, 1984. **15**(4). 257-364.
93. J.M.Haschke, T.H.Allen, and J.L.Stakebacke, *Journal of Alloys and Compounds*, 1996. **243**. 23.
94. J.D.Farr, R.K.Schulze, and M.P.Neu, *Journal of Nuclear Materials*, 2004. **328**. 124-136.
95. F.Weigel, J.J.Katz, and G.T.Seaborg, *The Chemistry of the Actinide Elements*, ed. J. J. Katz, G. T. Seaborg, and L. R. Morss. Vol. 1. 1986: Chapman & Hall, New York. 680 - 702.
96. V.Neck and J.Kim, *Radiochimica Acta*, 2001. **89**(1). 1.
97. J.D.Farr, R.K.Schulze, and B.D.Honeyman, *Radiochimica Acta*, 2000. **88**(9-11). 675.
98. J.M.Haschke, Chapter 1, in *F-Element Chemistry: Synthesis of Lanthanide and*, Kluwer Academic Publishers.

99. J.M.Haschke, Los Alamos Science, 2000. **11**(26).
100. J.M.Haschke and J.C.Martz, The Encyclopaedia of Environment Analysis and Remediation. Vol. 6, New York: John Wiley and Sons. 3740.
101. L.Black, F.Miserque, T.Gouder, L.Havela, J.Rebizant, and F.Wastin, Journal of Alloys and Compounds, 2001. **315**(1-2). 36-41.
102. G.C.Allen and N.R.Holmes, Journal of Nuclear Materials, 1988. **152**(2-3). 187-193.
103. H.Holleck, Thermodynamics of Nuclear Materials. Vol. 2. 1975, Vienna: IAEA. 213-263.
104. L.Havela, F.Wastin, J.Rebizant, and T.Gouder, Physical Review B, 2003. **68**. 085101.
105. G.J.Hutchings, C.S.Heneghan, I.D.Hudson, and S.H.Taylor, Nature, 1996. **384**(6607). 341-343.
106. C.S.Heneghan, G.J.Hutchings, S.R.O'Leary, and S.H.Taylor, Catalysis Today, 1999. **54**. 3.
107. L.G.Gordeeva, Journal of Nuclear Materials, 1995. **218**. 202.
108. Q.Wu, B.V.Yakshinskiy, and T.E.Madey, Surface Science, 2003. **523**(1-2). 1-11.
109. M.N.Hedhili, B.V.Yakshinskiy, T.W.Sclereth, T.Gouder, and T.E.Madey, Surface Science, 2004. **574**(1). 17-33.
110. H.Madhavaram and H.Idriss, Journal of Catalysis, 2002. **206**(1). 155-158.
111. H.Madhavaram and H.Idriss, Journal of Catalysis, 1999. **184**(2). 553-556.
112. H.Madhavaram and H.Idriss, Catalysis Today, 2000. **63**(2-4). 309-315.
113. H.Madhavaram and H.Idriss, Temperature programmed desorption of ethylene and acetaldehyde on uranium oxides. Evidence of furan formation from ethylene, in 3rd World Congress on Oxidation Catalysis. 1997, ELSEVIER SCIENCE PUBL B V: Amsterdam. p. 265-274.
114. H.Idriss and H.Madhavaram, Abstracts of Papers of the American Chemical Society, 1998. **215**. 028-CATL.

115. C.Heinemann, H.H.Cornehl, and H.Schwarz, *Journal of Organometallic Chemistry*, 1995. **501**(1-2). 201-209.
116. H. Madhavaram and H. Idriss, *Journal of Catalysis*, 2002. **206**(1). 155-158.
117. H.Madhavaram, P.Buchanan, and H.Idriss, *Journal of Vacuum Science & Technology a-Vacuum Surfaces and Films*, 1997. **15**(3). 1685-1691.
118. C.Muggelberg, M.R.Castell, G.A.D.Briggs, and D.T.Goddard, *Surface Review and Letters*, 1998. **5**(1). 315-320.
119. T.Gouder, C.A.Colmenares, and J.R.Naegele, *Surface Science*, 1995. **342**(1-3). 299-306.
120. S.H.Taylor, C.S.Heneghen, G.J.Hutchings, and I.D.Hudson, *Catalysis Today*, 2000. **59**(3-4). 249-259.
121. M.A.Banares, J.L.G.Fierro, and J.B.Moffat, *Journal of Catalysis*, 1993. **142**(2). 406-417.
122. R.H.Harris, V.J.Boyd, G.J.Hutchings, and S.H.Taylor, *Catalysis Letters*, 2002. **78**(1-4). 369-372.

CHAPTER 2

Experimental

2.1 Experimental

The photoelectron spectrometer used in the study of thorium and uranium has facilities for XPS and UPS and has been described in detail elsewhere [1]. All data reported for neptunium and americium were acquired at the Institute for Transuranium Elements (ITU) using a Leybold-Heraeus LHS-10 spectrometer modified for work with radioactive materials as described elsewhere [2]. Appendix 2 provides a more detailed description of the instrumentation used in the work reported in this thesis.

The uranium and thorium foils (19.5 mm x 9.5 mm x 1 mm) were purchased from Goodfellow Metals. Uranium was cleaned in nitric acid and thorium in a solution of 50:50 HNO₃ and water plus 0.1% HF, before mounting in the spectrometer in order to remove most of the thick native oxide layer. The metal surface was subsequently cleaned in situ by argon ion sputtering. Research-grade oxygen (99.99 %), nitrogen dioxide (99.99 %), nitric oxide (99.99 %), nitrous oxide (99.99 %) and nitrogen (99.99 %) were used without further purification. All exposures are quoted in Langmuirs (1 L = 10⁻⁶ Torr-sec). XPS spectra were acquired with non-monochromatic Al K α radiation (1486.6 eV). UPS spectra were acquired using He II (40.8 eV) and He I (21.2 eV) radiation. Spectra were acquired using commercial data-acquisition software (SPECTRA; R. Unwin) and analyzed using commercial software (CASAXPS; Neil Fairley) and software developed in house [3]. Adatom surface concentrations (atoms cm⁻²) were calculated from integrated adsorbate and substrate core-level peak intensities according to the method described by Carley and Roberts [3, 4]. Depths were calculated using angle resolved XPS (ARXPS) and ARctick software [5]. By acquiring spectra at a few different angles of emission a more accurate depth measurement can be made. ARctick, a computer spreadsheet, was developed at the National Physical Laboratory (NPL). Having reviewed different quantification

algorithms they developed a computer spreadsheet which allows one to apply the simplest and most reliable approaches to aid in the quantification of ARXPS data. Inelastic mean free paths were calculated using the TPP-2 equation [6].

Thin films of neptunium and americium were prepared in situ by DC sputtering of neptunium and americium. The plasma triode deposition source has been described in detail elsewhere [7]. The deposition rates of neptunium and americium were controlled by varying the voltage of the Np/Am target (-100 to -900 V). The plasma in the diode source was maintained by injecting electrons of 50 – 100 eV kinetic energy. The neptunium and americium targets were rods of diameter approximately 3mm, produced at the ITU. Typical parameters for Np/Am deposition were electron energy 50 – 100 eV, target bias -700 V and 4×10^{-3} mbar Ar. XPS spectra were acquired with non-monochromatic Al K α radiation (1486.6 eV). UPS spectra were acquired using He II (40.8 eV) and He I (21.2 eV) radiation from a windowless UV rare gas discharge source. Spectra were acquired using software developed in house at the ITU by Thomas Gouder and analyzed using commercial software (CASAXPS; Neil Fairley). Again, adatom surface concentrations (atoms cm⁻²) were calculated from integrated adsorbate and substrate core-level peak intensities according to the method described by Carley and Roberts [3, 4]. Depths were calculated using standard equations (see Data Analysis) as it was not possible to collect data at different angles of emission at the ITU. Inelastic mean free paths were calculated using the TPP-2 equation [6].

2.2 Data Analysis

On the most basic level quantification means relating photoelectron peak intensities to surface composition. However determination of peak area is influenced by the peak shape and the underlying background. In addition, correct estimation of surface concentration needs supplementary knowledge of information depth. Many of these issues are not trivial and uncritical use of universal methodologies may introduce error.

2.2.1 Inelastic Background – Background types

Determination of the line intensities is complicated by the inelastic background onto which the primary signal superimposes. This background is produced by photoelectrons, which during motion from the point of creation to the surface of the solid are scattered inelastically. Strictly speaking, there is no universal unambiguous method to remove this background, but several pragmatic approaches are available.

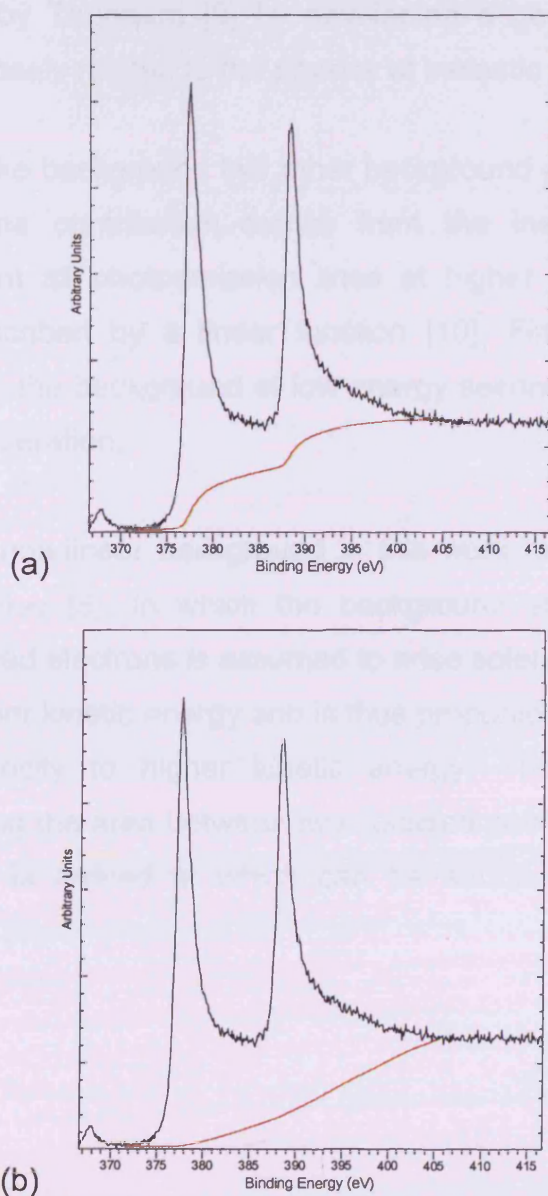


Figure 2.1 $U(4f)$ spectra with background estimated by the (a) Shirley and (b) Tougaard methods.

There are three different types of background. The most important comes from inelastically scattered photoelectrons from the corresponding primary peak, forming a step like background. It is closely related to the loss function $T(E, \Delta E)$, i.e. the probability of an electron of energy E to undergo an energy loss of ΔE .

The first numerical treatment was proposed by Shirley [8] (figure 2.1), who assumed a constant loss function, resulting in an inelastic background, which is proportional to the integrated intensity at higher kinetic energy. The model was refined later by Tougaard [9] by developing a general loss function, which was more closely related to the physics of inelastic scattering.

Besides the step like background two other background contributions should be mentioned. One contribution comes from the inelastically scattered photoelectrons from all photoemission lines at higher kinetic energy and which is best described by a linear function [10]. Finally for low kinetic energies ($<100\text{eV}$), the background of low energy secondary electrons must be taken into consideration.

The removal of a non-linear background in this work relies on the method developed by Shirley [8], in which the background at any point due to inelastically scattered electrons is assumed to arise solely from the scattering of electrons of higher kinetic energy and is thus proportional to the integrated photoelectron intensity to higher kinetic energy. The process involves iteratively integrating the area between two selected points until a converged background value is arrived at which can be subtracted from the peak intensity (Figure. 2.2).

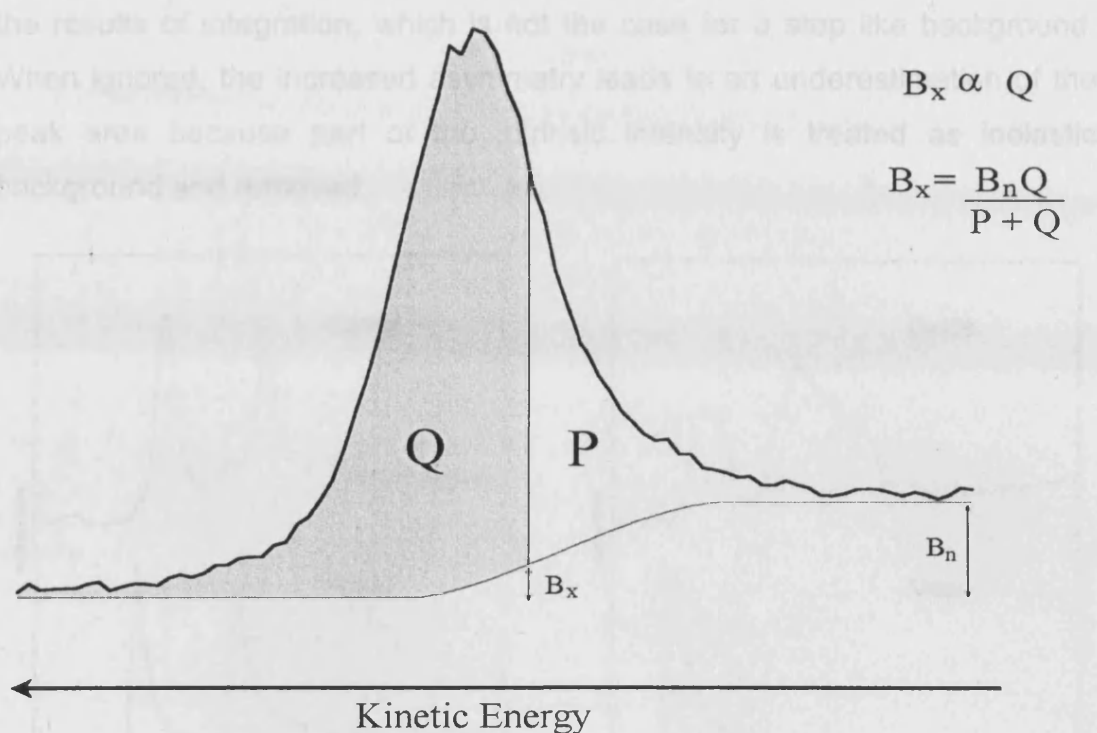


Figure 2.2. Non-linear background removal in XPS.

2.2.2 Complication for Actinides: Asymmetric Tail

In addition, there is some arbitrariness in distinguishing the true inelastic background from intrinsic peak asymmetry. This is particularly true for metallic actinide systems, as typical narrow-band systems, which are characterized by a high density of states at the Fermi level $N(E_F)$; there is a pronounced peak asymmetry, produced by low-energy losses by scattering electrons at the Fermi level into empty states [11]. The asymmetry disappears when the intensity at the Fermi level disappears e.g. due to oxidation at the surface.

Figure. 2.3 compares spectra of U metal, which has a high density of states at the Fermi level, with UO_2 . For the U (4f) lines in UO_2 , a step like background can be assumed, but the treatment of the 4f lines in U metal is ambiguous. These lines have a continuously decreasing tail on the high binding energy side. Therefore, the choice of the end-point strongly affects

the results of integration, which is not the case for a step like background. When ignored, the increased asymmetry leads to an underestimation of the peak area because part of the intrinsic intensity is treated as inelastic background and removed.

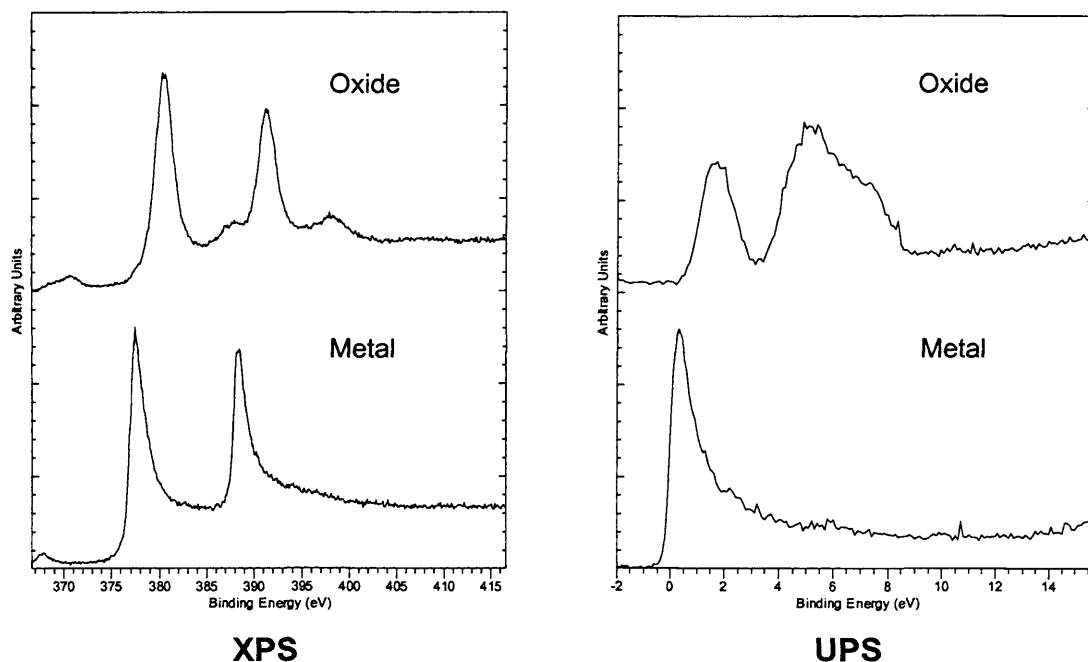


Figure 2.3 $U(4f)$ and UPS He II spectra of U -metal and UO_2 showing asymmetry of the $U(4f)$ metal peaks and the UPS indicates the density of states at the Fermi level.

2.2.3 Spectral Smoothing

Smoothing can be used to minimize the effects of poor signal-to-noise ratio brought about by low sensitivity or where time constraints prohibit prolonged scanning (particularly relevant for the study of the highly reactive actinide metal surfaces). Smoothing of the spectrum improves the signal to noise ratio. The technique was initially developed by Savitsky and Golay [12]. A least squares approach is used where a polynomial is fitted to the data over an odd number of points known as the smoothing interval. Increasing the number of points used in the smoothing interval increases the degree of smoothing, with the optimal value being 70% of the data points in the full width half maximum (FWHM) of the peak [13]. Spectra distortion (figure 2.4) is always a concern with any smoothing operation, therefore the data presented in this work is unsmoothed.

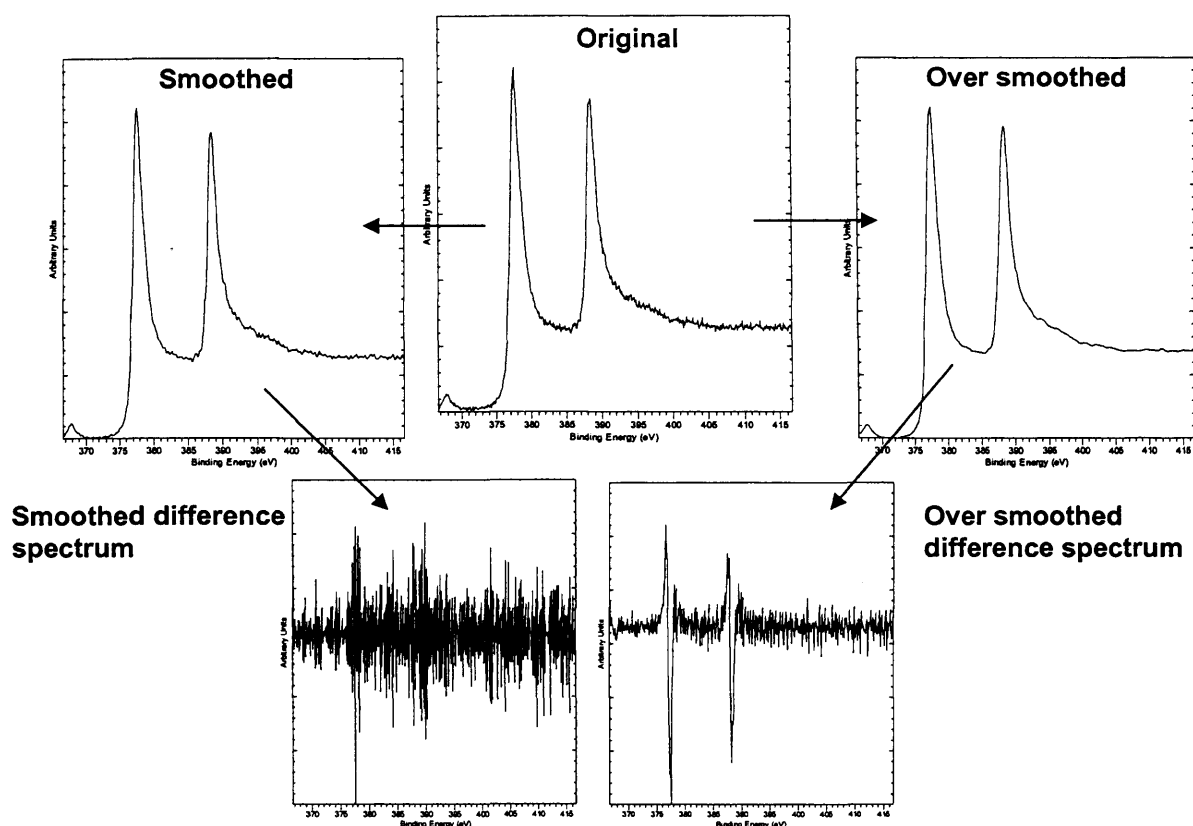


Figure 2.4 Clean uranium metal U (4f) spectra showing broadening of the U (4f) metal peaks, and the appearance of extra features in the difference spectrum, as a result of spectral smoothing.

2.2.4. Spike removal

Spikes, irregular points, in the photoelectron spectra are occasionally caused by power surges and should be removed before any data analysis is carried out. Anomalous points may seriously effect smoothing and curve fitting operations. Such points are automatically detected and removed by the software used.

2.2.5. Spectral subtraction

This process involves the point-by-point subtraction of one spectrum from another to produce a difference spectrum. The application of this technique to XPS is very sensitive to the alignment and normalization of the spectra, generating false results unless carried out with great care and attention.

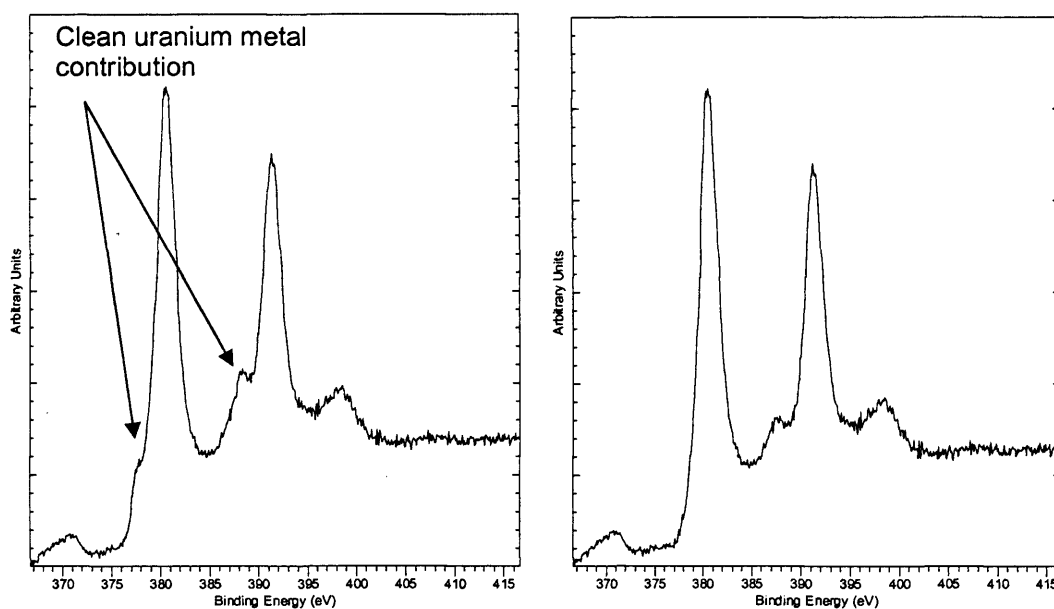


Figure 2.5 Spectral subtraction. The spectrum on the left shows the U (4f) peaks of an oxidized surface. The spectrum contains a residual metal contribution to the peaks which we wish to subtract. The box on the right shows the resulting subtraction of the metal contribution to the peaks. This process is useful in depth determination when an accurate calculation of the oxide contribution to the peak area is required.

This facility is required when a peak arises in the spectrum in a position such that it is superimposed on another, already present peak. Uranium studies show the N (1s) region overlaps with one of the uranium oxide (4f) shake-up satellite peaks. The removal of the satellite contribution from the spectra increases the accuracy of the determined N (1s) peak intensity. This was particularly valuable when undertaking the adsorption studies of the nitrogen oxides on a uranium surface.

Prior to subtraction the peak which is to be subtracted is scaled to match the intensity of the equivalent peak in the composite spectrum (figure 2.5). Care must be taken however as improper scaling can result in the emergence of artificial peaks or troughs in the difference spectrum.

2.2.6. Curve Fitting

Composite spectra may be formed by the overlap of two or more peaks arising from differing chemical states of a particular surface species. Curve

fitting is a method by which each component of the composite peak may be resolved. Curve fitting allows for a number of Gaussian (or other) curves to be fitted to the peak by an iterative least squares fit following background removal. Through the predefinition of the number of species present within the composite spectra, the user may then select initial values for the intensity, energy and FWHM. These parameters form Gaussian peaks, which in turn are summed to give an approximate fit.

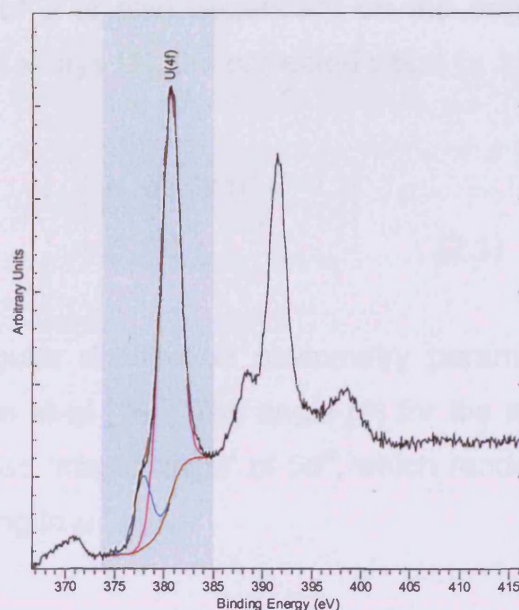


Figure 2.6 Curve fitted U (4f) spectra of uranium oxide with a residual uranium metal peak.

Clearly some subjectivity is involved in the predetermination of these parameters thus an understanding of the chemistry of the system and the use of reference data is essential if meaningful quantitative results are to be obtained.

2.2.7. Quantification

In order to calculate the surface coverage of a species the area of its photoelectron peak must be known. After prior removal of the background the peak area is measured by integrating the intensity, above a baseline, between two points on either side of the peak. The peak intensity values can then be converted to surface concentrations via the Carley and Roberts [4] equation developed by Madey et al [14] which has been modified to include

the photo-ionization cross section. The photo-ionization cross section (μ) is the probability that an electron will be ejected from a particular orbital of a particular atom. Values of μ are influenced by the size and shape of the orbital as well as the ionizing photon energy.

The photo-ionization cross sections for both Mg $K\alpha$ and Al $K\alpha$ radiation have been tabulated by Scofield [15] relative to the cross section of the C (1s) orbital. The value of μ is also dependant on the angle of detection with regard to the incident x-rays (θ), the corrected value (μ') being given by:

$$\mu' = \left[1 - \frac{\beta}{2} \left(\frac{3 \cos^2 \theta - 1}{2} \right) \right] \quad (2.1)$$

where β is the angular distribution asymmetry parameter calculated and tabulated by Reilman et al [16]. The angle (θ) for the spectrometer used in Cardiff is the so-called 'magic angle' of 55° , which renders the term $3 \cos^2 \theta$ equal to unity resulting in $\mu' = \mu$.

Madey et al. [14] derived a first principles equation relating measured intensities of photoemission from a bulk metal and an adsorbed layer. Later modified by Carley and Roberts [4], it reduces to the simple form:

$$I_a(X_a) / I_m(X_m) = \mu_a(\theta, X_a) \sigma_a / \mu_m(\theta, X_m) n_m \lambda_m(\epsilon_i) \cos \Phi \quad (2.2)$$

Where $I_a(X_a)$, $I_m(X_m)$ are the measured intensities of the XP signals from the adsorbed layer and metal respectively, n_m is the density of emitting atoms in the metal, $\lambda_m(\epsilon_i)$ the mean free path of photoelectrons from level X_m in the metal and σ_a is the surface concentration of adsorbed species.

The equation for calculating surface concentrations was then updated to the following form:

$$\sigma_A = \frac{KE_A}{KE_S} \times \frac{I_A}{I_S} \times \frac{\mu_S N \lambda_S \rho_S \cos \phi}{\mu_A M_S} \quad (2.3)$$

where,

σ = Surface concentration (cm^{-2})

A = adsorbate

S = substrate

I = integrated peak intensity

KE = kinetic energy

μ = modified photoionization cross section

ϕ = photoelectron take-off angle with respect to the surface normal

N = Avogadro's number

λ_S = escape depth of photoelectrons through the substrate

M_S = molar mass of the substrate

ρ_S = Substrate density

Many of these parameters are constant for a particular adsorbate, substrate and spectrometer so that we can simplify the equation to,

$$\sigma_A = \frac{I_A}{I_S} \times A \quad (2.4)$$

where A is a constant for a particular substrate/adsorbate system.

The Carley-Roberts equation (equation 2.2 and 2.3) makes the assumption that the adsorbate is non-attenuating; surface coverages greater than a monolayer are therefore underestimated as the scattering by the adsorbate cannot then be considered negligible. Once the surface coverage is greater than a monolayer depth calculations must then be undertaken in order to calculate a surface covering.

2.2.8. Inelastic mean free path and Depth Calculations

Improved calculation of the inelastic mean free path (IMFP), λ , has recently been done, taking the physics of the scattering process more into consideration. Tanuma et al [6] have developed the following TPP-2 analytical expression for λ :

$$\lambda = E / \{E_p^2[\beta \ln(\gamma E) - (C/E) + (D/E^2)]\} \quad (2.5)$$

where,

λ = the IMFP (in Å)

E = the electron energy (in eV),

$E_p = 28.8 (N_v \rho / M)^{1/2}$ and is the free-electron plasmon energy (in eV)

ρ = the density (in g cm⁻³)

N_v = the number of valence electrons per atom (for elements) or molecule (for compounds)

M = the atomic or molecular weight

The terms β , γ , C and D in Eq. (2.5) are regarded simply as adjustable parameters in the fits to the calculated IMFPs. Values of β , γ , C and D derived from the fits to the IMFPs for 27 elements and 14 organic compounds were analysed to yield the following expressions in terms of material parameters [17]:

$$\beta = 0.10 + 0.944 / (E_p^2 + E_g^2)^{-1/2} + 0.069\rho^{0.1} \quad (2.6)$$

$$\gamma = 0.191 \rho^{-0.50} \quad (2.7)$$

$$C = 1.97 - 0.91U \quad (2.8)$$

$$D = 53.4 - 20.8U \quad (2.9)$$

$$U = N_v \rho / M = E_p^2 / 829.4 \quad (2.10)$$

Where E_g is the bandgap energy (in eV) for nonconductors. This new formalism has been applied to elements, inorganic and organic compounds and shows much improved RMS deviations compared to earlier formulations.

Depth calculations for the thorium and uranium experiments detailed within this thesis were calculated using ARXPS and the ARCTICK software [5]. ARXPS measurements were not possible when conducting the work on neptunium and americium at the ITU and therefore the following method of depth calculation was utilized. Inelastic mean free paths for thorium, uranium, neptunium and americium were all calculated using the TPP-2 equation [6].

The above method of surface coverage calculation assumes that the adsorbate is non-attenuating, the calculation of surface coverages greater than a monolayer using this equation will be liable to serious underestimation since in this case the scattering effect of the adsorbate cannot be considered negligible.

For large surface coverages the thickness (d) can be estimated using the following equation based on the attenuation of the substrate signal,

$$\frac{I}{I_0} = e^{-\frac{d}{\lambda} \cos \phi} \quad (2.11)$$

where,

I = integrated substrate intensity after film deposition

I_0 = integrated intensity of the clean substrate

d = film thickness

λ = inelastic mean free path of the substrate photoelectrons through the adsorbed film

ϕ = photoelectron emission angle with respect to the surface normal

2.3 References

1. A.F.Carley, S.D.Jackson, M.W.Roberts, and J.O'Shea, *Surface Science*, 2000. **454-456**. 141-146.
2. J.R.Naegele, *Journal of Physics (Paris)*, 1984. **45**. C2-841.
3. A.F.Carley, Ph.D. Thesis, University of Bradford, 1980
4. A.F.Carley and M.W.Roberts, *Proceedings of the Royal Society: London A*, 1978. **363**. 403.
5. P.Cumpson, 1998: ARCTick, National Physical Laboratory, UK
6. C.J.Powell, A.Jablonski, I.S.Tilinin, S.Tanuma, and D.R.Penn, *Journal of Electron Spectroscopy and Related Phenomena*, 1999. **99**. 1-15.
7. T.Gouder, *Journal of Electron Spectroscopy and Related Phenomena*, 1999. **101-103**. 419-422.
8. D.A.Shirley, *Physical Review B*, 1972. **5**. 4709.
9. S.Tougaard, *Surface Science*, 1989. **216(3)**. 343-360.
10. H.E.Bishop, *Surface and Interface Analysis*, 1981. **3(6)**. 272-274.
11. A.Kotani and J.Toyazawa, *Journal of the Physical Society Japan*, 1974. **37**. 17.
12. A.Savitsky and M.J.E.Golay, *Analytical Chemistry*, 1964. **52**. 2315.
13. A.Proctor and P.M.A.Sherwood, *Analytical Chemistry*, 1980. **52**. 2315.
14. T.E.Madey, J.T.Yates, and N.E.Erickson, *Chemical Physics Letters*, 1973. **19**. 487.
15. J.H.Scofield, *Journal of Electron Spectroscopy and Related Phenomena*, 1976. **8**. 129.
16. R.F.Reilman, A.Msezane, and S.T.Manson, *Journal of Electron Spectroscopy and Related Phenomena*, 1976. **8**. 389.
17. S.Tanuma, C.J.Powell, and D.R.Penn, *Surface and Interface Analysis*, 1994. **21(3)**. 165-176.

CHAPTER 3

Photoemission Studies of the Surface Reactivity of Thorium: O₂, NO, NO₂ and N₂O adsorption studies

3.1. Introduction

This chapter investigates the surface reactivity of thorium metal with respect to O₂, NO, NO₂ and N₂O. Thorium metal, at the beginning of the actinide series in the periodic table, has the valence electronic configuration of 6d²7s² (containing no 5f states). It is therefore a good system for comparison with uranium, neptunium, plutonium and americium (which all have 5f occupation) for investigating the role of 5f electrons in surface reactions and bonding. 5f electron behaviour is of fundamental interest in understanding actinide chemistry. Thorium metal therefore allows us to investigate a 5f⁰ system and the behaviour of 6d7s valence electrons.

The effect of nitrogen oxides (NO, NO₂, N₂O) on the oxidation of thorium metal has not previously been investigated. It is of interest to study the surface reaction of these gases with Th metal and compare to oxidation by O₂. NO₂ and N₂O can act as chemical sources of oxygen atoms [1-4], while NO can be considered to undergo bonding with metals similar to CO. The intent of this investigation was to examine and compare the chemisorption and initial stages of reaction of O₂, N₂O, NO and NO₂ on a clean thorium surface.

3.2. Results

3.2.1 Oxygen (O₂) Adsorption

The 4f core-level photoelectron spectra of Th metal and after the metal surface has been exposed to increasing doses of oxygen are shown in figures. 3.1 and 3.2. The shape and binding energies of the 4f peaks prior to exposure to oxygen corresponds to those of Th metal (342.4 and 333.1 eV

for the 4f_{5/2} and 4f_{7/2} peaks, respectively) [5]. The satellites, which are located at about 2.2 eV higher binding energy, are understood to be due to the screening of the 4f photoelectron core hole, produced during the photoemission process, involving the 6d electrons (poorly screened peak), whereas the main lines reflect the screening by the 5f states (well screened peak), which are above E_F in the ground state, but become populated in the presence of the 4f photoelectron core hole [6]. (an explanation of screening mechanisms can be found in references [7, 8] or there is a brief introduction in appendix 1). The satellites lie in positions deceptively close to where one would anticipate thorium oxide peaks to appear (figure 3.1). However the area under these satellites constitutes approximately 30 % of the total peak area, and it is difficult to believe that 30 % surface oxide would not be detected by UPS and XPS i.e. O (2p) and O (1s) peaks in the spectra. Furthermore, the relatively high cross section of O (2p) states for He II excitation makes the He II spectra a very sensitive indicator of any contamination. It is superior to the standard monitoring of the O (1s) line in XPS as an indicator of oxidation, and we would therefore expect to observe an O (2p) contribution in the UPS spectrum if any oxide were present on the surface.

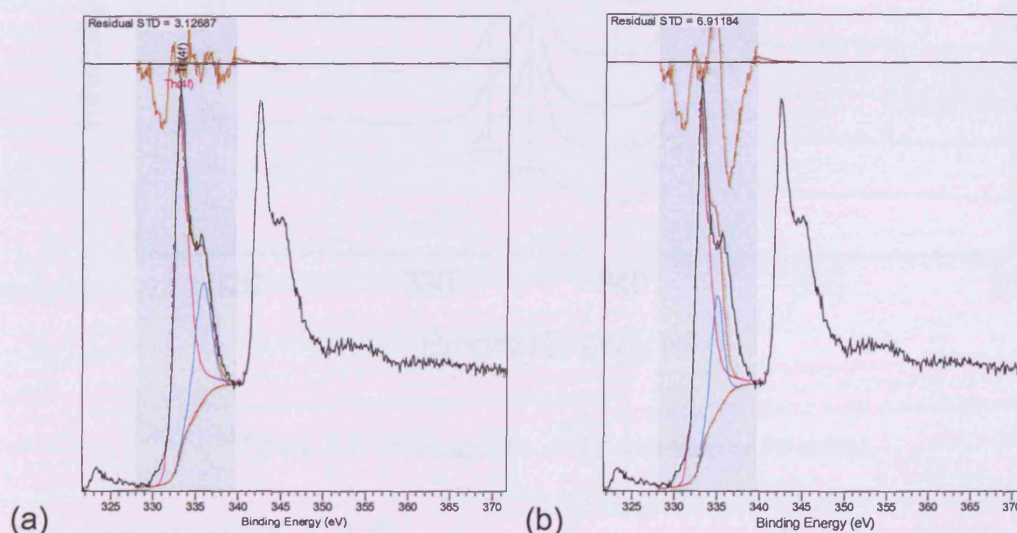


Figure 3.1. Th(4f) spectrum of Th metal showing the curve fitted well and poorly screened contributions to the metal peak. (a) poorly screened peak best fit (b) Th (4f) poorly screened peak fitted with FWHM and peak position of ThO₂, showing that the satellite is not due to oxidation.

Figure 3.1 also shows that when the poorly screened peak is fitted using the FWHM and peak position parameters of the ThO₂ peak (figure 1(b)), following 3000 L exposure of oxygen, the residual shows clear structure on the higher BE side of the well screened peak and a large standard deviation from the clean metal peak structure. In contrast the best fit of the poorly screened peak exhibits a residual with almost no structure on the higher binding energy side of the well screened peak and a much smaller standard deviation. The absence of O (2p) and O (1s) intensity together with the poor fit to the thorium (4f) metal peak using the FWHM and peak position of ThO₂, confirms the cleanliness of the metal surface.

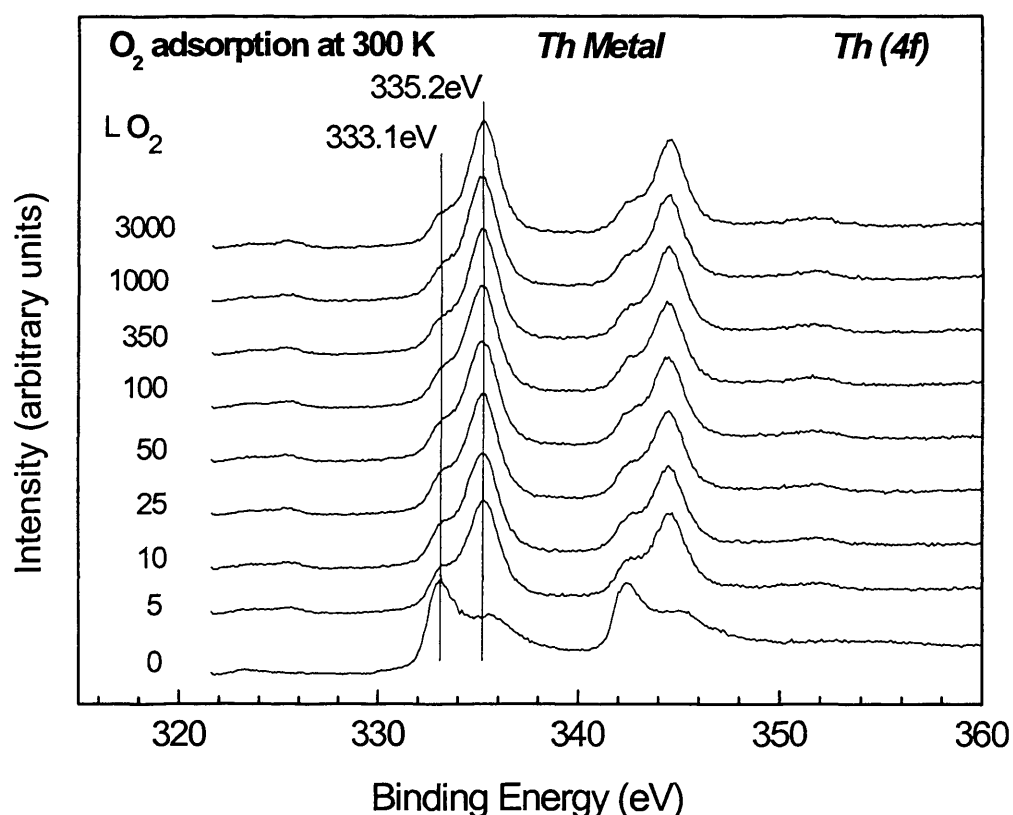


Figure 3.2. Th(4f) spectra of the oxidation of Th metal

The gradual oxidation of Th by increasing exposures of oxygen results in the increase of a peak coincident with the higher binding energy (BE) satellite of the clean metal (4f_{7/2}) peak at 335.2 eV (figure. 3.2). A shake up satellite at 343 eV contributes to the shoulder on the low binding energy side of the Th

(4f_{5/2}) peak. The shake up satellite can be seen at approximately 352 eV. Satellites at these energies are characteristic of bulk ThO₂ [9]. The shoulder on the low binding energy side of the oxidised Th (4f_{7/2}) peak suggests the presence of unoxidised metal in the near surface region. Contributions to the Th (4f) peak envelope indicative of the presence of metallic thorium are still present, even at the highest exposures of O₂. This is most likely due to metal emission from under the oxide film, implying that the oxide layer formed is not very thick. Calculations support this showing an approximate oxide depth of 1 nm indicating that Th metal is still within the information depth of XPS. Photoemission spectra of polycrystalline ThO₂ has been reported and show a symmetric 4f peak shape [10] with no residual metal shoulder. Therefore the oxide film formed following exposure to O₂ retards further oxidation (diffusion of oxygen ions) at the surface, leaving a metal contribution to the 4f peak envelope within the information depth of XPS.

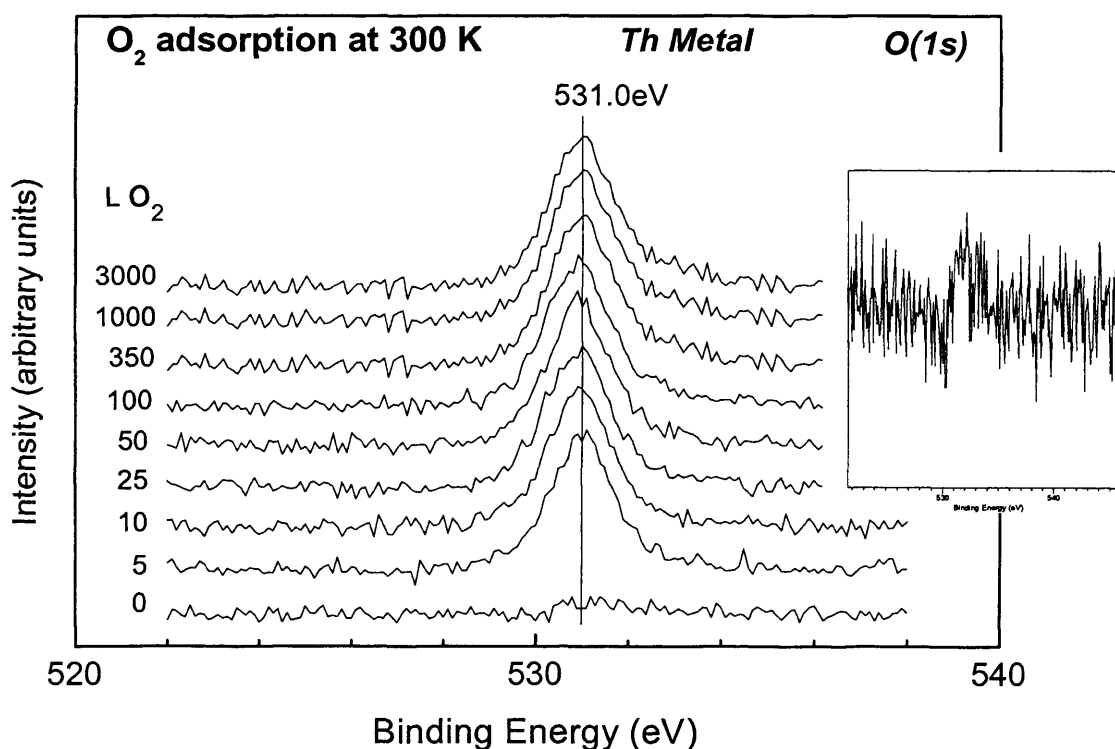


Figure 3.3. O(1s) spectra following oxidation of Th metal. Inset difference spectrum showing the result of a subtraction of the spectrum following 25 L exposure from the spectrum following 350 L exposure.

With increasing O₂ exposure a symmetric O (1s) peak at 531 eV binding energy, assigned to O²⁻ species in ThO₂ [10], increases in intensity (figure 3.3), associated with surface oxide. Increasing exposures (>25 L) of O₂ do not cause a significant increase in intensity of the O (1s) feature (inset figure 3.3), confirming that the reaction has slowed considerably. The oxide layer thickness is still within the sampling depth of XPS (residual metal peaks are observed in the Th (4f) spectra and the oxide depth is calculated to be only approximately 1 nm), and therefore the lack of change in the spectra can not be attributed to the oxide depth being greater than the XPS sampling depth. The difference spectrum also shows that there is no development of intensity on the higher binding energy side of the main O (1s) peak.

UPS He (I) and He (II) spectra of a Th surface exposed to increasing O₂ doses are shown in figures 3.4 and 3.5. The spectrum of the clean surface is typical for Th metal [11], exhibiting Valence-band (6d7s) states extending from E_F down to ~3 eV BE. The valence states exhibit similar intensity in the He I and He II spectra confirming the 6d7s character and the absence of 5f electrons. For any admixture of 5f states there would be an increase in intensity of the valence band in the He II spectra, when compared to the He I, due to the increased photoionisation cross-section for 5f states at the higher photon energy. The metallic spectra exhibits a density of states (DOS) with a maximum at about 0.6 eV BE, from which it decreases towards E_F. The exposure to oxygen produces an immediate change in the UPS spectra. The intensity close to E_F decreases to zero and an O (2p) band exhibiting a two peak structure forms. The two peak O (2p) structure is typical for the formation of actinides dioxides [5]. The oxidized thorium shows a broad (5.7 eV) band, with the main intensity centred at 5.5 eV. The higher binding energy region of the O (2p) valence band contains the largest admixture of cation d-electron wave function that results from cation-anion hybridisation; the region is usually referred to as the bonding part of the band. Therefore the higher binding energy O (2p) feature involves states hybridized predominantly with the Th (6d) states. The lower binding-energy part of the O

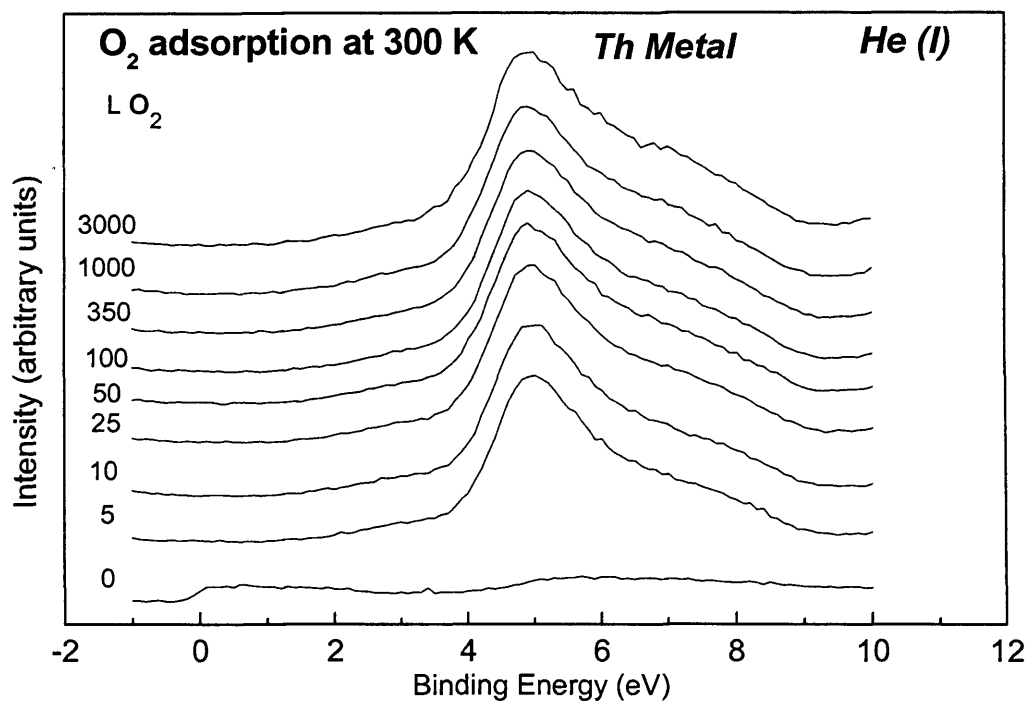


Figure 3.4. UPS He (I) (21.2 eV) spectra of Th oxidation

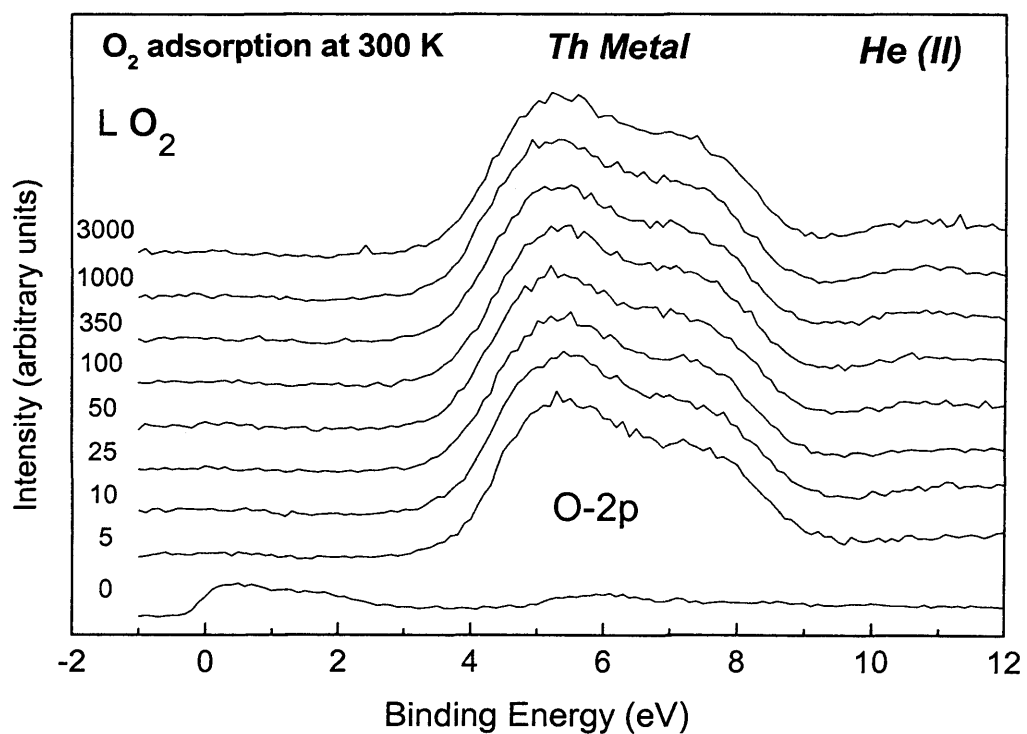


Figure 3.5. UPS He (II) (40.8 eV) spectra of Th oxidation

(2p) valence band is referred to as the nonbonding region, since it contains less cation d-electron character. Comparing the He I and He II spectra, increasing the photon energy from 21.2 to 40.8 eV results in a slight increase in the relative intensity of the higher binding energy feature of the O (2p) band, presumably because of the larger cross section for emission from d orbitals at higher photon energies than from the p orbitals. The decrease in metallic (6d7s) emission close to E_F is consistent with the oxidation of Th metal, which has a DOS at E_f , to ThO₂ which being an insulator, has none.

3.2.2. Nitric Oxide NO Adsorption

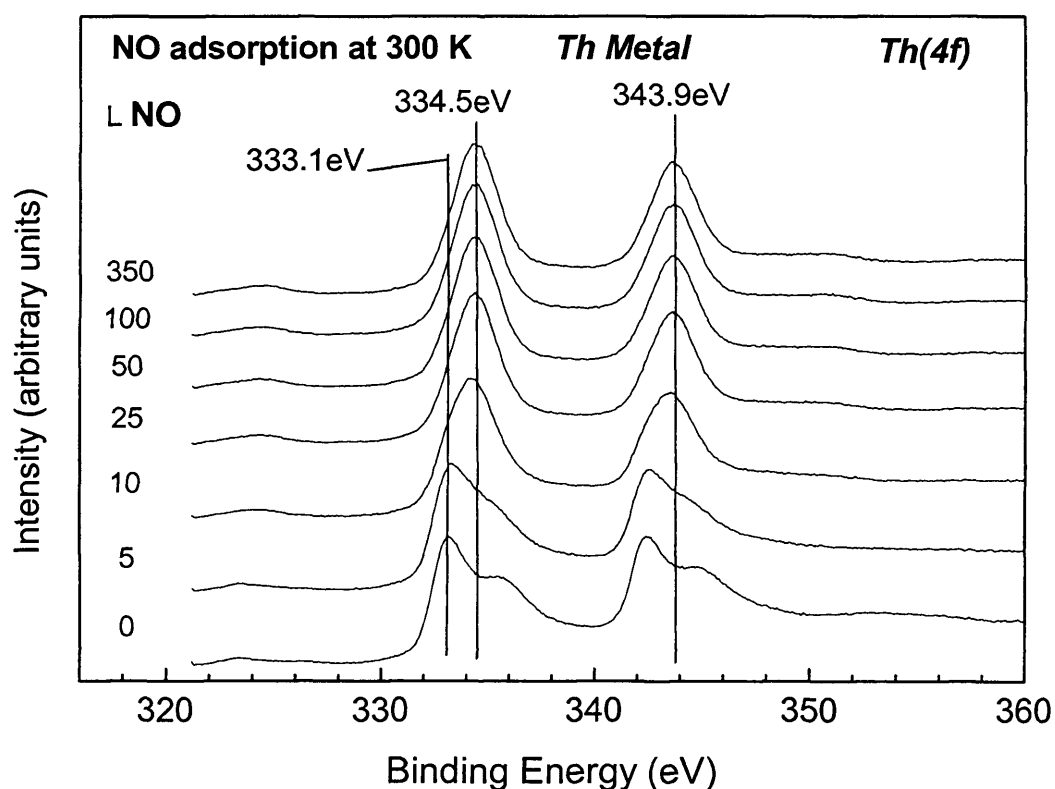


Figure 3.6. Th(4f) spectra for NO adsorption

Figure 3.6 shows the 4f core-level photoelectron spectra of Th metal when exposed to increasing doses of NO gas. Early stages of NO reaction with the thorium surface result in the decrease of the metallic signal and an increase in intensity of an oxide peak at 334.5 eV. The increase of this peak combined with the decrease in intensity of the metal emission gives rise to the

asymmetric peak shape observed following 5 L exposure (figure 3.7). On increasing the exposure further (> 10 L), there is a rapid increase in the intensity of the peaks at 334.5 and 343.9 eV and after only 50 L exposure the metallic contribution to the Th (4f) spectrum has been completely attenuated.

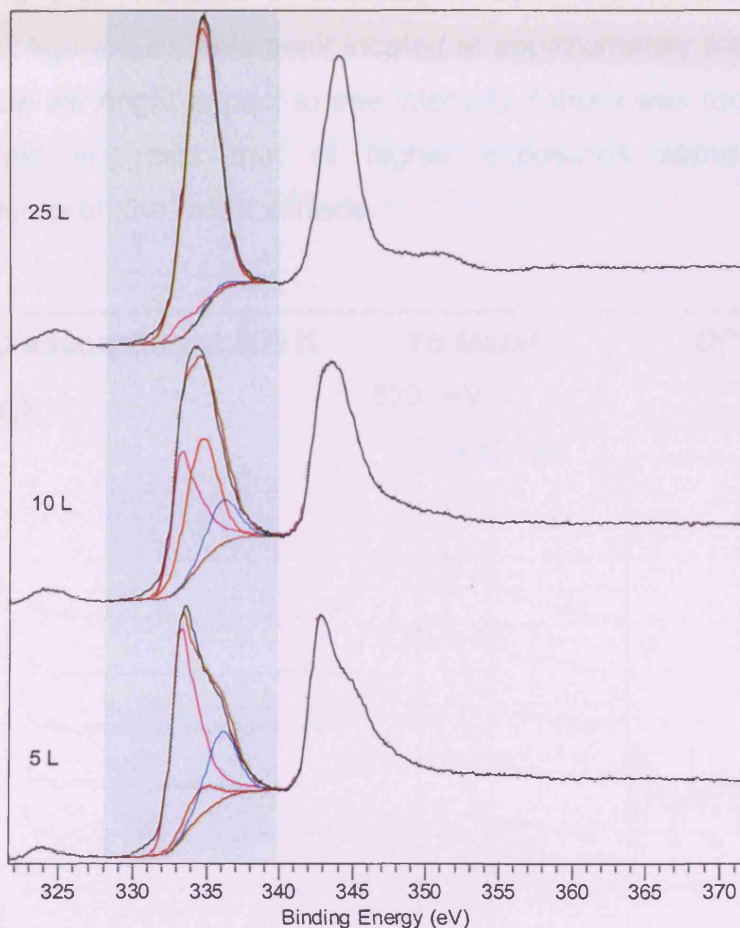


Figure 3.7. Curve fitted Th(4f) spectra for NO adsorption. Th metal well screened peak: Pink, Thorium metal poorly screened peak: blue, oxide peak: red.

Further exposures to NO, up to 3000 L, lead to no changes in the Th (4f) envelope. The chemical shift in the Th (4f) core level peaks due to oxidation with NO (1.4 eV) is smaller than that observed following exposure to O₂ and the formation of ThO₂ (2.1 eV), suggesting that an oxide other than ThO₂ is produced on the surface.

The O (1s) region exhibits a single peak due to O²⁻ with a binding energy of 530.9 eV, which does not shift with increasing exposures to NO (figure. 3.8),

and for exposures greater than 50 L there is negligible change in peak intensity. Initially, for NO exposures in the range of 5 – 25 L, a single peak appears in the spectrum at 530.9 eV indicating oxide formation. At exposures above 25 L there is a very slight increase in intensity on the higher BE side of the main peak. This increase in intensity is confirmed in the difference spectrum (inset figure 3.8). This peak located at approximately 532.7 eV is in a position where we might expect to see intensity if there was molecular NO adsorption. This suggests that at higher exposures some NO may molecularly adsorb on the oxide surface.

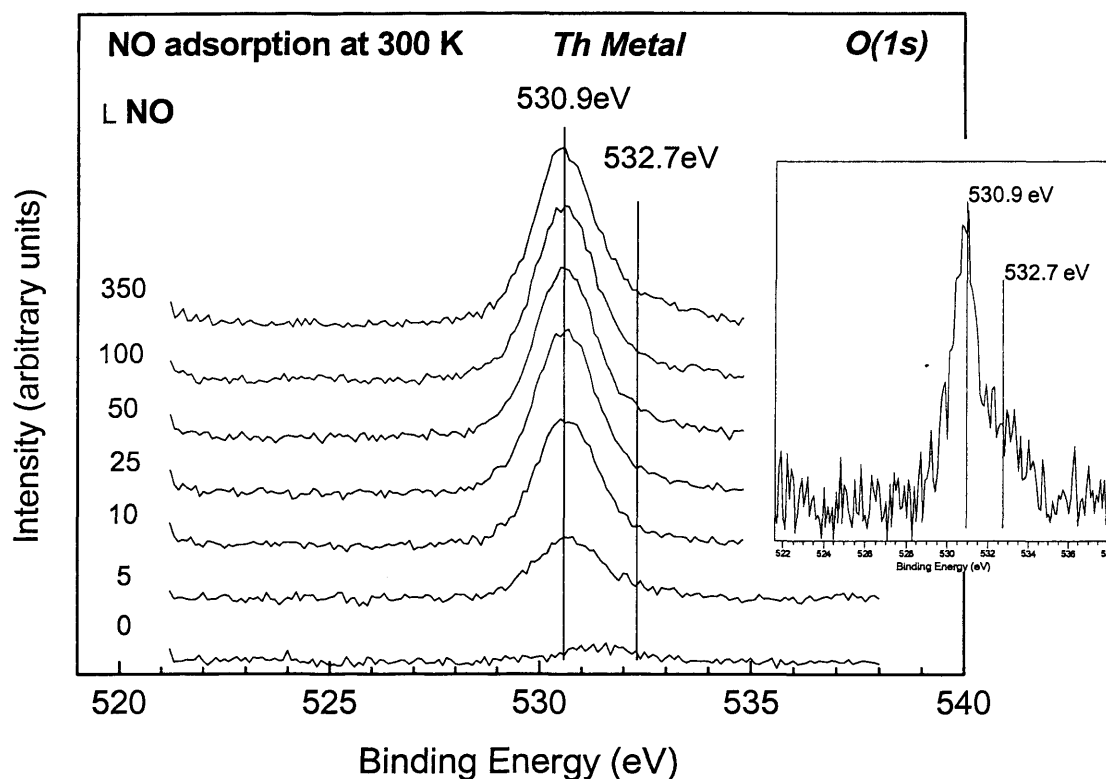


Figure 3.8. O(1s) spectra for NO adsorption. Inset difference spectrum showing the result of a subtraction of the spectrum following 25 L exposure from the spectrum following 350 L exposure.

An increase in intensity of a peak at 396.2 eV is observed in the N (1s) photoemission region (figure. 3.9), a binding energy which is similar to previously reported values for N(a), UN [12] and other nitrides. The N (1s)

peak then shifts with increasing exposure to a slightly lower BE, 395.8 eV. At higher exposures of NO (>25 L) although no change in the peak at 395.8 eV is observed a peak at 399.5 eV in the N (1s) spectra appears at a position where we expect to see nitrogen emission from molecularly adsorbed NO (inset figure 3.9). This is associated with the extra feature observed at higher exposures in the O (1s) spectra. The ratio of N:O for the peaks at 532.7 eV in the O (1s) and 399.5 eV in the N (1s) is approximately 0.92, therefore allowing for slight error in calculation indicates a ratio of approximately 1:1, supporting the proposal of molecular NO adsorption.

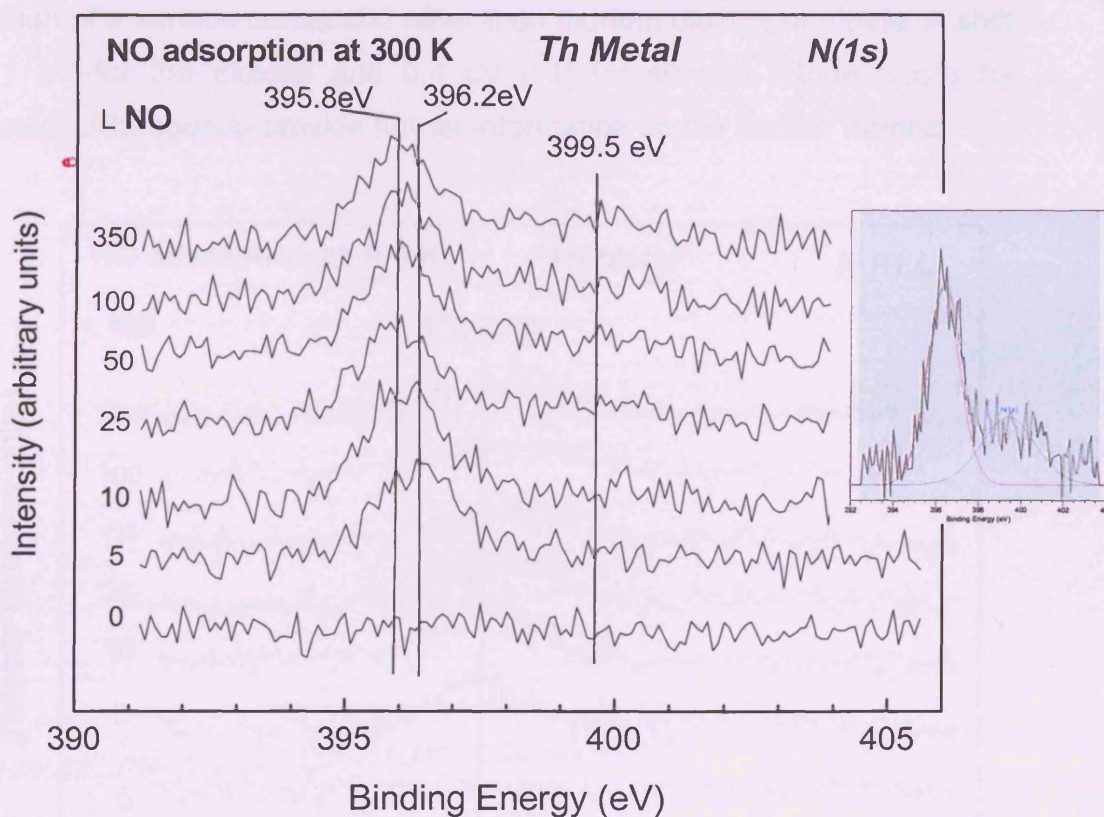


Figure 3.9. N(1s) spectra for NO adsorption. Inset, curve fitted spectra following exposure of 350 L NO.

Nitrogen KLL Auger spectra also show the development of a feature following exposure to NO (figure 3.10). This peak decreases in intensity with increasing exposure. The nitrogen KLL peak is much more surface sensitive

than the N (1s) feature. The outgoing photoelectron has a relatively small amount of kinetic energy hence it has a small inelastic mean free path (see experimental chapter). This results in a limited escape depth for the nitrogen Auger photoelectrons and an increase in the surface sensitivity. Therefore this could imply that there is incorporation of nitrogen into the subsurface region resulting in a decrease in intensity of the Auger peak.

Although it has been established from the O (1s), N (1s), and nitrogen Auger spectra that both oxygen and nitrogen species are present on the surface, the chemical shift of 1.4 eV in the Th (4f) binding energy indicates the formation of a surface compound other than thorium dioxide or nitride. A shift of 2.1 eV for the dioxide and 0.4 eV [11] for surface nitride would be expected. UPS spectra provide further information on the "oxide" formed.

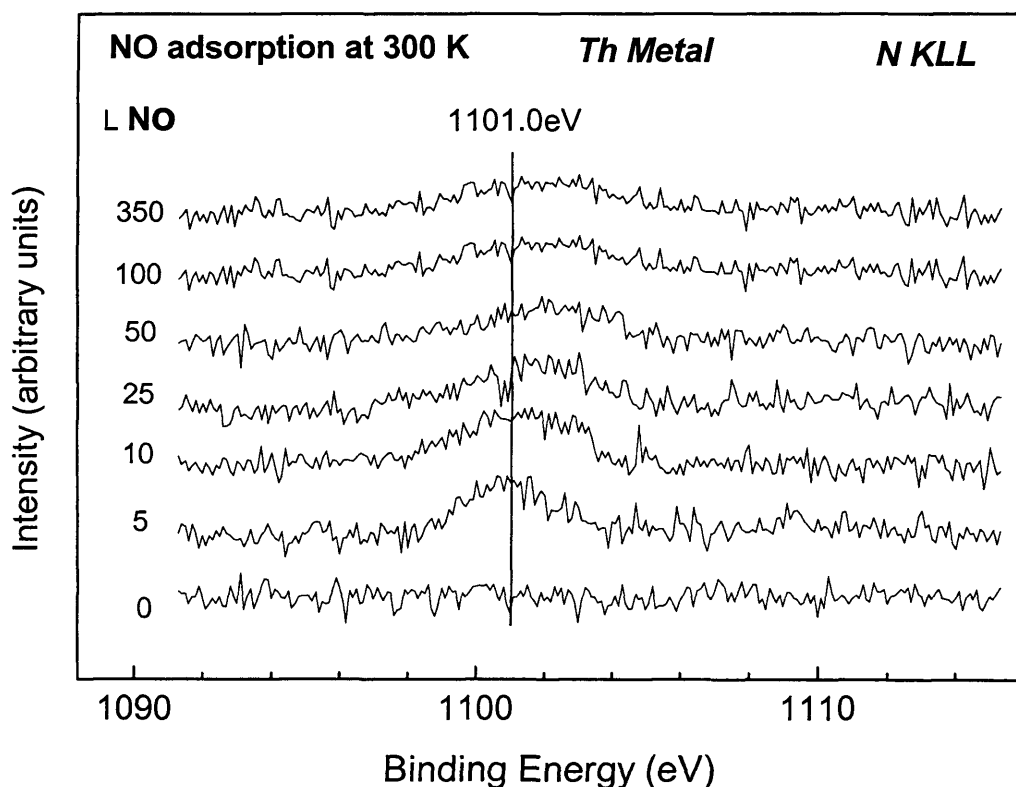


Figure 3.10. X-ray induced N Auger spectra for NO adsorption

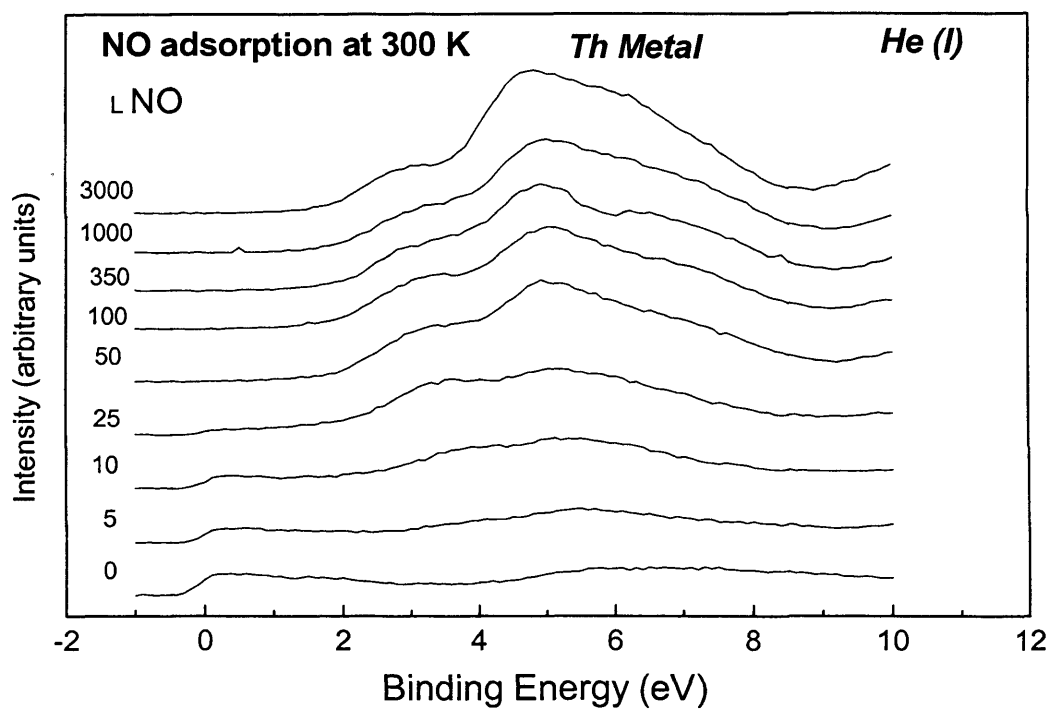


Figure 3.11. UPS He(I) spectra of NO adsorption on Th

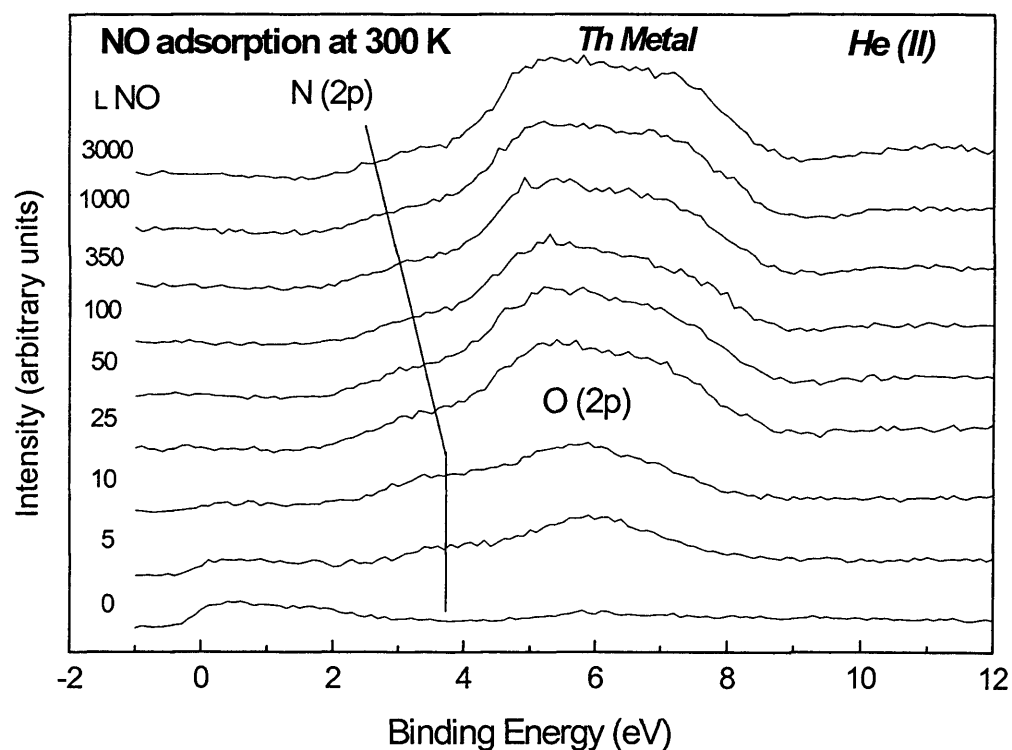


Figure 3.12. UPS He(II) spectra of NO adsorption on Th

In the UPS He I and He II spectra (figure 3.11 and 3.12), NO exposures below 10 L result in a slight decrease in the emission at E_F , and a broad peak between 2 – 8 eV is observed. This is composed of a symmetric oxide peak centred at ca 6eV, which is typical for O (2p) emission from surface oxide [13], and one centred at ca 3 eV characteristic for 2p states of ThN [12]. Simultaneously the conduction band signal decreases in intensity, due to the transfer of the 6d7s-electrons into Th-N and Th-O bonds (appearing in the spectra as N (2p) and O (2p) bands). The O (2p) peak, at 10 L and below, looks very different from that of ThO₂. ThO₂ has a broad 5.7 eV wide two peak O (2p) band in contrast the O (2p) peak following exposures <10 L NO is symmetrical and narrower (~ 3 eV). The experiments previously discussed for O₂ adsorption have shown that thorium dioxide is formed even in the presence of metal and no intermediate oxide is formed. However the symmetric O (2p) peak observed indicates the formation of an oxide where thorium is in a lower oxidation state than +4 as observed in the dioxide. The presence of chemisorbed oxygen, giving rise to the symmetric O (2p) peak, can be ruled out as we would expect a less broad, much sharper peak centered between 5 and 6 eV [14]. Therefore the spectra obtained indicate the formation of a thorium oxide lower in oxidation state than ThO₂ (of which no bulk oxide is known) stabilized by the presence of nitrogen on the surface. We therefore propose the formation of an “oxynitride” species. Further exposure to NO, 10 L and above, results in the development of an O (2p) feature at a slightly higher BE (approximately 7 eV) producing a two peak O (2p) band. Concomitantly there is an increase in intensity centred at ca 5 eV and the O (2p) band begins to resemble the O (2p) band of ThO₂. The shift in the N (2p) peak from 4 to 3 eV is typical of Th₃N₄ nitride formation [11]. There is a concomitant decrease in emission at E_f . At these higher exposures all 6d7s states are transferred into the N (2p) and O (2p) bands. The DOS at the Fermi-level drops to zero, and the resulting compound is an insulator.

3.2.3. Nitrogen Dioxide (NO₂) Adsorption

Initially, for an exposure of 5 L, the Th (4f) spectrum is essentially as was found for NO adsorption (figure 3.13 and 3.14), a Th (4f_{7/2}) component at 334.5 eV developing and by 50 L exposure there is no evidence of a metal component in the spectrum. This shift in core levels is similar to that seen after exposure to NO (1.4 eV), and compares with a 2.1 eV shift for ThO₂ [10]. The O (1s) spectra observed following exposure to NO₂ are similar to the spectra acquired following exposure to NO. For exposures up to 25 L a single O (1s) peak with a binding energy of 530.9 eV is observed (figure 3.15). A second oxygen species appears at 532.8 eV for higher exposures (> 25 L) of NO₂. Again this is similar to what is observed for NO, although this peak is slightly more intense than the analogous peak following NO exposure. The higher binding energy O (1s) peak contributes approximately 8 % and 20 % of the surface oxygen for NO and NO₂ exposure respectively.

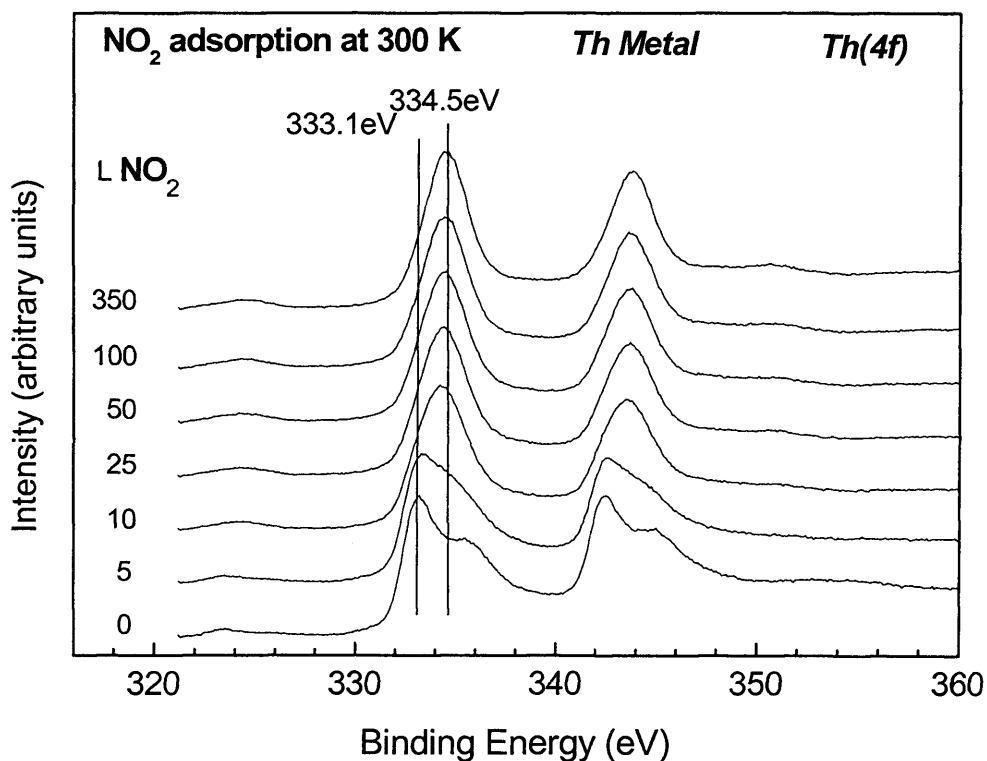


Figure 3.13. Th(4f) spectra for NO₂ adsorption

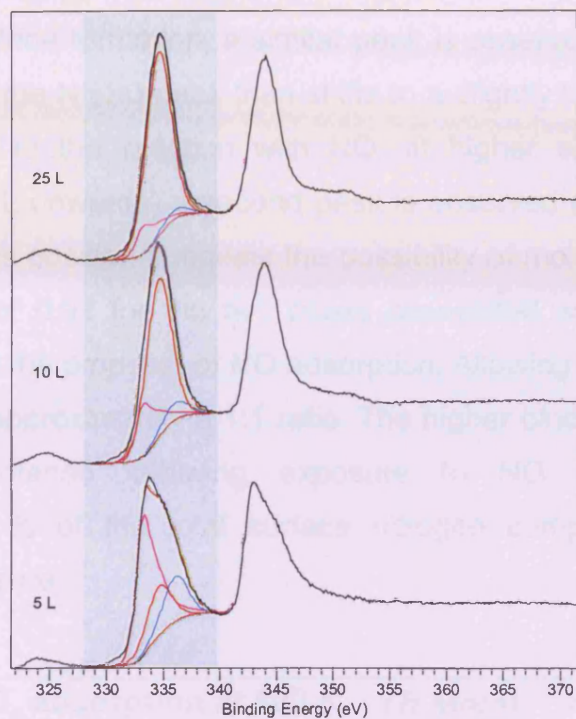


Figure 3.14. Curve fitted Th(4f) spectra for NO₂ adsorption. Th metal well screened peak: Pink, Thorium metal poorly screened peak: blue, oxide peak: red.

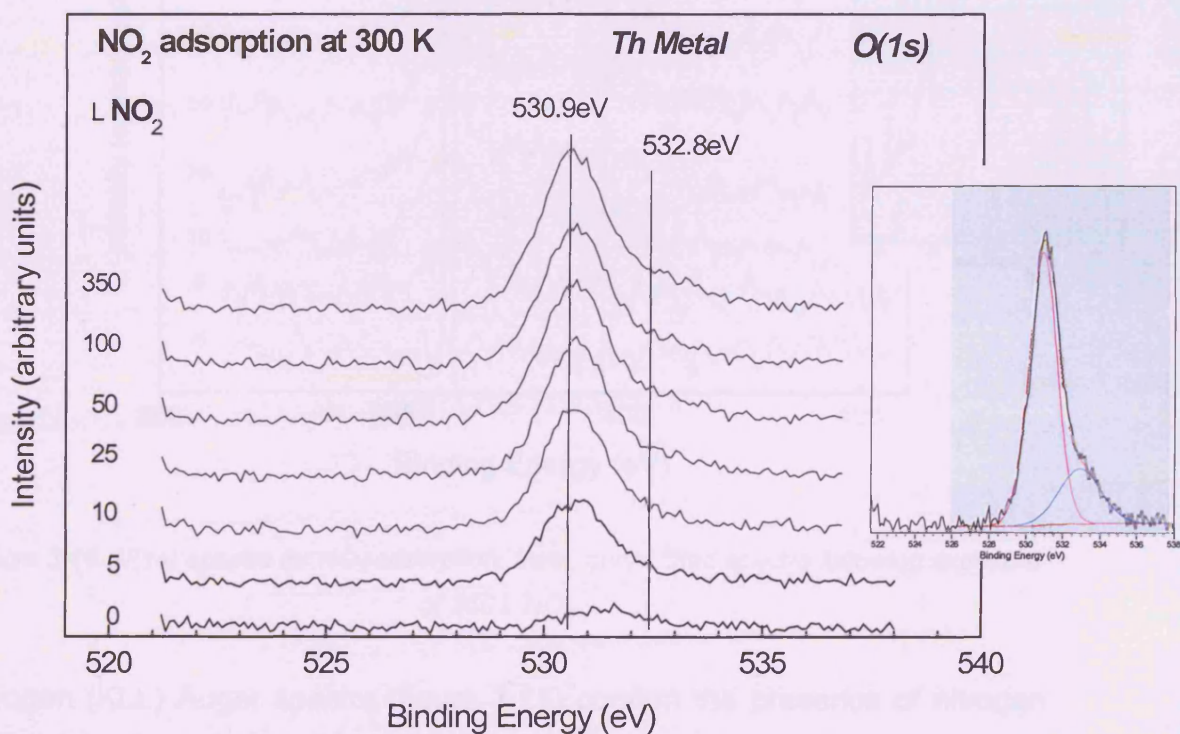


Figure 3.15. O(1s) spectra for NO₂ adsorption. Inset, curve fitted spectra following exposure of 350 L NO₂.

The N (1s) spectra (figure 3.16) show the growth of a peak at 396.2 eV, characteristic of nitride formation; a similar peak is observed for UN [12]. As observed with NO the N (1s) peak then shifts to a slightly lower BE, of 395.8 eV. Again similar to the reaction with NO, at higher exposures of NO₂ (approximately 25 L onwards) a second peak is observed at 399.5 eV in the N (1s) spectra. This position suggests the possibility of molecularly adsorbed NO. A N:O ratio of 0.92 for the two peaks associated with molecular NO adsorption support the proposal of NO adsorption. Allowing for slight errors in calculation this is approximately a 1:1 ratio. The higher binding energy N (1s) peak is more intense following exposure to NO₂ and contributes approximately 40 % of the total surface nitrogen compared with 20 % following NO exposure.

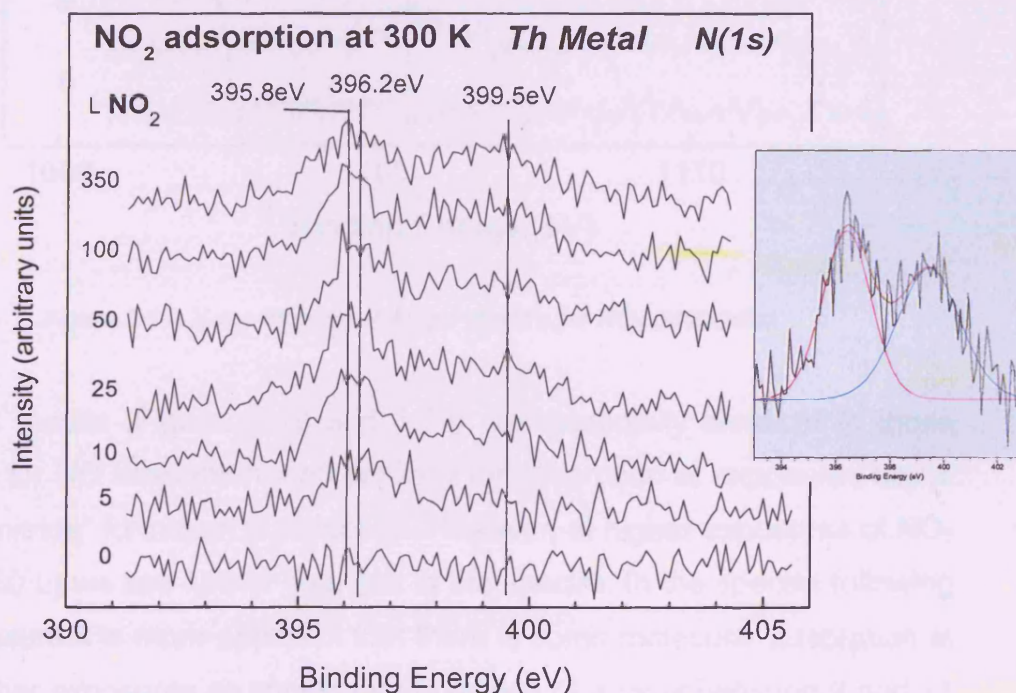


Figure 3.16. N(1s) spectra for NO₂ adsorption. Inset, curve fitted spectra following exposure of 350 L NO₂.

Nitrogen (KLL) Auger spectra (figure 3.17) confirm the presence of nitrogen species on the surface and a slight decrease in intensity is observed for increasing exposures similar, but not as pronounced, to the spectra obtained

following exposure to NO. A similar explanation for the decrease in intensity of the peaks, due to the low kinetic energy of the photoelectrons resulting in a limited escape depth, is offered.

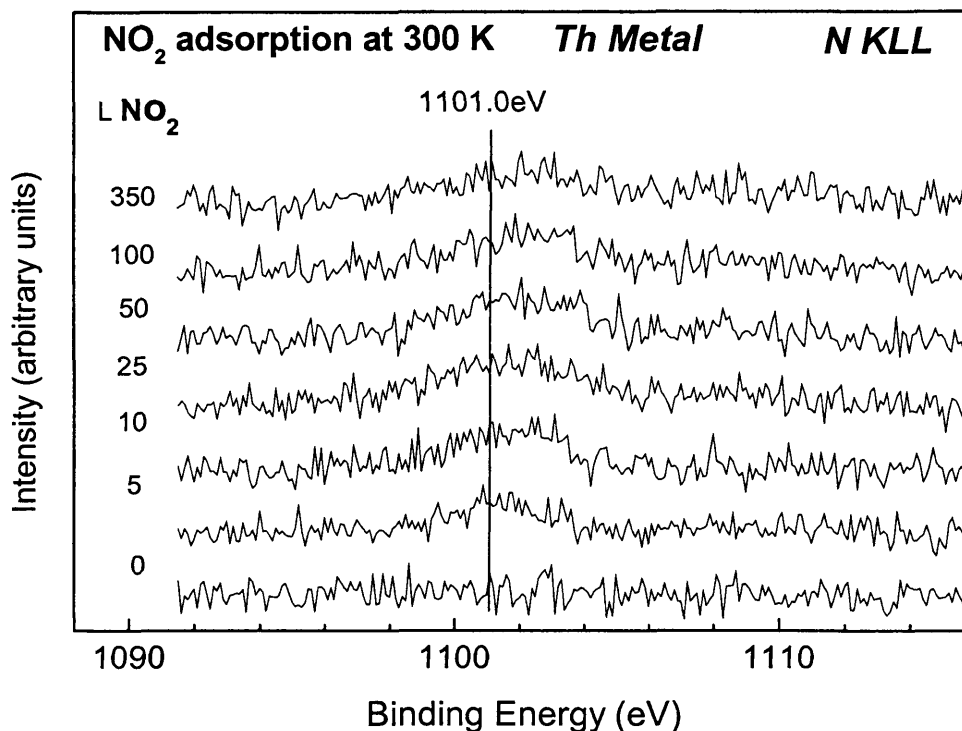


Figure 3.17. X-ray induced N Auger spectra for NO₂ adsorption

The UPS results (Figure. 3.18 and 3.19) are essentially identical to those observed for NO adsorption, and similarly for adsorption at exposures below 10 L "oxynitride" formation is proposed. However, at higher exposures of NO₂ (above 350 L) we see further changes in the spectra. In the spectra following NO₂ exposure it is more apparent that there is some molecular adsorption at these higher exposures as shown by the growth of a peak between 9 and 11 eV. This is in the region where we would expect to see molecular adsorption of NO [15]. The first band for gaseous NO is observed between 9 and 10.5 eV resulting from the removal of the antibonding 2p electron. This observation supports the O (1s) and N (1s) spectra which indicate increased molecular NO adsorption following NO₂ exposure.

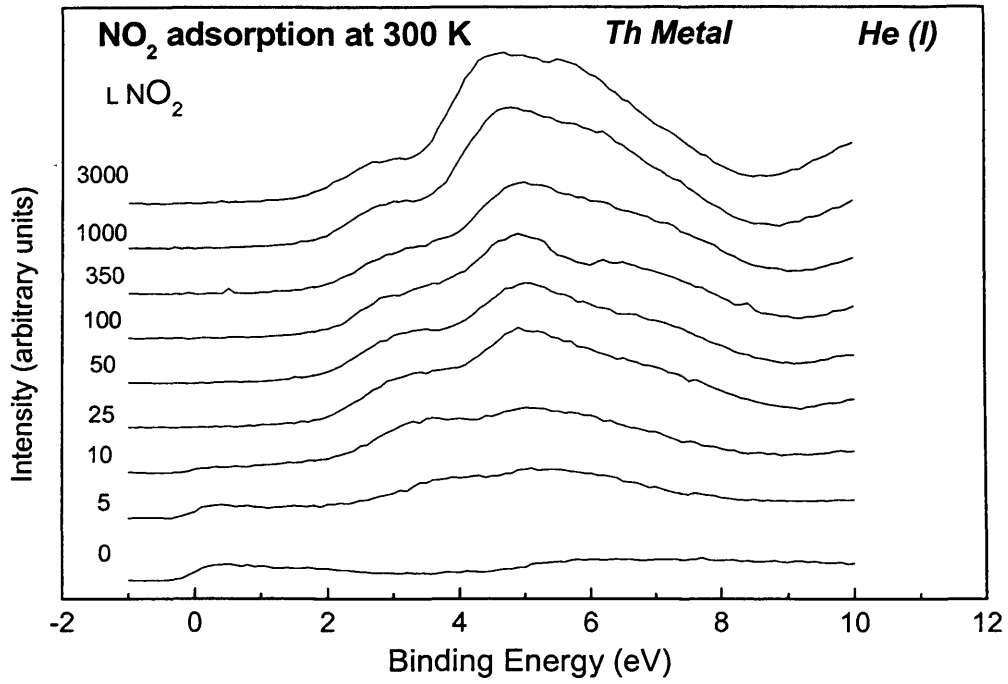


Figure 3.18. UPS He(I) spectra of NO₂ adsorption on Th

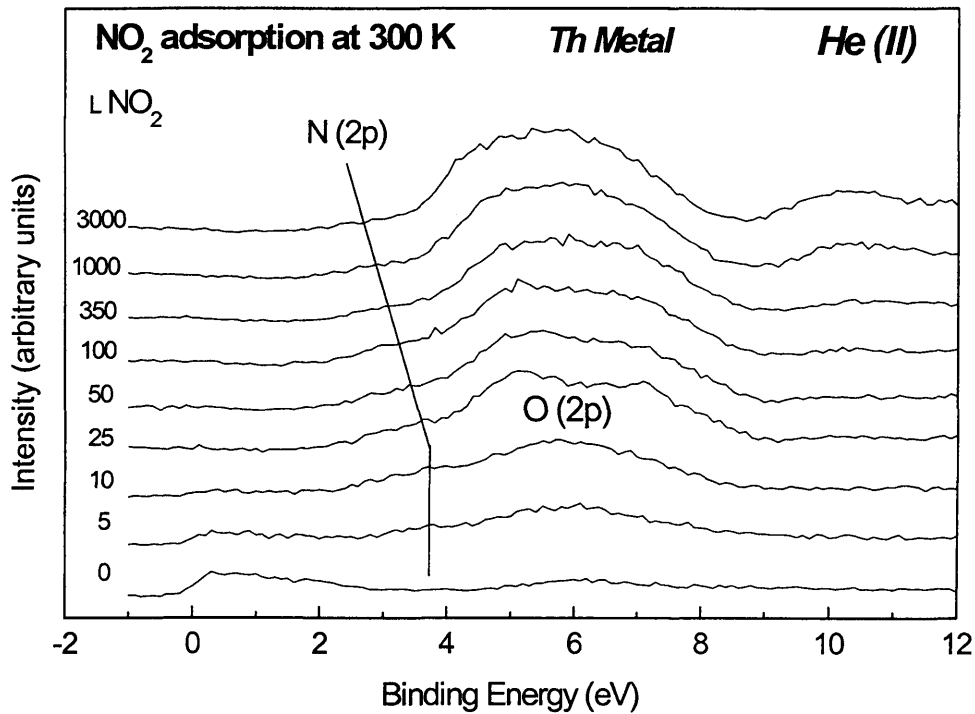


Figure 3.19. UPS He(II) spectra of NO₂ adsorption on Th

Exposures to NO₂ above 10 L result in a similar change in the spectra as observed following exposure to NO: the development of a peak on the higher binding energy side of the O (2p) band resulting in a two peak structure following 25 L exposure and an increase in intensity centred at ca 5 eV. The O (2p) peak at these exposures begins to resemble that observed following dioxide formation. The shift in the N (2p) peak from 4 to 3 eV is typical of a change from ThN to Th₃N₄ nitride [11].

The results obtained following NO₂ exposure suggest that NO₂ reacts with the thorium surface in a similar way to NO, at least up to 350 L exposures. Above 350 L exposure the O (1s), N (1s) and UPS spectra produced following NO₂ adsorption suggest increased molecular NO adsorption following exposure to NO₂.

3.2.4. Nitrous Oxide (N₂O) adsorption

Figure 3.20 shows the 4f photoelectron core-level spectra of Th metal exposed to increasing doses of N₂O gas. Initially, after 5 L exposure, there is almost no change in the Th (4f) spectra. Following 10 L exposure of N₂O, an increase in a peak centred at 334.8 eV and a slight decrease in the metallic contribution to the 4f envelope is observed. For exposures above 25 L the Th (4f) peaks at 334.8 eV and 344.2 eV dominate the spectra and the metallic contribution is greatly attenuated. These new peaks are shifted 1.7 eV from the well screened metallic peaks at 333.1 eV and 342.5 eV. This is, as was observed for NO and NO₂ exposures, intermediate between that of ThO₂ (2.1 eV) and Th₃N₄ (0.4 eV). However there is a slightly larger shift in the 4f binding energy following N₂O exposure, when compared to NO and NO₂.

Intensity on the lower binding energy side of the oxide (4f) peaks, at 25 L and above (inset figure 3.20), shows there is also a contribution from underlying metal or surface ThN formation, which both reside at the same binding energy, 333.1 eV [11]. The presence of nitrogen on the surface, confirmed by the N (1s) spectra (figure 3.22), indicates that the contribution could possibly

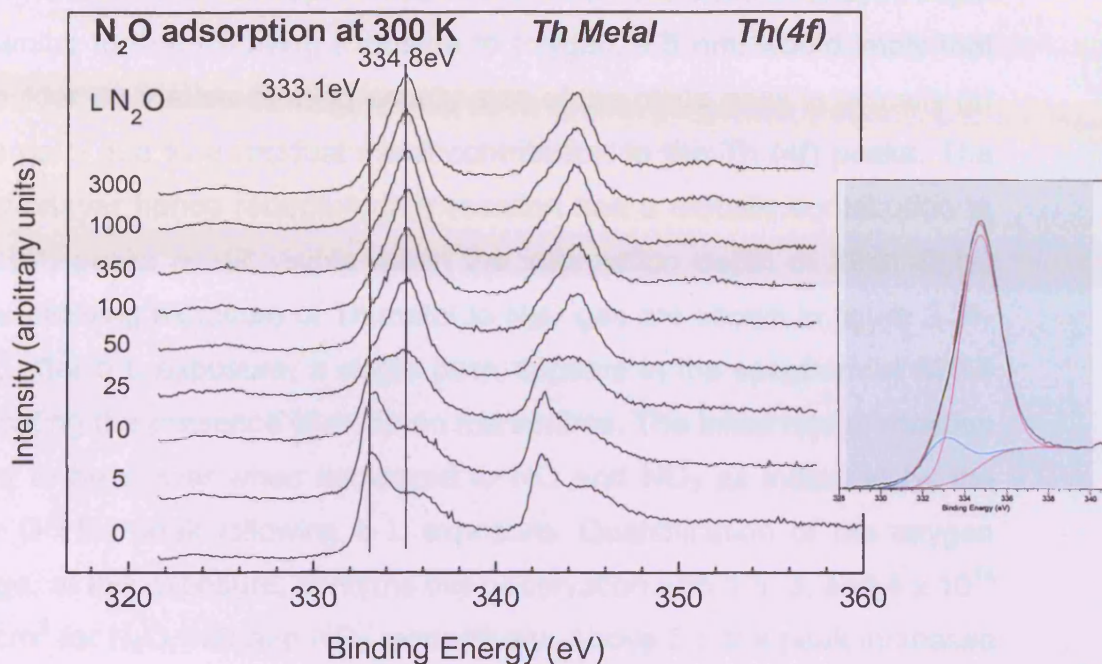


Figure 3.20. Th(4f) spectra for N₂O adsorption. Inset, curve fitted Th (4f_{7/2}) peak following 350 L exposure of N₂O.

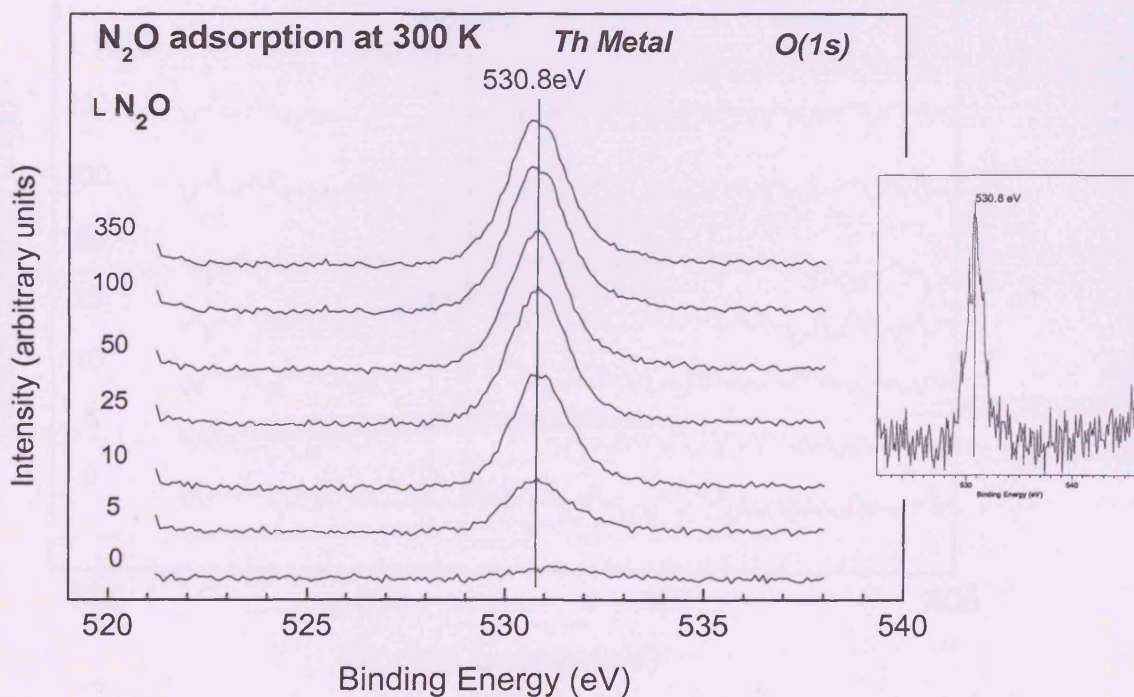


Figure 3.21. O(1s) spectra for N₂O adsorption. Inset difference spectrum showing the result of a subtraction of the spectrum following 25 L exposure from the spectrum following 350 L exposure.

be from nitride. However depth calculations which show the overlayer depth to be similar to that following exposure to oxygen, 1.5 nm, would imply that the shoulder on the low binding energy side of the oxide peak is actually (at least in part) due to a residual metal contribution to the Th (4f) peaks. The oxide overlayer hence retards further reaction and a metallic contribution to the Th (4f) peaks is still visible within the information depth of XPS. O(1s) spectra following exposure of Th metal to N₂O gas are shown in figure 3.21. Initially, after 5 L exposure, a single peak appears in the spectrum at 530.9 eV indicating the presence of oxide on the surface. The initial rate of reaction appears to be slower when compared to NO and NO₂ as indicated by the weaker O (1s) peak following 5 L exposure. Quantification of the oxygen coverage, at this exposure, confirms this observation with 1.5, 3, and 4 x 10¹⁴ atoms/cm² for N₂O, NO and NO₂ respectively. Above 5 L the peak increases in intensity. Only the single oxide peak is observed.

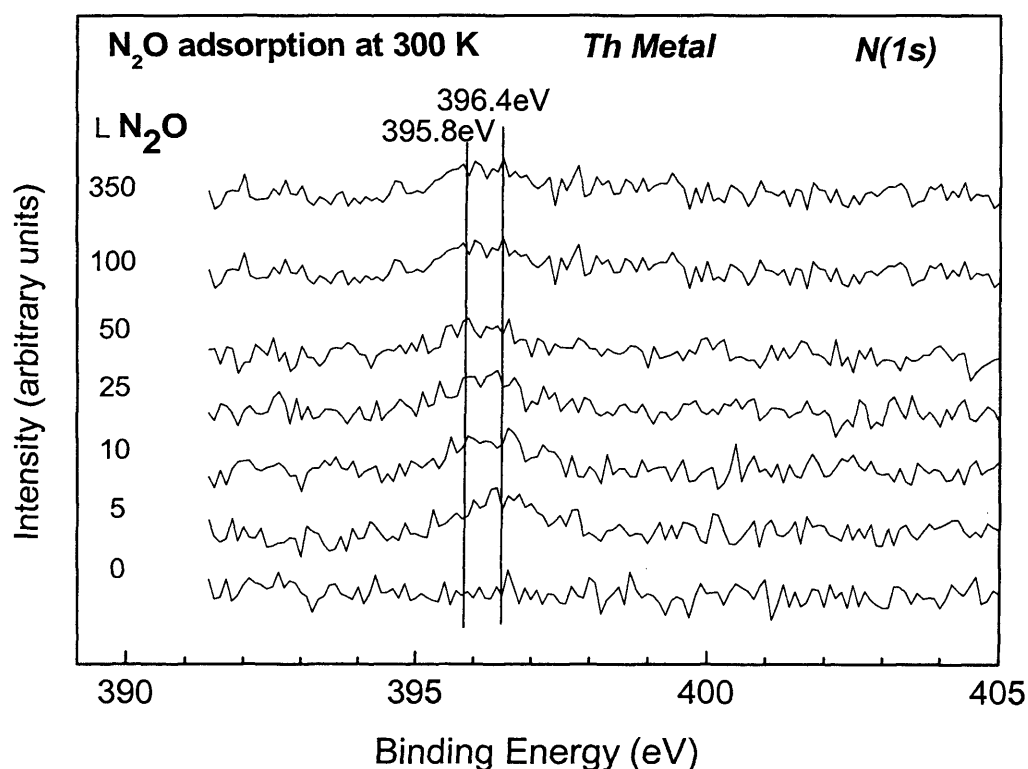


Figure 3.22. N(1s) spectra for N₂O adsorption

The N (1s) spectra show an increase in intensity of a peak at 396.4 eV following 5 L exposure of N₂O (figure. 3.22). There is very little change in this peak upon increasing exposures, only a shift to slightly lower binding energy of 395.8 eV and what appears to be a slight decrease in intensity. This observation is confirmed by calculations which show a decrease in surface coverage from 1×10^{14} to 5×10^{13} atoms/cm² between 10 and 25 L exposures. The presence of nitrogen is once again confirmed by the x-ray induced N Auger spectra (figure 3.23), which also shows the decrease in intensity with exposure. This may suggest that as discussed previously nitrogen diffusion to a subsurface position, penetrating deeper into the thorium lattice than the oxygen occurs. However the decrease in intensity of both the N (1s) and Auger peaks following exposure to N₂O indicates that the nitrogen may actually recombined and leave the surface as N_{2(g)}.

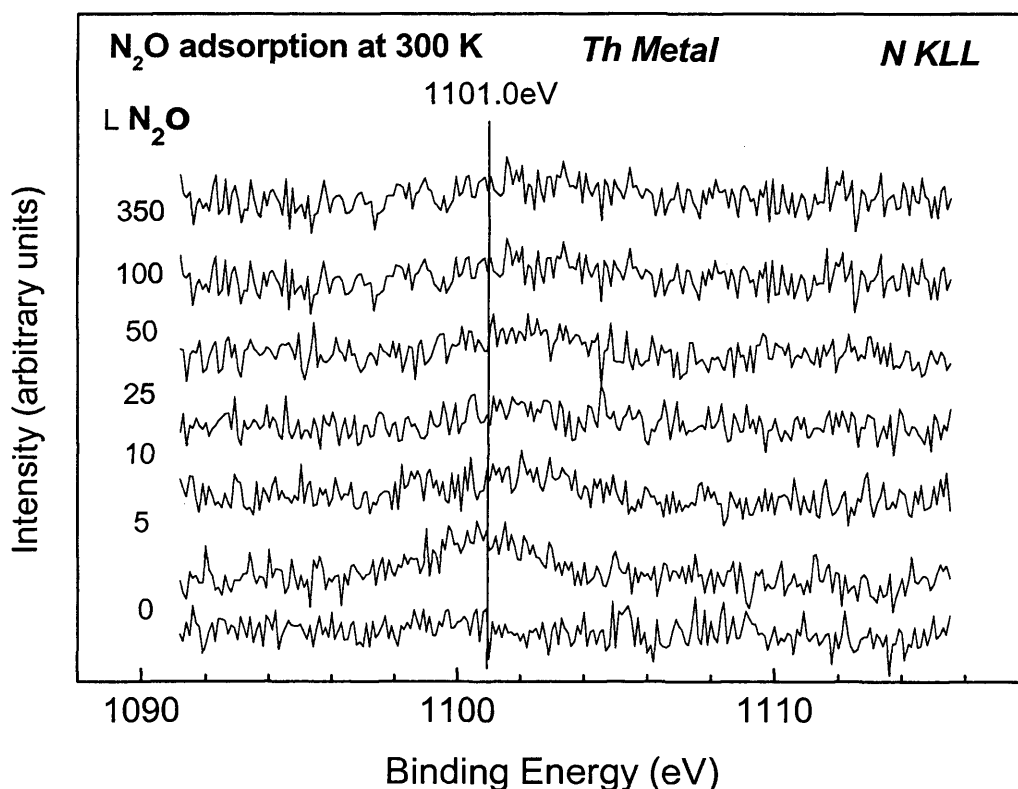


Figure 3.23. X-ray induced N Auger spectra for N₂O adsorption

The He I and He II UPS spectra show that with increasing exposures of N₂O, the N (2p) and O (2p) bands grow between 2 and 8 eV (figure 3.24 and 3.25).

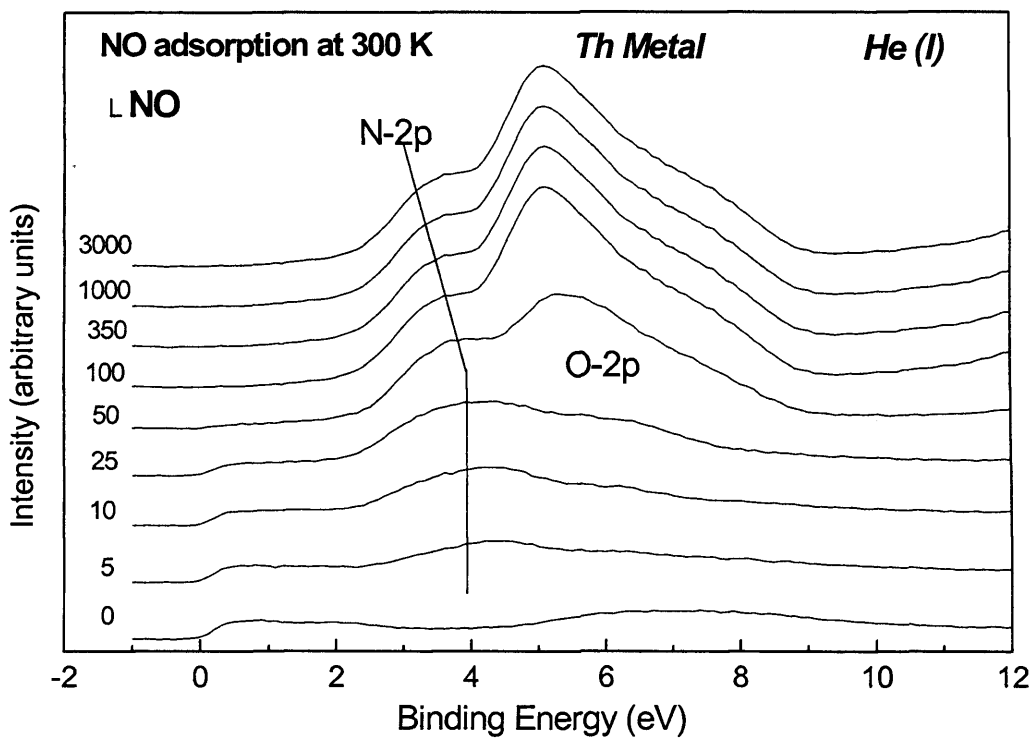


Figure 3.24. UPS He(I) spectra of N₂O adsorption on Th

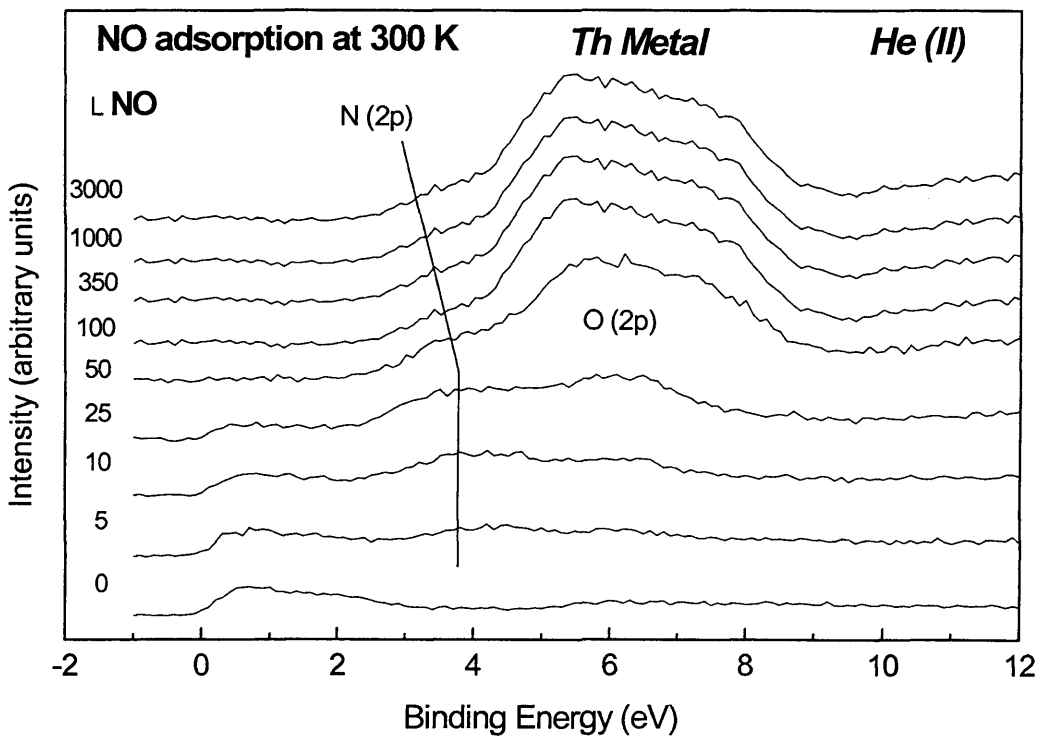
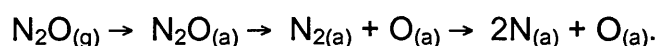


Figure 3.25. UPS He(II) spectra of N₂O adsorption on Th

The reaction appears to proceed at a slower rate when compared to the NO and NO₂ reaction, and there also appears to be more nitrogen adsorbed initially following N₂O exposure. Adsorbed oxygen:nitrogen ratios support this observation showing a smaller ratio for initial (5 L) reaction of N₂O. The calculations showed ratios of 0.5, 1 and 1.3 for N₂O, NO and NO₂ respectively. The calculated ratio of 0.5 following 5L exposure of N₂O suggests complete dissociative adsorption of 2N_(a) and O_(a) ((a) = adsorbed), a possible reaction scheme is



The conduction band signal does not decrease to zero intensity until exposures greater than 25 L. N (2p) states of the nitride are centered at 4 eV. O (2p) states of the oxide are centered at 6eV. For exposures up to 25 L, the UPS spectra are similar to those observed for NO and NO₂ adsorption. It appears that up to 25 L there is similarly the formation of a metallic "oxynitride" overlayer. The symmetric O (2p) shape, adsorbed nitrogen and the intermediate Th (4f) peak shift support this proposal. However, when we increase the exposures of N₂O above 25 L we see a slight difference in the spectra when compared to NO and NO₂. The emission at E_F does similarly decrease to zero and we have the formation of an insulator at 50 L. However in contrast to the spectra obtained for NO and NO₂ it appears that there is increased oxidation. In contrast to the slight increase in a higher binding energy contribution to the O (2p) peak at higher exposures of NO and NO₂ we have a definite two peak O (2p) structure almost identical to that produced following exposure to O₂. The slight increase in shift of the Th (4f) peaks for N₂O exposure (1.7 eV) compared to NO and NO₂ adsorption (1.4 eV) also support the increased oxidation following exposure to N₂O.

3.3. Quantification

Initial exposure up to 5 L produce the expected ratios of oxygen:nitrogen for all three nitrogen oxides (Figure. 3.26) indicating complete dissociation for all three gases on the clean metal surface i.e.

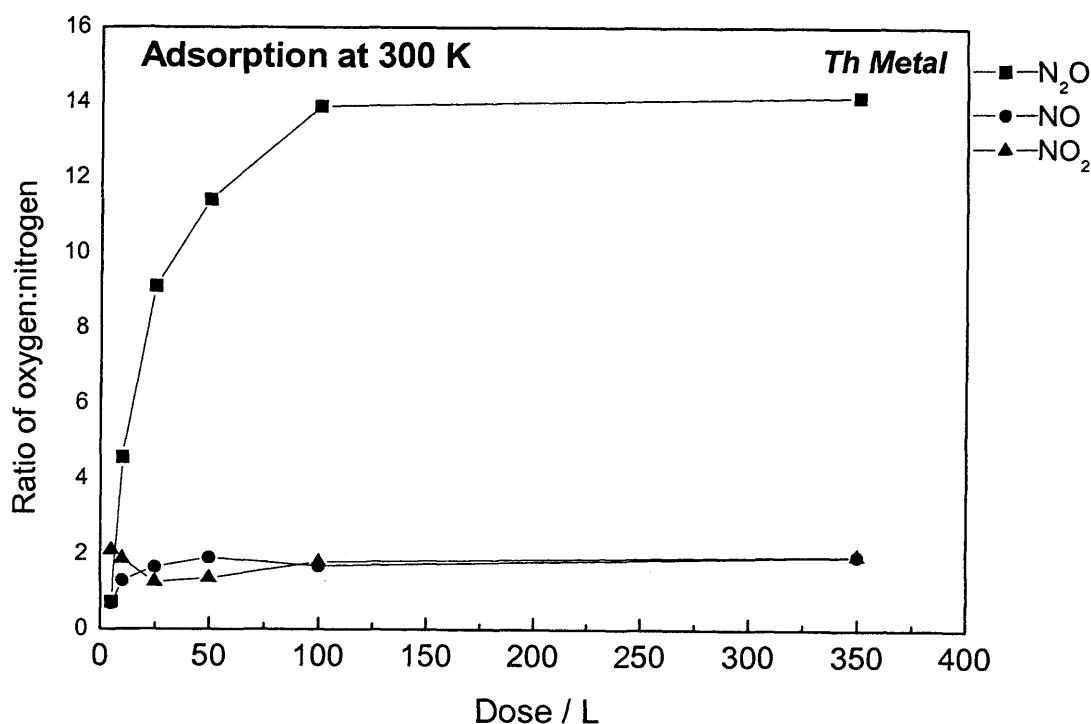
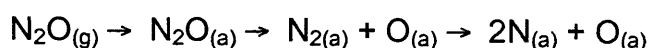
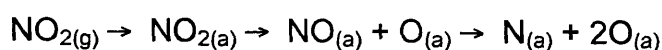
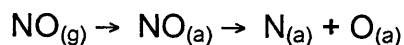


Figure 3.26. Oxygen:nitrogen ratio following increasing exposures of NO, NO₂ and N₂O

For exposures between 5 and 25 L, a higher oxygen to nitrogen ratio than the expected 1:2 or 1:1 for adsorbed and dissociated N₂O and NO respectively is calculated (Figure. 3.26). NO₂ reaction did however result in approximately 2:1 oxygen to nitrogen ratio. Assuming that nitrogen is not lost in the gas phase during exposure to N₂O and NO, the conclusion has to be either that free nitrogen produced by the dissociation of N₂O or NO has dissolved into

the bulk of the polycrystalline thorium crystal, or that the nitrogen atoms had recombined and left the surface as N_{2(g)}. The N (1s) combined with the N KLL Auger spectra suggest that following exposure to N₂O nitrogen atoms recombine and desorb from the surface as N_{2(g)}. Both N (1s) and nitrogen Auger spectra show a decrease in intensity with exposure above 5 L. If the nitrogen had dissolved into the bulk we would expect a more pronounced change in the highly surface sensitive N KLL Auger peak when compared to the N (1s) peak. The limited escape depth of the N KLL Auger photoelectrons would mean Auger photoelectrons originating from dissolved nitrogen would not escape the surface resulting in a decrease in intensity of the Auger peak. In contrast the N (1s) photoelectrons have a greater escape depth and a decrease in intensity of the N (1s) peak would occur later, if at all, when compared to the N KLL Auger peak. The results obtained for NO and to a lesser degree NO₂ suggest nitrogen dissolves into the bulk. A decrease in intensity of the Auger peak but no change in the N (1s) intensity is observed. The results suggest that nitrogen adsorbed on the surface following exposure to NO and NO₂ diffuses to a subsurface position, penetrating deeper into the thorium lattice than the oxygen.

Figure 3.26 also shows a rapid increase in oxygen:nitrogen ratio observed for N₂O exposures above 25L, much greater than for NO and NO₂, indicating that only oxygen adsorbs on the "oxynitride" covered surface i.e. N₂O_(g) → N_{2(g)} + O_(a). In the early stages, <25 L, there is some N₂O_(g) → 2N_(a) + O_(a) where complete dissociation occurs at the most reactive metal sites. These calculations suggest that N₂O only partially dissociates (N₂O → N_{2(g)} + O_(a)) on the surface oxynitride and the nitrogen gas formed does not react with surface. Only oxygen incorporation is observed which gives rise to the increased oxygen:nitrogen ratio above 25 L and the increased oxidation observed in the spectra.

Oxygen and nitrogen coverage calculations (figure 3.27) show that for oxygen exposure we observe the most rapid uptake of oxygen. Oxygen uptake slows after only 5 L and there is no further increase above 25 L. The

oxide surface produced following exposure to oxygen inhibits further oxidation and the XPS spectra show that there is still metal within the information depth of XPS. The oxygen now has to adsorb on the less reactive oxide surface and diffuse through the oxide layer to reach the metal gas interface where dissociation and further oxidation can occur. This slows the reaction considerably. Initially, for exposures of 5 L, NO, NO₂ and N₂O adsorption show a much slower uptake of oxygen when compared to O₂ adsorption.

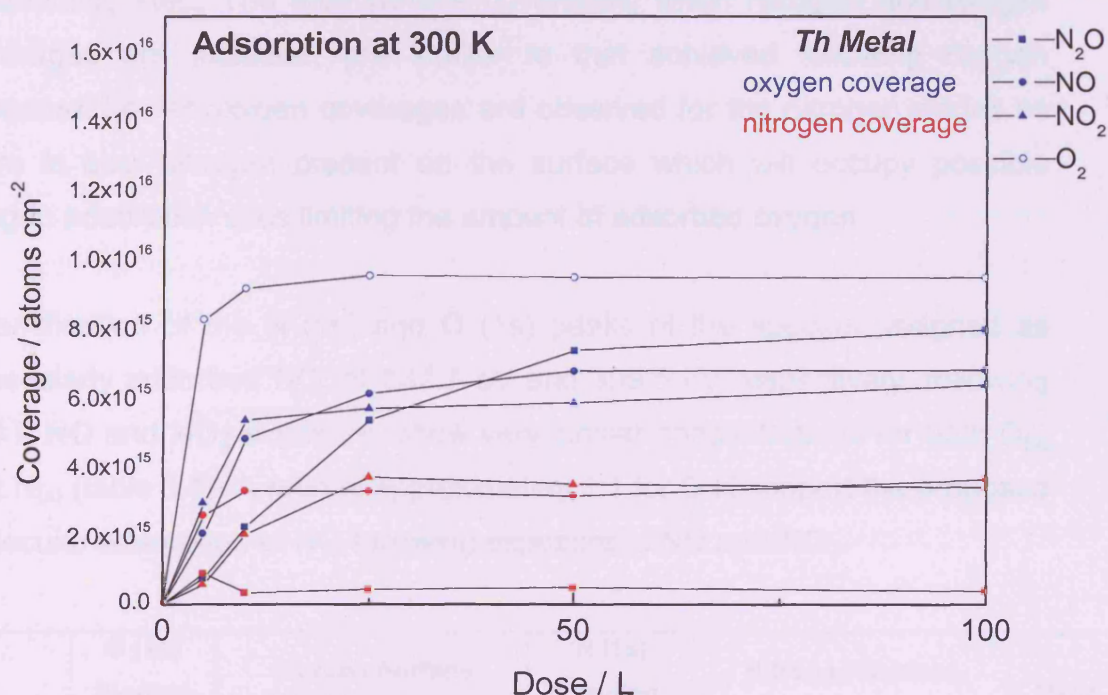


Figure 3.27. Oxygen and nitrogen coverage following increasing exposures of O₂, NO, NO₂ and N₂O

Initially, following 5 L exposure, N₂O adsorption results in the lowest oxygen coverage. Above 5 L exposure oxygen uptake increases and nitrogen coverage decreases. Nitrogen no longer adsorbs on the surface and there is even a decrease in the amount of nitrogen adsorbed on the surface as it recombines and leaves the surface (discussed previously). Oxygen surface coverage continues to increase and dissociation to N_{2(g)} and O_(a) results in an increase in the amount of surface oxygen. Nitrogen and oxygen surface

coverages following exposures of NO show again, as already discussed for the oxygen:nitrogen ratios, that initially following exposures <5 L oxygen and nitrogen uptake is approximately the same. However, 5 – 25 L exposures, a greater increase in surface oxygen is observed and supports the earlier proposal that surface nitrogen dissolves further into the bulk than oxygen therefore appearing as though the nitrogen surface coverage does not increase. The initial rate of reaction for all three nitrogen oxides is slower than oxygen suggesting that adsorption prior to dissociation is the rate determining step. The final surface coverages, when nitrogen and oxygen coverages are included, are similar to that achieved following oxygen exposure. Lower oxygen coverages are observed for the nitrogen oxides as there is also nitrogen present on the surface which will occupy possible oxygen adsorption sites limiting the amount of adsorbed oxygen.

Quantification of the N (1s) and O (1s) peaks of the species assigned as molecularly adsorbed NO, at 532.7 eV and 399.5 eV respectively, following 350 L NO and NO₂ exposure, show very similar concentrations for both O_(a) and N_(a) (table 3.1). A ratio of approximately 1:1 for O:N support the proposed molecular adsorption of NO following exposure to NO and NO₂.

	O (1s) Binding Energy (eV)	Oxygen Surface Coverage ($\times 10^{15}$ atoms/cm ²)	N (1s) Binding Energy (eV)	Nitrogen Surface Coverage ($\times 10^{15}$ atoms/cm ²)	Ratio O:N
NO (350 L)	532.7	1.21529	399.5	1.06375	1.14
NO ₂ (350 L)	532.7	2.28117	399.5	2.18082	1.04

Table 3.1. Oxygen and nitrogen coverage calculations using the N (1s) and O (1s) peaks of the species assigned as molecularly adsorbed NO.

Film thicknesses, figure 3.28, are calculated (as described in Chapter 2) by integrating the area under the “oxide” and metal contributions to the Th (4f) peak and measuring the attenuation of the metal contribution as a function of

exposure. For O₂ adsorption we observed the most rapid initial uptake of oxygen, but upon the formation of an oxide layer, approximately 1 nm thick, oxidation slows dramatically and further oxidation is slow, indicating that oxygen diffusion to the metal oxide interface is inhibited. Adsorption of N₂O results in a slower uptake below 5 L. For exposures above 5 L the oxide thickness increases more rapidly and saturates, for exposures > 20 L, at a value similar to that observed following O₂ exposures. In both cases (N₂O and O₂) the overlayer inhibits further reaction and thorium metal is still observed within the information depth of XPS. Initially the rate reaction following NO and NO₂ exposures is slower than that following exposure to oxygen. However for higher exposures (> 20 L) the oxide thickness develops more rapidly than for O₂. This would indicate that dissociative adsorption and diffusion to the metal gas interface is more thermodynamically favourable for NO and NO₂ in the presence of the proposed "oxynitride" surface than for oxygen and an oxide layer. The overlayer produced is also thick enough so that thorium metal is no longer, following NO and NO₂ exposure, within the information depth of XPS.

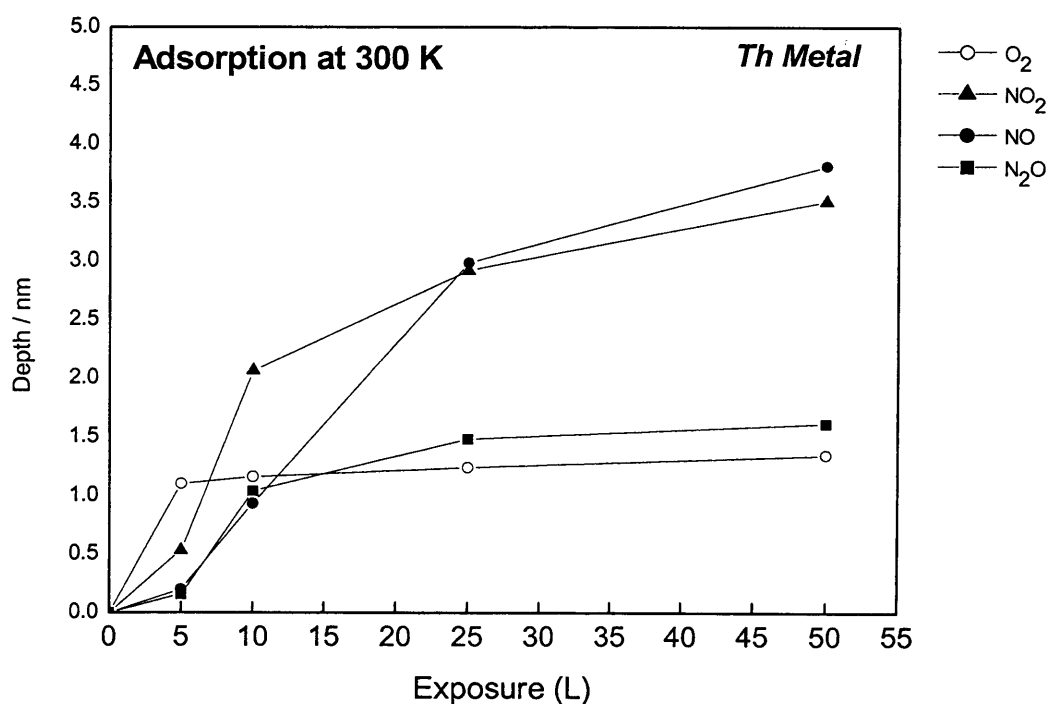


Figure 3.28. Depth analysis following increasing exposures of O₂, NO, NO₂ and N₂O

3.4 Discussion

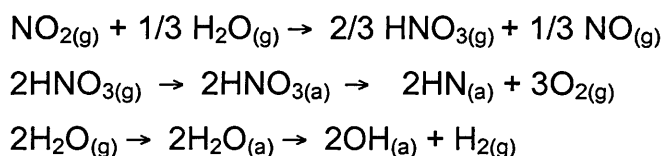
The data for low exposures (~5 L) of the nitrogen oxides (N₂O, NO and NO₂) do not support ThO₂, ThN or Th₃N₄ formation. The binding energies for the Th (4f) and a symmetrical O (2p) peak in the valence band indicate the formation of an oxide lower in oxidation state than thorium dioxide, although there are no stable lower bulk oxides of thorium known. Instead ThO₂ forms even in the presence of Th metal, and no intermediate pure oxide is formed. As with uranium where a lower uranium oxide is stabilized by impurities, i.e. in reality oxynitrides/carbides [16], the formation of a thorium "oxynitride" following low exposures to N₂O, NO and NO₂ is therefore proposed, in which the lower oxide of thorium is stabilised by the presence of nitrogen on the surface.

The thermodynamic criterion governing NO dissociation on metals rests on the ability of the metal to form a stable oxide and nitride, as is the case with Th metal [11]. Nitric oxide adsorbs dissociatively on the uranium surface at 298 K producing atomic oxygen and atomic nitrogen. It is proposed that the interaction of nitrogen and oxygen produces an oxynitride layer. Following exposures of NO, 25 L and above, the UPS spectra show further reaction the O (2p) peak begins to form intensity at slightly higher BE and a two peak structure develops typical of actinide dioxide formation. A shift in the N (2p) peak from 4 to 3 eV is also typical of ThN to Th₃N₄ nitride formation [11]. At these higher exposures all 6d7s states are transferred into the N (2p) and O (2p) bands. The DOS at the Fermi-level drops to zero, and the resulting compound is an insulator. In contrast to the UPS spectra no shifts in the Th (4f) XPS spectra suggesting dioxide formation are observed. A single peak shifted 1.4 eV from the clean metal peak remains unchanged up to 350 L. Upon increased exposures, 25 – 350 L, the probability of a NO molecule landing on a site with vacant nearest neighbours is decreased, so dissociation of adsorbed NO molecules is inhibited and hence molecular adsorption is observed. The appearance of peaks at higher binding energy with regard to the oxide and nitride peaks in the O (1s) and N (1s) spectra

along with the quantification of these peaks indicate that some molecular NO adsorption occurs at higher exposures.

Adsorption of NO₂ on the metal surface could result in either complete dissociation or in partial dissociation, yielding NO adsorbed on the surface. The complete dissociative adsorption of NO₂ and the breaking of the N-O bonds are evidenced by presence of a nitride peak. Nitrogen dioxide reacts in a similar way to nitric oxide, for exposures up to 350 L, producing atomic oxygen and atomic nitrogen, which as with NO adsorption is proposed to generate an oxynitride layer. Again as with NO, molecular NO adsorption is observed at higher exposures. Quantification of the relevant N (1s) and O (1s) peaks support this proposal.

We must however consider the possibility that the second peak in both the N (1s) and O (1s) spectra following exposure to NO and NO₂ may be caused by the presence of small amounts of H₂O, producing NH (appearing in the N (1s) spectra) and also OH (appearing in the O (1s) spectra). The reaction of NO and NO₂ with H₂O produces nitric acid and therefore the dissociative adsorption of HNO₃ would produce NH. Dissociative adsorption of H₂O would give rise to the OH peak in the O (1s) region. A possible reaction scheme involving water would be:



However it does seem unlikely that OH groups would only appear during NO and NO₂ exposures, since these were performed under the same conditions as O₂ and N₂O exposures. The O (1s) spectra following exposure to O₂ and N₂O show only a single oxide peak with no shoulder on the higher BE side. Furthermore an increase in intensity of the H₂O peak was not observed in the mass spectrum of the gas phase NO and NO₂ under exposure conditions.

This increased amount of molecular NO adsorbed following exposure to NO₂ compared with NO maybe explained as follows. In the literature it is well reported that the decomposition of NO is inhibited by the presence of oxygen [17]. Therefore since the decomposition process expected for NO₂ following formation of the oxynitride layer is $\text{NO}_2 \rightarrow \text{NO}_{(a)} + \text{O}_{(a)}$, the presence of the oxygen may inhibit the decomposition of the now adsorbed NO and a greater proportion, when compared with NO exposures, remains molecularly adsorbed.

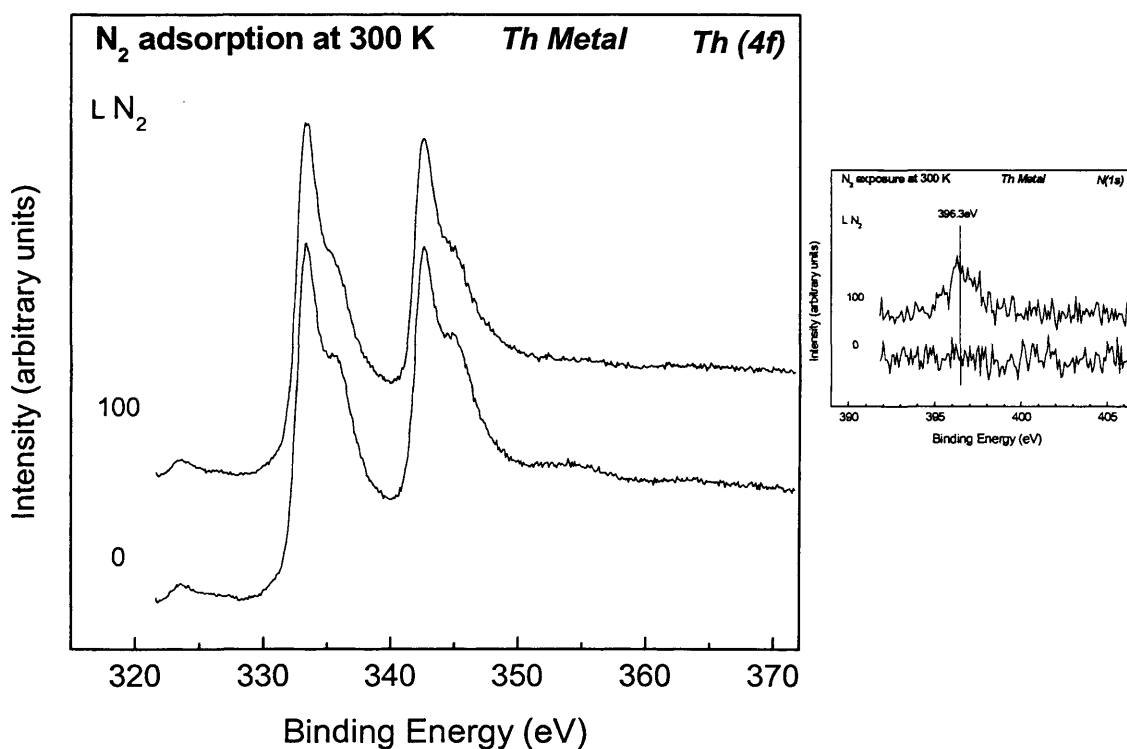


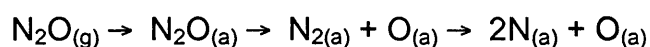
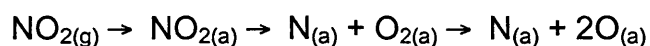
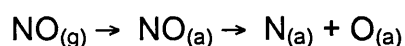
Figure 3.29. Th (4f) and N (1s) spectra of N₂ adsorption on thorium metal.

N₂O adsorbs dissociatively on uranium, initially with the adsorption of both oxygen and nitrogen on the surface. At higher exposures (>5 L) it appears that dissociative adsorption is followed by the desorption of N₂ (g) and only oxygen then adsorbs on the oxidised surface. The reaction of metallic thorium with N₂ has been shown to only proceed at elevated temperatures e.g. reaction with N₂ at 1200 K leads to the formation of ThN [18] (later identified as Th₃N₄ [11]). However the polycrystalline Th metal surface used

in these experiments has been exposed to pure N₂ and at 298K thorium nitride formation was observed (figure 3.29). Nitride formation was confirmed by the N (1s) peak at 396.3 eV and the shape of the Th (4f) peaks, following 100 L exposure of N₂, both typical for ThN formation [11]. The well screened Th (4f) peak does not shift or decrease in intensity. A broadening of the well screened peak and what appears to be a slight shift of the poorly screened satellites towards the main lines indicate ThN formation [11]. The formation of thorium nitride from N₂ exposure at 298 K may well be due to defects on the polycrystalline surface. Therefore this would suggest that N₂ formed during the dissociative adsorption of N₂O at exposures up to 5L reacts with defects on the clean polycrystalline metal surface. Nitrogen no longer adsorbs on the metal surface at exposures >5 L suggesting the most reactive metal adsorption sites are occupied. Increased exposure > 5L results in the partial dissociation of N₂O ($N_2O \rightarrow N_{2(g)} + O_{(a)}$) on the oxynitride surface and only oxygen adsorption is observed. Concomitantly the decrease in intensity of the N (1s) and the N KLL Auger peaks, together with the nitrogen coverage calculations show that adsorbed nitrogen recombines and N_{2(g)} desorption is observed. Exposures of N₂O >50 L result in further change in the UPS spectra. The O (2p) peak begins to form a shoulder on the higher BE side and a two peak structure typical of actinide dioxide formation develops. A shift in the N (2p) peak from 4 to 3 eV typical of the formation of Th₃N₄ from ThN [11] is also observed. This appears very similar to the reaction with NO and NO₂. However in contrast to NO and NO₂ the two peak O (2p) shape is more pronounced and is very similar to the O (2p) shape of ThO₂. Surface coverage calculations show that above 50 L exposure of N₂O a greater oxygen surface coverage when compared to NO and NO₂ exposures is observed. The final oxygen surface coverage is just below that of O₂ adsorption and supports the increased oxidation indicated from the O (2p) peak shape in the UPS spectra. This increased surface oxygen concentration may explain also the slight increase in BE shift observed in the Th (4f) spectra (N₂O (1.7 eV) compared to NO and NO₂ (1.4 eV)).

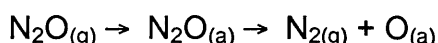
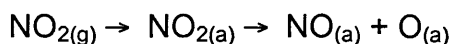
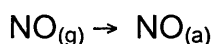
3.4. Conclusion

Initially all three nitrogen oxides display similar reactivity towards the polycrystalline thorium surface. Complete dissociative adsorption i.e.



results in the formation of what is proposed to be a metallic thorium oxynitride, in which a lower oxide of thorium is stabilised by the presence of nitrogen. The O (2p) peak following exposures <5 L is symmetric and narrower than the two peak structure observed following exposure to O₂ and ThO₂ formation. Also a shift intermediate between ThO₂ (2.1 eV) and Th₃N₄ (0.4 eV) of 1.4 eV for NO and NO₂ and 1.7 eV following exposure to N₂O suggested the formation of an oxide lower in oxidation state than ThO₂. However no such bulk thorium oxide is known to be stable. Therefore it is proposed that the lower oxide of thorium is stabilized on the surface by the presence of ThN as an oxynitride.

For exposures above 25 L the probability of a N₂O, NO and NO₂ molecule landing on an adsorption site with vacant nearest neighbours decreases. Complete dissociation is inhibited and partial dissociation is observed. Oxygen adsorption and desorption of N_{2(g)} following increased exposures of N₂O and molecular NO adsorption following exposures of NO and NO₂ is observed i.e.



Thorium therefore partially dissociates N₂O, NO and NO₂ leaving a mixture of metal oxide, metal nitride, and for NO and NO₂ bound NO in the near surface region. All 6d7s electrons become involved in bonding and the resulting compound following exposure to all three gases is an insulator.

3.5. References

1. J. Grimblot, P. Alnot, R.J. Behm, and C.R. Brundle, *Journal of Electron Spectroscopy and Related Phenomena*, 1990. **52**. 175-183.
2. D.A. Hoffman and J.B. Hudson, *Surface Science*, 1987. **180**(1). 77-88.
3. T.E. Madey, N.R. Avery, A.B. Anton, B.H. Toby, and W.H. Weinberg, *Journal of Vacuum Science & Technology a-Vacuum Surfaces and Films*, 1983. **1**(2). 1220-1221.
4. A. Pashutski and M. Folman, *Surface Science*, 1989. **216**(3). 395-408.
5. J.Naegele and L.Mane, *Actinides - Chemistry and Physical properties*, in *Structure and Bonding*, L. Mane, Editor. 1985. p. 197.
6. W.F.Egelhoff, *Surface Science*, 1987. **6**. 253-415.
7. J.C.Fuggle, M.Campagna, Z.Zolnierrek, R.Lasser, and A.Platau, *Physical Review Letters*, 1980. **45**. 1597.
8. F.U.Hillebrecht and J.C.Fuggle, *Physical Review B*, 1982. **25**. 3350.
9. G.M.Bancroft, T.K.Sham, J.L.Esquivel, and S.Larsson, *Chemical Physics Letters*, 1977. **51**(1). 105-110.
10. W.McLean, C.A.Colmenares, R.L.Smith, and G.A.Somorjai, *Physical Review B*, 1982. **25**(1). 8-24.
11. T.Gouder, L.Havela, L.Black, F.Wastin, J.Rebizant, P.Boulet, D.Bouexiere, S.Heathman, and M.Idiri, *Journal of Alloys and Compounds*, 2002. **336**(1-2). 73-76.
12. L.Black, F.Miserque, T.Gouder, L.Havela, J.Rebizant, and F.Wastin, *Journal of Alloys and Compounds*, 2001. **315**(1-2). 36-41.
13. J.Kuppers and G.Ertl, *Surface Science*, 1978. **77**. L647.
14. T.Gouder, C.Colmenares, J.R.Naegele, and J.Verbist, *Surface Science*, 1990. **235**(2-3). 280-286.
15. D.W.Turner, *Molecular photoelectron spectroscopy*. 1970: Wiley-Interscience. 386.
16. M.P.Ames, A.S.Wilson, and E.E.Rundle, Report CN-1495, 1944.
17. D.T. Wickham, B.A. Banse, and B.E. Koel, *Surface Science*, 1991. **243**(1-3). 83-95.

CHAPTER 3. Photoemission Studies of the Surface Reactivity of Thorium:
O₂, NO, NO₂, and N₂O adsorption Studies

18. P.R.Norton, R.L.Tapping, D.K.Creber, and W.J.L.Buyers, Physical Review B, 1980. **21**. 2572-2577.

CHAPTER 4**The interaction of uranium metal with nitrogen oxides:
the formation of an oxynitride**

4.1. Introduction

Studying the interaction of actinide metals with reactive gases allows us to investigate the role of the U (5f) electrons in chemical reactions. Both physical and chemical properties of the light actinides, such as uranium, neptunium, or plutonium are influenced by the 5f electrons which are responsible, for example, the mixed valence and magnetic properties. The participation of the 5f electrons in chemical bonding, i.e. their delocalization, and the reactivity of the uranium surface is of fundamental interest.

Furthermore, the effect of nitrogen oxides (NO_x) on the oxidation of uranium is relevant to storage, because NO_x may be generated in a storage vessel by the radiolysis of air; in the presence of moisture nitric acid is also formed.

4.2. Results**4.2.1 Adsorption of nitrous oxide**

Figure 4.1 shows the U (4f) spectra of the uranium surface after exposure to increasing doses of N_2O at room temperature. The U (4f) peaks of the clean surface are typical for U metal [1], with narrow intense lines and a U ($4f_{7/2}$) binding energy of 377.4 eV. Upon exposure to N_2O a U ($4f_{7/2}$) component at 380.8 eV, indicative of UO_{2-x} oxide formation [1], appears and increases in intensity. Figure 4.2 shows that the position of the shifted U (4f) peak is in good agreement with that observed following exposure to oxygen (5 L). Contributions to the U (4f) peak envelope indicative of the presence of metallic uranium are still present, even at the highest exposures of N_2O used (3000 L). The observation of N (1s) features arising from the adsorption of N-containing species is complicated by the presence of a U (4f) satellite peak

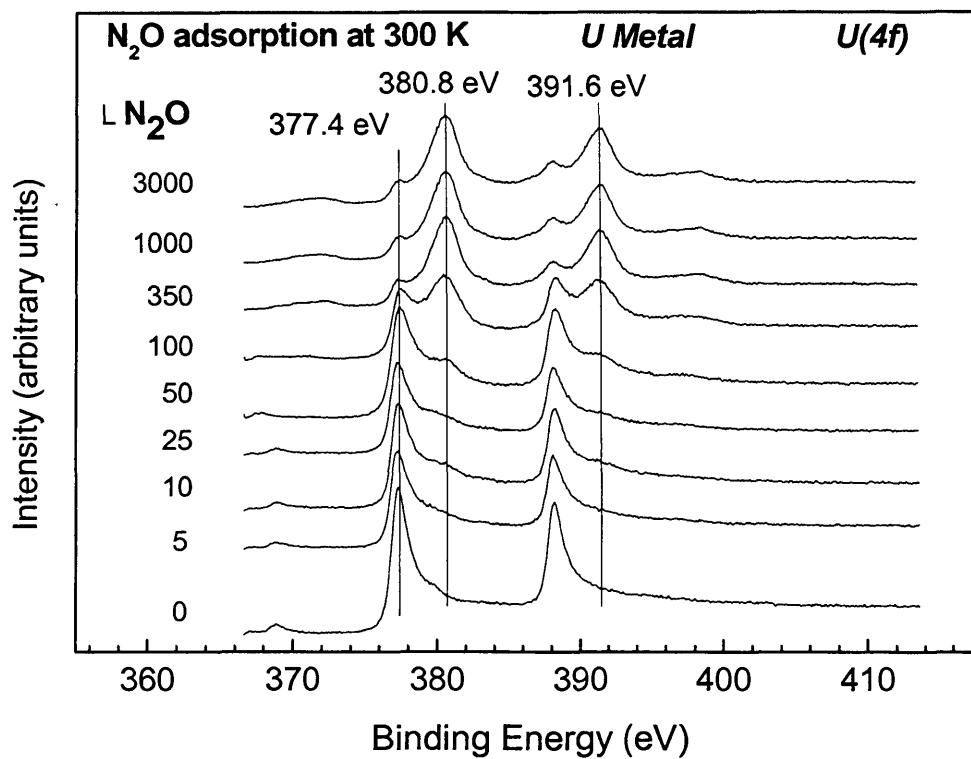


Figure 4.1. U (4f) spectra following exposure to N₂O

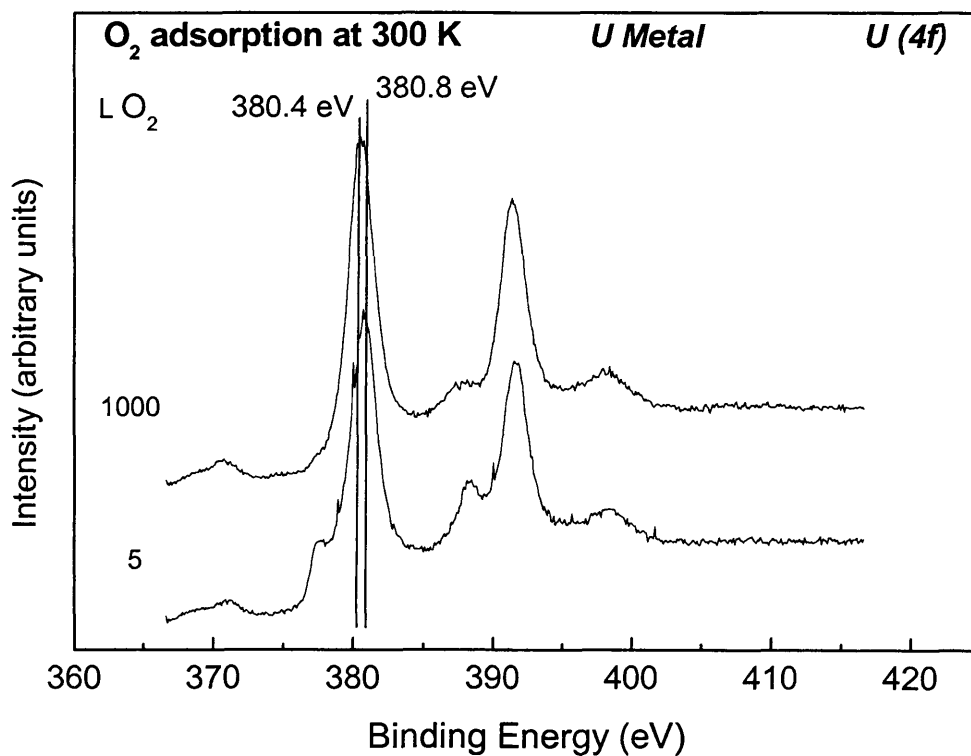


Figure 4.2. U (4f) spectra following exposure to O₂

resulting from an O (2p) to U (5f) shake-up process [1] which is associated with uranium dioxide formation. However, comparison of this spectral region for N₂O adsorption (figure 4.3) with that observed during the oxidation of uranium with pure O₂ suggests that there are no features present due to adsorbed nitrogen species. This is confirmed by the lack of an x-ray induced N (KLL) Auger peak (figure 4.4). With increasing N₂O exposure a symmetric O (1s) peak grows at 530.9 eV binding energy, assigned to O²⁻ species (figure 4.5), in agreement with the O (1s) binding energy following initial exposures (5 L) to O₂ (figure 4.6). The absence of adsorbed nitrogen and the presence of oxygen on the surface suggest that N₂O adsorbs dissociatively, the nitrogen desorbing as N₂ (g). N₂O has been reported to react in a similar way with Ni (100) [2], Al (100) [3], Ag (111) [4], and Ru (001) [5] where only oxygen was present on the surface following exposure to nitrous oxide. This contrasts to other metals where dissociative adsorption is observed and both oxygen and nitrogen remain on the surface [6, 7].

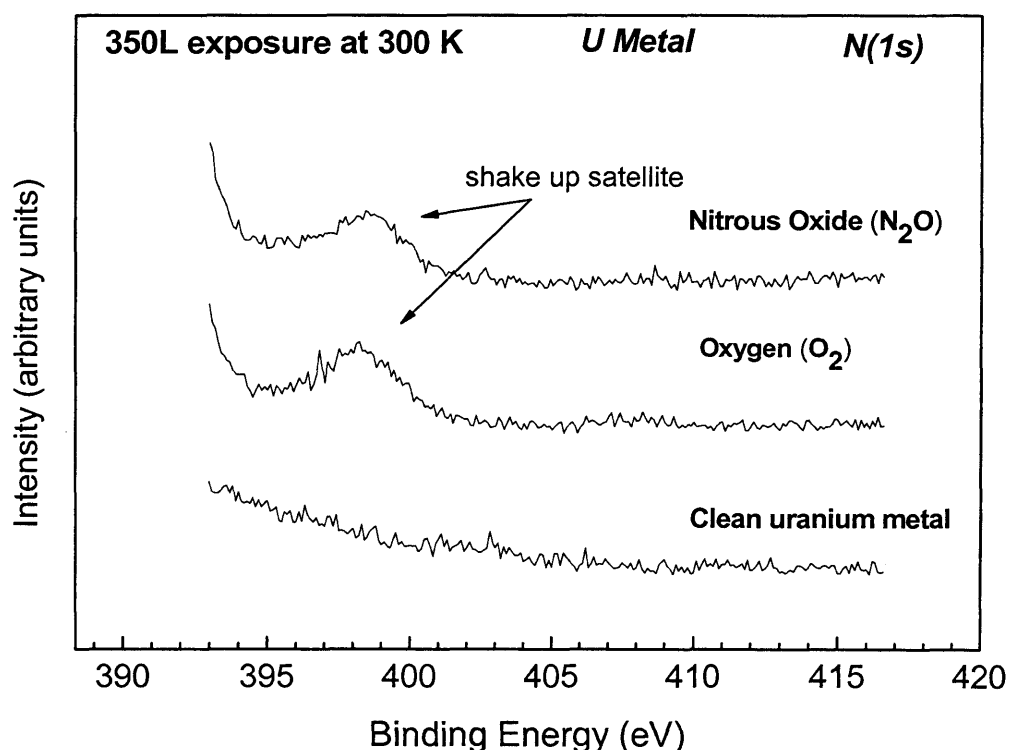


Figure 4.3. N (1s) spectra following exposure to 350 L N₂O and 350 L O₂

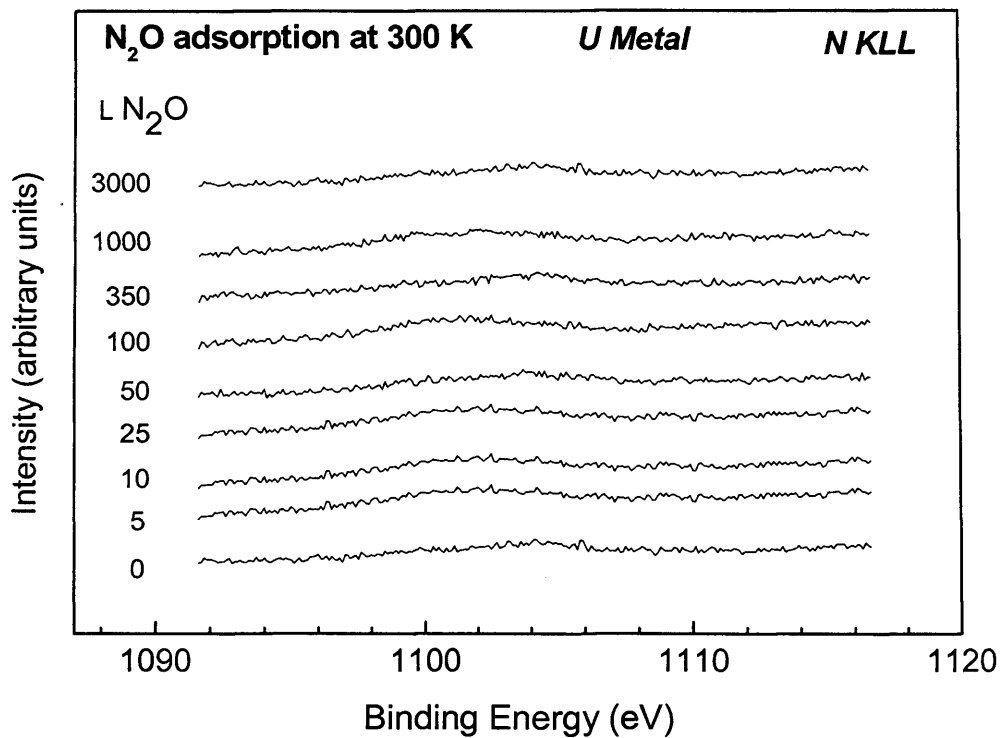


Figure 4.4. X-ray induced N Auger spectra for N₂O adsorption

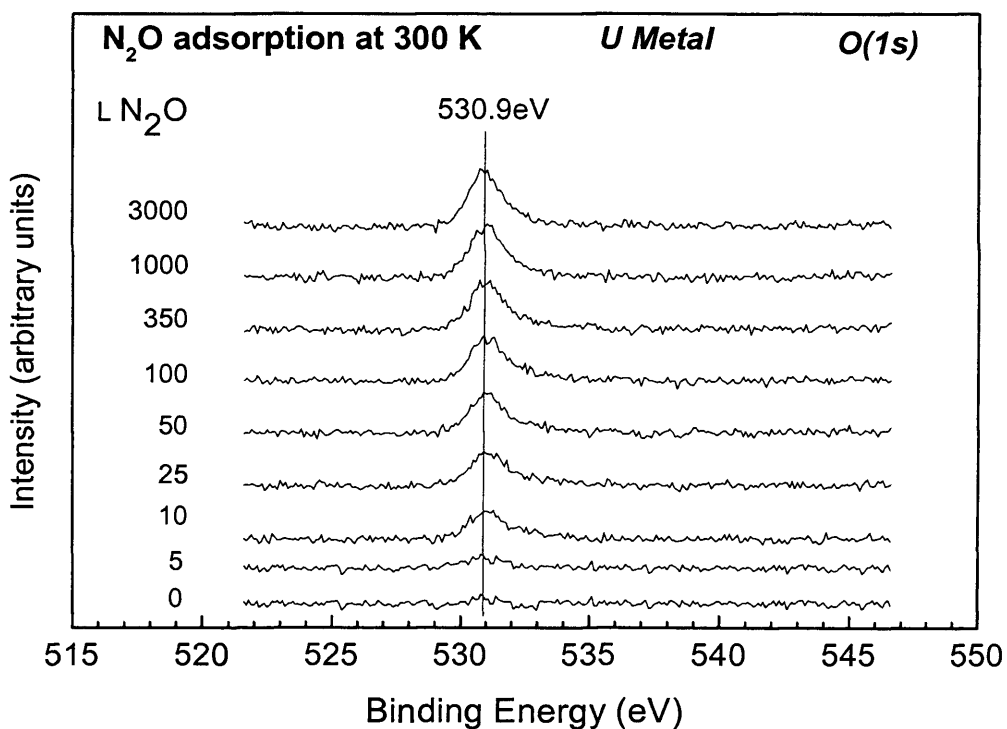


Figure 4.5. O(1s) spectra following exposure to N₂O

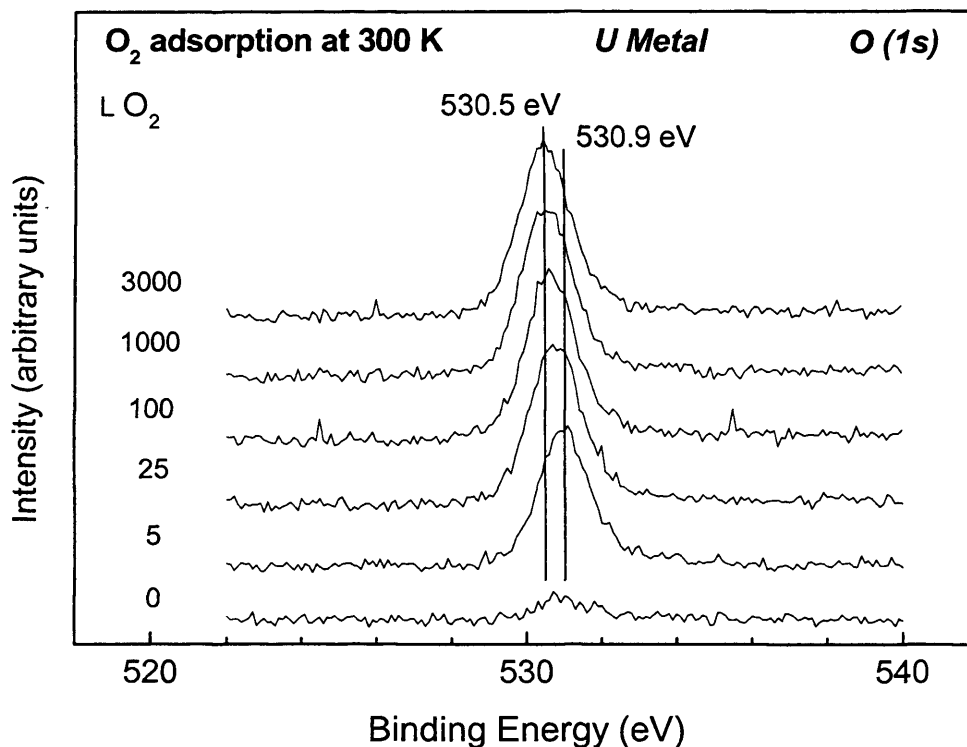


Figure 4.6. $O(1s)$ spectra following exposure to O_2

Increasing the N_2O exposures above 350 L caused very little change in the U ($4f$) spectra, a small contribution from the U ($4f_{7/2}$) metal component at 377.4 eV remaining. A similar trend is seen in the O ($1s$) spectra, with an initial increase in the intensity of the peak at 530.9 eV, associated with surface oxide. Increasing exposures (>350 L) of N_2O did not cause a significant increase in intensity of the O ($1s$) feature, confirming that the reaction has slowed considerably.

UPS He (II) spectra of a U surface exposed to increasing N_2O doses are shown in figure 4.7. The spectrum of the clean surface is typical for U metal [8], showing an intense and narrow photoemission feature at the Fermi level (E_F) attributed mainly to U ($5f$) states. The weak shoulder at 2.2 eV has been attributed to U ($6d$) states [8], although a recent study using angle-resolved photoemission [9] reported $5f$ character also at this energy. The shoulder is in a position where we would expect localized $5f$ emission due to surface oxide formation. However this shoulder is unlikely to be due to residual oxide as we

would expect O (2p) emission at around 6 eV for even small amounts of oxide. UPS (He II) is a sensitive indicator of oxygen contamination due to the higher photoionisation cross section of oxygen at the lower energy of UPS. The spectrum also agrees well with many previous studies on clean uranium surfaces which all show similar features [10].

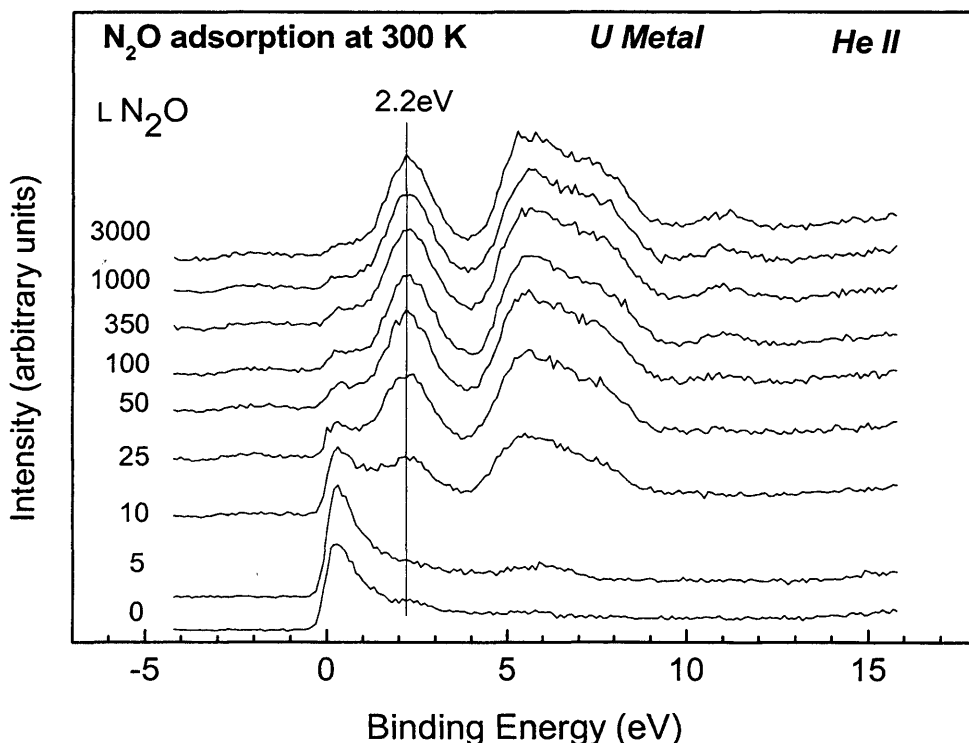


Figure 4.7. UPS-HeII spectra following exposure to N_2O

N_2O adsorption results in the development of two features at 2.2 eV and 4-9 eV, and a decrease in the intensity of the peak at E_f . After the adsorption has essentially ceased (350 L), the shape of the feature in the region 4 – 9 eV is similar to that observed for photoemission from the O (2p) states of UO_2 [11]. The O (2p) region is a two peak structure with the main intensity centered at 5 eV, and can, similarly to the O (2p) band in thorium oxide (chapter 3), be interpreted as bonding (high BE from cation-anion hybridization) and nonbonding (low BE) regions. The peak at 2.2 eV also increases with oxygen uptake, corresponding to emission from the localized U (5f) level of UO_{2-x} [12], indicating a shift in 5f electron behavior, from itinerant to localized, as the surface oxide is formed. The decrease in the

emission at E_f is consistent with the oxidation of U metal, which has a high density of states (DOS) at E_f , to UO_2 which being a semiconductor, has none. The intensity at E_f does not disappear entirely, which is consistent with the presence of metallic components in the U (4f) core-level spectra. We would also expect the peak at 2.2 eV to shift to a slightly lower BE when the metallic feature at E_f is lost, as is seen for increasing exposures of O_2 and the change from UO_{2-x} to UO_{2+x} [12] (figure 4.8). The residual metal intensity at E_f indicates that there is still metal within the information depth of UPS and that oxidation from UO_{2-x} to UO_{2+x} does not take place. This shift to lower BEs is attributed to changes in the Fermi-energy of the UO_2 semiconductor with oxygen content [12]. Substoichiometric UO_{2-x} is an n-type semiconductor while hyperstoichiometric UO_{2+x} is p-type. Oxidation, of UO_{2-x} to UO_{2+x} , results in a shift of the Fermi-energy towards the O (2p) valence band. As the BEs of photoemission lines for metals and semiconductors are referenced to the Fermi-level of the sample, such a shift of the Fermi-energy results in a shift of all the photoemission lines to lower BEs. Hence we would expect a shift in not only the localized 5f emission and the O (2p) emission, but all photoemission peaks if oxidation from UO_{2-x} to UO_{2+x} occurred following N_2O exposures similar to that observed following exposure to oxygen (figures 4.2, 4.6 and 4.8).

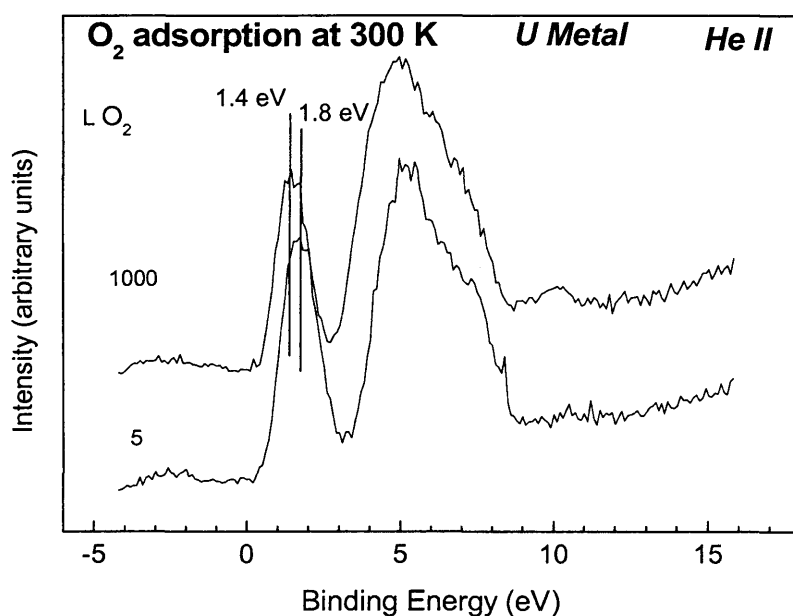
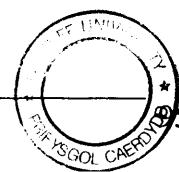


Figure 4.8. UPS-Hell spectra following exposure to O_2



4.2.2. Adsorption of Nitric Oxide

For low exposures (5 – 10 L) at 298 K, we observe only a slight increase in intensity of U (4f) components at 379.7 eV and 390.6 eV arising from surface oxide formation. However, on increasing the exposure further, there is a rapid increase in the intensity of these peaks and after only 100 L exposure the metallic contribution to the U (4f) spectrum has been completely attenuated. Further exposures to NO, up to 3000 L, lead to almost no changes in the U (4f) envelope (figure. 4.9). The chemical shift in the U (4f) core level peaks due to oxidation with NO (2.4 eV) is smaller than that observed following exposure to O₂ and the formation of UO₂ (3 eV) (Table 4.1).

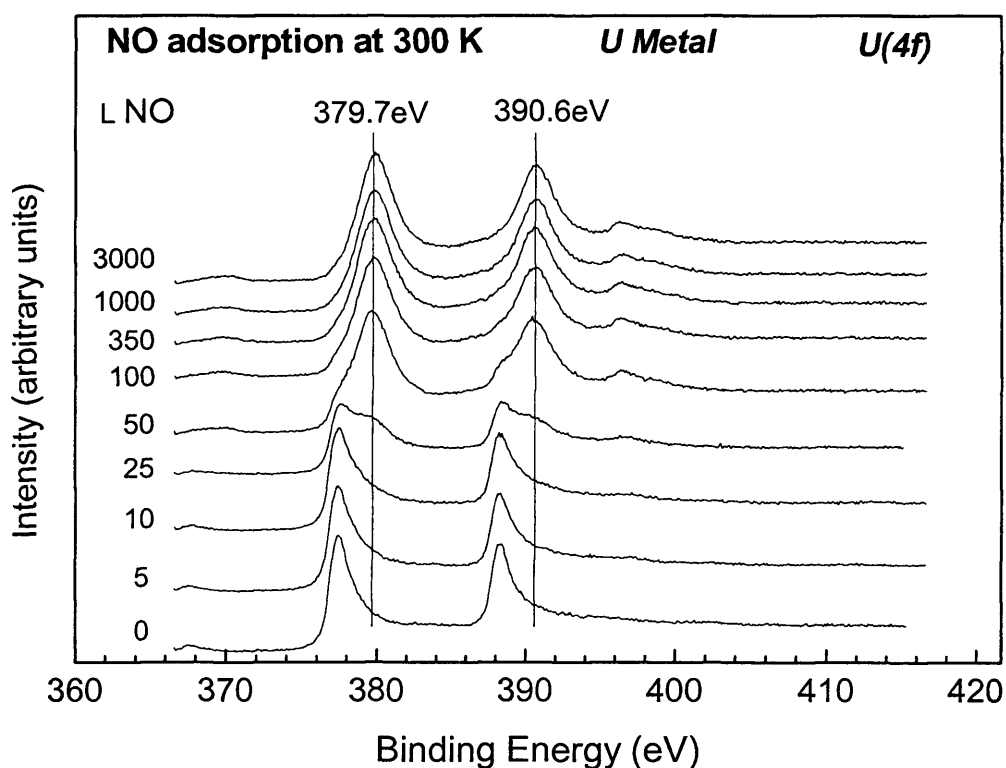


Figure 4.9. U (4f) spectra following exposure to NO

The O (1s) region exhibits a single peak due to O²⁻ with a binding energy of 530.6 eV (0.3 eV lower than observed for N₂O and similar to that observed for O₂ exposures >50 L (figure 4.6)), which does not shift with increasing exposures to NO (figure 4.10); for exposures greater than 50 L, there is negligible change in peak intensity. Despite the interference of the U (4f)

satellite peak (section 4.2.1) it is possible to observe the growth of a peak at 396.3 eV in the N (1s) photoemission region (figure 4.11), a binding energy which is similar to previously reported values for N(a), UN [13] and other nitrides. Nitrogen KLL Auger spectra (figure 4.12) also show the development of a feature following exposure to NO. Thus, although we have established from the O (1s), N (1s), and nitrogen Auger spectra that both oxygen and nitrogen species are present on the surface following exposure to NO, the chemical shift of 2.4 eV in the U (4f) binding energy indicates the formation of a surface compound other than uranium (+4) oxide or uranium (+3) nitride (table 4.1).

Level	Binding energy (eV)			
	UO ₂ film (in equilibrium with bulk U)		Uranium nitride Gouder et al. [14]	
	This work	Allen et al. [15]	UN	U ₂ N ₃
U (4f _{7/2}) (metal 377.4 eV)	380.4	380.3	377.4	378.4
U (4f _{5/2}) (metal 388.2 eV)	391.2	391.1	388.2	389.2

Table 4.1. U (4f) peak positions for UO₂, UN and U₂N₃

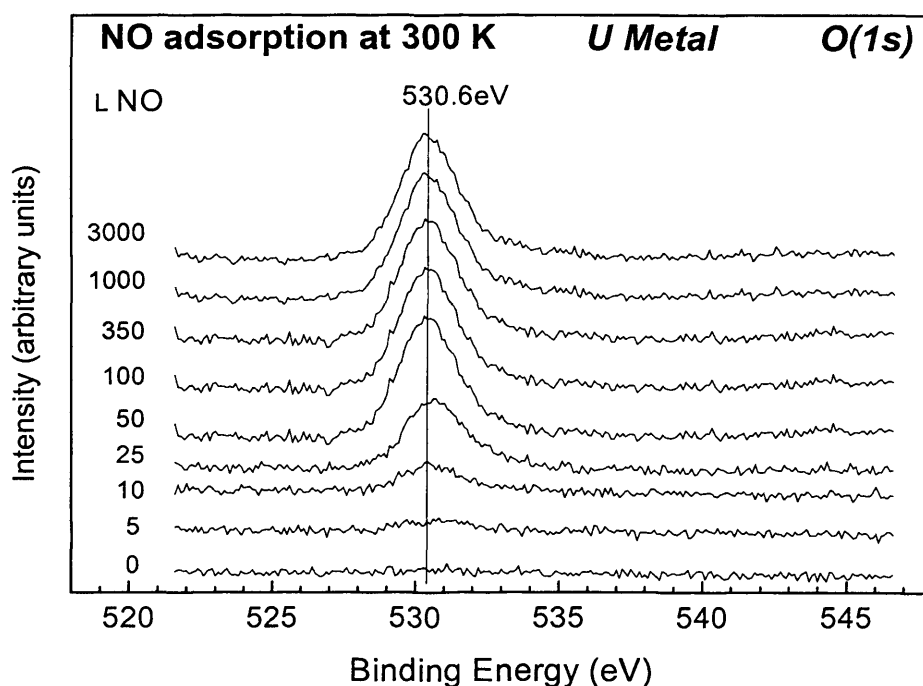


Figure 4.10. O (1s) spectra following exposure to NO

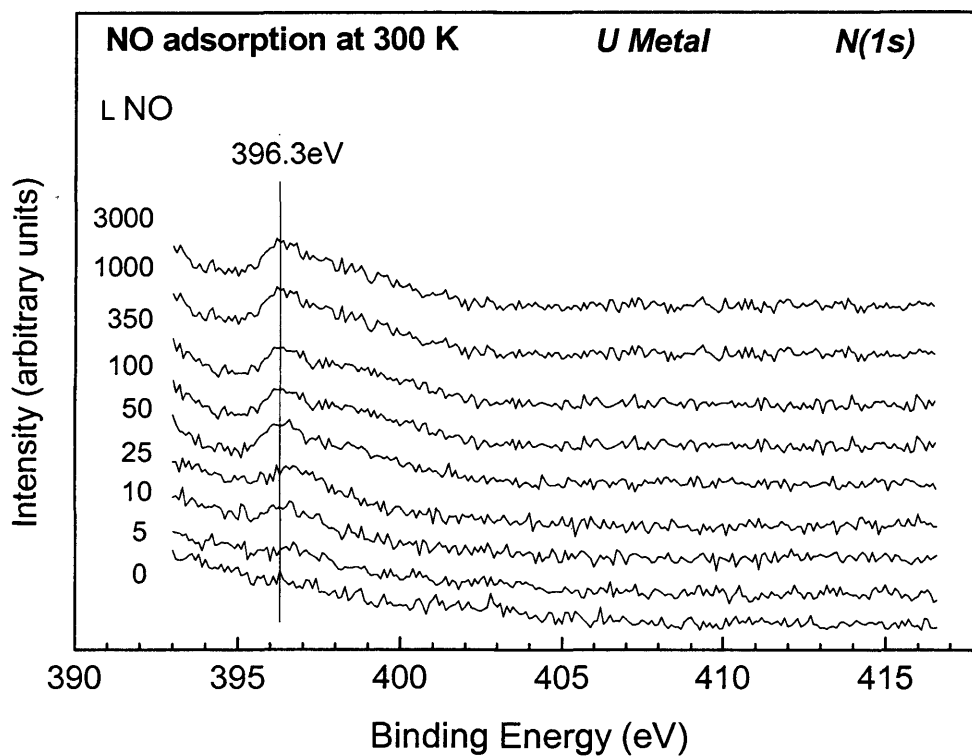


Figure 4.11. N(1s) spectra following exposure to NO

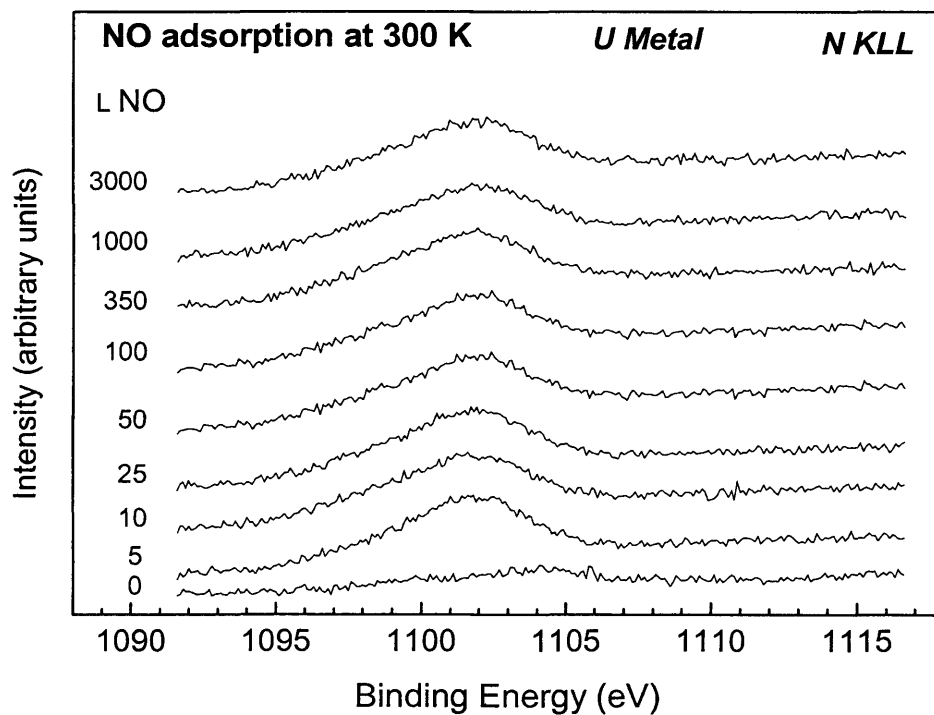


Figure 4.12. X-ray induced N Auger spectra for NO adsorption

In the UPS He II spectra (figure 4.13), NO exposures up to 10 L result in only a slight decrease in the emission at E_F , but we do observe the appearance of a broad peak between 2 – 8 eV, which is composed of a peak centered at ca 6 eV, which is typical for O (2p) emission [16], and one centered at ca 3 eV characteristic for 2p states of nitride [13]. The O (2p) contribution is broader than we would expect for chemisorbed oxygen [17] and the absence of a localized 5f peak around 2 eV along with the lack of asymmetry associated with the O (2p) contribution suggests an oxide other than UO_2 is formed. These spectra, below 25 L, are similar to those recently reported for thin films of UN_xO_y prepared by sputter deposition [18].

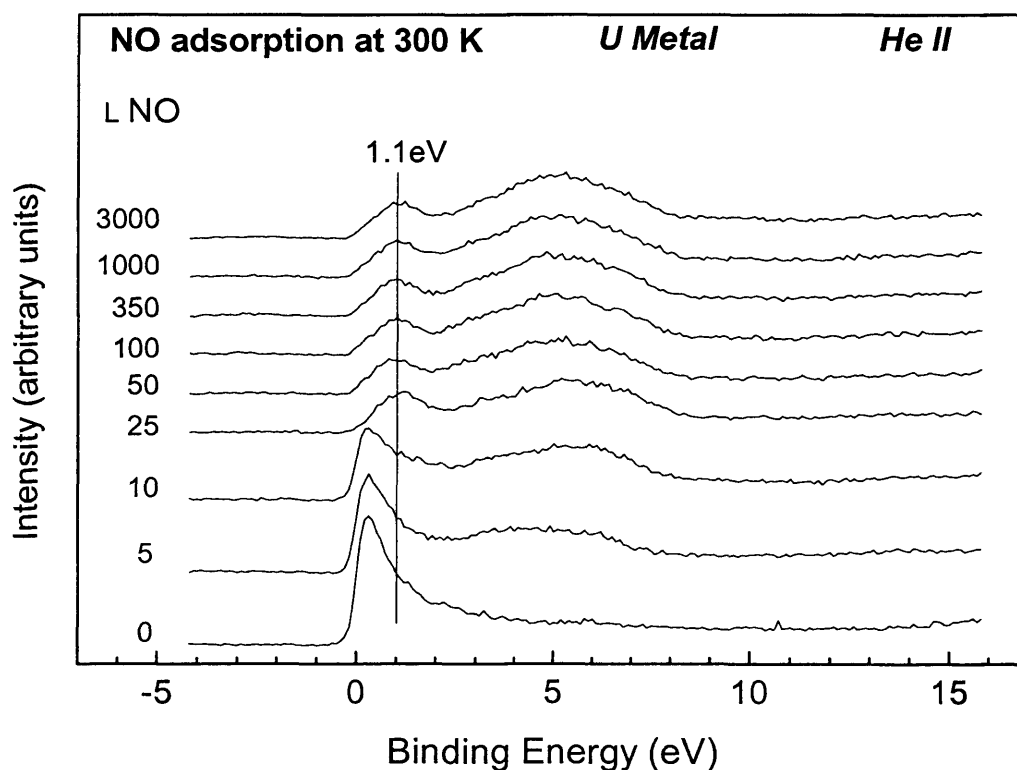


Fig 4.13. UPS-HeII spectra following exposure to NO

Further exposure to NO, above 10 L, results in the development of a localized 5f peak at 1.1 eV below E_F , and an increase in intensity centred at ca 5 eV. There is a concomitant decrease in emission at E_F showing a shift from itinerant to localized 5f behaviour. The broad feature between 2 and 8 eV is assigned to a combination of emission from O (2p) and N (2p) states [12, 13, 16]. The peak at 1.1 eV is consistent with neither uranium dioxide, for

which we would expect a more intense peak at around 1.4 eV, associated with a localised $5f^2$ electron configuration, nor UN which has a feature at E_f [13], not observed in our spectra. He II spectra for the higher nitride U_2N_3 [13] exhibit a peak at 0.8 eV, which is slightly lower than the localised 5f peak at 1.1 eV produced by NO adsorption. The localized 5f peak is also less intense than in UO_2 (figure 4.8) and U_2N_3 [14] indicating increased transfer of 5f electrons into bonding positions. This would account for the more symmetric O (2p) shape as the bonding 5f electrons would contribute to the higher BE region of the O (2p) peak (see section 4.2.1). The localized 5f peak is similar in intensity and located in a similar position to the localized 5f peak observed upon oxidation of uranium above UO_2 . Figure 4.14 shows increased oxidation of UO_2 towards UO_3 [19], produced by reaction with NO_2 , suggesting that following reaction with NO, > 25 L, uranium is in a higher oxidation state than +4 and there is increased 5f electron involvement in bonding.

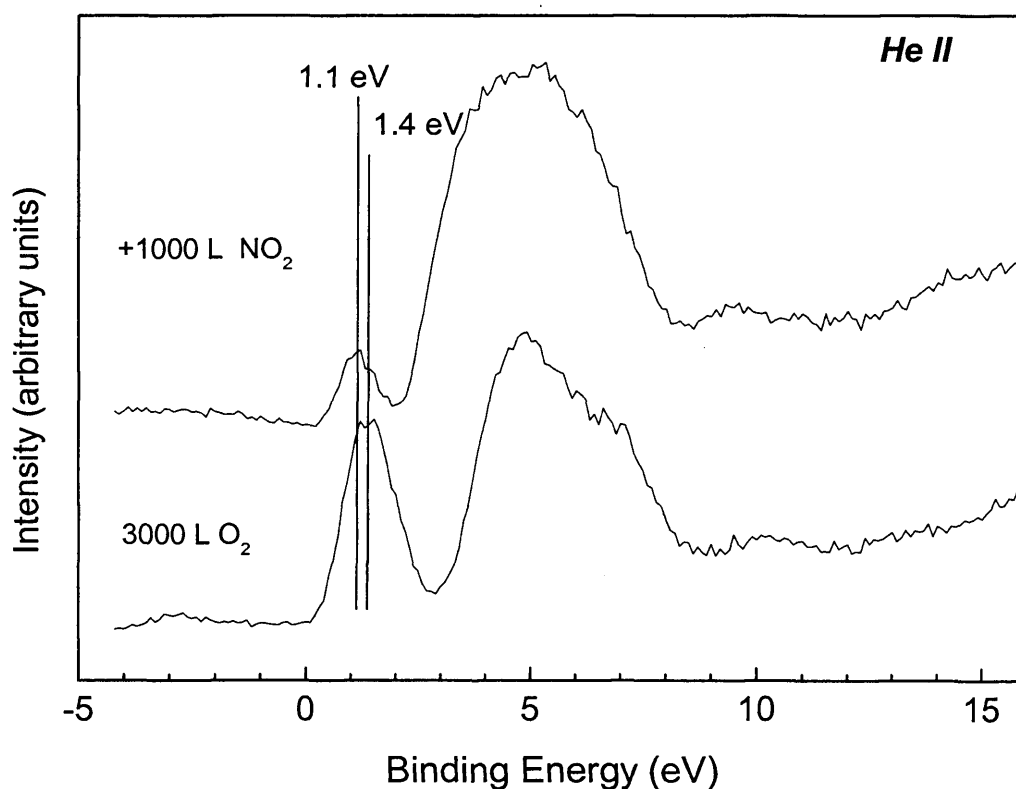


Fig 4.14. UPS-HeII spectra following exposure to 3000 L O_2 followed by 1000 L NO_2

4.2.3. Adsorption of Nitrogen Dioxide

Initially, for exposures of 5 – 10 L, the U (4f) spectra are essentially unchanged from the clean metal as was found for NO adsorption. After 25 L exposure a U (4f_{7/2}) component at 379.7 eV develops and by 100 L exposure the metal component in the spectrum is almost completely attenuated (figure. 4.15). This shift in core levels is similar to that seen with exposure to NO and once again not as pronounced as in UO₂, a shift of 2.4 eV as opposed to 3 eV for the formation of UO₂ [1] (table 4.1).

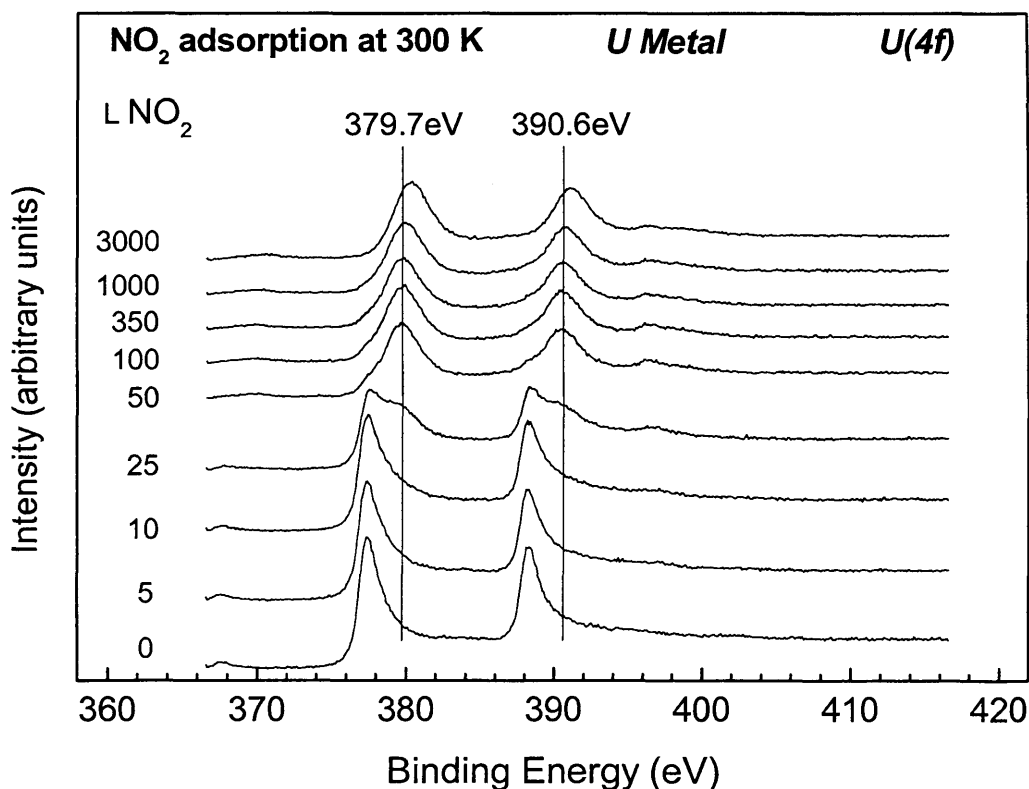


Figure 4.15. U (4f) spectra following exposure to NO₂

For NO₂ exposures greater than 350 L the U (4f_{7/2}) peak shifts further to 380.6 eV, characteristic of UO₂ [1]. A single O (1s) peak with a binding energy of 530.6 eV is observed (figure 4.16), which shifts with increasing exposure to NO₂ (>350 L) to 530.2 eV and increases in intensity, indicative of further oxidation [20]. The N (1s) spectra show the growth of a peak at 396.3 eV (figure 4.17), characteristic of UN [13]; nitrogen (KLL) Auger spectra (figure 4.18) confirm the presence of nitrogen species on the surface.

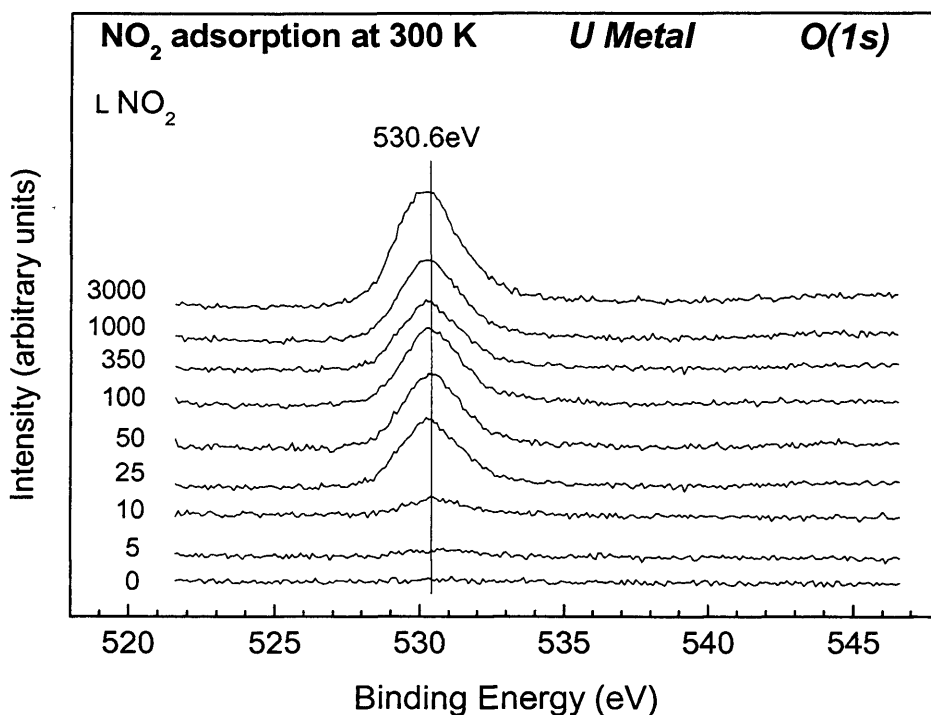


Figure 4.16. O (1s) spectra following exposure to NO₂

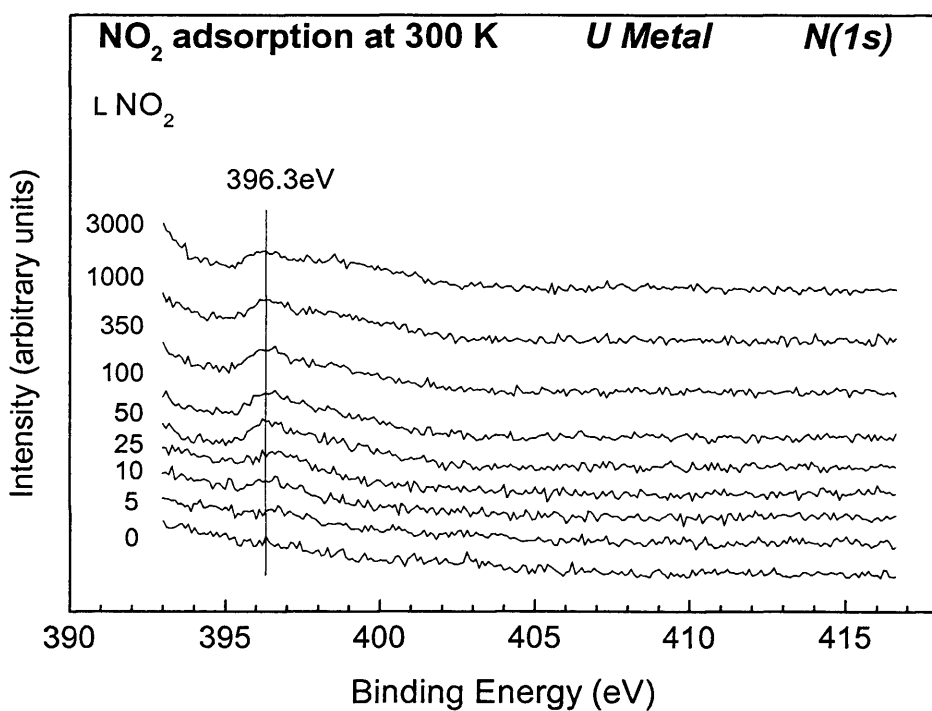


Figure 4.17. N (1s) spectra following exposure to NO₂

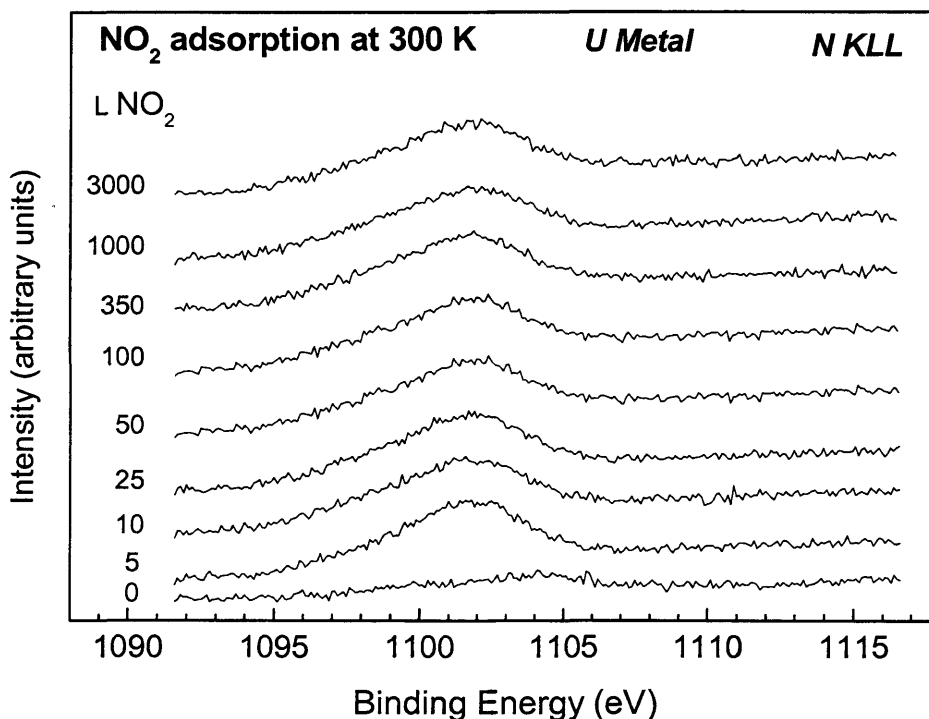


Figure 4.18. X-ray induced N Auger spectra for NO adsorption

We also see a broadening, when compared to the satellite produced following oxidation with O_2 , of the O (2p) to U (5f) shake up satellite peak above 350 L exposures of NO_2 (figure 4.17). An increase in intensity of this satellite at a slightly higher BE (8.7 eV compared to 6.7 eV separation from the U ($4f_{5/2}$) peak) has been observed for higher oxides of uranium, UO_{2+x}/U_4O_9 [21]. The shifts in the U (4f) and O (1s) peaks along with the broadening of the shake up satellite occur together suggesting a further increase in oxidation state of uranium at exposures of NO_2 greater than 350 L.

For exposures up to 350 L, the UPS results (Figure. 4.19) are essentially identical to those observed for NO adsorption. However, when we increase the exposures of NO_2 above 350 L we see further changes in the spectra. The localized 5f emission at 1.1 eV decreases further in intensity and the broad peak between 2-8 eV increases in intensity and becomes more symmetrical, reflecting further transfer of localised U (5f) states into the

'bonding' molecular orbitals as the surface oxidises. Concomitantly the decrease of the localised U (5f) level and the increase in intensity and changing shape of the O (2p)/N (2p) region indicate the formation of an oxidation state of uranium towards +6 similar to UO_3 [19]. However the oxidation state does not quite reach +6 as we would expect to see no localised U (5f) feature in the UPS spectra reflecting the fact that all the 5f electrons would be involved in bonding to oxygen and nitrogen atoms.

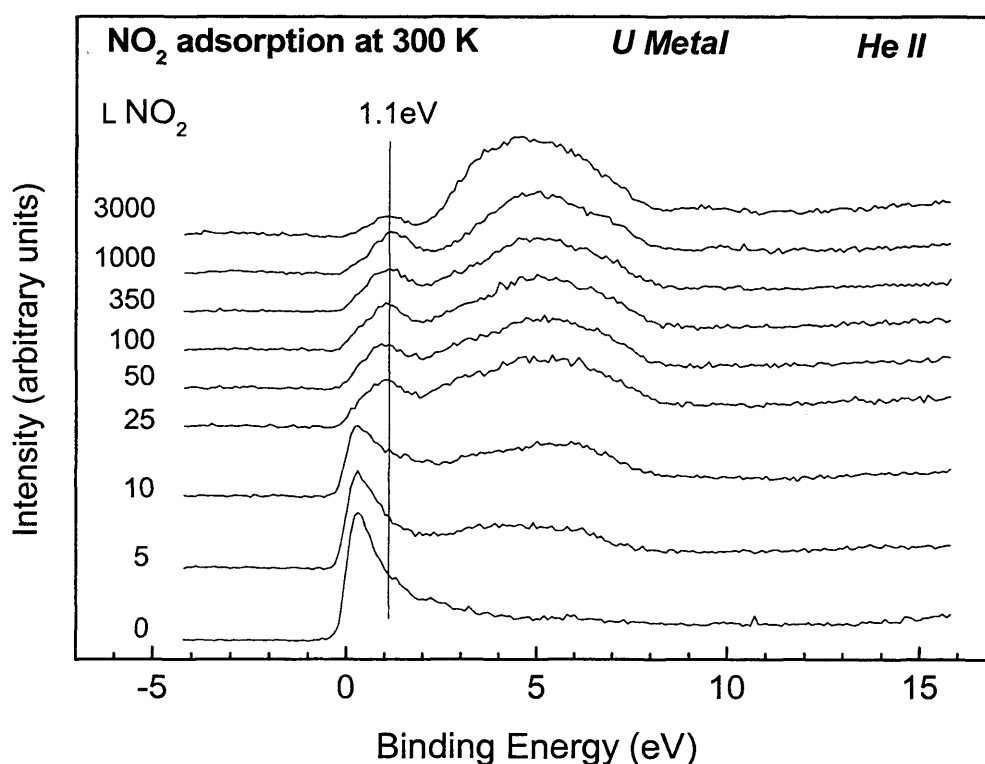


Figure 4.19. UPS-He II spectra following exposure to NO

The results obtained following NO_2 exposure suggest that NO_2 reacts with the uranium surface in a similar way to NO . Up to 350 L exposures both produce very similar results, including the same binding energy values for U (4f) peaks, O (1s) peak, and nitride peak in the N (1s) region. Above 350 L the spectra produced following NO_2 adsorption continue to change indicating that unlike NO where there appears to be very little change in the spectra above 350 L, NO_2 continues to react with the surface.

4.3. Discussion

The relative bond strengths (NN-O 167 kJ/mol, N-NO 945.3 kJ/mol, O-O 498.3 kJ/mol, ON-O 305 kJ/mol, N-O 630.6 kJ/mol) allow a purely thermodynamic insight into the possible reaction pathways. These along with the results obtained from the photoemission experiments will allow us to offer an explanation of the interaction of the nitrogen oxides with a uranium surface.

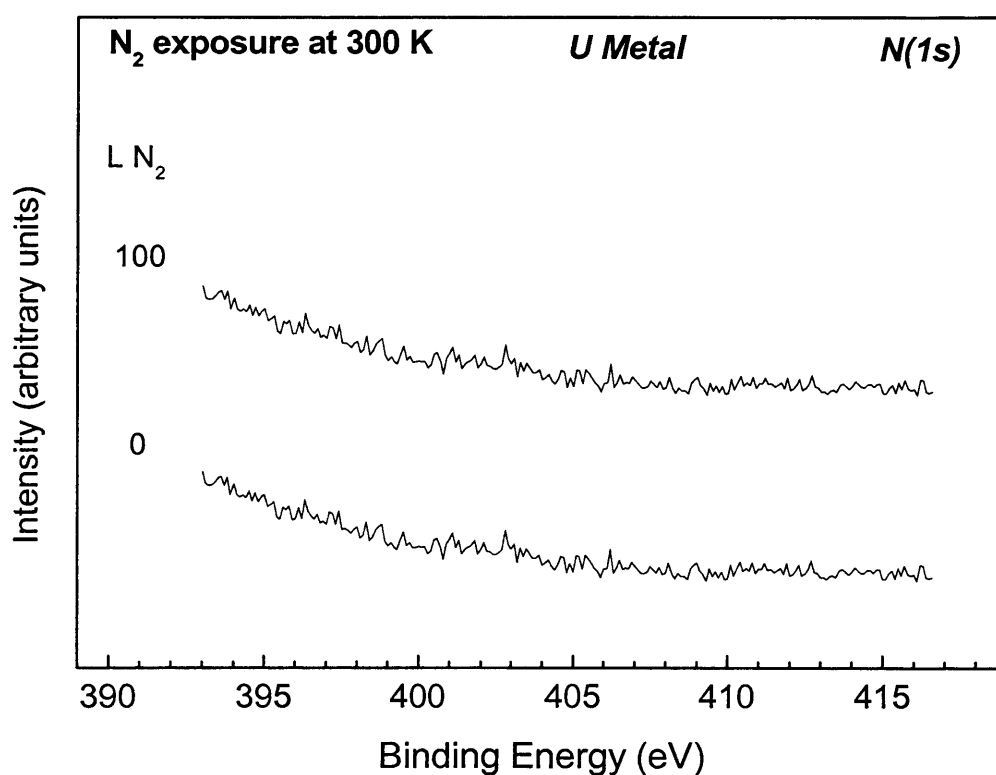


Figure 4.20. N(1s) spectra following exposure to NO₂

N₂O adsorbs dissociatively on uranium, followed by the desorption of N₂(g) from the oxidised surface. Figure 4.20 shows that N₂ is unreactive towards the uranium surface under UHV at 298 K. The reaction of metallic uranium with N₂ only proceeds at 850°C and leads to the formation of U₂N₃, which can then be decomposed to UN at 1150°C under vacuum [22]. The reaction with N₂O ceases after an exposure of approximately 350 L, presumably because the oxidized surface is unreactive to N₂O. Although N₂O has the weakest N-O bond strength of all three of the nitrogen oxides (NN-O 167

kJ/mol) the results obtained here suggest dissociative adsorption no longer takes place on the oxide surface produced above 350 L.

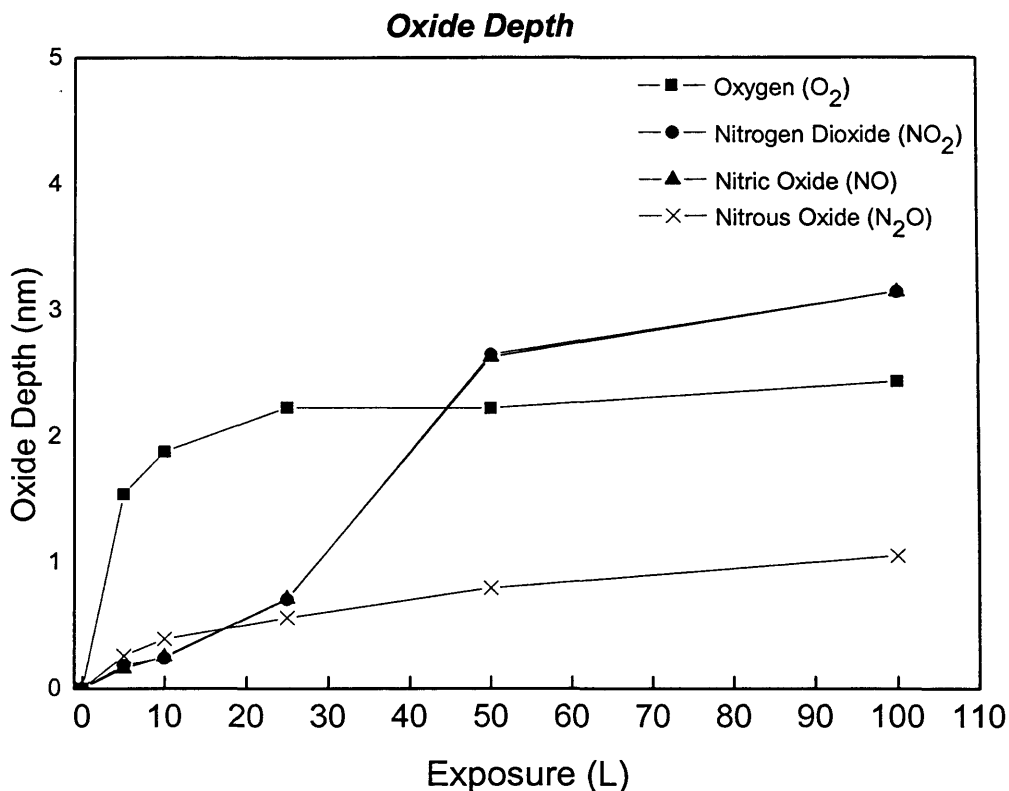


Figure 4.21. Depth analysis following increasing exposures of O₂, NO, NO₂ and N₂O

Surface coverage and depth calculations suggest that at approximately 350 L exposure of N₂O the uranium metal is covered by a thin oxide layer, of 1 nm thickness (figure. 4.21). This depth contrasts with an oxide layer thickness of 2 nm formed when the uranium surface was exposed to 350 L O₂. Depth and surface coverage calculations suggest that, following exposure to N₂O, the surface is covered by oxide and indicate that the residual metal contributions, seen in the U (4f) spectra, arise from the underlying bulk metal and not from unreacted surface metal atoms. The difference in thickness of the passive layers created by reaction with N₂O and O₂ could therefore be proposed to be due to inhibited diffusion of O²⁻ ions. However as dissociative adsorption in both cases results in only oxygen adsorption at the surface, similar surface uranium oxides would be expected. Oxygen diffusion would then be expected

to be proceeding in a similar way. Furthermore the N_2O passivated surface has been shown to further react when exposed to only 100L O_2 , figure 4.22. The resulting U (4f) spectra shows the residual metal peak has decreased in intensity and the O (1s) peak also shifts to a lower BE confirming further oxidation and that it is possible for diffusion of O^{2-} ions to still take place.

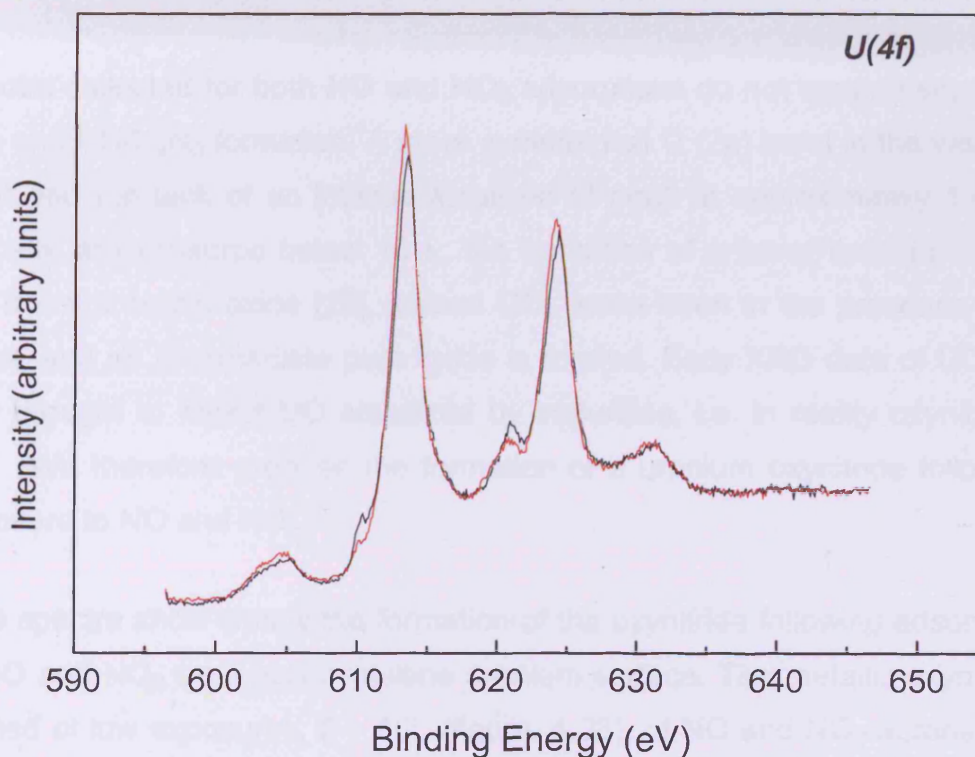


Figure 4.22. Black – U (4f) spectrum following exposure to 28000 L N_2O . Red – U (4f) spectrum following exposure to 28000 L N_2O + 100 L O_2 .

For O_2 , as the oxide thickness reaches 2 nm a dramatic reduction in the rate of oxidation is observed; after this point, the extent of the reaction is reduced significantly and the rate of oxide formation with time levels off. The reduction in rate of oxidation occurs as the oxide layer is now so thick that it retards diffusion of active oxygen species. A similar depth following exposure to N_2O would be expected to inhibit diffusion of oxygen ions. In contrast the reaction with N_2O appears to slow at a smaller thickness indicating that dissociative adsorption, producing O^{2-} , no longer takes place. Bond energies suggest that dissociation of N_2O to form N_2 and O is thermodynamically more favourable than dissociation of O_2 . Therefore it would seem that it is not

energetically favorable for N_2O to adsorb on the oxide surface produced. Indicating that at exposures above 350 L there are no longer sufficient adsorption sites and that dissociative adsorption only occurs at uranium metal sites. This, along with the depth calculations, supports the observation that the residual metal peak in the U (4f) spectra is from underlying metal as N_2O would in theory continue to react with unreacted surface metal atoms.

Spectra collected for both NO and NO_2 adsorptions do not support separate UO_2 and UN/ U_2N_3 formation. A more symmetrical O (2p) band in the valence band and the lack of an intense localized 5f peak at approximately 1.4 eV indicate, at exposures below 10 L, the formation of a lower uranium oxide. UO is not a stable oxide [23], indeed UO_2 forms even in the presence of U metal, and no intermediate pure oxide is formed. Early XRD data of UO are now thought to reflect UO stabilized by impurities, i.e. in reality oxynitrides [24]. We therefore propose the formation of a uranium oxynitride following exposure to NO and NO_2 .

UPS spectra show clearly the formation of the oxynitride following adsorption of NO and NO_2 on a polycrystalline uranium surface. The metallic oxynitride formed at low exposures, 5 – 10L (figure. 4.23), of NO and NO_2 agrees with the observations made by Eckle and Gouder [18]. The valence band spectrum of UO_xN_y shows a broad anion band which is interpreted as superposition of the narrow O (2p) and N (2p) bands. The maximum at 6 eV clearly comes from the O (2p) contribution while the smaller shoulder at 3 eV coincides with the N (2p) signal in UN. The O (2p) contribution cannot be associated with the presence of UO_2 , which has a main signal at 4 eV. UO is not stable as a pure oxide and it's thought that the nitrogen acts as a stabilizing agent in the oxynitride. At these low exposures there is no trace of the more localised U (5f) electrons seen at 1.1 eV for higher exposures confirming the metallic nature of the oxynitride formed at these lower exposures. At higher exposures it is also apparent that there is a slight contribution to the peak at E_F suggesting there is still an itinerant nature to the U (5f) electrons in the uranium oxynitride formed at exposures > 10 L. The broad anion band, at these higher exposures, looks different to the broad

asymmetric O (2p) peak for UO_2 . The contribution to the anion band intensity between 1.8 and 3 eV, not seen in the UO_2 spectra, is assigned to the N (2p) signal. Spectra clearly suggest the formation of a UO_xN_y species at the surface. Initial stages are in agreement with previous results [18] but we propose the continual formation of an oxynitride species at higher exposures.

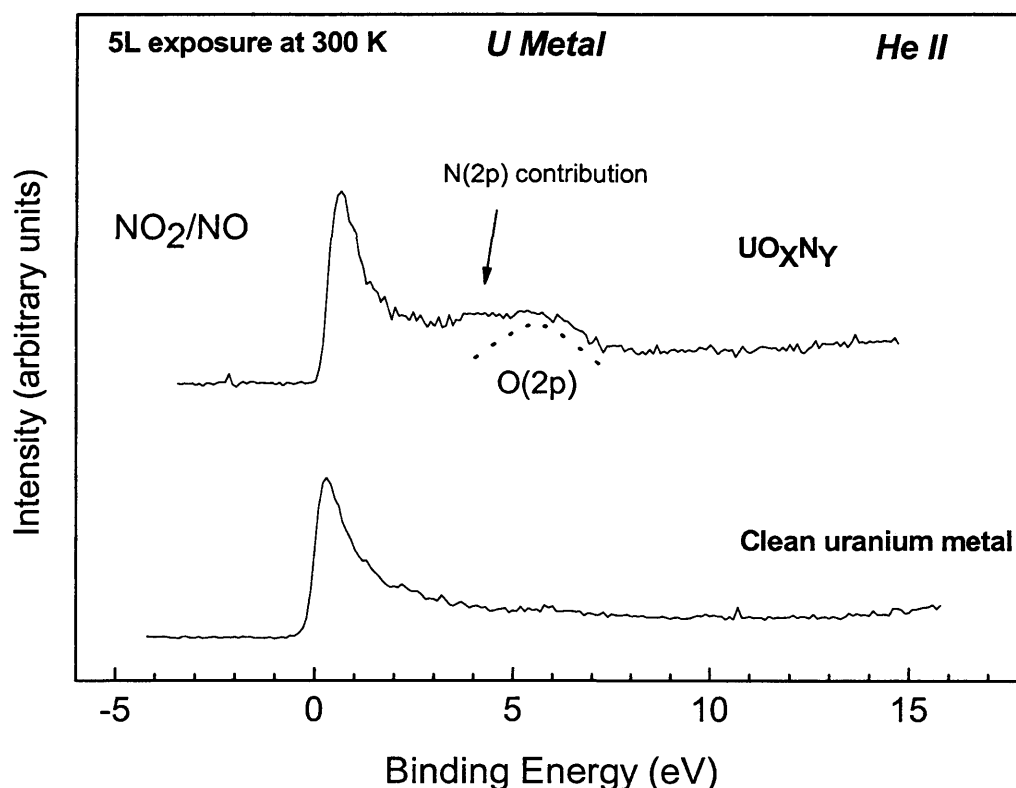


Figure 4.23. He II valence spectra of UO_xN_y

Nitrogen dioxide reacts in a similar way to nitric oxide, for exposures up to 350 L, producing atomic oxygen and atomic nitrogen, which we similarly propose to produce an oxynitride layer. Like NO this slows the rate of reaction but unlike NO, NO_2 continues to dissociate. The spectra suggest though that only oxygen now adsorbs at the oxynitride surface. We see an increase in surface oxygen concentration (figure 4.25), no change in nitrogen concentration, and also shifts in the U (4f) and O (1s) spectra, discussed in 4.2.3, indicating further oxidation. It has previously been reported that NO_2 is capable of oxidising lower oxides of uranium to UO_3 [25]. No nitrogen is seen to adsorb on the surface and the surface reaction with UO_2 can be

represented by the reaction, $\text{UO}_2 + \text{NO}_2 \rightarrow \text{UO}_3 + \text{NO}$. The results obtained here indicate that a similar process is occurring. We have also reacted the NO passivated surface with O_2 where no reaction is observed. NO_2 in contrast reacts with both O_2 (figure 4.14) and NO passivated surfaces to produce further oxidation.

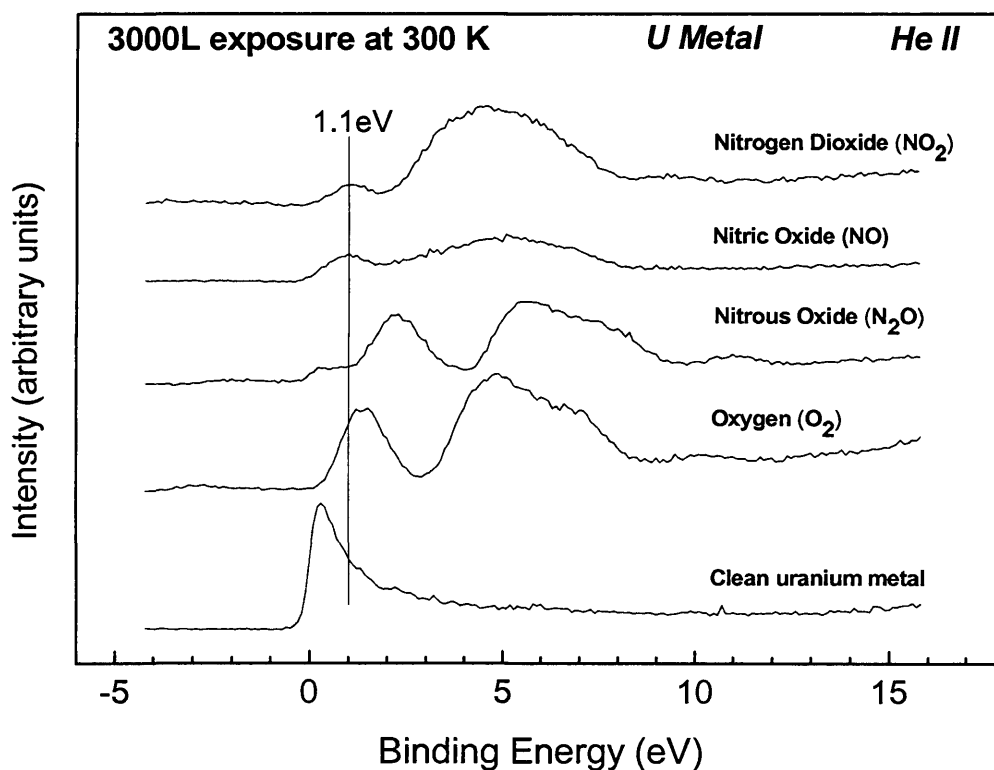


Figure 4.24. UPS spectra following exposure to 3000 L

The UPS He II data, figure 4.24, support the increased oxidation of uranium following NO_2 adsorption at higher exposures. The peak between 3 and 8 eV (the “bonding band”) increases and becomes more symmetrical, along with a decrease in the U (5f) intensity, reflecting the transfer of localised U (5f) states into the “bonding” molecular orbitals as the oxynitride surface oxidises. The 5f electrons participate minimally in the covalent bonding of uranium oxides, and the 5f character is lost when these electrons are transferred into covalent bonding states [26]. This covalent nature can be seen when we compare the O_2 and N_2O with the NO and NO_2 valence spectra. At 100 L we see that the 5f electrons involved in covalent bonding in the oxynitride formed by NO and NO_2 adsorptions contribute to a more symmetric “bonding band”

and a decrease in the localized U (5f) intensity is observed.

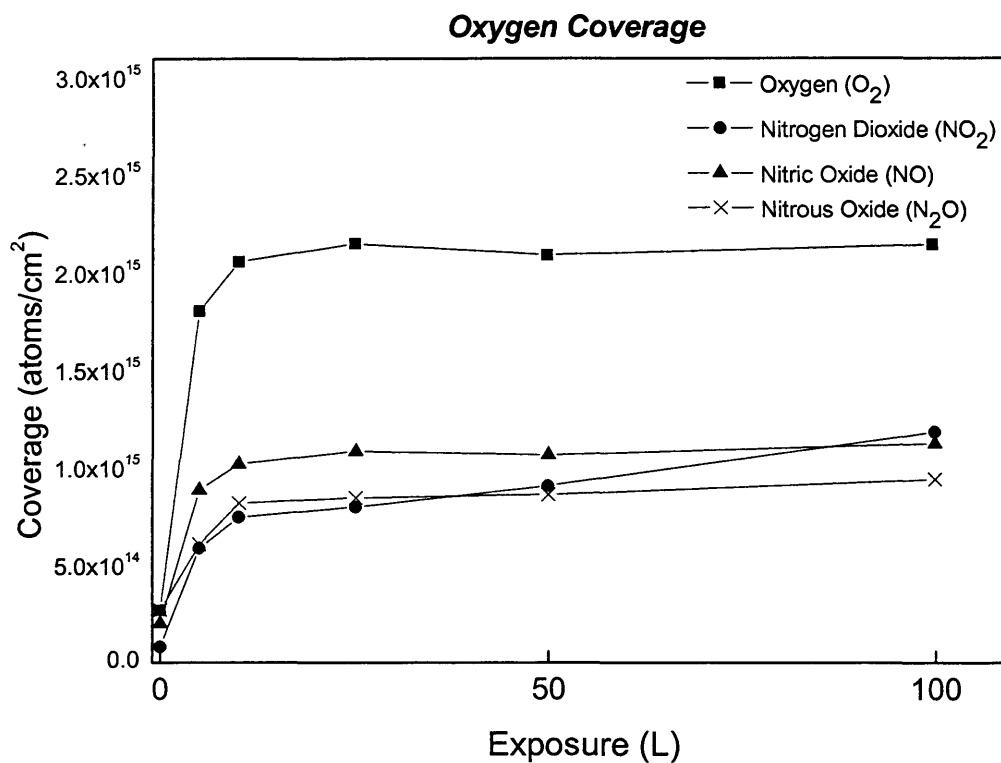


Figure 4.25. Oxygen coverage calculations following increasing exposures of O₂, NO, NO₂ and N₂O.

Quantification of the XPS data allows us to look in more detail at the interaction of the three gases with the uranium surface (figure. 4.21, 4.25, 4.27 - 4.32). The integration of the O (1s) peak allows us to determine the total amount of oxygen on the surface (chapter 2). It has been difficult to calculate the nitrogen surface coverages due to the proximity of the N (1s) peak to the U (4f) satellite, which means it is difficult to get an accurate peak area. Subtraction of the shake-up satellite from the N (1s) spectra (figure 4.26) may introduce error.

It is immediately evident from the plots of oxygen coverage against exposure that O₂ adsorption (figure 4.25) produces considerably more surface oxygen than any of the nitrogen oxides. This is due to a combination of reasons and will be influenced by the energy required for dissociation to atomic oxygen,

adsorption sites etc. Dissociative adsorption of N_2O , as previously discussed, on the oxide layer is not energetically favorable limiting the reaction. The oxygen coverage is therefore limited to approximately 1 monolayer. The presence of nitrogen on the surface following dissociative adsorption of NO and NO_2 limits the amount of surface oxygen. Nitrogen present on the surface occupies possible oxygen adsorption sites, hence producing lower oxygen coverages when compared to exposure of O_2 . It is interesting to see also that reaction with NO_2 continues to increase the oxygen surface coverage when the other gases have slowed. This suggests that it is energetically more favorable for dissociative adsorption of NO_2 producing surface oxygen atoms. The bond energies of the respective gases support this proposal with NO_2 having the weakest N-O bond (305 kJ/mol), other than N_2O for which we have shown that it does not adsorb on the oxide surface, even weaker than the oxygen O-O bond (498.3 kJ/mol).

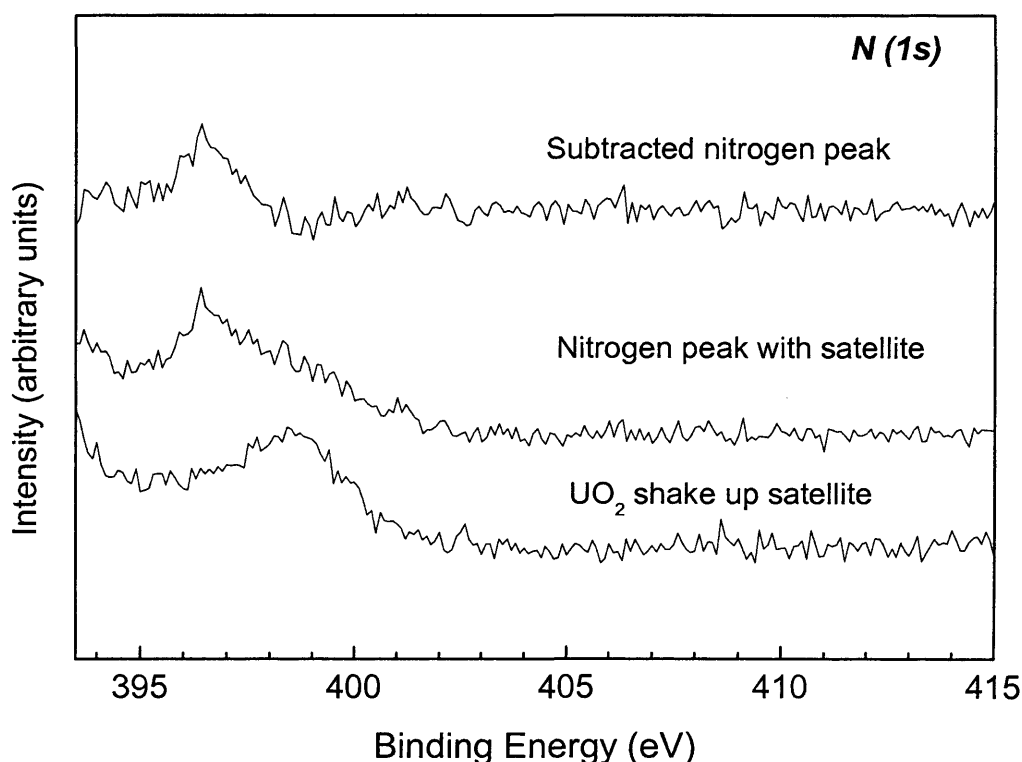


Figure 4.26. Subtraction of the UO_2 shake-up satellite from the $N(1s)$ spectra

Depth analysis, figure 4.21, is calculated as described in chapter 2. The depth following exposure of the uranium surface to O_2 and N_2O is similar to

the trend in surface coverage and again supports the XPS and UPS spectra obtained. N_2O adsorption forms a thin oxide as indicated, around 1 nm, upon which no further increase in depth is observed (discussed earlier). A reduction in rate of oxidation occurs, at approximately 2 nm following exposure to O_2 , as the oxide layer is now so thick that it inhibits diffusion of active oxygen species. The over layer following NO and NO_2 exposure shows a slower increase in depth when compared to the oxide layer formed following exposure to oxygen. However the final overlayer depth is greater than that following exposure to oxygen. This is in contrast to the oxygen coverage calculations which show a greater coverage following exposure to oxygen. This is because it is not the oxide depth that we are calculating but the overlayer depth, and following exposure to NO and NO_2 nitrogen also constitutes the overlayer. The greater depth produced also supports the UPS data showing increased 5f participation in bonding following exposures to NO and NO_2 when compared to N_2O and O_2 .

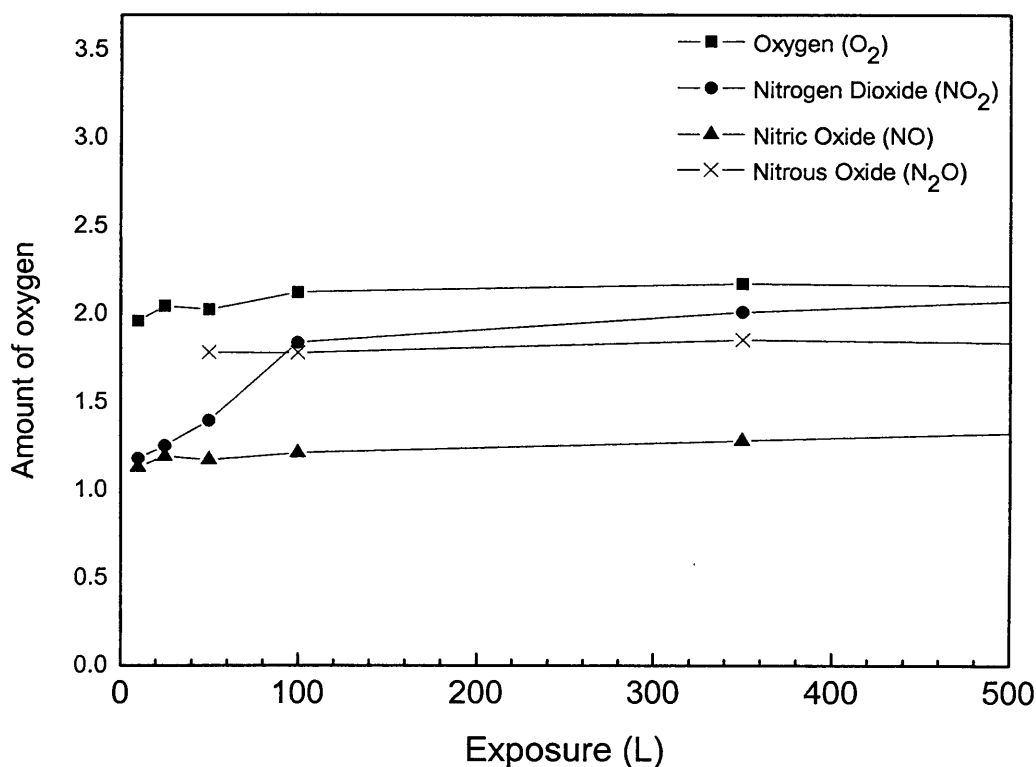


Figure 4.27. Amount of oxygen in the stoichiometry of UO_x following increasing exposures of O_2 , NO, NO_2 and N_2O

Figure 4.27, shows the value of X in the stoichiometry of the oxide produced (UO_x) following exposure to O_2 , N_2O , NO and NO_2 (stoichiometry involving nitride is calculated later). It is calculated by adjusting the integrated intensity of the specific peak (O (1s) and U (4f)) to take into consideration the photoionisation cross section. The oxide stoichiometry for a surface following O_2 adsorption is approximately two and hence gives us approximately UO_2 . We can compare this to the values for the surfaces produced following exposure to the three nitrogen oxides. N_2O adsorption as expected from the XPS and UPS spectra forms a surface oxide with stoichiometry lower than that of UO_2 indicating that reaction of N_2O with a uranium surface produces an oxide with stoichiometry approximately $UO_{1.8}$.

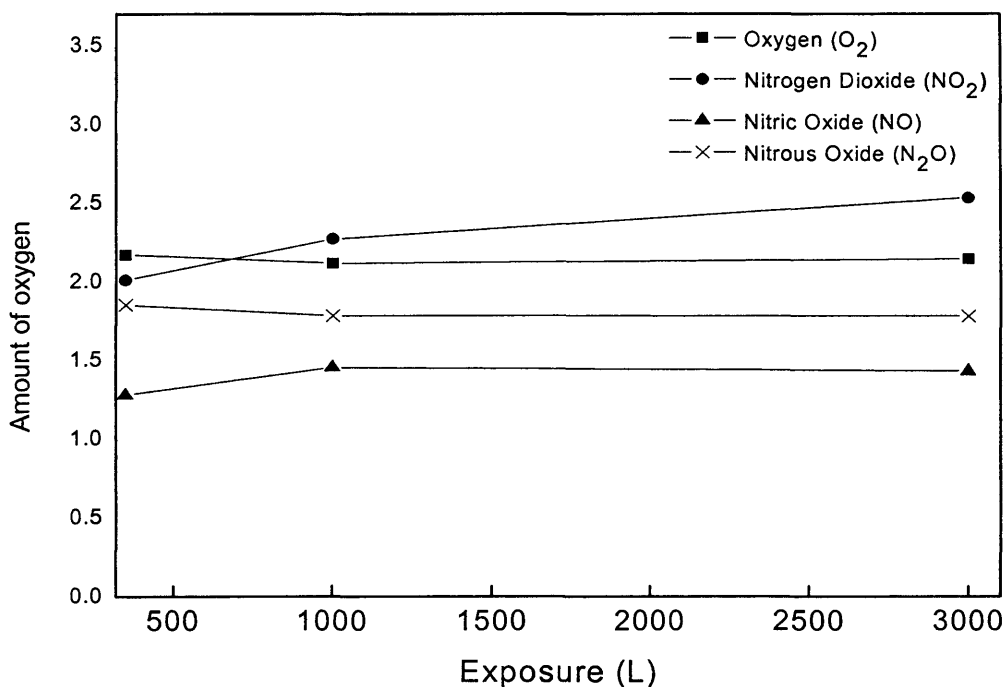


Figure 4.28. Amount of oxygen in the stoichiometry of UO_x following increasing exposures of O_2 , NO , NO_2 and N_2O

An interesting result obtained from the ratios is for NO and NO_2 exposure compared with O_2 . Below 100 L dosing the predicted oxynitride species means that the ratio is low due to the presence of the nitrogen. The reaction of NO with the oxynitride surface slows (discussed previously) and therefore the stoichiometry remains at approximately $UO_{1.3}$. NO_2 however continues to react with the oxynitride surface, with the XPS spectra suggesting that only

oxygen adsorbs onto the surface. This indicates that NO_2 dissociatively adsorbs producing atomic oxygen and NO, and as we have seen from the adsorption of NO, the reaction of NO with the oxynitride surface slows considerably. The stoichiometry of the oxide increases to a value above that of UO_2 (figure 4.28) suggesting that the oxidation state of U increases following increasing exposures of NO_2 . The increase in stoichiometry above UO_2 occurs at approximately 1000 L and is in agreement with the increasing shift in the U (4f) spectra (figure 4.15).

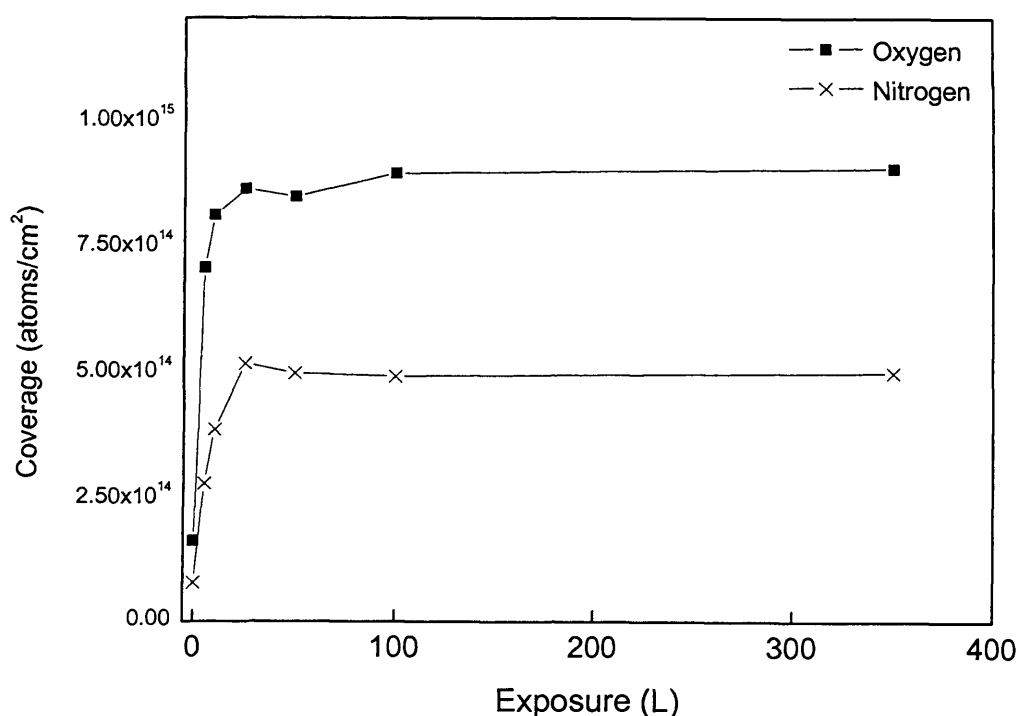


Figure 4.28. Oxygen and nitrogen surface coverage following exposure to NO

Figures 4.30 and 4.31, show the oxygen and nitrogen coverages following exposure to NO and NO_2 respectively. Surface coverages calculated for NO adsorption, show both oxygen and nitrogen concentrations increase at a similar rate and start to level off above 25 L as the presence of the oxynitride layer decreases the reaction rate. We can also see that the oxygen coverage is greater than that of the nitrogen. The trends, following exposure to NO and NO_2 are initially comparable however above 100 L, we see no further reaction

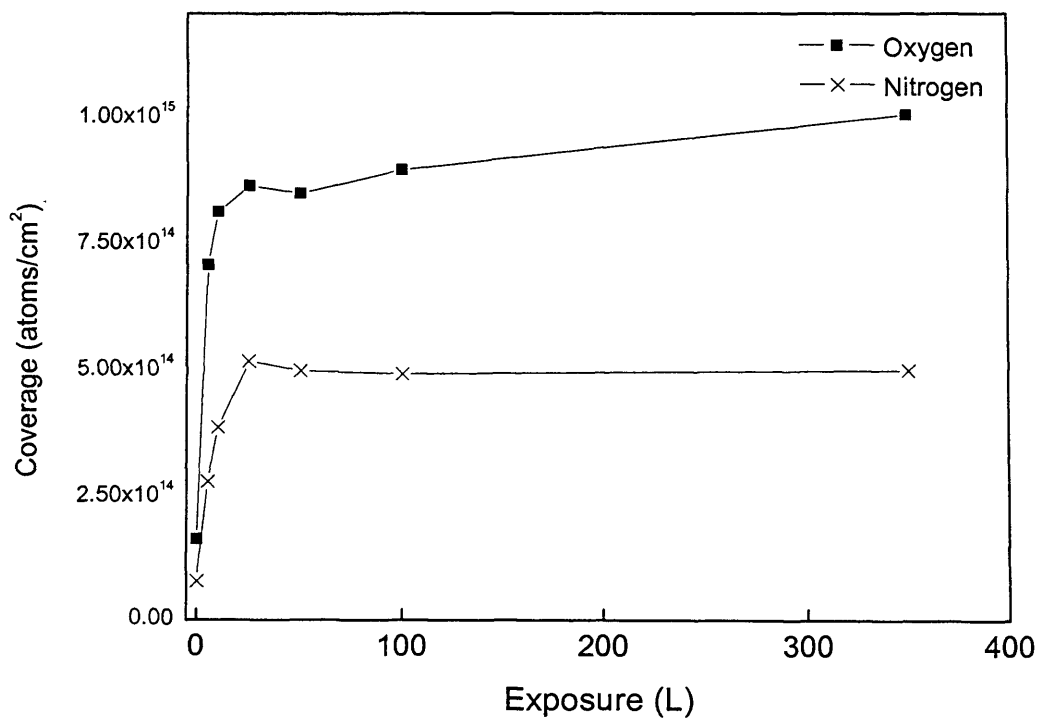


Figure 4.30. Oxygen and nitrogen surface coverage following exposure to NO₂

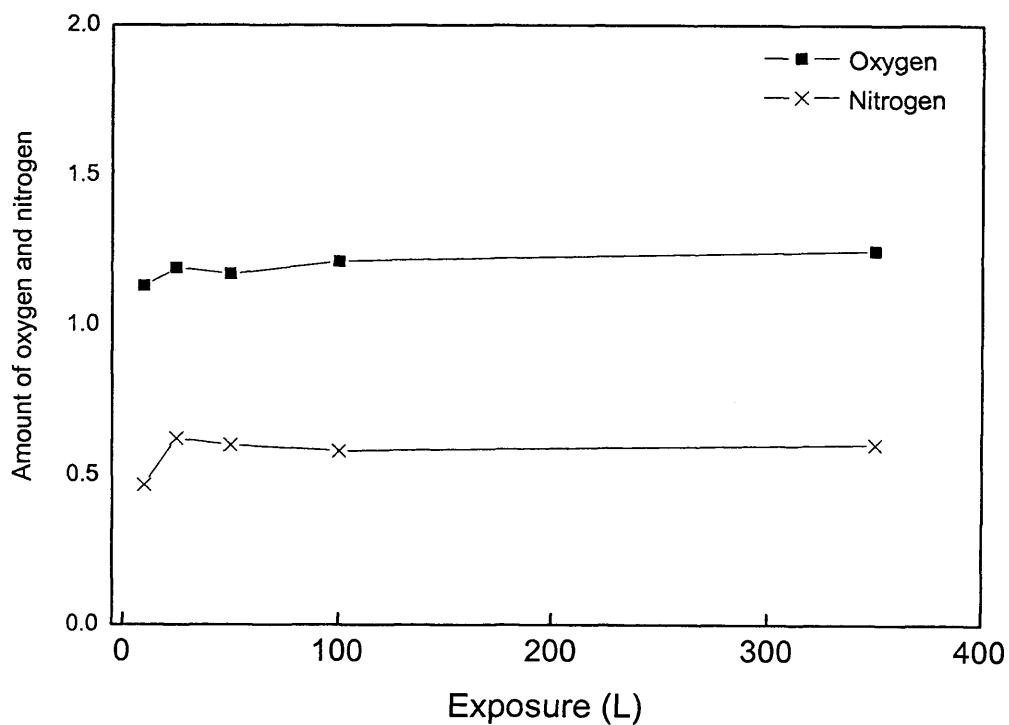


Figure 4.31. Stoichiometry UO_xN_y following exposure to NO.

with NO but with NO₂ we see an increase in the surface concentration of oxygen. This observation again supports what has been described earlier that NO₂ continues to react with the oxynitride surface with only oxygen adsorbing on the surface. It is possible now to propose a stoichiometry of the oxynitride layer. An approximate stoichiometry of the oxynitride can be estimated from the O (1s) N (1s) and the shifted U (4f) peak areas.

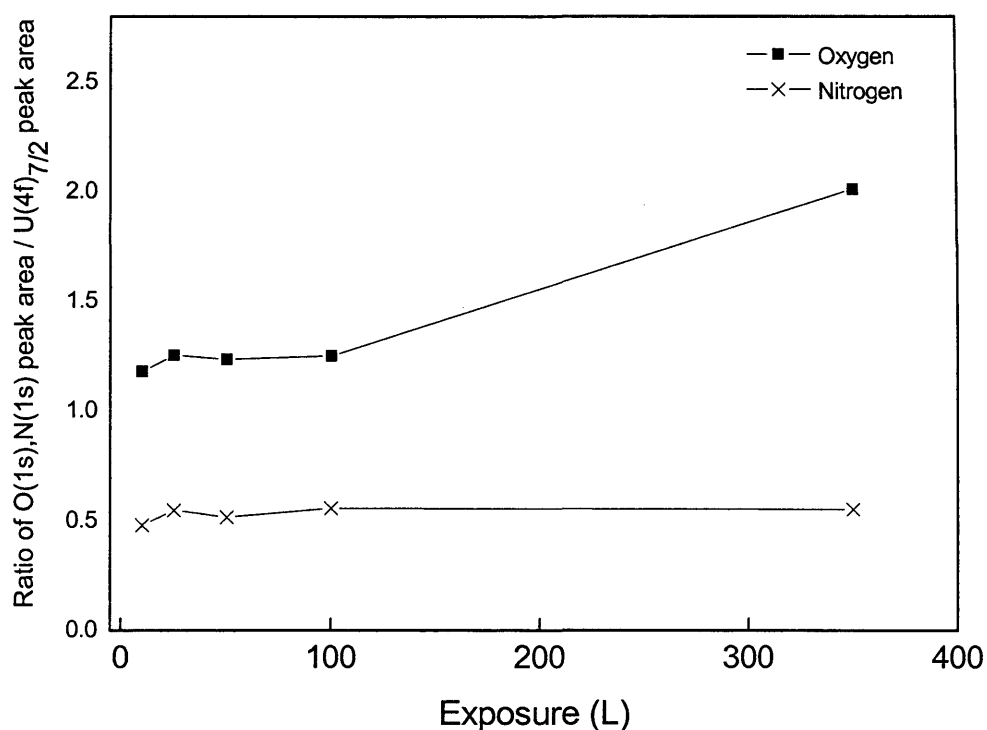


Figure 4.32. Stoichiometry UO_xN_y following exposure to NO₂.

A stoichiometry of approximately $UO_{1.2}N_{0.6}$ i.e. $U_5O_6N_3$ for the oxynitride (figure 4.31 and 4.32), at 100 L dosing of NO and NO₂, is proposed. This suggests that the oxidation state of U is slightly greater than IV, in keeping with the UPS spectra and the previous discussion suggesting increased 5f electron participation in bonding, compared to U^{IV} in UO₂. The stoichiometry of the surface following exposures of NO₂ above 100 L can also be approximated (figure 4.31), as $UO_2N_{0.6}$ i.e. $U_5O_{10}N_3$. Increasing the dosing up to 3000 L continues to increase the oxygen concentration and we see a stoichiometry of approximately $UO_{2.5}N_{0.6}$ i.e. $U_{10}O_{25}N_6$. This indicates the uranium oxidation state is close to VI, in keeping with the further decrease in

the localized U (5f) peak at 1.1 eV below E_F and the increase in the 'bonding' band seen in the UPS spectra. We would expect the localized 5f peak at 1.1 eV to be no longer present if all the surface uranium atoms were in the U^{VI} oxidation state, indicating all the 5f electrons are involved in bonding, as seen in the UPS spectra of UO_3 [27].

4.4 Conclusions

The reaction of N_2O with a polycrystalline uranium surface results in the formation of a thin oxide layer with no adsorbed nitrogen. Nitrogen, produced as a result of dissociative adsorption, desorbs from the surface as $N_{2(g)}$. Nitride formation is not observed in the UPS or XPS spectra. The oxide layer, $UO_{1.5}$, reduces the reactivity of the surface towards N_2O and the reaction slows considerably. A depth of approximately 1 nm was calculated in contrast to 2 nm produced following exposure to O_2 . The difference in reactivity is not due to inhibited oxygen diffusion as we have shown by reacting the N_2O passivated surface with O_2 that O^{2-} diffusion still occurs. Bond energies suggest that dissociative adsorption of N_2O should be the most thermodynamically favorable as the N-O bond strength is the weakest when compared to O_2 , NO and NO_2 and it also produces the stable $N_{2(g)}$. However the results obtained suggest that N_2O is unreactive towards the oxide surface produced and dissociative adsorption requires metal adsorption sites.

Below 10 L a metallic oxynitride is produced, following the reaction with NO and NO_2 , with itinerant 5f electrons located at E_F in the UPS spectra. The reaction up to 350 L then produces a surface oxynitride of approximate stoichiometry $UO_{1.2}N_{0.6}$. The stoichiometry indicates that the uranium is in an oxidation state slightly above U^{IV} , which is supported by the UPS spectra which show increased 5f participation in bonding when compared to UO_2 . The reaction between the surface and NO slows considerably when the surface is covered by uranium oxynitride. Unlike NO, NO_2 continues to react with the oxynitride surface giving rise to increased oxygen adsorption and forming a surface oxynitride of approximate stoichiometry, $UO_2N_{0.6}$. Shifts in

the U (4f) and O (1s) spectra support the increased oxidation. UPS spectra also indicate further 5f involvement in bonding as the localized 5f peak at 1.1 eV decreases in intensity above 350 L.

4.5 References

1. G.C. Allen, P.M. Tucker, and I.R. Trickle, *Philosophical Magazine B-Physics of Condensed Matter Statistical Mechanics Electronic Optical and Magnetic Properties*, 1981. **43**(4). 689-703.
2. D.A. Hoffman and J.B. Hudson, *Surface Science*, 1987. **180**(1). 77-88.
3. A. Pashutski and M. Folman, *Surface Science*, 1989. **216**(3). 395-408.
4. J. Grimblot, P. Alnot, R.J. Behm, and C.R. Brundle, *Journal of Electron Spectroscopy and Related Phenomena*, 1990. **52**. 175-183.
5. T.E. Madey, N.R. Avery, A.B. Anton, B.H. Toby, and W.H. Weinberg, *Journal of Vacuum Science & Technology a-Vacuum Surfaces and Films*, 1983. **1**(2). 1220-1221.
6. J.C. Fuggle, *Surface Science*, 1979. **79**(1).
7. W.M. Daniel, Y. Kim, H.C. Peebles, and J.M. White, *Surface Science*, 1981. **111**(2). 189-204.
8. F. Greuter, E. Hauser, P. Oelhafen, H.J. Guntherodt, B. Reihl and O. Vogt, in *Physica B*. 1980. 117.
9. Molodtsov SL, Boysen J, Richter M, et al., in *PHYS REV B*. 1998. 13241 - 13245.
10. J.Naegele and L.Mane, *Actinides - Chemistry and Physical properties*, in *Structure and Bonding*, L. Mane, Editor. 1985. p. 197.
11. J.R. Naegele, J. Ghijsen, and L. Manes, *Structure and Bonding*, 1985. **59-60**. 197-262.
12. T. Gouder, C. Colmenares, J.R. Naegele, and J. Verbist, *Surface Science*, 1990. **235**(2-3). 280-286.
13. L. Black, F. Miserque, T. Gouder, L. Havela, J. Rebizant, and F. Wastin, *Journal of Alloys and Compounds*, 2001. **315**(1-2). 36-41.
14. L.Black, F.Miserque, T.Gouder, L.Havela, J.Rebizant, and F.Wastin, *Journal of Alloys and Compounds*, 2001. **315**(1-2). 36-41.
15. G.C.Allen and P.M.Tucker, *Journal of the Chemical Society-Chemical Communications*, 1973(Dalton Trans). 470.
16. J. Kupperts and G. Ertl, *Surf Sci*, 1978. **77**. L647.
17. T.Gouder, C.Colmenares, J.R.Naegele, and J.Verbist, *Surface*

- Science, 1990. **235**(2-3). 280-286.
18. M. Eckle and T. Gouder, *Journal of Alloys and Compounds*, 2004. **374**(1-2). 261-264.
 19. T. Gouder, L. Havela, F. Miserque, F. Wastin, and J. Rebizant, Japan, *Actinides 2001*.
 20. G.C. Allen, P.A. Tempest, and J.W. Tyler, *Journal of the Chemical Society-Faraday Transactions I*, 1988. **84**. 4049-4059.
 21. G.C. Allen, P.M. Tucker, and J.W. Tyler, *Journal of Physical Chemistry*, 1982. **86**(2). 224-228.
 22. E. Kostic, *Nucl. Energy*, 1967. **4**. 6.
 23. K. Winer, F. Wooton, C.A. Colmenares, and R.L. Smith, *Surface Science*, 1986. **177**(3). 484-492.
 24. M.P. Ames, A.S. Wilson, and E.E. Rundle, Report CN-1495, 1944.
 25. R.J. McEachern and P. Taylor, *Journal of Nuclear Materials*, 1998. **254**(2-3). 87-121.
 26. B.W. Veal and D.J. Lam, *Physical Review B*, 1974. **10**. 4902.
 27. T. Gouder, L. Havela, F. Miserque, F. Wastin, and J. Rebizant, Japan, *Actinides 2001*.

CHAPTER 5

Gas adsorption Studies on Np metal by photoemission spectroscopy

5.1. Introduction

The light actinide elements (thorium to americium) display evidence of 5f electron involvement in chemical bonding, an excellent example of this behaviour being the binary oxides of these elements. The Np-O phase diagram shows that both tetra and penta-valent oxides, NpO_2 and Np_2O_5 , are stable [1]. Additionally, trivalent neptunium sesquioxide has been reported as a surface oxide [2], prepared under ultra high vacuum conditions from the surface segregation of oxygen dissolved in the Np metal sample. However, this compound has not been synthesised as a pure material. We have therefore investigated further the possible existence of this oxide phase. Here we report the first detailed gas adsorption studies (O_2 , CO and NO) on Np metal. The results are compared to previous measurements on Pu [3-5] and U [6-9].

Thin films of neptunium were used in this study. The neptunium films were prepared, at the Institute for Transuranium Elements (ITU), in situ by DC sputtering of neptunium. The plasma triode deposition source has been described in detail elsewhere [10] and briefly in appendix 2.

5.2. Results

5.2.1. Adsorption of Oxygen

The core-level and valence band photoelectron spectra following exposure of clean Np metal to increasing doses of oxygen at 300 K are shown in figures. 5.1 to 5.4. The XPS 4f core lines of the clean metal (411.4 and 399.6 eV for $4f_{5/2}$ and $4f_{7/2}$ respectively) are narrow and exhibit an asymmetric line shape that is typical for actinide systems with itinerant 5f electrons (figure 5.1). The main peak of the clean metal is denoted the well screened peak as the 4f

photoionisation core hole is efficiently screened by itinerant 5f electrons (screening by 6d electrons upon 5f localization gives rise to a poorly screened peak, see for example screening mechanisms for Th (chapter 3) and Am (chapter 6) metals or appendix 1). The asymmetry of the 4f peak is produced by low-energy losses by scattering of itinerant 5f electrons at E_F into empty states. The gradual oxidation of Np by increasing exposures of oxygen results in the growth of two peaks at about 1.6 and 3.9 eV higher binding energies than the clean well screened Np metal peaks. These values are in good agreement with values obtained by Naegele and Cox [2] in which oxidation of the surface was caused by a slow segregation of residual bulk oxygen impurities to the surface. In that study a high purity Np plate was cut from double electro-refined material, cleaned in situ by Ar sputtering at 400 K and then just before measurement cooled down to 80 K.

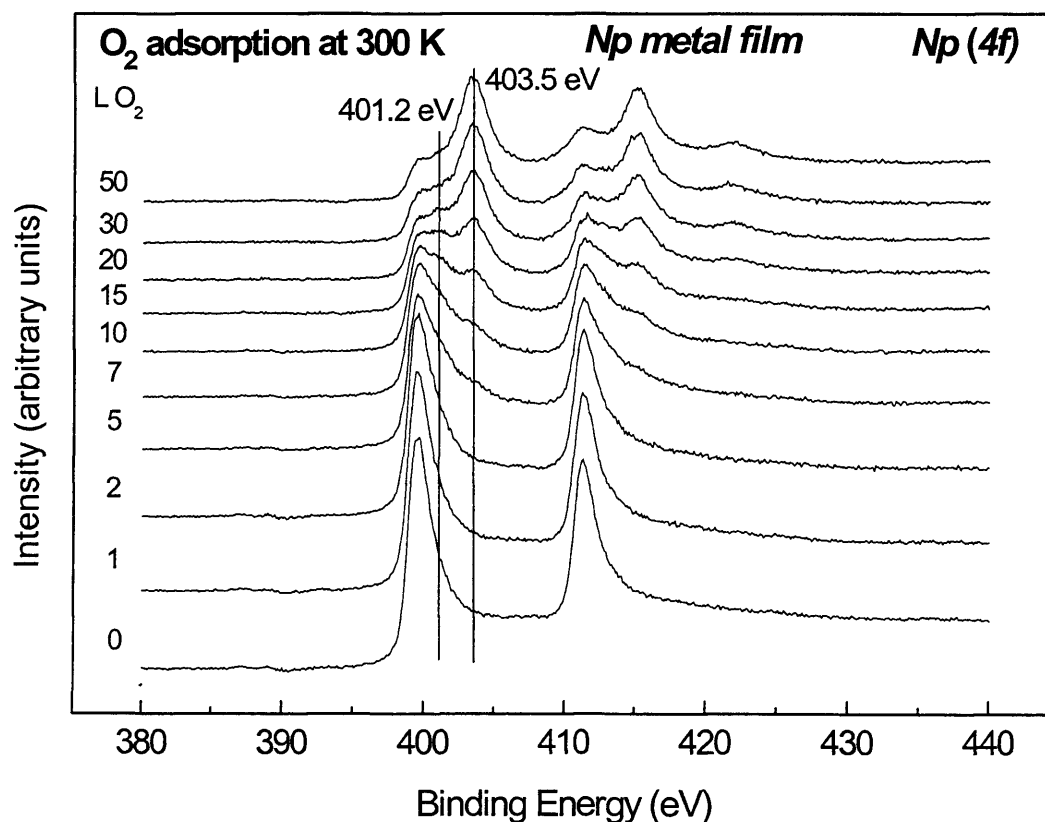


Figure 5.1. Np (4f) core level spectra for increasing surface oxidation of Np metal

The poorly screened peak with a chemical shift of 3.9 eV, from the well screened clean metal 4f peak, we propose is the formation of the dioxide

NpO_2 . The binding energy is in good agreement with that previously reported for neptunium dioxide [11, 12]. The symmetrical peak and the presence of a satellite, positioned 6.8 eV from the 4f peaks on the higher binding energy side, are characteristic of an actinide dioxide signal, as found in UO_2 , NpO_2 and PuO_2 . The presence of a peak at 401.2 eV, 1.6 eV higher BE than the metal $4f_{7/2}$ peak, indicates the formation of a lower Np oxide that, according to the Np phase diagram [13], does not exist as a stable bulk oxide. It is formed on the surface in the presence of the metal and decreases in intensity as the amount of metal at the surface declines. Concomitantly the dioxide peak increases in intensity. Figure 5.2 shows clearly that following 10 L exposure of oxygen there is Np metal, an intermediate oxide, and dioxide present within the information depth of XPS.

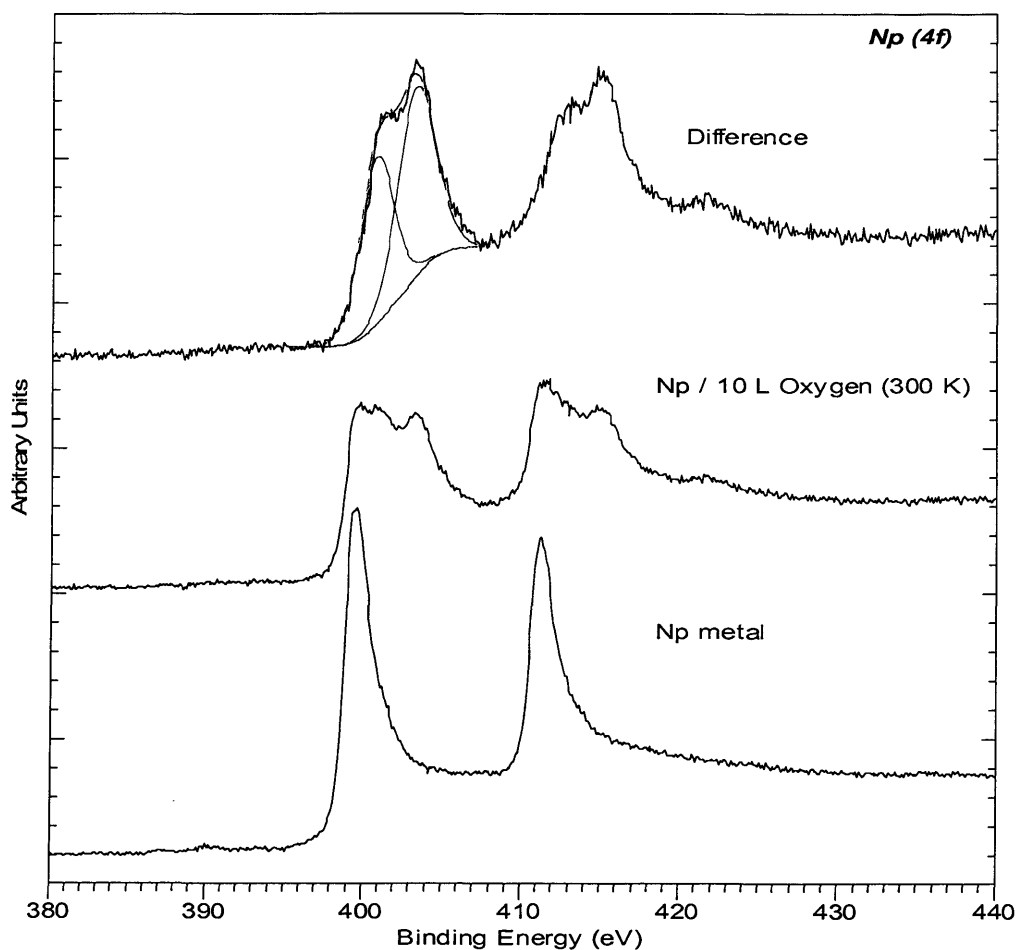


Figure 5.2. Np (4f) core level spectra for surface oxidation of Np metal

NpO_2 . The binding energy is in good agreement with that previously reported for neptunium dioxide [11, 12]. The symmetrical peak and the presence of a satellite, positioned 6.8 eV from the 4f peaks on the higher binding energy side, are characteristic of an actinide dioxide signal, as found in UO_2 , NpO_2 and PuO_2 . The presence of a peak at 401.2 eV, 1.6 eV higher BE than the metal $4f_{7/2}$ peak, indicates the formation of a lower Np oxide that, according to the Np phase diagram [13], does not exist as a stable bulk oxide. It is formed on the surface in the presence of the metal and decreases in intensity as the amount of metal at the surface declines. Concomitantly the dioxide peak increases in intensity. Figure 5.2 shows clearly that following 10 L exposure of oxygen there is Np metal, an intermediate oxide, and dioxide present within the information depth of XPS.

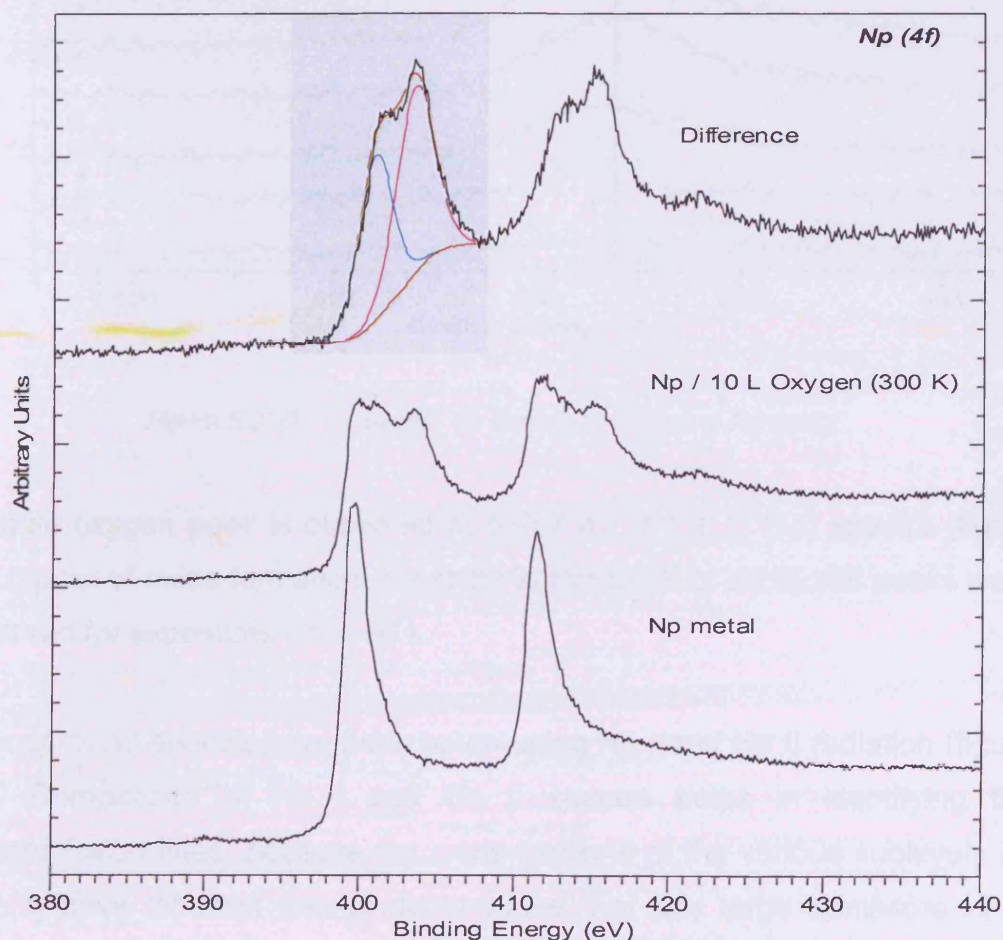


Figure 5.2. Np (4f) core level spectra for surface oxidation of Np metal

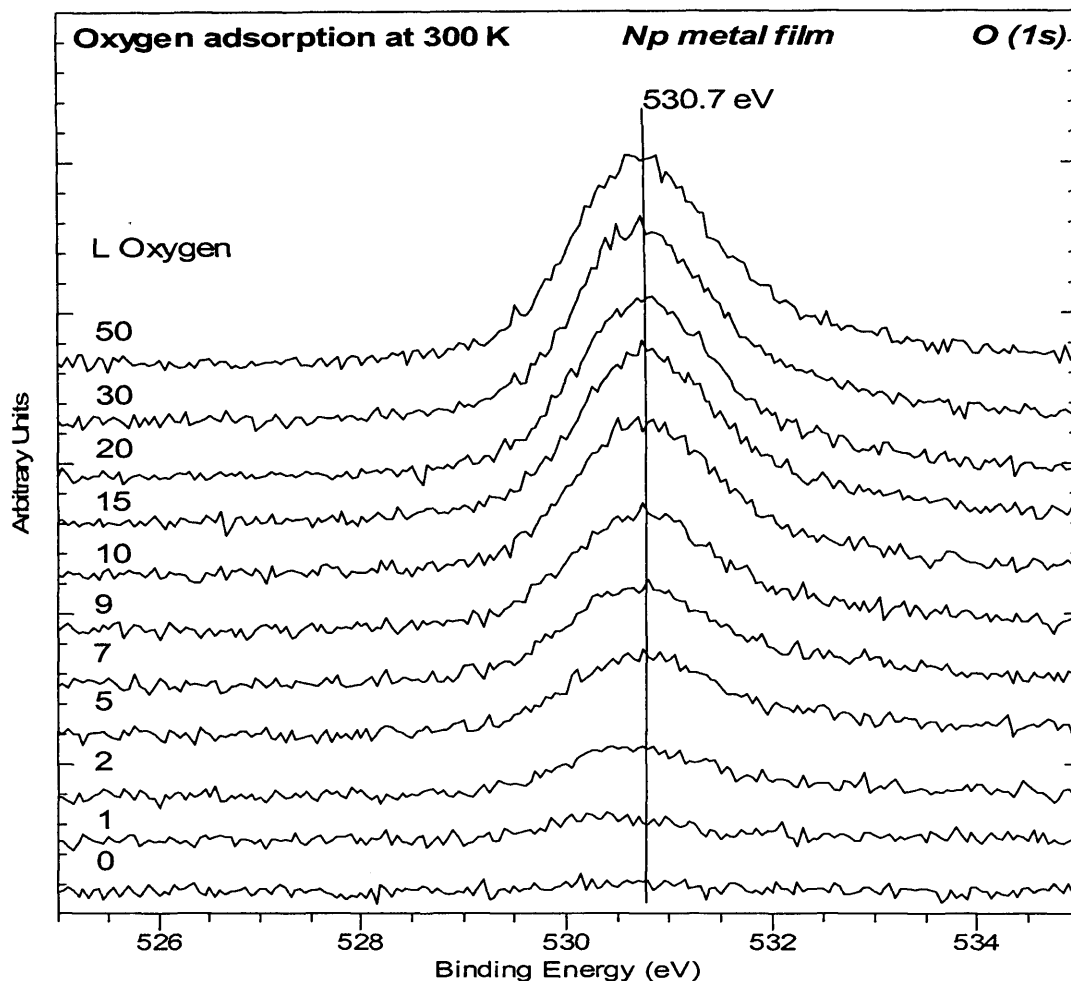


Figure 5.3. O (1s) spectra for surface oxidation of Np metal

A single oxygen peak is observed at 530.7 eV in the O (1s) spectra (figure 5.3) typical of oxide formation. No shifts in this peak or additional peaks were observed for exposures up to 50 L.

Valence band spectra have been taken using He I and He II radiation (figure 5.4). Comparison of He I and He II spectra helps in identifying the photoemission lines, because the cross-sections of the various sublevels (s, p, d, f) have different energy dependence. For any large admixture of 5f states in the He II spectra the corresponding spectral intensity in the He I spectra is suppressed, as the 5f photoexcitation cross-section for $h\nu = 21.2$ eV is very low.

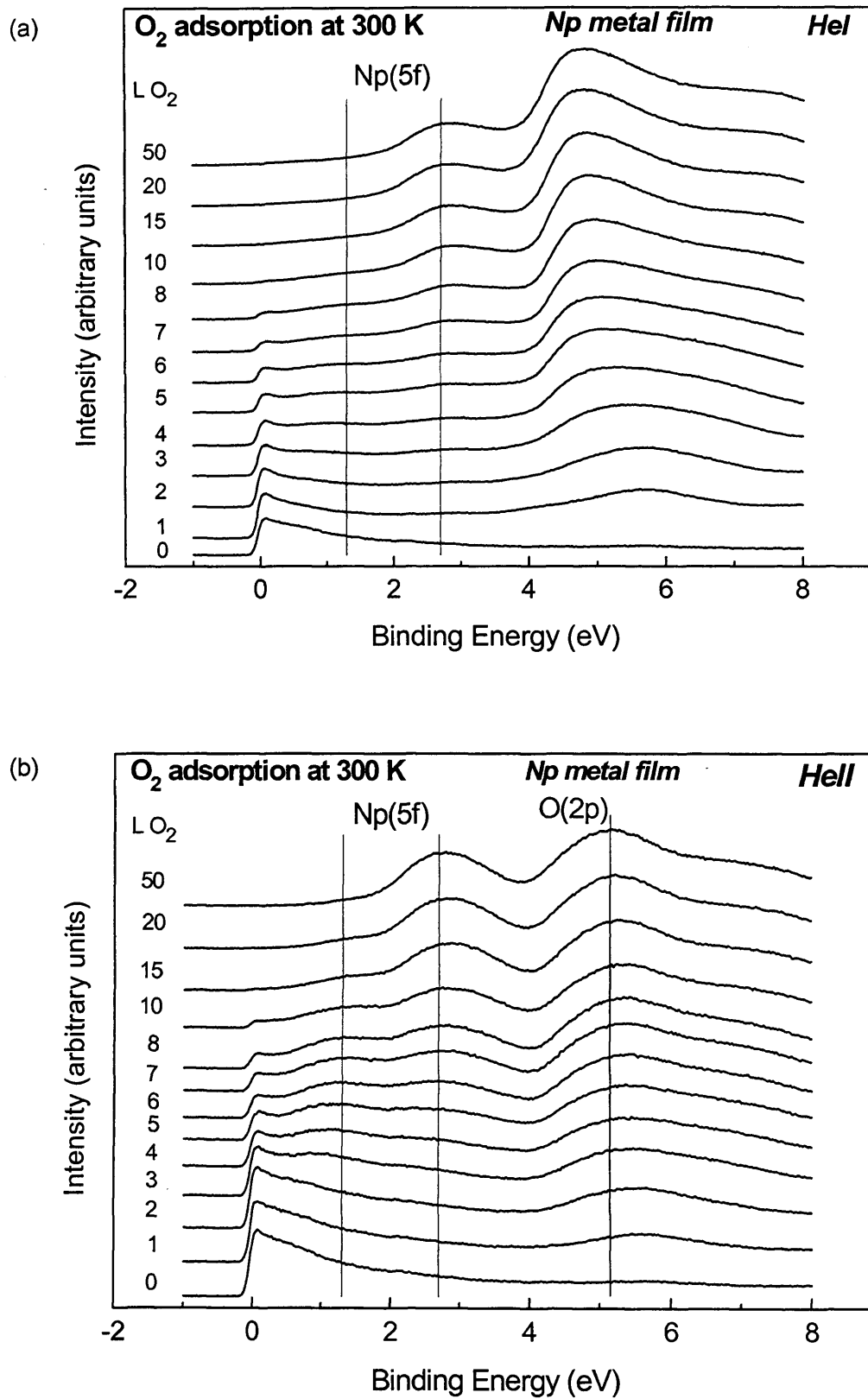


Figure. 5.4. (a) He I spectra for increasing surface oxidation at 300 K (He I, $h\nu = 21.2\text{eV}$). (b) He II spectra for increasing surface oxidation at 300 K (He II, $h\nu = 40.8\text{eV}$).

The He II UPS valence band spectra are dominated by an intense peak at the Fermi level (E_F) i.e. a high density of 5f states at E_F , confirming the itinerant character of the 5f electrons. The spectra also support the conclusions drawn from the 4f core level spectra, with the growth of two separate localized Np (5f) peaks at 1.5 and 2.7 eV, indicating the formation of two oxide phases at the surface. The intensities of the two peaks are weaker in the He I spectra confirming their 5f character. The emission at approximately 5.5 eV is assigned to O (2p) orbitals. It is more pronounced in He I than in He II because of the enhanced O (2p) and the reduced Np (5f) cross-sections in He I. Initially (below 3 L) it is sharp and symmetric, centered between 5 and 6 eV and approximately 1 eV wide, typical of chemisorbed oxygen [14]. The increase of the O (2p) peak is accompanied by an increase in intensity of the two localized 5f peaks. Initially (below 3 L) only the Np (5f) peak at 1.3 eV, corresponding to the lower oxide, is present. This localized peak at 1.3 eV is only present as long as the metal signal at E_F is visible. Above 3 L the O (2p) band broadens, a contribution at higher binding energy increases and it begins to exhibit an asymmetric shape typical of actinide dioxide formation. At this point above 3 L we also concomitantly see an increase in intensity of a localized 5f peak at 2.7 eV. The spectrum for complete oxidation within the information depth of UPS, at 50 L when there is no metal signal present, is characteristic of NpO_2 . The localized 5f peak at 2.7 eV and the asymmetric O (2p) peak centered at 5.2 eV confirm the presence of the Np^{IV} dioxide.

Valence band spectra for the oxidation of Np at 80 K (figure. 5.5) show an increased rate of reaction when compared to oxidation at 300 K. Complete oxidation, within the information depth of UPS, occurs at 10 L. As with oxidation at 300 K the loss of the itinerant metal peak is accompanied by the loss of intensity of the 5f peak at 1.3 eV. This indicates that the lower oxide is only stable in the presence of the itinerant metal peak at E_F . Loss of intensity of the metal and 1.3 eV localized 5f peak of the lower oxide leads to the increase in intensity of the localized 5f peak at 2.7 eV. The resultant spectra at 10 L exposure are similar to the spectra recorded for 50 L exposure at 300

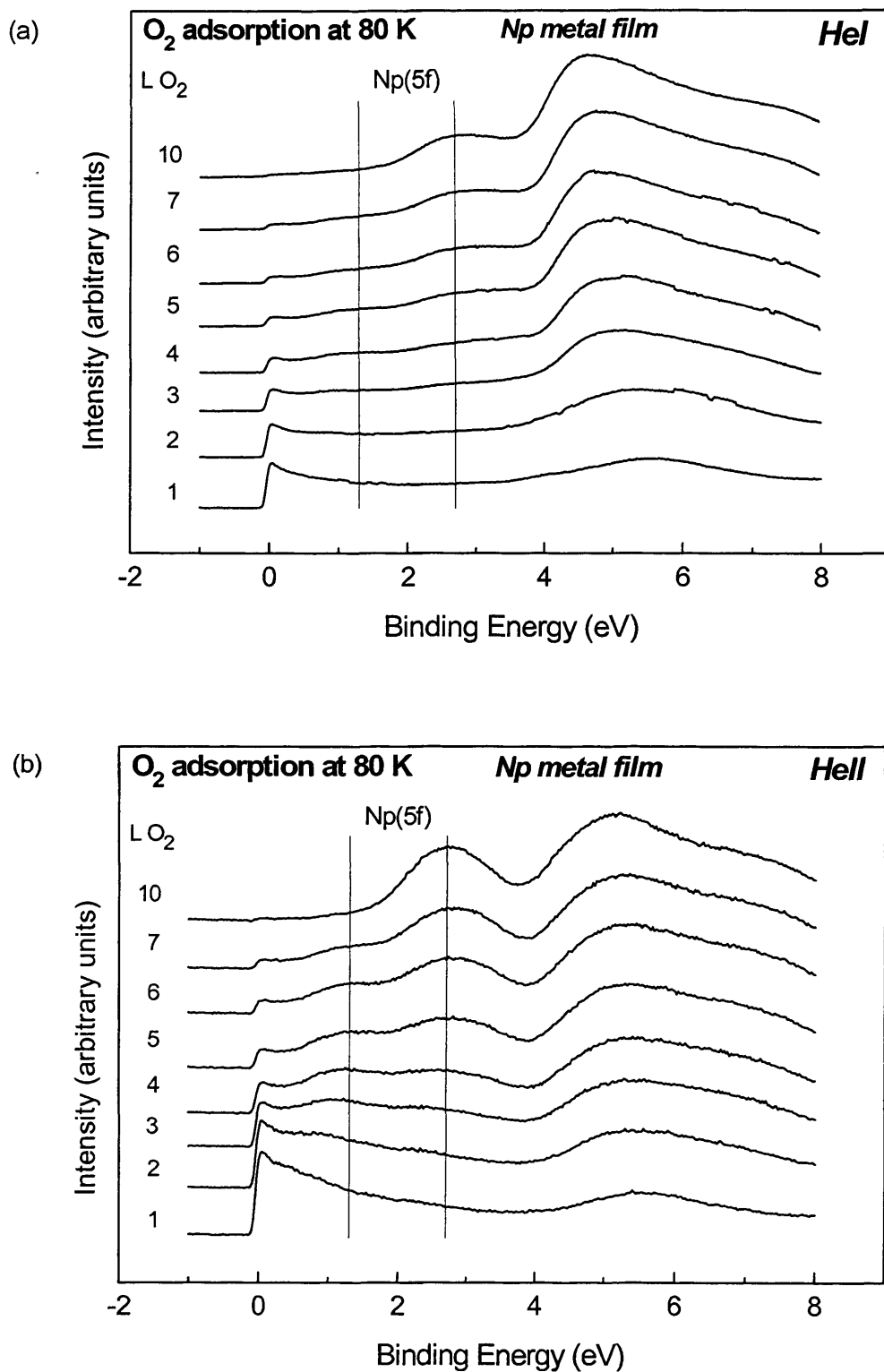


Figure 5.5. (a) He I spectra for increasing surface oxidation at 80 K (He I, $h\nu = 21.2\text{eV}$). (b) He II spectra for increasing surface oxidation at 80 K (He II, $h\nu = 40.8\text{eV}$).

K and again agree with previously reported spectra for NpO_2 [12]. Increased reactivity at low temperature involves an increased population of the precursor state and is discussed in section 5.3

5.2.2. Adsorption of CO

Figure 5.6 shows the Np (4f) core levels for reaction with CO. There appears to be very little change in the 4f spectra following exposure to 20 L CO, only a slight increase in intensity on the high binding energy side of the peaks. The slight increase in intensity of a poorly screened contribution and a slight decrease in the well screened peak suggests the 5f electrons become slightly more localized, in a position similar to the lower oxide formed following exposure to oxygen. C (1s) and O (1s) spectra are also shown in figure. 5.6.

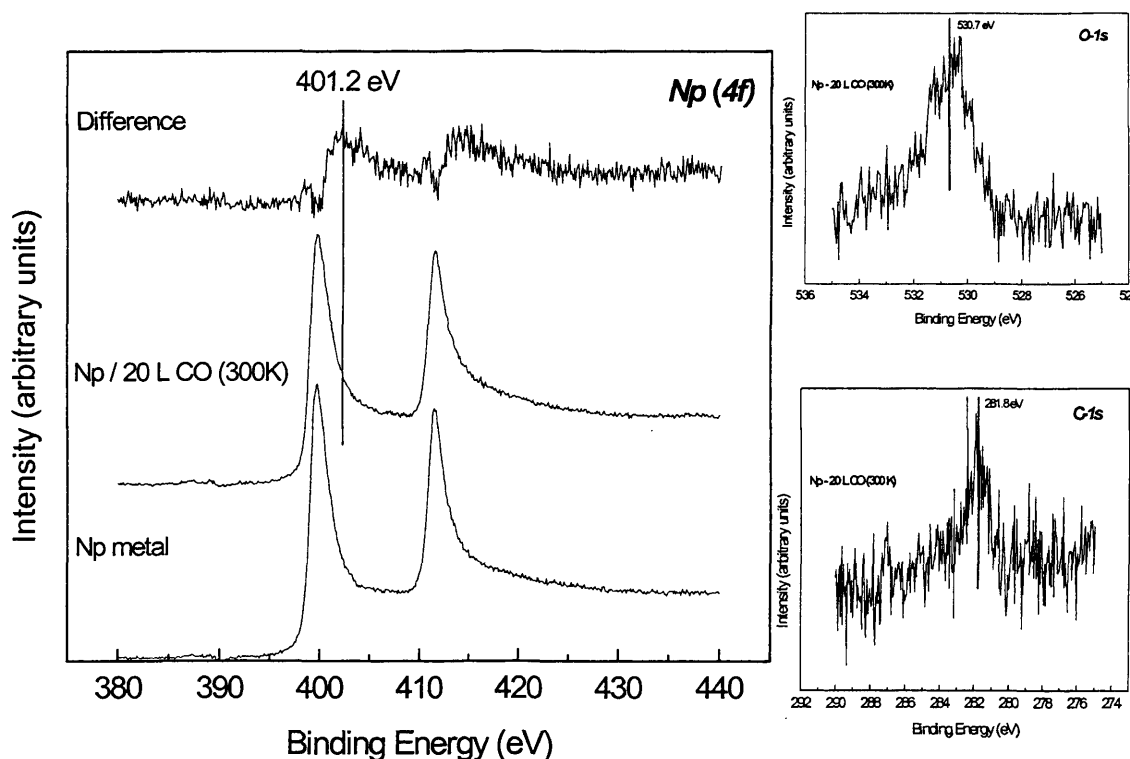


Figure. 5.6. Np (4f) core level, O(1s) and C(1s) spectra for CO exposure at 300 K.

A single carbon peak at 281.8 eV is observed which is close to published values for bulk transition metal carbides [15] and UC [9]. The single peak in

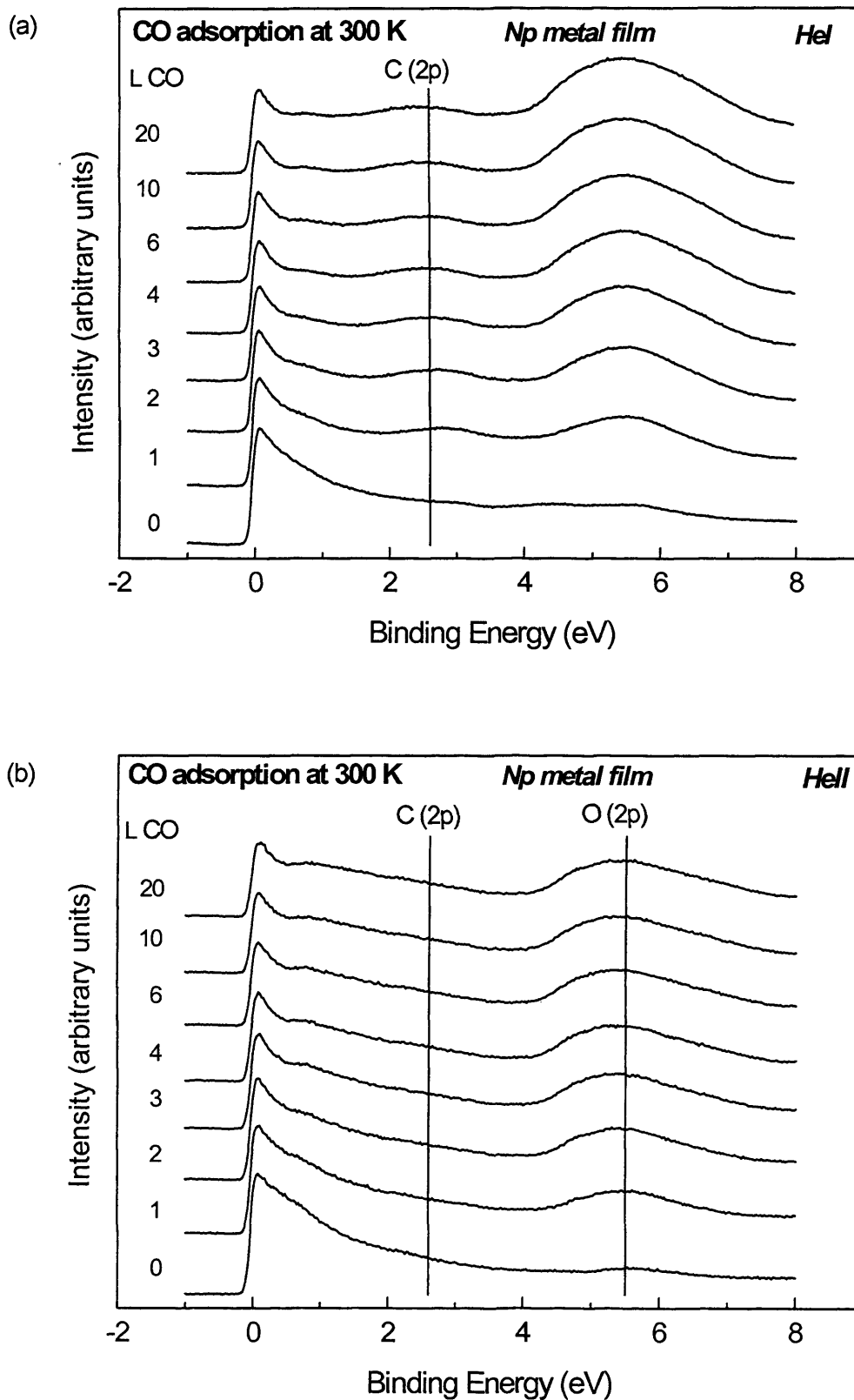


Figure 5.7. (a) He I spectra for increasing CO exposure at 300 K (He I, $h\nu = 21.2\text{eV}$). (b) He II spectra for increasing CO exposure at 300 K (He II, $h\nu = 40.8\text{eV}$).

the O (1s) region at 530.7 eV is in agreement with the peak obtained during the oxidation experiments and is assigned as surface oxide. Valence band spectra give further information on the nature of this oxide.

Figure 5.7 shows the He I and He II spectra taken following exposure of Np to CO at 300 K. The O (2p) peak at 5.5 eV is symmetrical and narrower (4 eV wide) than that observed for dioxide formation following exposure to oxygen (5.7 eV wide). The peak is however broader than the sharp, 1 eV wide, chemisorbed O (2p) peak observed for initial exposures of oxygen indicating the formation of a compound and not a chemisorbed phase. The O (2p) peak does not develop intensity at higher binding energy hence the asymmetric peak typical of dioxide formation is not observed. In addition the localized Np (5f) oxide emission at 2.7 eV, typical for NpO₂, is missing. A peak at approximately 2.6 eV appears in the He I spectra which can just be seen in the He II spectra. This peak is also observed in UC [9] and attributed to the C (2p) Valence band. The 2p character of this peak is confirmed by the increased intensity in He I spectra compared to the He II, typical for the C (2p) cross-section. During initial adsorption the intensity at E_F decreases only slightly while the area of the O (2p) emission grows linearly pointing to a constant reaction probability. The slight decrease in intensity at E_F is accompanied by an increase in intensity at approximately 1.3 eV, indicating a shift from itinerant to localized 5f behavior following reaction with CO. The 5f character of the emission at 1.3 eV is confirmed by the suppressed signal in the He I spectra. The peak at 1.3 eV is at a similar position to that of the lower oxide formed following exposure to oxygen and similarly indicates that the Np is at a lower oxidation state than the Np^{IV} dioxide.

Figure 5.8 shows the 4f core level spectra following exposure to 40 L of CO at low temperature. They show very little change, although a slight increase in intensity of a peak on the high binding energy side of the well screened metal peak shifted approximately 1.6 eV is observed. The spectra after 40 L exposure to CO at 80 K and 20 L exposure at 300 K are essentially the same. The UPS spectra (described below) show an increased rate of reaction; however it appears that the reaction does not proceed further than

that achieved following exposure to 20 L CO at 300 K. Therefore it appears when the surface is covered with a monolayer the reaction with CO essentially ceases.

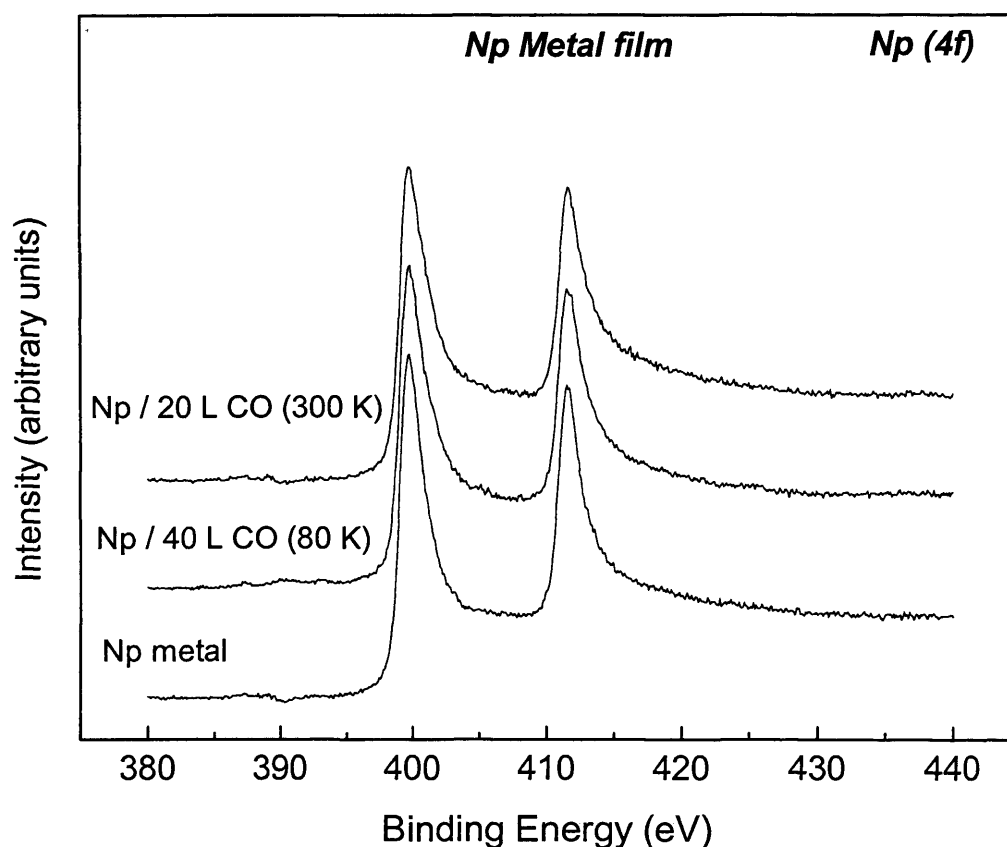


Figure 5.8. Np (4f) core level spectra following exposure to CO

Exposing the Np surface to CO at low temperature, similar to the reaction with oxygen at low temperature, results in an increased rate of reaction. A similar UPS spectrum to that obtained following 20 L exposure CO at room temperature is achieved after only 2 L at low temperature. A similar explanation to that following oxygen exposure for the increased reactivity at low temperature involving increased population of the precursor state is offered and discussed in section 5.3. Figure 5.9 shows the He I and He II spectra recorded for increasing doses of CO at 80 K. Initially, up to 2 L, the reaction is the same as recorded at 300 K but we then see further reaction

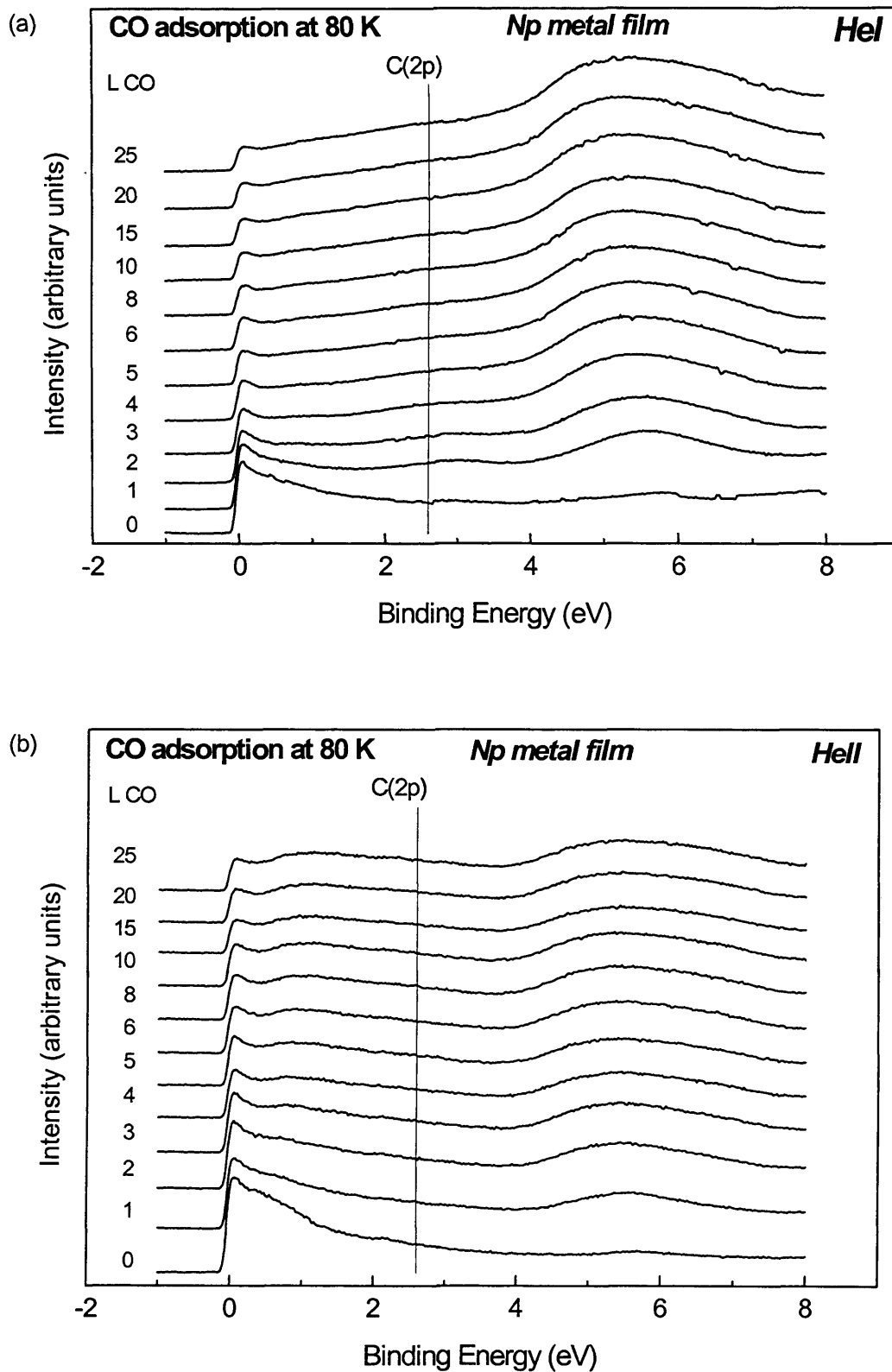


Figure. 5.9. (a) He I spectra for increasing CO exposure at 80 K (He I, $h\nu = 21.2\text{eV}$). (b) He II spectra for increasing CO exposure at 80 K (He II, $h\nu = 40.8\text{eV}$).

above 2 L. Increases in the amount of surface carbon and oxygen, as seen in the He I spectra at exposures above 2 L, are confirmed by the corresponding suppressed signal in the He II spectra. The C (2p) and O (2p) peaks, at 2.6 eV and 5.5 eV respectively, continue to increase up to approximately 10 L when the rate of reaction appears to slow considerably and there is very little change in the spectra. Although increasing in intensity the O (2p) peaks remain almost symmetrical and the asymmetric peak shape typical of dioxide formation was not observed. A similar trend is observed with the increase in localized 5f intensity at 1.3 eV which then changes very little above 10 L. There is also no localized 5f peak at 2.7 eV even at the higher exposures indicating further reaction to form the dioxide does not take place. Therefore the absence of both an asymmetric O (2p) band and a localized 5f emission at 2.7 eV indicate that surface dioxide formation does not take place.

5.2.3. Adsorption of NO

Figure 5.10 shows the Np (4f) core levels for the reaction of Np with NO at 300 K. There appears to be very little change in the 4f spectra following exposures up to 5 L NO, with only a slight increase in intensity on the high binding energy side of the well screened peaks being observed. The increased intensity at approximately 1.6 eV higher binding energy, in a position similar to the lower oxide formed following exposure to oxygen and that observed with CO adsorption, suggests the 5f electrons become slightly more localized. Upon further exposure (10 – 30 L) the growth of an “oxide” peak at 2.6 eV higher binding energy than the clean 4f peak is observed. The increase in intensity of this poorly screened peak indicates increased localization of the 5f electrons, also resulting in a decrease in intensity of the well screened metal peak (where the photohole is screened by f states). The position of this peak is further shifted than the intermediate oxide peak, shifted 1.6 eV, formed following low exposures of O₂, CO and NO. The peak shift of 2.6 eV is however not as high as the observed 3.9 eV shift following dioxide formation. A similar intermediate shift in the 4f peaks is observed following NO exposure on thorium (chapter 3) and uranium (chapter 4) and is assigned as oxynitride formation at the surface. The reaction of NO with Np

may similarly produce surface oxynitride giving rise to the peak shifted 2.6 eV. Dissociative adsorption of NO is confirmed from the N (1s) and O (1s) regions. The N (1s) region is visible in the Np (4f) spectra (figure. 5.10) and a peak situated at 396.3 eV typical of nitride formation is observed. The O (1s) region shows a single oxide peak typical for oxide formation. Therefore the dissociative adsorption of NO and the presence of both oxygen and nitrogen at the surface may lead to the formation of a surface oxynitride.

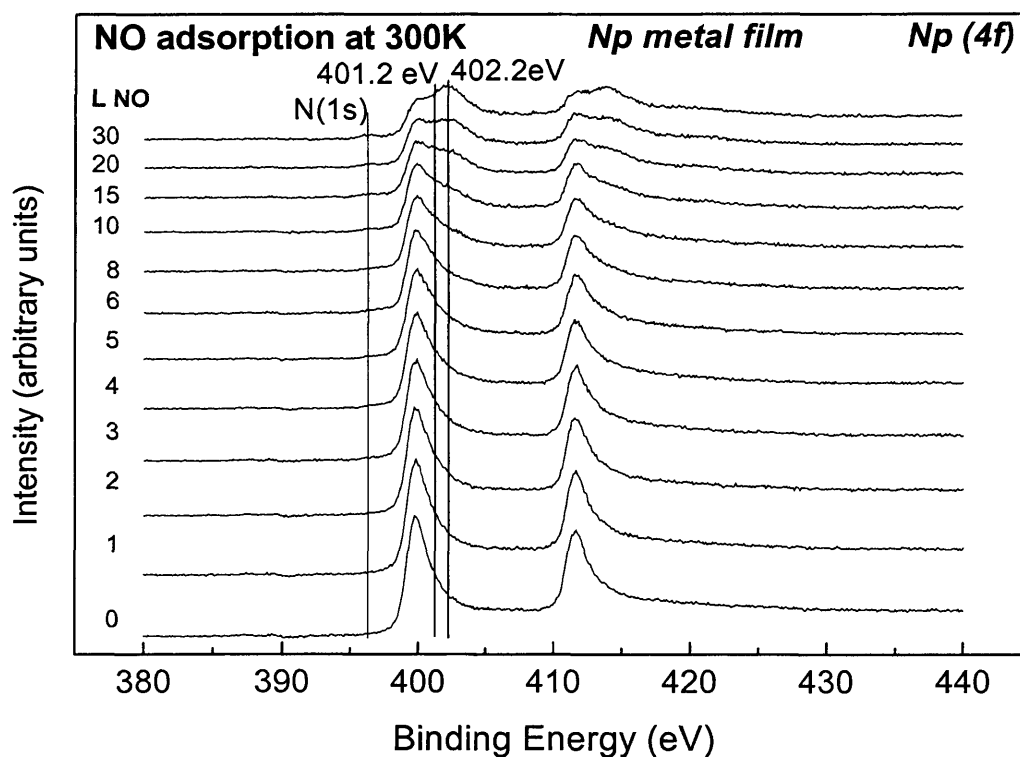


Figure. 5.10. Np (4f) core level spectra for increasing NO exposure at 300K

Figure 5.11 shows the He I and He II spectra taken following exposure of Np to NO at 300 K. Similar to the reaction with CO, the O (2p) peak at 5.5 eV is symmetrical and narrower than that observed for dioxide formation following exposure to oxygen. It is again however broader and not as sharp as the O (2p) peak observed for chemisorbed oxygen [14] indicating the formation of an oxide. The absence of both asymmetry associated with the O (2p) peak

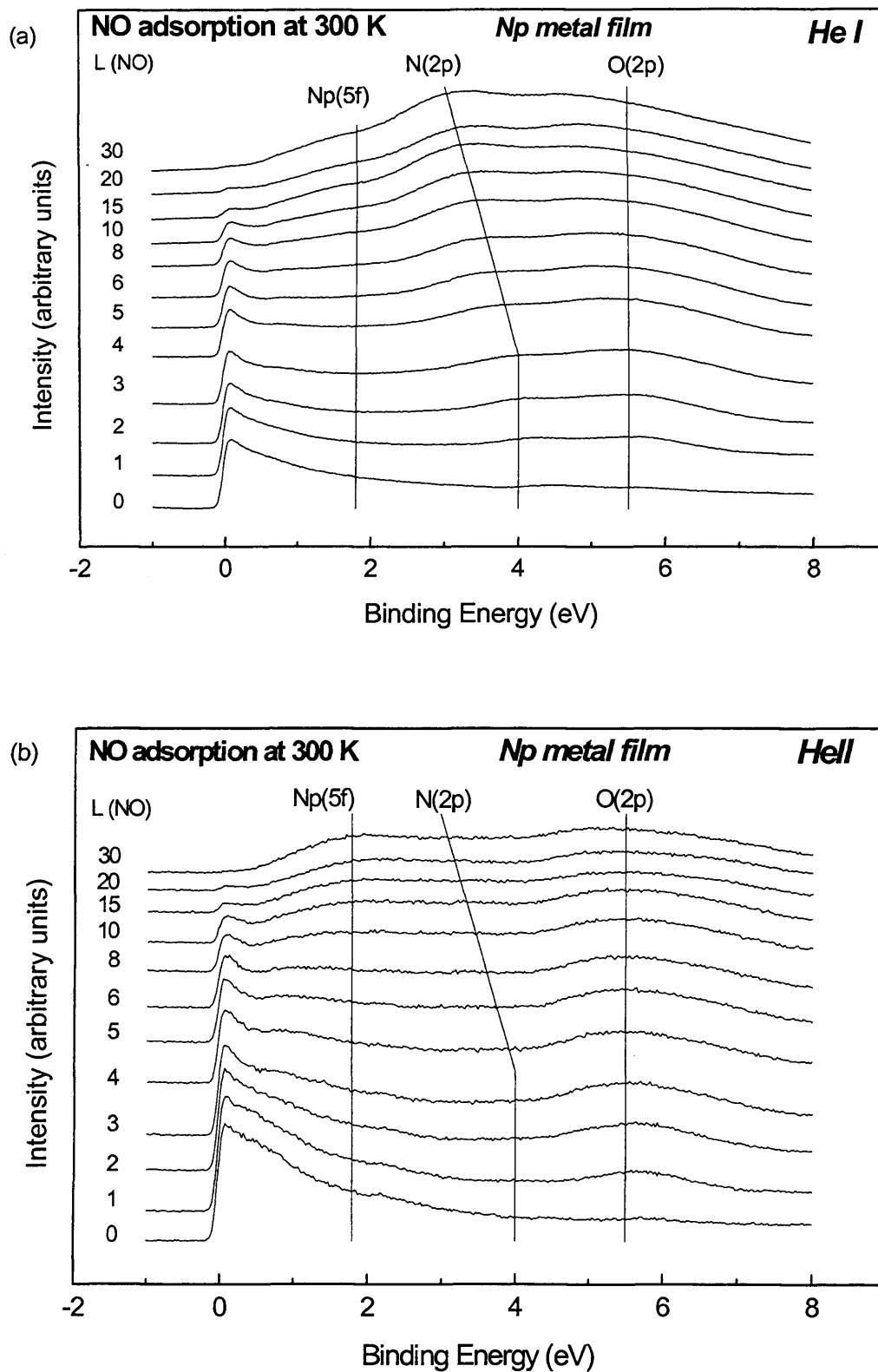


Figure. 5.11. (a) He I spectra for increasing NO exposure at 300 K (He I, $h\nu = 21.2\text{eV}$). (b) He II spectra for increasing NO exposure at 300 K (He II, $h\nu = 40.8\text{eV}$).

and a localized 5f emission at 2.7 eV suggest that it is not NpO_2 . A peak at approximately 4 eV appears in the He I spectra which can just be seen in the He II spectra. This peak is in a position where we expect to see N (2p) states and shifts to a lower BE indicative of nitride formation [16]. The 2p character of this peak is confirmed by the increased intensity in He I spectra compared to the He II. The N (2p) peak is not as pronounced in the He II spectra, when compared to the reactions with thorium and uranium, because of the large number of Np 5f-states, which have a high photoemission cross-section in He II. During initial adsorption the intensity at E_F decreases only slightly.

The decrease in intensity at E_F is accompanied by an increase in intensity at approximately 1.3 eV. Indicating a shift in 5f intensity, confirmed by the suppressed signal in the He I spectra, from itinerant to localized behavior. Further exposure of NO, above 10 L, results in the transfer of 5f intensity from E_F to a broad peak centered at 1.8 eV. Again the suppression of the signal at 1.8 eV in the He I spectrum confirms the 5f character of this peak. The resulting compound following 30 L exposure of NO has no DOS at E_F indicating that all the 5f electrons become localized or take part in bonding with oxygen and nitrogen.

5.3 Discussion

Oxidation of a neptunium surface by di-oxygen results in the formation of two separate oxide species. The data presented here for the formation of an intermediate oxide following exposure to O_2 , agree well with data reported previously for oxidation caused by slow segregation of residual bulk oxygen impurities where the intermediate oxide was assigned as Np_2O_3 [2]. However the original assignment of this surface sesqui-oxide phase was made by comparison with PES data obtained for Pu surface oxidation [4, 5]. It should be noted that, in contrast to the Np-O phase diagram which shows that the sesqui-oxide is not thermodynamically stable, according to the Pu-O binary phase diagram Pu_2O_3 can be prepared as a single phase material [7]. Furthermore, Pu_2O_3 is thermodynamically stable with respect to PuO_2 in the

presence of Pu metal [8], such that thin surface films of PuO₂ undergo a facile auto-reduction to Pu₂O₃ in UHV at room temperature [9].

Attempts were made to isolate, as a single phase, the intermediate oxide species giving rise to the Np (4f_{7/2}) XPS and the valence band peaks centred at 401.2 and 1.3 eV, respectively. Controlled oxygen exposures, at 80 K, afforded similar data to that acquired at room temperature albeit with an enhanced sticking coefficient (discussed below). There was also no change in the photoelectron spectra of a sample that had been pre-exposed to oxygen, so that both surface oxide species were present in the XPS and UPS spectra, and heated to 473 K for short periods. As no change was observed for Np oxidation as a function of temperature, this would imply that the intermediate oxide phase is thermodynamically stable. However, phase diagram studies for the system Np-O [1] show that NpO₂ is the lowest stable bulk oxide of Np and exclude the existence of any oxide with stoichiometry less than NpO₂. If the intermediate oxide was a stable phase of Np it would be expected that a single phase of this material could be prepared. A single phase of the intermediate oxide material however could not be prepared in this study.

The thermodynamic data [13] and the failure to produce a single phase of the intermediate oxide would suggest that the intermediate peaks observed, at a binding energy between the peaks due to Np metal and NpO₂, are due to surface Np (chem) states, associated with a chemisorption phase consisting of Np atoms bonded to less than two oxygen atoms prior to dioxide formation. The spectra obtained and the quantification of the curve fitted Np (4f) peaks (figure 5.12) support the proposal of a chemisorption stage. XPS spectra of the Np (4f) peaks show that the intermediate oxide peak, shifted 1.6 eV, increases in intensity up to approximately 5 L upon which we see the development of the 3.9 eV shifted dioxide 4f peak. A decrease in intensity of the metal peak is accompanied by a decrease in intensity of the intermediate peak, while the dioxide 4f peak continues to increase. The increase in the dioxide peak and the concomitant decrease in the intermediate peak would suggest that the intermediate oxide is a precursor to the formation NpO₂ i.e.

a chemisorption stage. The curve fitted Np ($4f_{7/2}$) peaks (figure 5.12) show clearly the development of the chemisorbed and dioxide phases as well as the decreasing intensity of the metallic well screened peak.

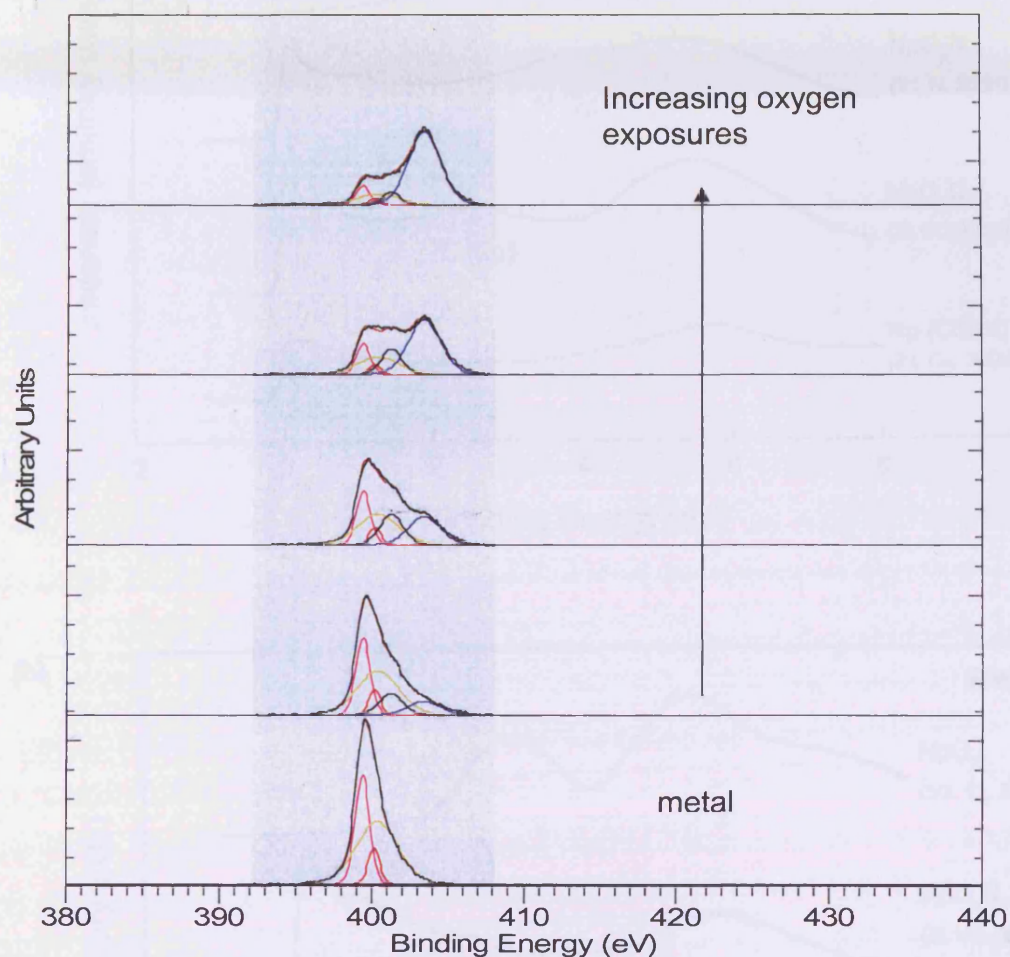


Figure 5.12. Curve fitted Np ($4f$) spectra following exposure to O_2 . The background has already been subtracted from the spectra. Metal: pink, yellow and red. Intermediate oxide: black. Dioxide: blue.

In order to achieve an accurate fit the single asymmetric metal peak was actually fitted with three separate symmetric peaks as this was found to give a better fit than introducing asymmetry parameters. The FWHM, peak position and relative peak areas of these three peaks were locked, once the best fit of the clean metal peak was attained, and then applied to the rest of

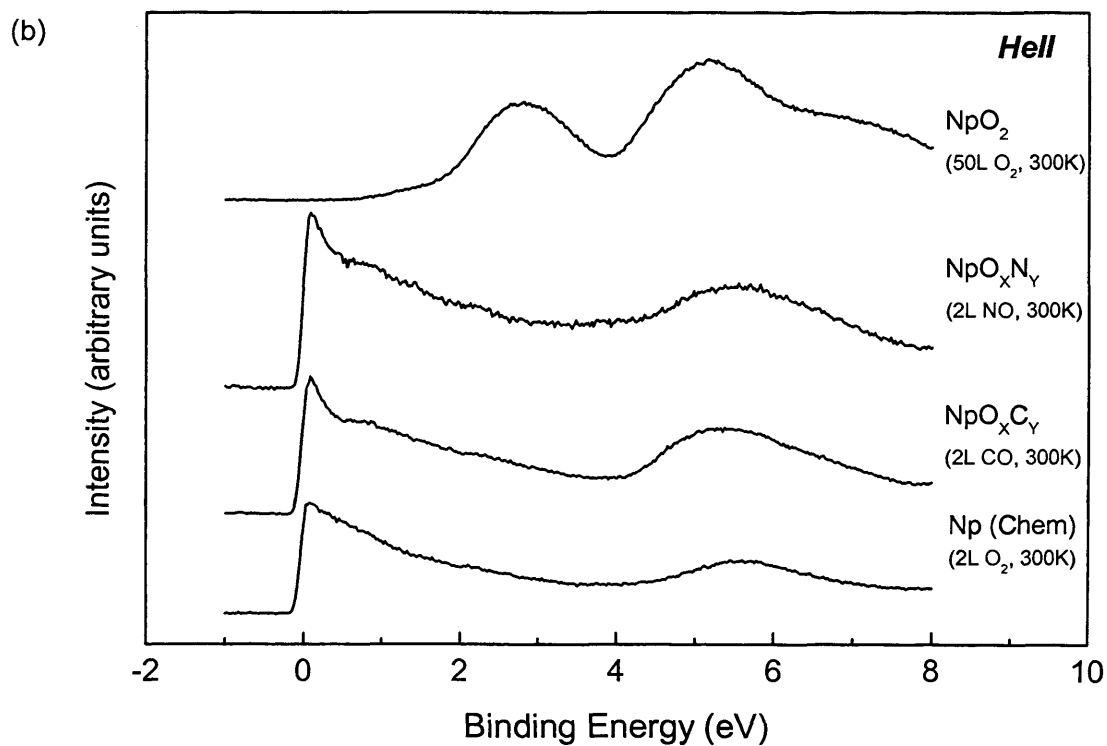
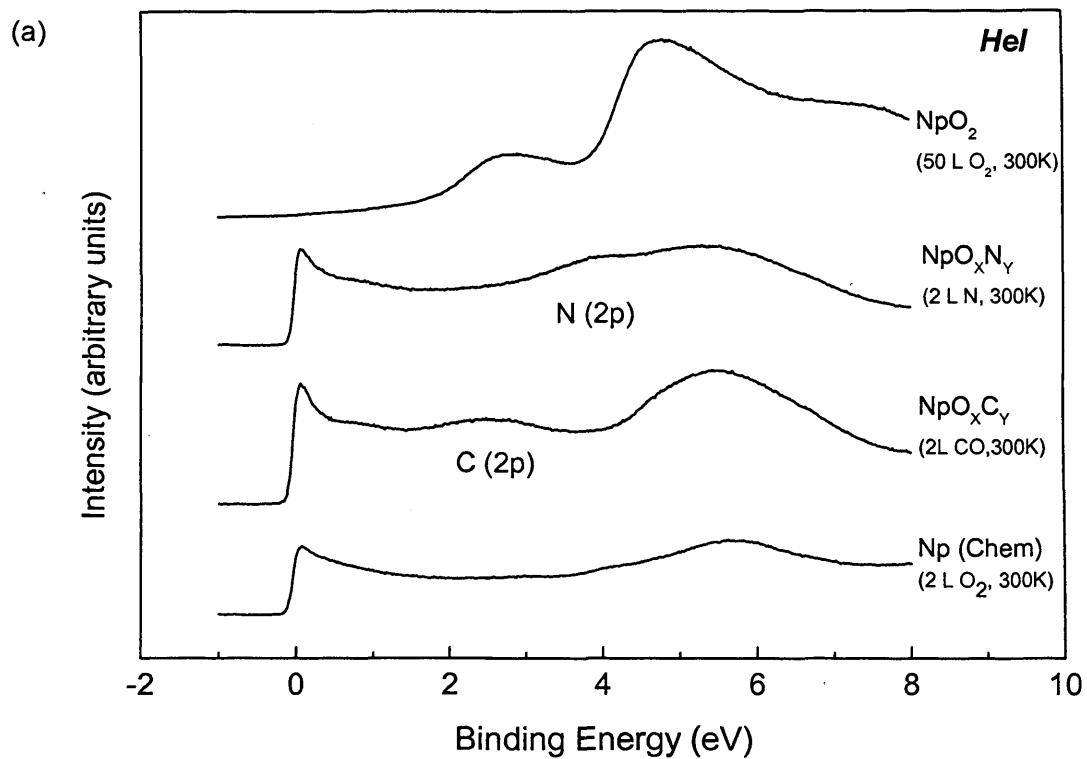


Figure. 5.13. (a) He I spectra of NpO_2 , NpO_xN_y , NpO_xC_y and $\text{Np}(\text{chem})$ (He I, $h\nu = 21.2\text{eV}$).

(b) He II spectra of NpO_2 , NpO_xN_y , NpO_xC_y and $\text{Np}(\text{chem})$ (He II, $h\nu = 40.8\text{eV}$).

the spectra. The intermediate and dioxide 4f peaks were fitted with single symmetric peaks. The position and FWHM of the dioxide peak was ascertained from fitting the spectra following 50 L exposure when the dioxide peak was most intense. The position and the FWHM was then locked and fitted to the other spectra. The intermediate peak position and FWHM was similarly ascertained from the spectra where the peak was most intense and these were locked when fitting to the rest of the spectra.

The UPS spectra (figure 5.13) also support the proposal of a chemisorbed stage. The localized 5f peak, at 1.3 eV, of the intermediate oxide develops along with a sharp symmetrical O (2p) peak typical for chemisorbed oxygen [14] with no trace of the localized 5f peak at 2.7 eV indicative of dioxide formation. Upon the development of the localized peak at 2.7 eV the sharp symmetric O (2p) peak develops intensity at a higher binding energy and begins to resemble the asymmetric O (2p) shape typical for actinide dioxides. Supporting the observations made from the XPS spectra upon development of the dioxide localized 5f peak the localized 5f peak at 1.3 eV and the Np metal emission at E_F begin to decrease in intensity indicating again that the intermediate oxide is a precursor to dioxide formation i.e. chemisorption.

A plausible mechanism is that the chemisorbed state consists of a single layer of oxygen islands which grow to completely cover the surface at approximately 5 L. The onset of oxidation, evidenced by the appearance of Np^{4+} species in the XPS and UPS begins at around 5 L, only after the surface is completely covered by chemisorbed oxygen. From 5 L onwards oxide island nuclei grow to completely cover the surface by ca 50 L (within the information depth of UPS). Quantitative analysis of the curve-fitted Np ($4f_{7/2}$) XP spectra (figure 5.14) suggest three different oxidation stages: a first chemisorption stage up to ~5 L; a second stage when the surface is completely covered by chemisorbed oxygen and dioxide formation begins up to ~20 L exposures; and a third stage characterized by a slow growth where further oxidation is inhibited by oxygen diffusion to the metal gas interface above 20 L.

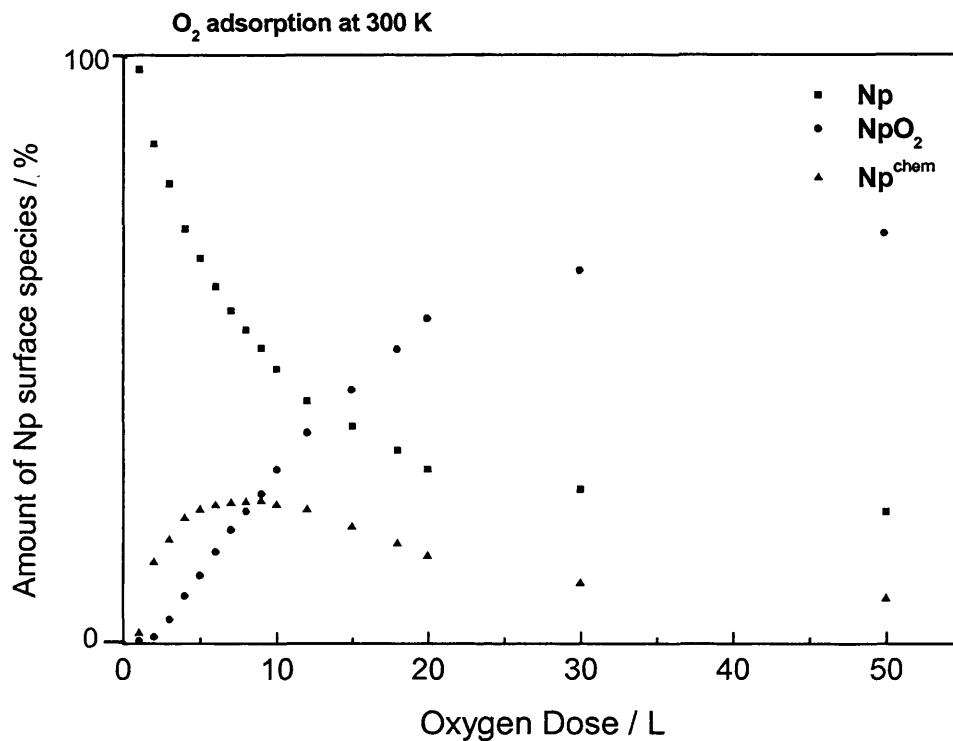


Figure 5.14. O₂ adsorption on Np at 300 K. Evolution of Np (4f) spectral features of NpO_(Chem) and NpO₂

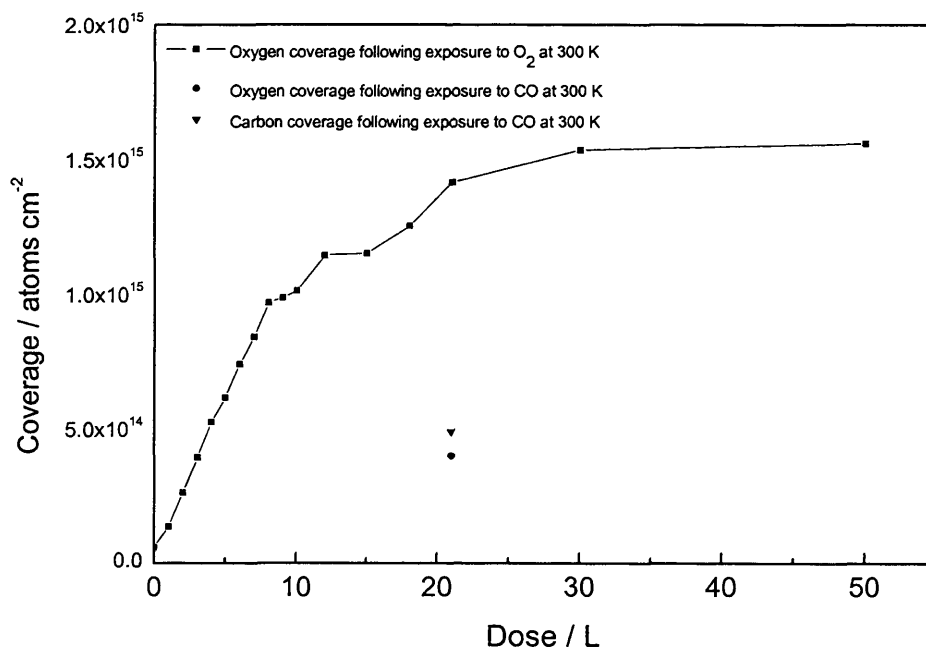


Figure 5.15 Surface coverages following exposure to O₂ and CO

Oxygen coverage calculations (figure 5.15) following oxygen adsorption shows a rapid uptake below 10 L. At approximately 10 L exposure the surface is completely covered by oxygen. Agreeing well with the proposal of a chemisorbed layer growing to cover the surface at approximately 5 L made from analysis of the spectra obtained following exposure to oxygen. The rate of oxidation then appears to slow between 10 and 30 L as the surface begins to oxidize and the oxygen now has to diffuse through the oxide layer to the metal gas interface.

Depth analysis (figure 5.16) shows a similar behavior as described for coverage calculations following exposure to oxygen. A rapid increase in depth is observed up to 10 L at which parabolic behavior appears to begin as the oxygen has to diffuse through the oxide layer produced. A calculated depth of 1.5 nm is consistent with the XPS spectra which show that there is metal within the information depth of XPS at 50 L exposure.

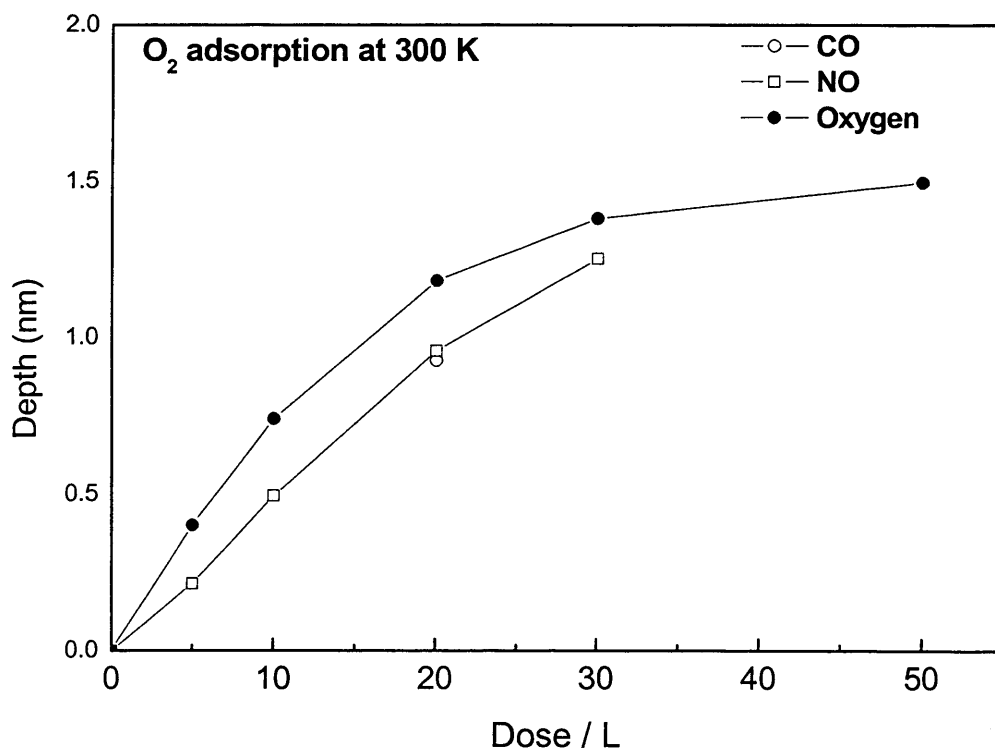


Figure 5.16. Depth of overlayer for increasing doses of O_2 , NO and CO

The spectra achieved in this investigation combined with the thermodynamic data of the Np-O phase diagram support the proposal of a chemisorbed phase. However an unambiguous identification of the intermediate surface oxide as a chemisorbed phase or as previously predicted Np_2O_3 [17] cannot be made without surface structural measurements e.g. XRD.

Exposing the Np surface to O_2 at 80 K afforded similar data to that acquired at room temperature albeit with an enhanced sticking coefficient and hence an increase in the rate of reaction of O_2 compared to the reaction at room temperature. The increased residence time of the molecules results in a greater population of the precursor state (figure 5.17). The residence time (τ) of a physisorbed molecule will depend on the surface temperature and is given by the Frenkel equation [18] ($\tau = \tau_0 \exp(E_a/kT)$), where τ_0 is the period of oscillation of the molecule at the surface). The value of τ_0 is typically 10^{-13} s, yielding a residence time of only 10^{-8} s at room temperature. Decreasing the temperature will increase the value of τ_0 giving $\tau_{100\text{K}} \sim \tau_{298\text{K}} \times 10^8$. Hence there will be a greater number of molecules with the energy required to overcome the barrier to chemisorbed state (E_a). Even at low temperature this energy barrier will be small due to the highly reactive Np surface.

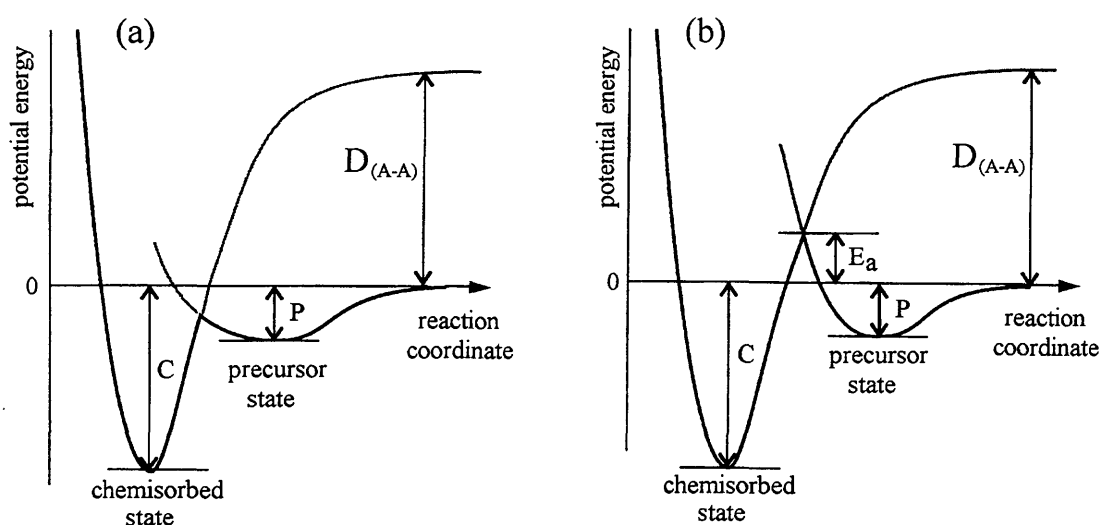


Figure 5.17. Potential energy diagrams for non-activated (a) and activated (b) chemisorption processes

A similar enhanced sticking coefficient and therefore rate of reaction is also observed following exposure to CO at low temperature and a similar explanation is offered.

The reaction of CO with Np at room temperature appears to be similar to the reaction of CO on uranium at 298 K [8] and similarly we believe CO dissociation on Np is followed by formation of an oxycarbide. UPS data (figure 5.13) show the shape of the O (2p) emission following exposure to CO to be narrower and more symmetric than the asymmetric O (2p) peak observed for dioxide formation. However unlike the sharp 1 eV wide O (2p) peak observed for the proposed chemisorbed phase following oxygen adsorption, the O (2p) peak following exposure to CO is approximately 4 eV wide and the shape indicates oxide formation. However as already discussed for oxygen adsorption results NpO_2 is the lowest stable bulk oxide of Np known. Neptunium dioxide formation can be ruled out as the typical broad asymmetric O (2p) band and the localized 5f emission at 2.7 eV associated with dioxide formation are not observed. This indicates the formation of a thermodynamically stable lower oxide of Np. If the oxide produced was not a stable compound we would expect to see further oxidation to the thermodynamically stable dioxide. Therefore it appears that the oxide produced on the surface following exposure to CO is not a stable bulk oxide and is thermodynamically stabilized on the surface by the presence of carbon. As described earlier the spectra show that adsorption of CO results in a C-induced emission which lies at 2.6 eV. The increase in intensity of this peak in the He I compared to the He II spectra confirm the 2p nature of this peak and rule out the possibility of it being from localized 5f emission associated with dioxide formation. We therefore ascribe the 2.6 eV peak following CO adsorption to neptunium carbide or, neptunium oxycarbide. We believe the presence of the carbon on the surface stabilizes the lower oxide as an oxycarbide. Coverage calculations following exposure of CO (figure 5.15) show that approximately half a monolayer of both carbon and oxygen are adsorbed following 20 L exposure. This equates to one monolayer coverage of oxycarbide and would help explain the apparent slowing of the reaction above 20 L observed from the spectra. The CO now has to, similar

to oxygen, diffuse through the surface overlayer to the metal gas interface.

Following exposure at low temperature (80 K); as is the case of oxygen adsorption results, we see an increase in rate of reaction as previously described. However in contrast to the reaction of CO with Pu and U at low temperature (80 K) we see no molecular chemisorption as seen with Pu [3] nor physisorption as observed on U [8]. Only dissociative adsorption to form what is proposed to be an oxycarbide is observed. Molecular CO adsorption would result in a C (1s) peak at approximately 285 eV [19], chemisorbed CO would produce three emission lines at 8.6 and 10.6 eV for the $5\sigma/1\pi$ and 4σ orbitals respectively of chemisorbed CO [20], and physisorbed CO would produce emission lines at 9.4, 12.3 and 15 eV typical for $5\sigma, 1\pi$ and 4σ orbitals respectively of gaseous CO [21]. None of the described emissions typical of adsorbed CO were observed following exposure of Np to CO at 80 K.

The room temperature reaction of NO with Np appears to be similar in many ways to the reaction with CO up to 10 L. Initially up to 10 L dissociative adsorption of NO results in the growth of 4f peak shifted 1.6 eV from the well screened metal peak as was also observed following CO adsorption. UPS results (figure 5.13), again similar to those following exposure to CO, show the formation of an O (2p) peak which cannot be ascribed either to chemisorbed oxygen or dioxide formation. This indicates the formation of an oxide lower in stoichiometry than NpO_2 which, according to the Np-O phase diagram, is not a stable bulk oxide. Nitride or oxynitride formation is confirmed by the presence of an N (1s) peak at 396.3 eV and also an N (2p) band in the UPS spectra. The 2p character of this band is again confirmed by its increased intensity in the He I spectra compared to the He II. Therefore it is proposed that, similarly to the reaction with CO, the presence of nitrogen on the surface stabilizes the otherwise thermodynamically unstable oxide. It has been shown from oxygen adsorption experiments that, without the presence of carbon or nitrogen on the surface, NpO_2 is the lowest stable surface oxide.

Exposures of NO greater than 10 L produce further reaction with the oxynitride surface. This is in contrast to the reaction with CO where the reaction slows and no further change in the spectra is observed. The XPS spectra for NO exposure show the development of a peak shifted 2.6 eV from the well screened metal 4f peak which increases in intensity at exposures above 10 L. This peak is not as shifted as that observed for dioxide formation. An intermediate shift is similarly observed for the proposed oxynitride formation on thorium and uranium following exposure to NO. The UPS spectra also show further change as the itinerant 5f emission at E_F decreases in intensity and by 30 L there are no DOS at E_F . This indicates the 5f electrons have undergone a Mott-Hubbard type transition from itinerant to localized behavior. The localized 5f emission shifts from 1.3 to 1.8 eV upon loss of the itinerant 5f emission at E_F and increases in intensity, indicating increased localization of the 5f electrons upon further reaction with NO. The N (2p) peak shifts to a slightly lower binding energy indicating increased nitride formation. The O (2p) peak however remains almost symmetrical suggesting the further reaction for exposures above 10 L still does not result in dioxide formation at the surface.

Depth calculations (figure 5.16) following exposure of the neptunium surface to NO show a similar trend to that seen following exposure to oxygen. There appears to be a rapid uptake up to 10 L but in comparison to the reaction with oxygen the overlayer depth appears to continue to increase at the same rate up to 20 L. This would agree with the spectra obtained where we see continued reaction and change in the spectra up to 30 L. Above 10 L the spectra show increased 5f localization as the reaction proceeds. In comparison the reaction with CO slows following approximately 20 L exposure and 1 nm depth. No change in the UPS spectra is observed above 10 L and although we have no further XPS data for CO exposures above 20 L it would suggest that the reaction has essentially ceased.

5.4 Conclusion

We have undertaken a study of the oxidation of neptunium thin films using

XPS and UPS. The results obtained here for reaction with O₂ are similar to those reported previously for the surface segregation of dissolved oxygen. An intermediate oxide, with a 4f peak shifted 1.6 eV from the well screened metal peak and a localized 5f peak at 1.3 eV is observed, along with dioxide formation confirmed by the 3.9 eV shift in the 4f peaks and the UPS spectra with localized 5f emission at 2.7 eV together with an asymmetric O (2p) peak typical of actinide dioxide formation. The formation of NpO₂ at oxygen exposures above 5 L and an intermediate species as long as there is metal present at the surface (approximately 10 L in the UPS spectra) is observed. From the spectra collected, quantitative analysis of the XPS data, and thermodynamic data from the Np-O phase diagram [13], we propose the existence of a chemisorbed phase consisting of a layer of chemisorbed oxygen islands which grow to completely cover the surface at ~5 L prior to oxide formation. Exposure to CO results in dissociative adsorption, and in the formation of a surface compound ascribed to be neptunium oxycarbide. The shape of the O (2p) peak suggests the formation of an oxide and not chemisorbed oxygen. However the lack of asymmetry associated with the O (2p) band and no localized 5f emission at 2.7 eV suggest an oxide other than the dioxide. The Np-O phase diagram shows that NpO₂ is the lowest stable Np oxide. Therefore it appears that the oxide formed following exposure to CO is stabilized by the presence of carbon on the surface as an oxycarbide. Adsorption of NO on an Np surface results in dissociative adsorption, and in the formation of a surface compound ascribed to be neptunium oxynitride. Up to 10 L the reaction is similar to that following exposure to CO as we see again lower oxide formation confirmed by the O (2p) in the UPS spectra. As with the presence of carbon, nitrogen on the surface appears to stabilize this oxide. However above 10 L unlike CO, NO reaction proceeds further; a decrease in 5f intensity at E_F and complete localization of the 5f electrons at 1.8 eV is observed.

5.5 References

1. K. Richter and C. Sari, *J. Nuc. Mat*, 1987. **148**. 266.
2. J.R. Naegele and L.E. Cox, *Inorganica Chimica Acta*, 1987. **139**(327-329).
3. T. Almeida, L.E. Cox, J.W. Ward, and J.R. Naegele, *Surf Sci*, 1993. **287/288**(141).
4. D. Courteix, J. Chayrouse, L. Heintz, and R. Babtist, *Solid State Communications*, 1981. **39**. 209.
5. D.T. Larson, *J. Vac. Sci. Technol.*, 1980. **17**. 55.
6. W. McLean, C.A. Colmenares, R.L. Smith, and G.A. Somorjai, *Physical Review B*, 1982. **25**(1). 8-24.
7. T. Gouder, C. Colmenares, J.R. Naegele, and J. Verbist, *Surface Science*, 1990. **235**(2-3). 280-286.
8. T. Gouder, C.A. Colmenares, J.R. Naegele, J.C. Spirlet, and J. Verbist, *Surface Science*, 1992. **264**(3). 354-364.
9. J.G. Dillard, H. Moers, H. Klewenebenius, G. Kirch, G. Pfennig, and H.J. Ache, *Journal of Physical Chemistry*, 1984. **88**(22). 5345-5352.
10. T.Gouder, *Journal of Electron Spectroscopy and Related Phenomena*, 1999. **101-103**. 419-422.
11. L.E. Cox and J.D. Farr, *Physical Review B*, 1989. **39**(15). 11142-11145.
12. B.W. Veal and D.J. Lam, *PHYS REV B*, 1976. **15**(6). 2929-2942.
13. K.Richter and C.Sari, *Journal of Nuclear Materials*, 1987. **148**. 266.
14. T.Gouder, C.Colmenares, J.R.Naegele, and J.Verbist, *Surface Science*, 1990. **235**(2-3). 280-286.
15. L.I. Johansson, *Surf. Sci. Rep.*, 1995. **21**. 177.
16. L.Black, F.Miserque, T.Gouder, L.Havela, J.Rebizant, and F.Wastin, *Journal of Alloys and Compounds*, 2001. **315**(1-2). 36-41.
17. J.R.Naegele and L.E.Cox, *Inorganica Chimica Acta*, 1987. **139**(327-329).
18. J.Frenkel, *Kinetic Theory of Liquids*. 1946: Clarendon Press.
19. T.Almeida, L.E.Cox, J.W.Ward, and J.R.Naegele, *Surface Science*, 1993. **287/288**(141).
20. R.Miranda, K.Wandelt, D.Rieger, and R.D.Schnell, *Surface Science*, 1984. **139**. 430.

21. E.W.Plummer, T.Gustafsson, W.Gudat, and D.E.Eastman, Physical Review A, 1977. **15**. 2339.

CHAPTER 6

Gas Adsorption Studies on Am Metal by Photoemission Spectroscopy

6.1. Introduction

This chapter investigates the surface reactivity of americium metal, and are the first gas adsorption studies on an americium metal surface. Americium provides an interesting contrast to previous studies on thorium, uranium, neptunium and plutonium as it is considered to be the first actinide with completely localized 5f electrons. The transition between itinerant and localized 5f behavior occurs between plutonium and americium. Indeed many of the properties of americium metal support the observation that it is the first rare-earth-like metal in the actinide series [1], supported also by theoretical calculations [2]. The f states in Am are therefore situated close to the border of the intriguing localization (or Mott-Hubbard) transition, which makes their behavior particularly interesting. Indeed, recently it was shown that the Am 5f states are only weakly localized and at increased pressuring the 5f states become itinerant again [3]. Another route towards delocalization could in principle be through hybridization of the 5f electrons with ligand orbitals. This line of research has not yet been pursued. The limited availability and highly radioactive nature of this element has limited the amount of Am compounds synthesized.

Gas adsorption studies involving O₂ and NO have been investigated. The intent of this investigation was to examine the initial stages of reaction with O₂ and NO to determine the extent of involvement of the localized 5f electrons of Am.

6.2. Results

6.2.1. Adsorption of Oxygen

The Am (4f) core-level, O (1s) and valence band photoelectron spectra following exposure of clean Am metal to increasing doses of oxygen at 300K

are shown in figures 6.1, 6.2, 6.3, and 6.4 respectively. The Am (4f) core level photoelectron spectrum from the clean metal is dominated by nearly symmetrical Am ($4f_{7/2}$) and ($4f_{5/2}$) peaks. Each peak is accompanied by a satellite located at approximately 4 eV lower binding energy from the main symmetrical peaks. The peaks are identical to previously reported data for Am metal [4] and are similarly attributed to “poorly” and “well” screened peaks. The main symmetrical peak is attributed to “poor screening” by (6d7s) conduction electrons. The satellite, at 4 eV lower binding energy, is due to “good screening” by 5f electrons; its intensity is weak since the 5f hybridization is poor, i.e., the 5f states are almost completely localized. Screening mechanisms are discussed in more detail by Fuggle et al. [5]. Essentially the 4f photoelectron core hole pulls screening levels, that are not occupied in the ground state (i.e., above E_F), down below E_F into the occupied part of the conduction band. The occupation of these levels, either by 5f or by (6d7s) electrons, lowers the total energy of the final state characteristically; the occupation probability depends on the hybridization with the conduction states in the initial state (5f states delocalized, $4f^{13}5f^7(6d7s)^3$ final states: “well screened” peak at low binding energy; 5f states localized, $4f^{13}5f^6(6d7s)^4$ final state: “poorly screened” peak at higher binding energy). The dominant “poorly screened” peak in Am metal is in contrast to the light actinide metals (Th, U, Np and Pu) where the “well screened” peak dominates the 4f spectra highlighting the itinerant nature of the 5f electrons within the light actinides.

The gradual oxidation of Am by increasing exposures of oxygen results in very little change to the spectra. The main “poorly screened” peak changes very little, the only noticeable change being a slight increase in intensity. Concomitantly, increasing exposures of oxygen result in a gradual decrease in intensity of the “well screened” peak. The peak has almost entirely disappeared by 10 L, and is no longer visible following 25 L exposure. This indicates that the 5f electrons within Am become completely localized and the partial hybridization, leading to the “well screened” contribution to the metal (4f) peaks, no longer exists. Interestingly there is no chemical shift of the Am (4f) peak positions upon oxidation (see “Actinides: An alternative view

on chemical shifts" in appendix 1).

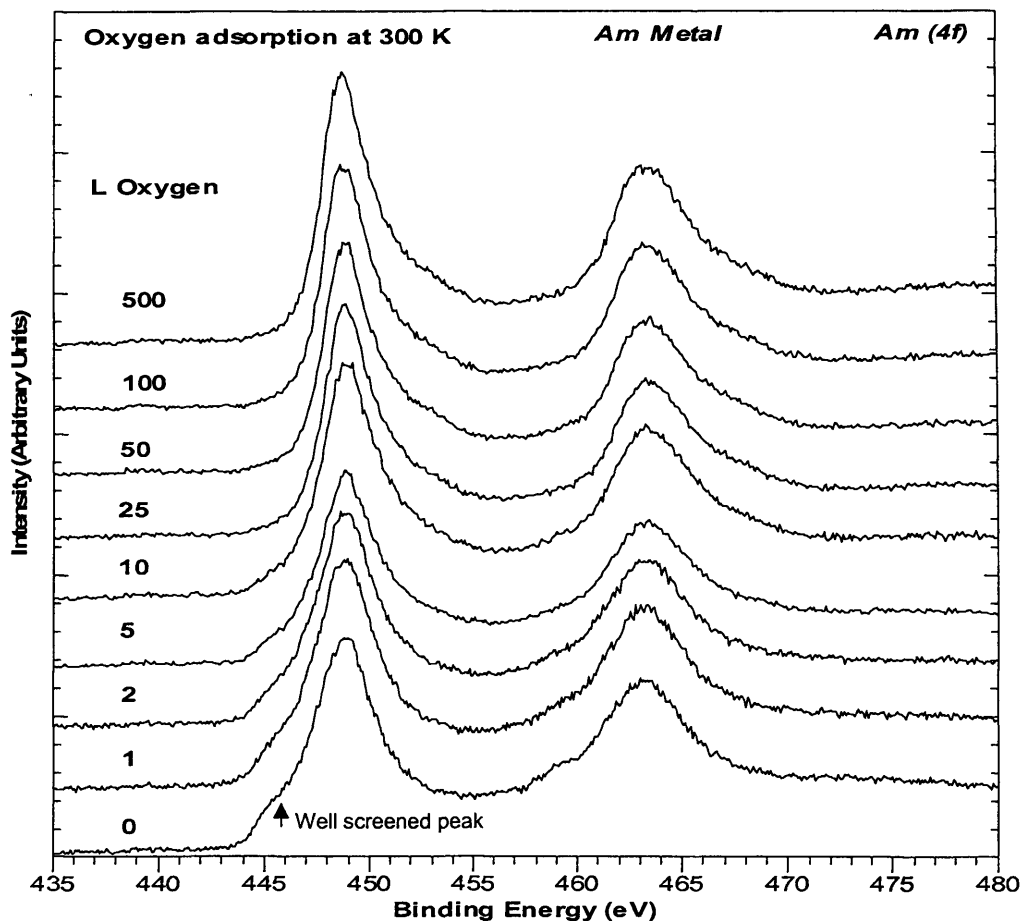


Figure 6.1. Am (4f) core level spectra for increasing surface oxidation of Am metal

No change in the 4f spectra occurs for exposures above 50 L. Indicating that dioxide formation at the Am metal surface does not occur suggesting that under these experimental conditions Am cannot be oxidized to the tetravalent state. The formation of AmO₂ would be expected to be accompanied by the formation of shake-up satellites at higher binding energy typical of actinide dioxide formation [6]. Quantification of the XPS data will provide an indication of the oxidation state achieved following exposures to oxygen (vida infra).

O (1s) spectra recorded following increasing exposures of oxygen are shown in figure 6.2. A single peak positioned at 530.3 eV, associated with oxide formation, increases in intensity in line with increasing exposures of oxygen. A small shoulder on the high binding energy side of the oxide peak arises

and increases in intensity for exposures of 50 L and above. This shoulder is in a position where we would expect to see chemisorbed oxygen, indicating that oxygen adsorbs on the surface but diffusion through the oxide layer and further oxidation does not take place. Subsequent heating of the sample following 500 L exposure, figure 6.3, results in the loss of the high binding energy (chemisorbed oxygen) shoulder of the O (1s) peak. Suggesting the oxygen chemisorbed on the oxide surface desorbs or reacts. As there is no increase in the O (1s) oxide peak nor any change in the Am (4f) spectra it would suggest the chemisorbed oxygen desorbs from the surface when heated to 473 K.

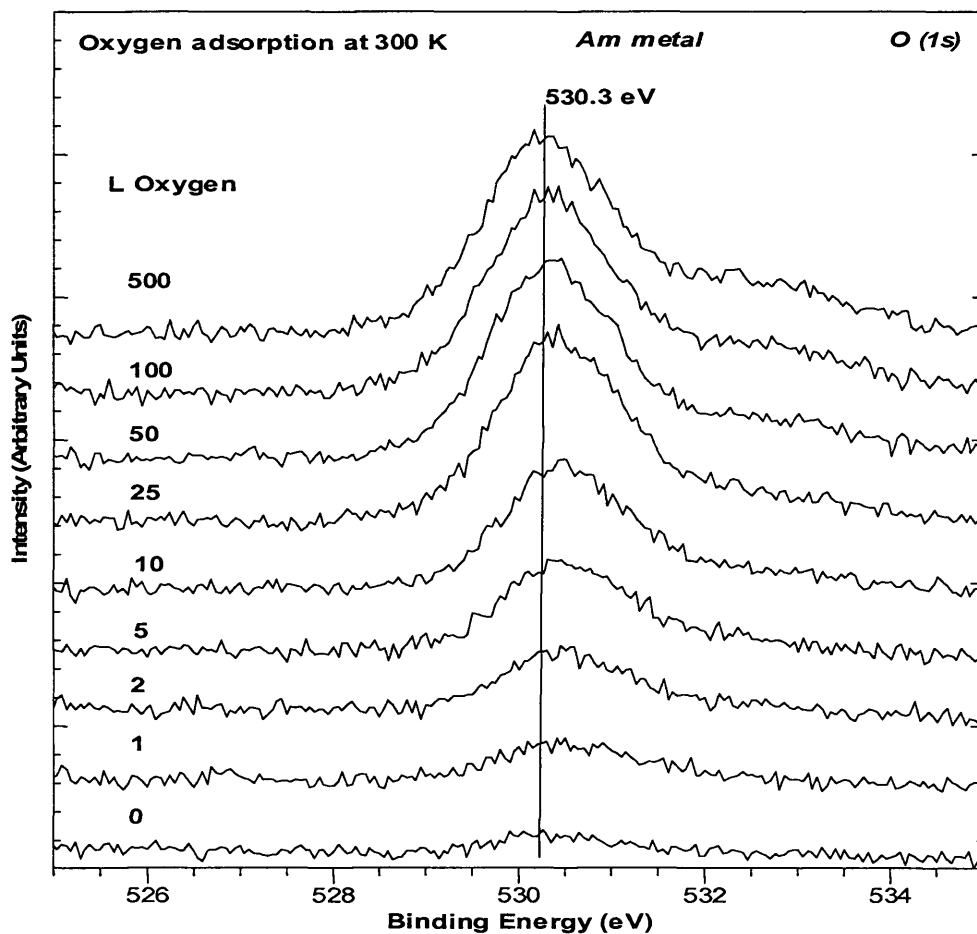


Figure 6.2. O (1s) core level spectra for increasing surface oxidation of Am metal

Valence band spectra have been taken using monochromatic UV radiation from the He I and He II resonances (figure 6.4). The spectra show the 5f level completely withdrawn from the Fermi level. 5f character of the emission around 2.8 eV is confirmed by the decrease in intensity of the corresponding

peaks in the He I spectra. This is a direct verification of 5f electron localization in Am, and is in agreement with previous studies on Am metal [4].

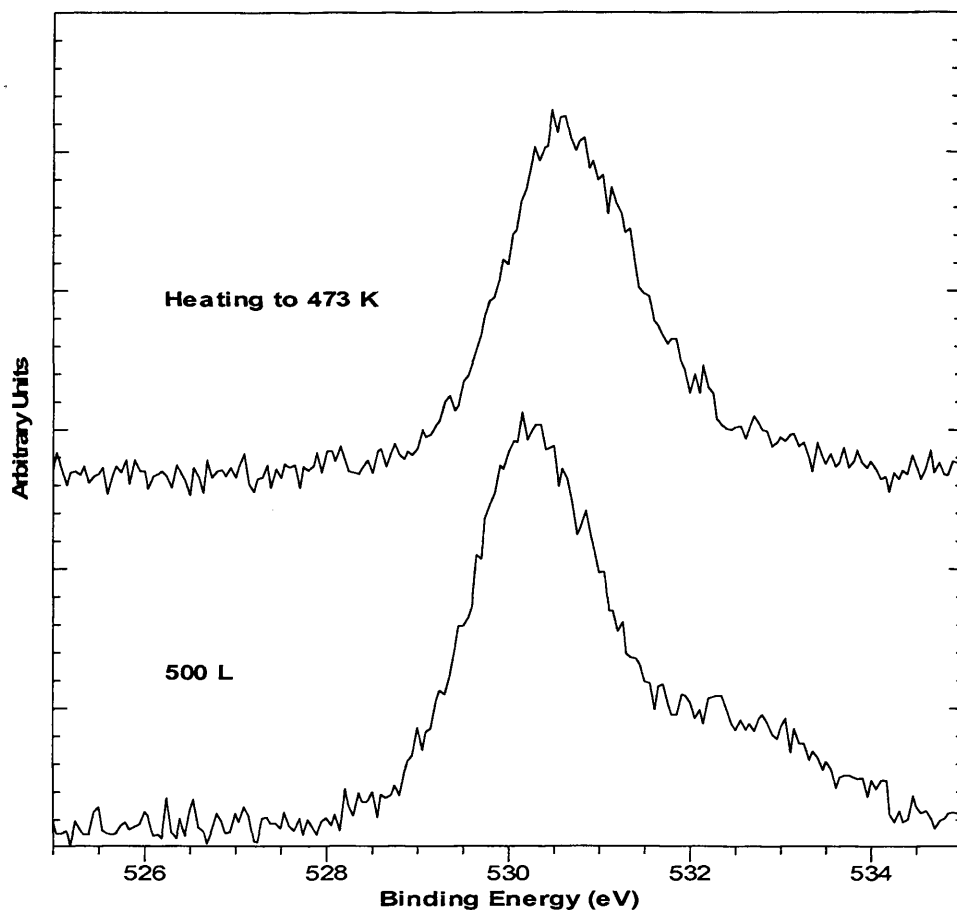


Figure 6.3. O (1s) core level spectra following exposure to 500 L O₂ and subsequent heating to 473 K

Localization of the 5f electrons results in a final-state multiplet structure similar to that observed in the rare-earth metals [7, 8]. The He II spectrum is dominated by a broad double structure at 2 – 3 eV, and a relatively sharp feature at 1.8 eV is clearly resolved. The exact nature of this peak structure is still a matter of debate; however a possible interpretation of the spectra has previously been proposed [9], and provides a plausible explanation of the features observed. This involved a bulk and a surface $f^6 \rightarrow f^5$ contribution which explain the structure between 2 - 3 eV. A divalent surface peak was also proposed ($f^7 \rightarrow f^6$) to explain the feature at 1.8 eV. In the He I spectra there are also features observed close to the Fermi level. These originate from delocalized (spd) conduction electrons which are more clearly seen in

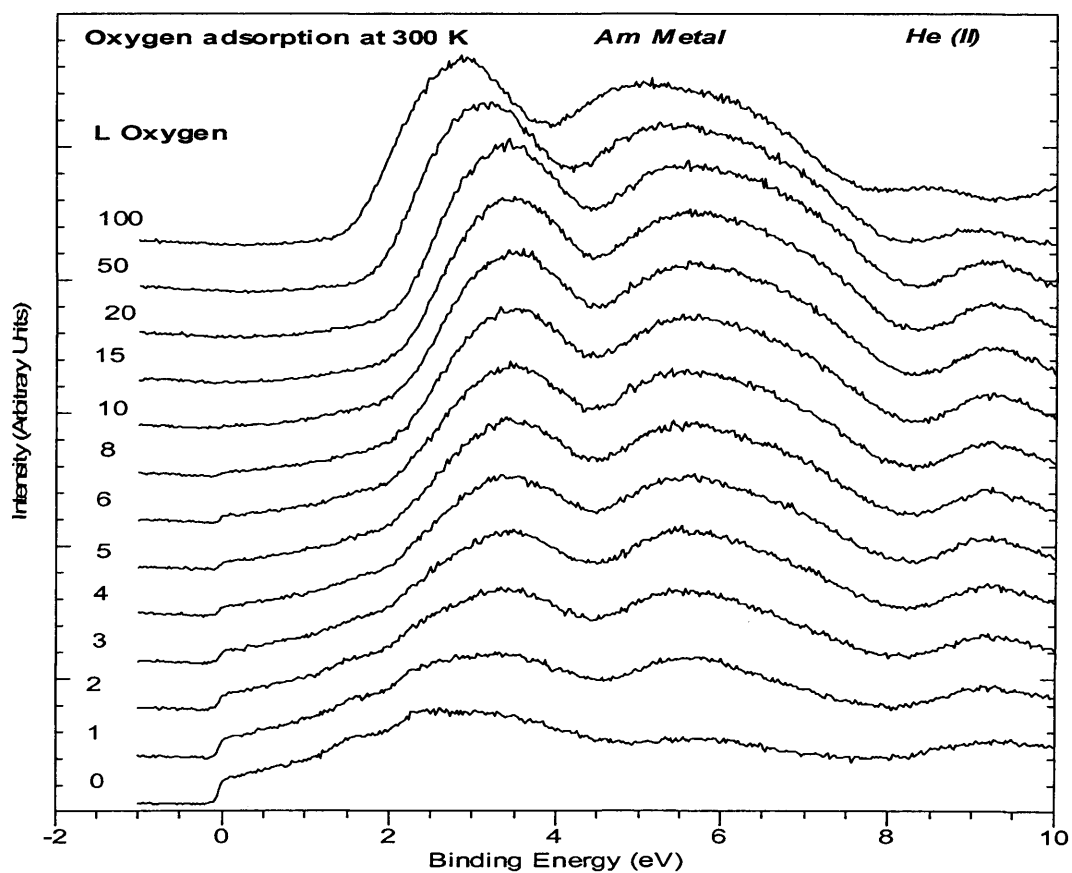
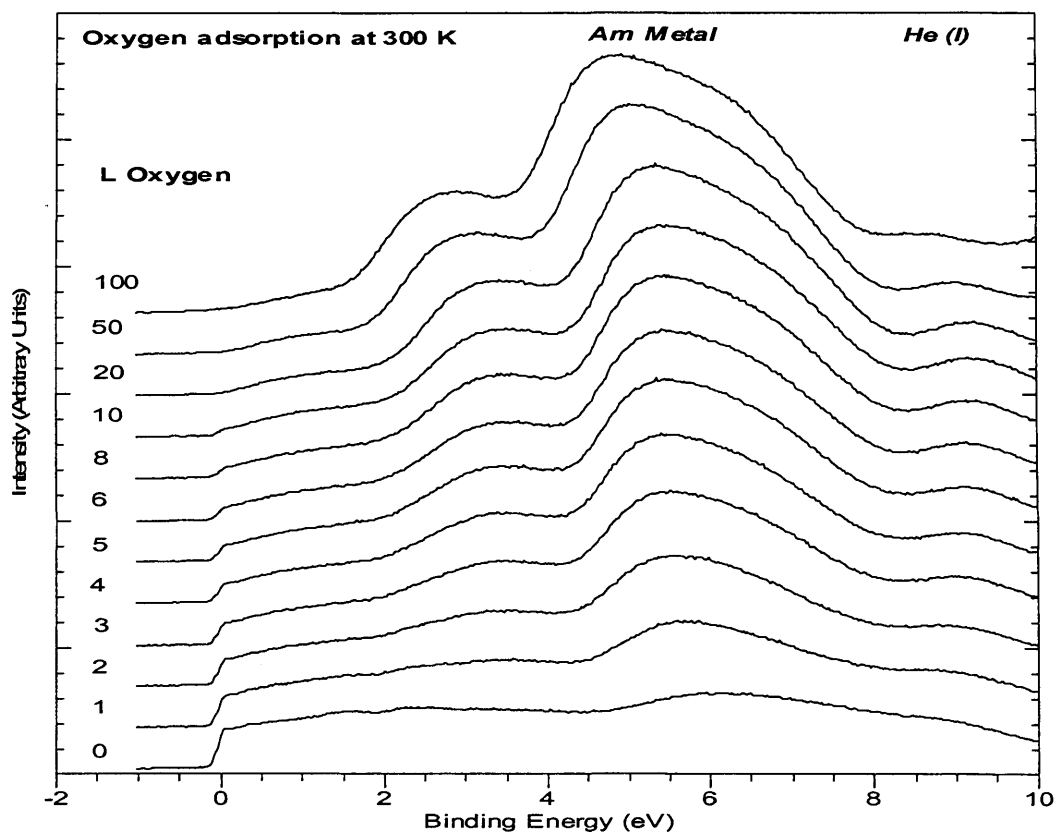


Figure 6.4. UPS spectra, He I and He II, of Am oxidation

the He I spectra because of the decreased dominance of the 5f contribution at these low-photon energies. Upon exposure to increasing doses of oxygen a decrease in intensity of the emission at the Fermi level, and an increase in the localized 5f at 3.5 eV is observed. The intensity of the peak at 3.5 eV is suppressed in the He I spectra confirming the 5f character. The emission at 5.5 eV is due to the presence of oxygen. It is more pronounced in He I than in He II because of the enhanced O (2p) and the reduced Am (5f) photoionisation cross-section in He I. The increase of the O (2p) peak centered at approximately 5.5 eV is accompanied by an increase in intensity of the localized 5f peak.

Complete loss of intensity at the Fermi level, signifying a transfer of all 6d7s conduction electrons into bonding states with the oxygen, essentially stops the reaction and we see no further change in the spectra following increasing doses of oxygen above 20 L. The lack of pronounced asymmetry in the O (2p) band, typical for actinide dioxide formation, indicates that the 5f electrons do not take part in the reaction and oxidation past the trivalent state does not take place.

6.2.2. Adsorption of NO

Figure 6.5 shows the Am (4f) core levels for the reaction with NO at 300 K. The XPS core lines of the clean metal are as previously described, with the main contribution from a poorly screened peak. The shoulder, located at 4 eV lower binding energy, is attributed to a well screened peak.

There appears to be very little change in the 4f spectra following exposures up to 150 L NO, only a decrease in intensity of the “well screened” contribution. The spectra obtained are very similar to that following exposure to oxygen. The main “poorly screened” peak changes very little, concomitantly, increasing exposures of NO result in a gradual decrease in intensity of the “well screened” peak. The peak has almost entirely disappeared by 10 L, and is no longer visible following 20 L exposure. This indicates that again similar to the oxidation reaction the 5f electrons within

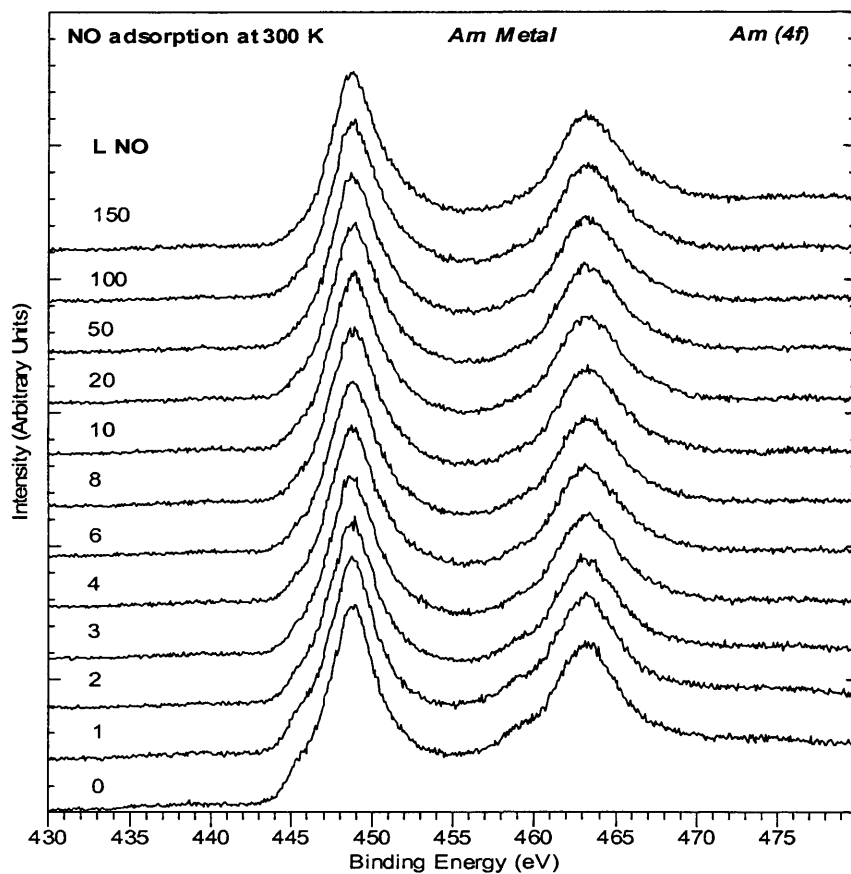


Figure 6.5. Am (4f) core level spectra following increasing exposures of NO

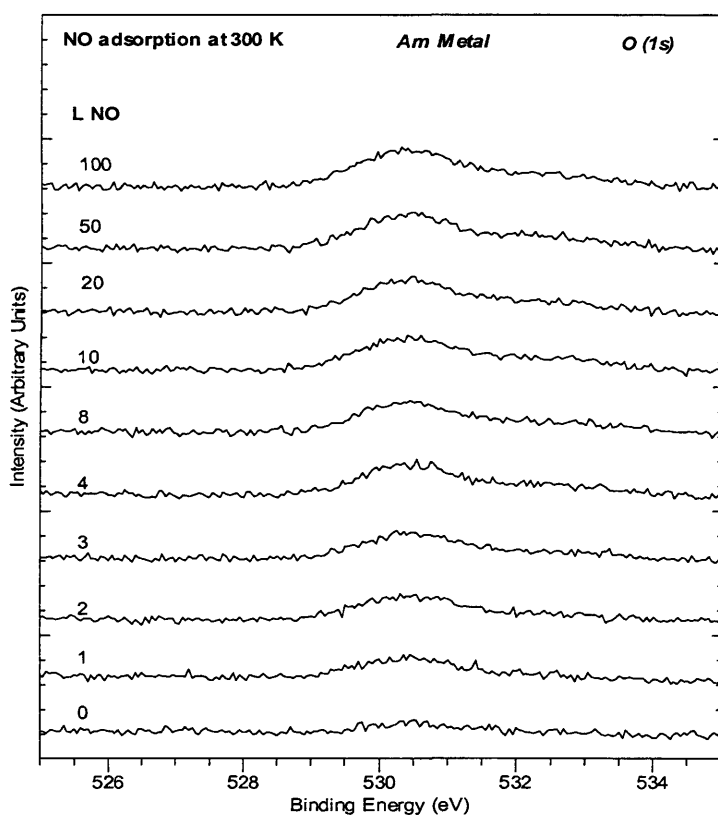


Figure 6.6. O (1s) core level spectra for increasing exposures of NO

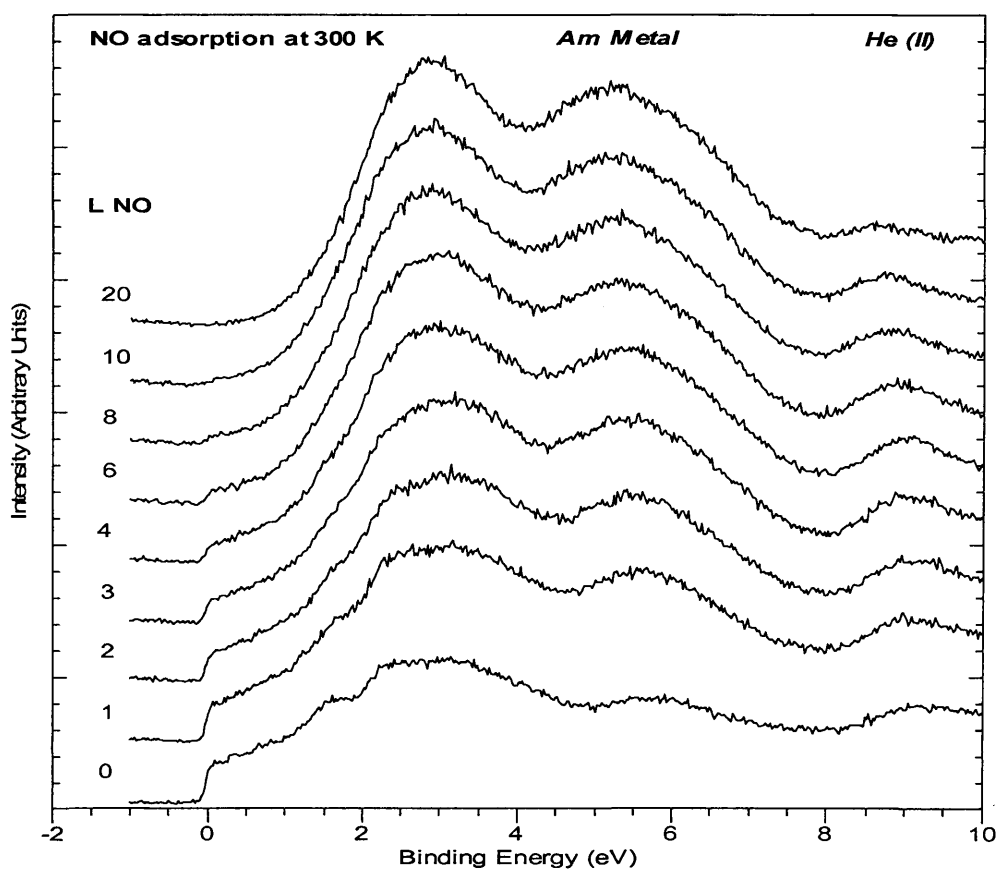
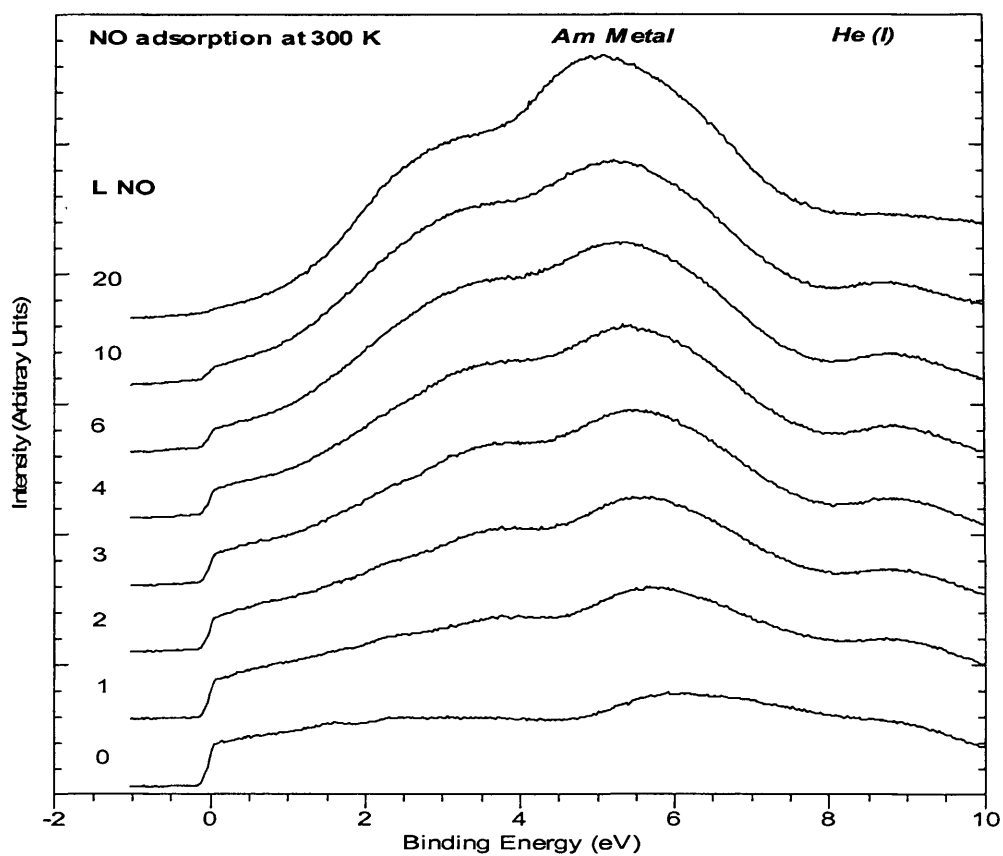


Figure 6.7. UPS spectra, He I and He II, of Am following exposure to NO

Am become completely localized and the partial hybridization, leading to the “well screened” contribution to the metal (4f) peaks, no longer exists.

O (1s) spectra recorded following increasing exposures of NO are shown in figure 6.6. A single peak positioned at 530.3 eV, associated with oxide formation, increases in intensity in line with increasing exposures of oxygen. Similarly N (1s) spectra show a single peak at 396.2 eV associated with nitride formation. The single peaks observed in the O (1s) and N (1s) spectra are indicative of the dissociative adsorption of NO.

Figure 6.7 shows the He I and He II spectra taken following exposure of Am to NO at 300K. The emission at 5.5 eV is due to the presence of oxygen and is from O (2p) levels. A peak at approximately 4 eV appears in the He I spectra, which cannot be seen in the He II spectra due to the dominance of 5f states, is in a position where we expect to see N (2p) states. Again similar to the spectra following oxidation there is a decrease in intensity at E_F as the 6d7s electrons become involved in oxide and nitride formation. This in turn results in the increase in the localized 5f emission at 2.5 eV, not as shifted when compared with 3.5 eV following oxidation. The reaction essentially ceases and no further change in spectra is observed once all 6d7s states are transferred to bonding states, suggesting once more that the 5f electrons do not take part in the reaction.

6.3 Discussion

Oxides of americium are well characterised and a fairly large amount of research has been carried out on them. The di- and sesquioxides of americium are known to exist, but oxides higher than AmO_2 have not been observed [10, 11]. The structure of AmO_2 was determined by Zachariasen [12, 13] to be cubic, fluorite type, analogous with the other actinide dioxides. The sesquioxide, Am_2O_3 , exists in two crystallographic forms. It was first reported by Eyring et al. [14] who heated the dioxide in hydrogen at 600°C and obtained a red-orange coloured product. Its structure was determined by Templeton and Dauben [11] who found it isostructural with the cubic type

rare earth sesquioxides. These workers also reported another sesquioxide prepared by ignition of americium oxalate at 850°C followed by heating in hydrogen at 800°C. The material was pale brown and its structure was hexagonal corresponding to the hexagonal form of the rare earth sesquioxides. The cubic to hexagonal transition has been reported to occur at about 800°C [15]. However oxygen adsorption experiments have not previously been investigated under UHV, and our results suggest that it is not possible to produce the dioxide via oxygen adsorption at 300 K under UHV.

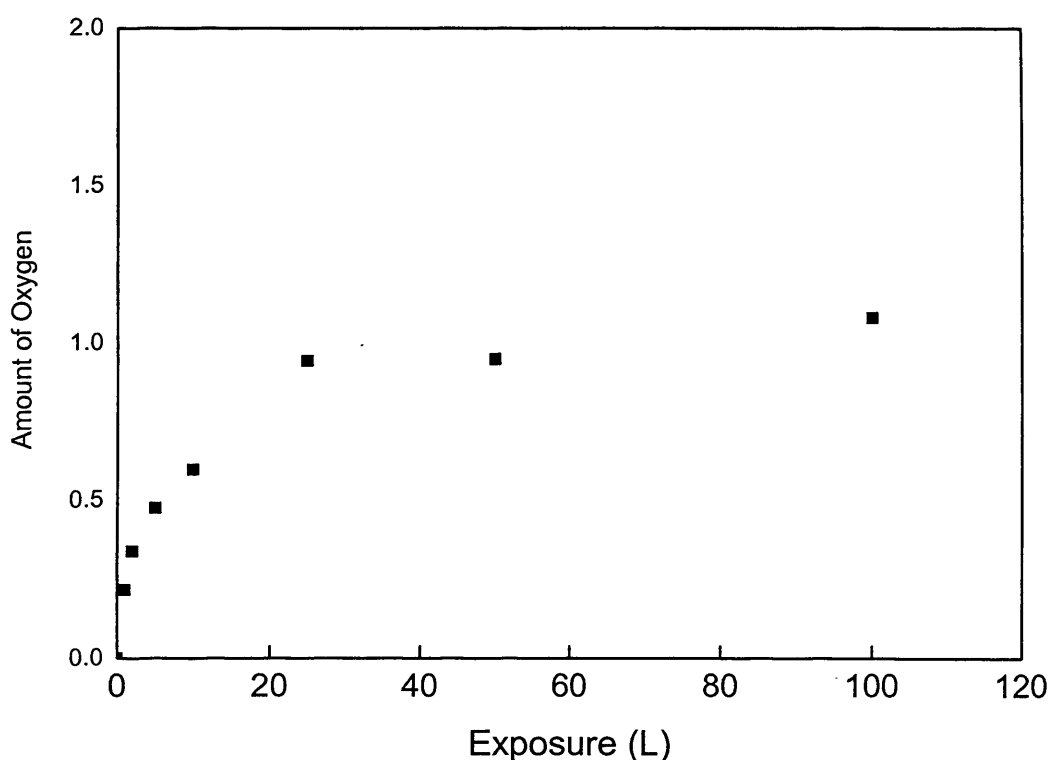


Figure 6.8. O_2 adsorption on Am at 300 K. Amount of oxygen in the stoichiometry of AmO_x

Spectra acquired during this investigation, showing the valence band of Am metal following 50 L exposure of oxygen are in agreement with previously reported spectra of Am_2O_3 [16], prepared by reactive sputter deposition from an Am metal target in an oxygen atmosphere. Localized 5f states of trivalent Am are observed. No conduction band is observed in the vicinity of E_F for Am_2O_3 , in accordance with the expected ionic bonding. Quantification of the XPS data, figure 6.8., supports the spectra in which no indication of oxidation above the trivalent state is observed. Shake up satellites associated with

actinide dioxide formation on the higher binding energy side of the Am (4f) peaks and an asymmetric O (2p) peak in the valence band indicative of dioxide formation are not observed. The ratio of O (1s) to Am (4f) peak areas, corrected for photoionisation cross-section, gives a maximum O:Am ratio of 1.1. The spectra and quantification highlight that it is extremely difficult to push the oxidation state of Am past the +3 oxidation state without using physical methods and forcing oxidation. Oxides of Am have previously been prepared by reactive sputter deposition from an Am metal target in an oxygen atmosphere [17]. AmO₂ formation was observed following oxidation via this method. The shake-up satellites, associated with dioxide formation, are observed in the Am (4f) spectra supporting AmO₂ formation via sputter deposition of Am in an oxygen atmosphere, figure 6.9.

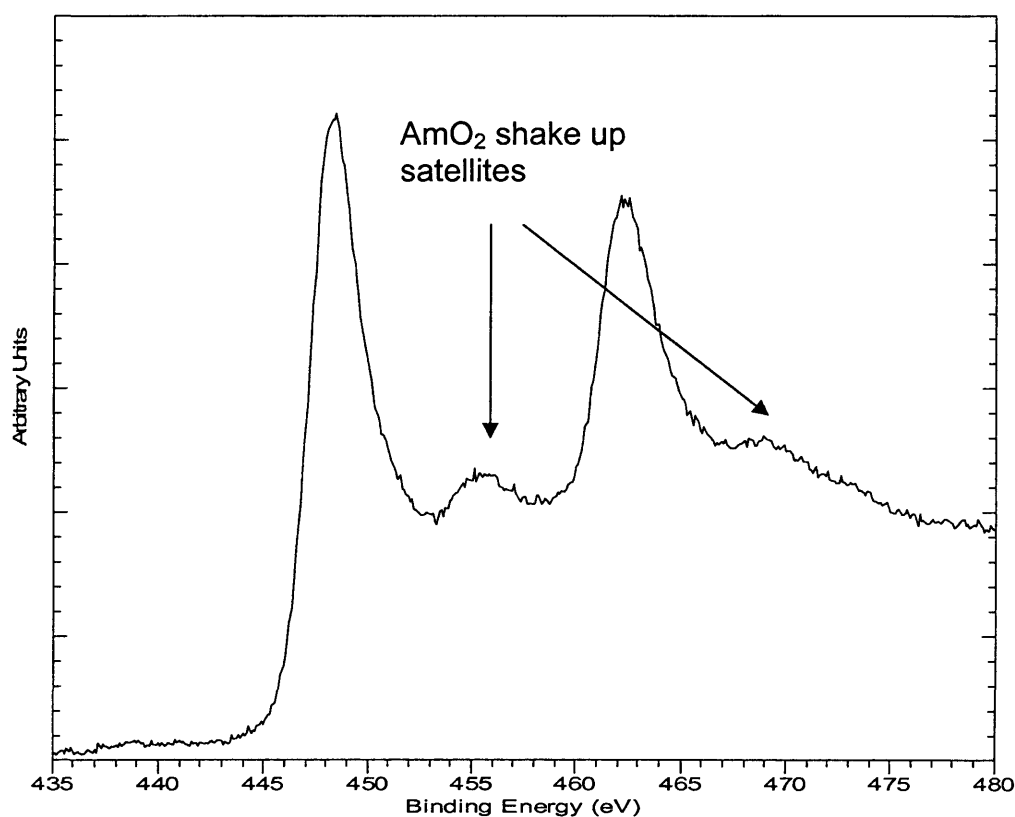


Figure 6.9. Am oxide prepared by reactive sputter deposition from an Am metal target in an oxygen atmosphere[17].

This would indicate that oxidation, following gas dosing, to the dioxide is not thermodynamically viable and can only take place if physically forced conditions are utilised. This suggests that the 5f electrons are completely localised and do not participate in the surface reactions.

Addition of NO results in very similar Am (4f) and valence band spectra to those achieved following oxidation. The Am (4f) region exhibit similar changes associated with the loss of the partially hybridized 5f screening states. Dissociative adsorption of NO is confirmed by the single peaks in the O (1s) and N (1s) indicative of oxide and nitride formation.

However with closer inspection especially of the valence band there are noticeable differences associated with the presence of nitrogen on the surface. An increase in intensity at approximately 4 eV in the He I spectra associated with N (2p) states supports the N (1s) spectra and confirms the presence of nitrogen adsorbed on the metal surface. Also in comparison to the valence band spectra following oxidation, where a large separation between the localized 5f emission and E_F is observed confirming the oxide formed is an insulator, the 5f states are situated at approximately 2.5 eV compared to 3.5 eV following oxidation. The UPS spectra show the 5f electrons following exposure to NO to be localized, i.e., withdrawn from E_F , but located closer to E_F when compared to the spectra following exposure to oxygen. This would indicate a slightly more covalent type bonding than the ionic bonding predicted for the surface oxide formed following oxidation studies.

6.4 Conclusion

We have undertaken a study of the oxidation and reaction with NO of americium thin films using XPS and UPS. The formation of Am_2O_3 is observed and it was found that it is not thermodynamically viable to produce a higher oxidation state of Am via gas dosing (at 300 K under UHV). The oxide formed is an insulator. Adsorption of NO on the surface results in the dissociative adsorption of N and O, and in the formation of a surface compound which is again an insulator. However the 5f electrons are slightly less withdrawn from E_F than following oxygen adsorption. The gas dosing experiments performed indicate that the Am (5f) electrons do not participate in surface reactions and bonding.

6.5 References

1. H.L.Skriver, O.K.Andersen, and B.Johannsson, Physical Review Letters, 1980. **44**. 1230.
2. H.L.Skriver, O.K.Andersen, and B.Johannsson, Physical Review Letters, 1978. **41**. 42.
3. S. Heathman, Phys. Rev. Lett., 2000. **85**. 2961.
4. J.R.Naegele, L.Manes, J.C.Spirlet, and W.Muller, Physical Review Letters, 1984. **52**(20). 1834.
5. J.C.Fuggle, M.Campagna, Z.Zolnierok, R.Lasser, and A.Platau, Physical Review Letters, 1980. **45**. 1597.
6. J.M.Fournier, Actinides - chemistry and physical properties, Structure and Bonding, 1985. **59/60**. 127 - 196.
7. J.K.Lang, Y.Baer, and P.A.Cox, Journal of Physics F, 1981. **11**. 121.
8. F.Gerken, Journal of Physics F, 1983. **13**. 703.
9. N.Martensson, B.Johannsson, and J.R.Naegele, Physical Review B, 1987. **35**. 1437.
10. J.J.Katz and D.M.Gruen, Journal of the American Chemical Society, 1949. **71**. 2106.
11. D.H.Templeton and C.H.Dauben, Journal of the American Chemical Society, 1953. **75**. 4560.
12. W.H.Zachariasen, Physical Review, 1948. **73**. 1104.
13. W.H.Zachariasen, Acta Crystallogr, 1949. **2**. 388.
14. L.Eyring, H.R.Lohr, and B.B.Cunningham, Journal of the American Chemical Society, 1952. **74**. 1186.
15. J.C.Wallmann, Journal of Inorganic and Nuclear Chemistry, 1964. **26**. 2053.
16. T.Gouder, P.M.Oppeneer, F.Huber, F.Wastin, and J.Rebizant. in 34^{emes} Journees des Actinides. 2004. Heidelberg.
17. T.Gouder and F.Huber, Personal communication, 2005

CHAPTER 7**Conclusion**

7.1 Introduction

This chapter compares and contrasts the data of the light actinides presented in this thesis. The effect of itinerant/localised bonding behaviour, of the 5f electrons, with respect to surface reactivity is discussed.

The photoemission spectra of actinide metals and dioxides have been extensively studied and compared previously [1], and therefore will not be discussed here. This chapter will concentrate on a comparison of the surface reactivity of thorium, uranium, neptunium and americium metal surfaces separately with oxygen and NO.

7.2 Actinide Oxidation

The simplest surface reaction is the adsorption of oxygen to afford the binary metal oxides. There have, however, been no previous studies of oxygen adsorption on neptunium and americium. It is now possible to compare and contrast the oxidation (oxygen adsorption studies on the clean metal surfaces) of thorium, uranium, neptunium, and americium.

We will initially compare how oxide depth varies as a function of oxygen exposure for Th, U, Np and Am (figure 7.1). Oxide depths were calculated as described previously (Chapter 2 – Experimental).

After 5 L exposure uranium shows the thickest oxide layer, followed by thorium. Neptunium and americium appear to oxidise at a very similar, however slower rate when compared to uranium and thorium. Parabolic behaviour associated with diffusion controlled reaction appears to set in earliest following the reaction with Th at 5 L. Uranium oxidation begins to slow down at 10 L and levels off at 25 L. Neptunium is slightly different as we see a much slower and gradual levelling off; in fact the oxide layer growth is almost

linear up to 50 L. It is difficult to ascertain when the slowing down of oxide layer growth occurs for americium as the metal peak (the “well screened” peak was used as indication of metallic presence within the information depth of XPS) is no longer visible above 10 L in the spectra and therefore depth analysis cannot be carried out.

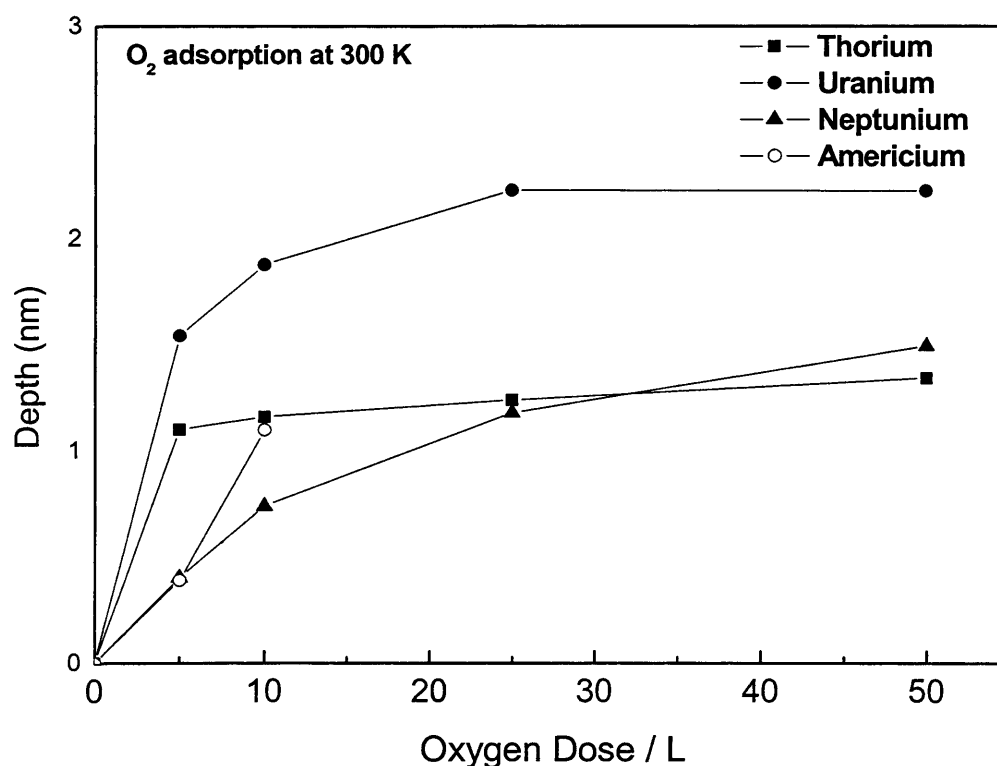


Figure 7.1. A graph showing oxide depth as a function of oxygen exposure.

Uranium oxidation proceeds at the fastest rate, and to the most extent, this can be related to the availability of the 5f electrons for reaction. Itinerant 5f electron involvement increases the rate of reaction with uranium when compared to thorium, which does not have 5f occupation. However neptunium does not appear to show the same high surface reactivity, due to involvement of itinerant 5f electrons, towards oxygen as might be expected. This may be related to the chemisorbed phase which occurs prior to oxidation as discussed previously (chapter 5). Initially it appears from the spectra that only the Np 6d7s electrons are involved in bonding to the chemisorbed oxygen. The 5f electrons experience a slightly greater nuclear charge, as the 6d7s electrons are involved in bonding, and become slightly more localised. This can be

related to the sensitivity of the 5f states to increases in the core potential upon oxidation. The 5f states become localized and further ionization (necessary for formation of higher oxidation states), becomes more difficult. Island growth may slow the initial reaction and therefore decrease the rate of oxidation which would explain the slower, almost linear rate at which the oxide depth increases.

Localisation of the 5f electrons at americium would suggest a less reactive surface when compared to uranium and neptunium. Both thorium and americium surface reactivity involves only the 6d7s valence electrons. Thorium has a valence electron configuration of $6d^27s^2$ and readily forms the tetravalent dioxide. Americium in contrast is dominated by the trivalent state and was shown (chapter 6) to only form the sesquioxide following oxygen exposures at room temperature under UHV. Slower oxidation of thorium when compared to uranium is related to the lack of 5f participation. The availability of the Th (6d7s) valence electrons and the willingness to form the dioxide accounts for the increased thorium oxide depth when compared to neptunium and americium. Both neptunium and americium oxidation initially involves solely the 6d7s electrons and the formation of in both cases approximately a trivalent oxide species. However the 5f electrons within neptunium although partially localised are still available for reaction and the dioxide is formed. In contrast the 5f electrons within americium are completely localised and do not take part in the reaction, hence only the sesquioxide is formed.

The He II spectra (figure 7.2) help to explain and enhance the understanding of what the data in figure 7.1 have shown. The asymmetric O (2p) band shape is the same for all the dioxides formed, ThO_2 , UO_2 and NpO_2 . The lack of pronounced asymmetry in the O (2p) band following oxidation of americium indicates that the Am (5f) electrons do not take part in the reaction and oxidation past the trivalent state does not take place at room temperature under UHV. The intensity of the band closest to E_F in the U, Np, and Am spectra reflects the localised 5f population. No 5f band is observed for thorium as it has no 5f occupation. The 5f band moves closer to the O (2p) band in going from U to Am. This highlights that the 5f electrons are growing more and

more core like as we move across the light actinides. He II spectra of oxygen adsorption on a Pu surface at 77 K [2] shows a similar trend. The localised 5f band is positioned at 2.5 eV and shows a gap between the 5f and the O (2p) band which appears to be intermediate between the results presented here for Np and Am. The increasing core like behaviour of the 5f electrons, upon oxidation, across the period would indicate a reason for the decreased rate and extent of oxidation for Np and Am when compared to uranium.

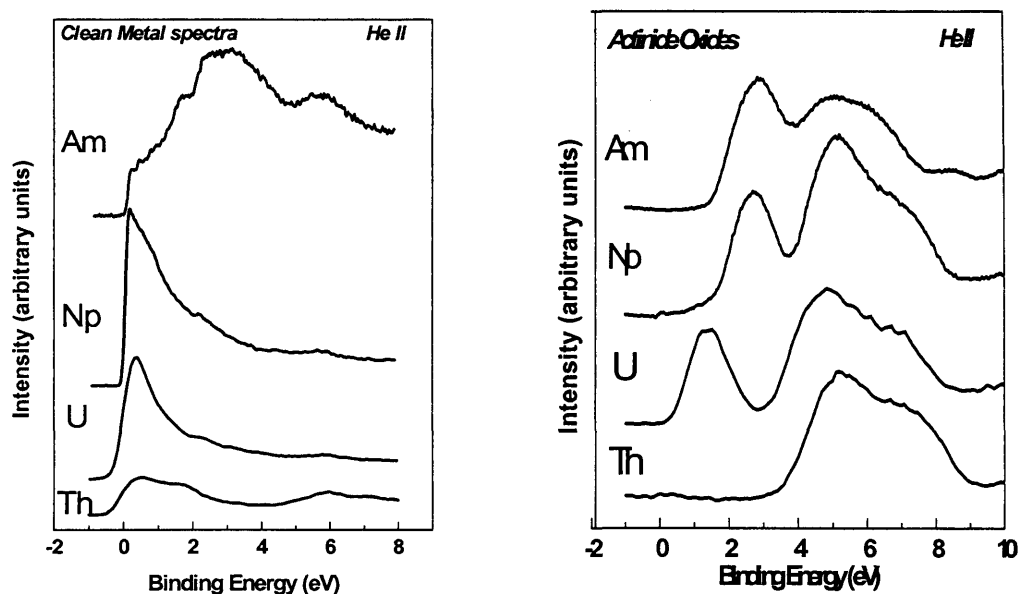


Figure 7.2. UPS He II spectra of Th, U, Np and Am metals and following exposure to oxygen (100 L).

Shake up satellites observed in the 4f spectra (figure 7.3) for thorium, uranium and neptunium after exposure to oxygen, are characteristic of actinide dioxide formation. In all cases the satellite is located at approximately 7 eV higher binding energy to the $4f_{5/2}$ and $4f_{7/2}$ peaks. Approximately similar separations between the 4f peaks and satellites have been reported previously [3]. The similar separation between the 4f peak and the satellite for all three dioxides would suggest a similar separation between the O (2p) band and the unoccupied or incompletely occupied orbital to which the shake up occurs. Inverse photoelectron spectroscopy may hold the answer to this and confirm the separation between the O (2p) and the unoccupied band. Americium does not have these typical shake up satellites following oxidation (under identical conditions), indicating the lack of AmO_2 formation. Trivalent Pu oxide in

comparison to plutonium dioxide also does not have shake up satellites associated with the Pu (4f) peaks [4]. From this and knowledge of the Am-O binary phase diagram it is possible to infer that the Am oxide is the bcc alpha sesquioxide.

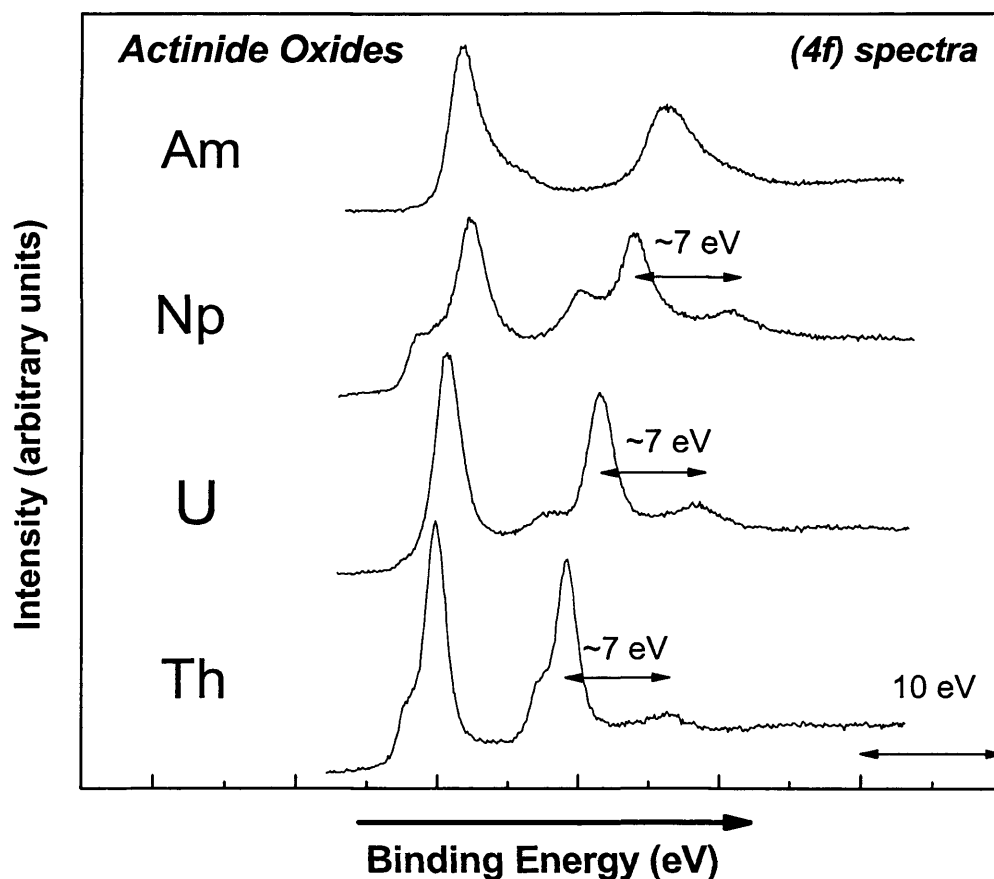


Figure 7.3. (4f) core level photoemission spectra of Th, U, Np and Am following exposure to oxygen (100 L).

7.3 Reaction with NO

The reaction of NO with actinide metal surfaces allows again the possibility to compare and contrast 5f electron involvement in surface reactions and bonding across the light actinides. The surface reactivity of thorium, uranium, neptunium and americium metal separately with NO has not previously been investigated.

Figure 7.4 shows a plot of over layer depth as a function of increasing NO exposure. Initially, up to 10 L, the reaction with americium proceeds quickest and appears to show the highest surface reactivity towards NO. The overlayer depth however levels off at 10 L and no further increase in depth is observed. Americium is the only metal which shows the same increase in depth following exposures of oxygen and NO.

Thorium, uranium and neptunium proceed slowly below 5 L. Thorium then reacts rapidly and a large increase in over layer depth is observed between 5 and 50 L. Uranium and Neptunium both react in a similar manner up to approximately 25 L showing an almost linear increase in depth as a function of exposure. Uranium continues to linearly increase up to 50 L; however neptunium begins to level off between 25 and 50 L exposure.

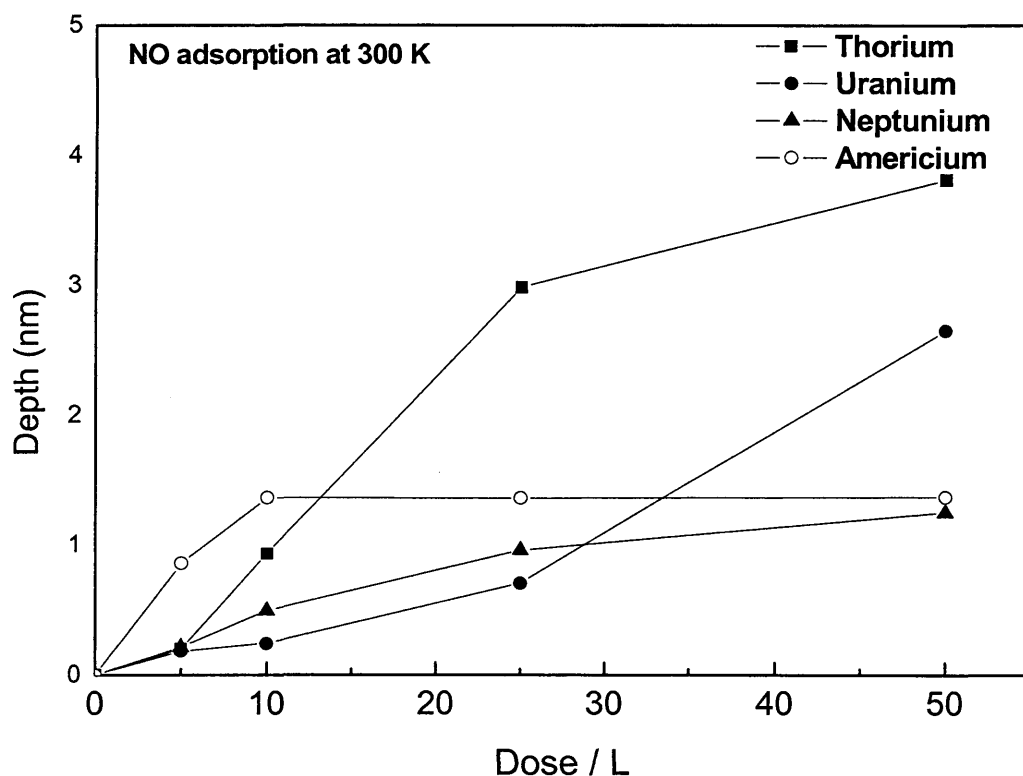


Figure 7.4. A graph showing oxide depth as a function of NO exposure.

The slower increase in depth as a function of exposure of NO observed for the reactions with thorium, uranium and neptunium when compared with the oxygen reactions can be related to the relative bond strengths (O-O 498.3

kJ/mol, N-O NO 630.6 kJ/mol). This allows a thermodynamic insight into the possible reaction pathways and offers an explanation for the increase in rate observed for oxygen exposure when compared to exposure of NO.

The anomalous behaviour of americium may be due to the difficulty in deciphering the exact metal contribution to the Am (4f) peak due to the complications arising from the screening processes associated with Am having localised 5f electrons.

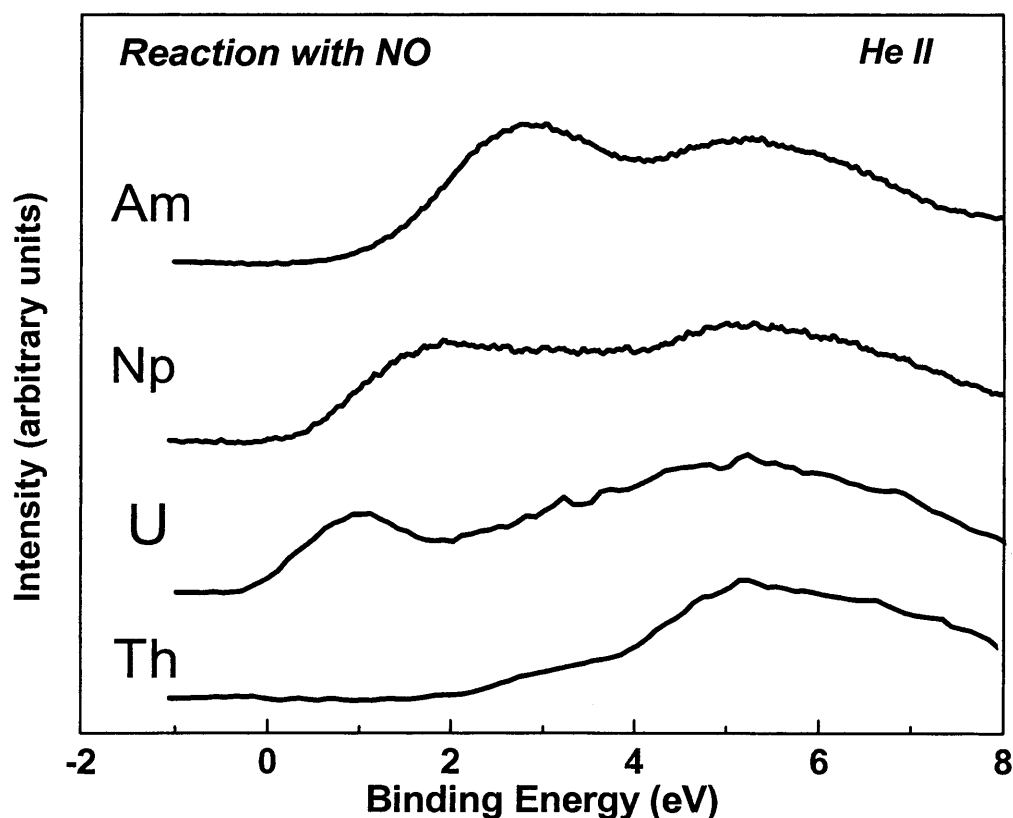


Figure 7.5. UPS He II spectra of Th, U, Np and Am following exposure to NO (100 L).

Figure 7.5 shows the He II data acquired for the reaction with NO after 25 L exposure. These spectra support the depth plot and the increasing localisation behaviour of the 5f electrons across the period resembles the oxidation behaviour observed for oxygen exposures. The reaction with thorium is the only reaction where an asymmetric O (2p) peak is observed. In all four spectra the O (2p) peak is centred at approximately 5.5 eV. Uranium, neptunium and americium all show symmetric O (2p) shapes. This would indicate that it is only

following exposure of a thorium surface to NO that we observe dioxide formation on the surface. Uranium, neptunium and americium are all limited to lower oxide formation. Lower oxides of uranium and neptunium, which are not thermodynamically stable, are stabilized by the presence of nitrogen on the surface.

The increasing core like behaviour of the 5f electrons across the period is reflected in the shift of the 5f band shifts closer to the O (2p) band, from uranium to americium. This would account for the decreased surface reactivity of neptunium when compared to uranium. The availability of the 5f electrons for reactions decreases and therefore a decrease in surface reactivity upon increasing exposures of NO is observed. As the 6d7s electrons become involved in metal-nitrogen and metal-oxygen bonding, the 5f electrons experience an increased core potential and become localised in uranium and neptunium. The greater nuclear charge on neptunium compared to uranium produces the increased core like behaviour of the 5f electrons within Np.

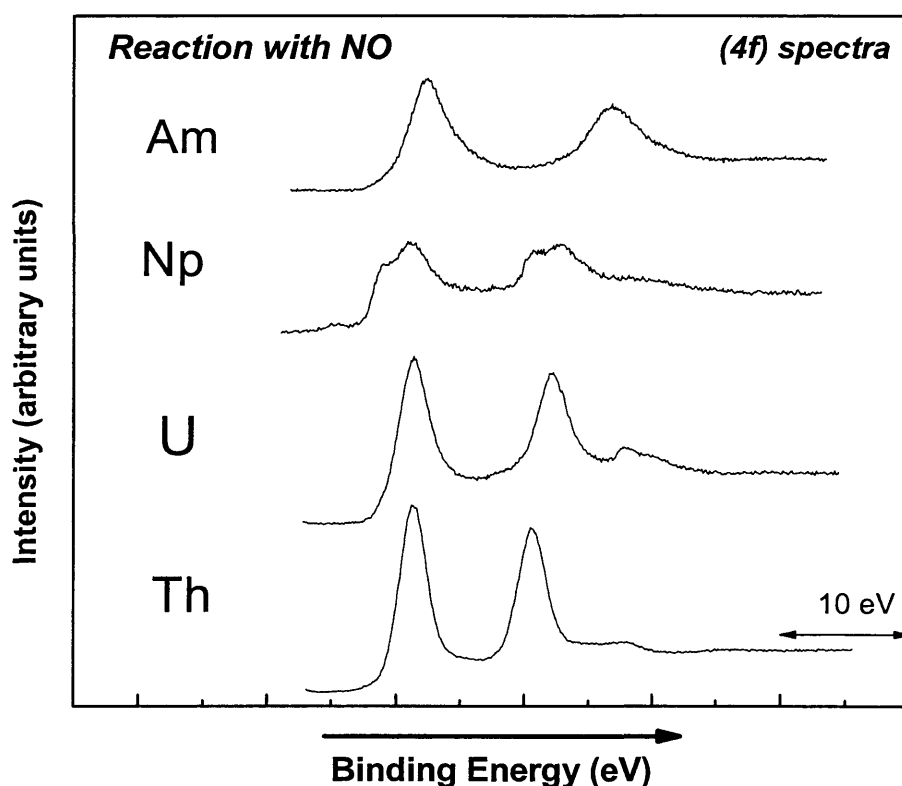


Figure 7.6. (4f) core level photoemission spectra of Th, U, Np and Am following exposure to NO (100 L).

When we compare the spectra obtained for the four metals we see that initially Th, U and Np are all very similar producing what we propose is a metallic oxynitride species. The symmetric O (2p) peak indicates an oxide stoichiometry lower than the lowest stable oxide (the actinide dioxide) where we would expect an asymmetric peak. Therefore we propose that this otherwise unstable lower oxide is stabilized by the presence of nitrogen on the surface as an oxynitride. Upon further exposures to NO, we see that thorium is more likely to further react with NO to form the actinide (IV) dioxide (as shown by the asymmetry in the O (2p) peak and also the appearance of weak shake up satellites on the higher binding energy side of the Th (4f) peaks) and respective nitride, resulting in all the $6d^27s^2$ states being transferred into the N (2p)/O (2p) band. In comparison the reaction with neptunium and americium slows at 25 L and we see no further reaction (we have taken exposures up to 100 L). It appears that $6d7s$ electrons are transferred into the N (2p)/O (2p) band and the 5f electrons become localized slowing the reaction. This can, similar to the observations made following oxidation with O₂, be related to the sensitivity of the 5f states to increases in the core potential upon oxidation. The 5f states become localized and further ionization (necessary for formation of higher oxidation states), becomes more difficult. Localization of the 5f states within uranium is also observed however to a lesser degree and the reaction therefore progresses further than that of Np and Am as the 5f electrons are only partially localized and therefore may have a limited participation in the surface reactions.

Similar to the localization phenomenon observed following oxidation with O₂, increased 5f localization is observed across the period (shifts in the 5f intensity to higher BE) U to Am due to the increasing core like behavior of the 5f electrons.

7.4 Conclusion

Finally, the work contained in this thesis is the first evidence that the surface chemical reactivity of the light actinides is dependent on itinerant 5f electrons.

With little or no itinerant 5f behaviour, for example in Am, the onset of lanthanide like surface chemical behaviour is observed.

7.5 References

1. J.Naegele and L.Mane, Actinides - Chemistry and Physical properties, in Structure and Bonding, L. Mane, Editor. 1985. p. 197.
2. T.Almeida, L.E.Cox, J.W.Ward, and J.R.Naegele, Surface Science, 1993. **287/288**(141).
3. B.W.Veal and D.J.Lam, Physical Review B, 1976. **15**(6). 2929-2942.
4. D.T.Larson, Journal of Vacuum Science & Technology a-Vacuum Surfaces and Films, 1980. **17**. 55.

Appendix 1

Photoelectron Spectroscopy (PES)

A1.1 Basics of Photoelectron Spectroscopy

Photoelectron spectroscopy utilises photo-ionization and energy-dispersive analysis of the emitted photoelectrons to study the composition and electronic state of the surface region of a sample. It is based on the photoelectric effect, where irradiating the surface with energetic photons ($>5\text{eV}$) leads to the ejection of photoelectrons with characteristic kinetic energies (KE), which are directly related to the binding energy (BE) of the electrons by

$$\text{BE} = h\nu - \text{KE} - \Phi \quad (\text{eq. A1.1})$$

where $h\nu$ is the photon energy and Φ the work function of the spectrometer. BEs are referenced to the Fermi-level. Energy analysis of these emitted photoelectrons can provide important information concerning the electronic states from which they originated. Probably the most important characteristic of these excited electrons is their limited escape depth and therefore the application of this technique to solid surfaces. Since the largest part of any measured photoelectron signal will originate from a sample depth of less than 20 \AA , this technique is ideally suited to examine adsorbates present in surface concentrations as low as a fraction of a monolayer.

Either X-rays or UV light are normally used as excitation radiation. X-rays give access to the core-level electrons (require incident radiation energy $>1000\text{eV}$), which are element specific and used for determination of the composition. Ultraviolet photoelectron spectroscopy (UPS) gives access only to the valence band region (lower energy radiation $<50 \text{ eV}$), but the energy resolution is one order of magnitude higher than for the core levels.

A1.1.1 X-ray Photoelectron spectroscopy (XPS)

XPS has its origins in the investigations of the photo-electric effect (discovered by Hertz in 1887) in which X-rays were used as the exciting photon source. When a solid absorbs a photon with energy in excess of the binding energy of an electron, a photoelectron is emitted and the kinetic energy of the photoelectron is related to the energy of the photon. Deep-core electrons do not participate in bonding, and their energies are characteristic of the atom from which they originate. To a first approximation, the energy of core electrons do not depend on the environment of the atom (but see later – chemical shift). Therefore, XPS is particularly useful for elemental analysis of a sample. Not only can XPS identify the composition of a sample but also it can be used to determine the composition quantitatively. The modern application of XPS owes much of its development to Siegbahn and co-workers in Uppsala. Kai Siegbahn, whose father Manne became a Nobel laureate in 1924, was awarded the 1981 Nobel Prize for his contributions.

XPS is a variant of photoemission spectroscopy involving the ejection of core level electrons from atoms resulting from their excitation by an incident X-ray photon of energy $h\nu$. The incident X-ray flux can be monochromatic or, as is the case for the Cardiff, the ITU and AWE X-ray sources, non monochromatic. The most common non-monochromatic source consists of a dual anode X-ray tube which is switchable between aluminium (Al $K\alpha$ at 1486.6eV) and magnesium (Mg $K\alpha$ at 1253.6eV) radiation. At these excitation energies ejected core level electrons can be detected from all elements in the periodic table except hydrogen and helium, and the photoelectron energy analysed in terms of its kinetic energy (E_K). A plot of photoelectron kinetic energy against intensity (counts per second) then yields the X-ray induced photoelectron spectrum.

The measured kinetic energy is related to the energy of the incident X-ray photon and not to the intrinsic properties of the material being investigated. A binding energy can be calculated using the relationship in eq. A1.1. The derived energy is electron-specific both in terms of the emitting atom's atomic

number and the core energy level. The photoelectron spectrum mirrors the electronic structure of the atom reasonably accurately and is shown in figure A1.1 where the core electronic structure of uranium is evident from the acquired X-ray induced photoelectron spectrum. Those photoelectrons that escape from the material without energy loss contribute to the discrete core level peaks. Electrons that suffer inelastic scattering energy losses contribute to the background together with the photoemission from the Bremsstrahlung radiation associated with non-monochromatised X-ray photon sources.

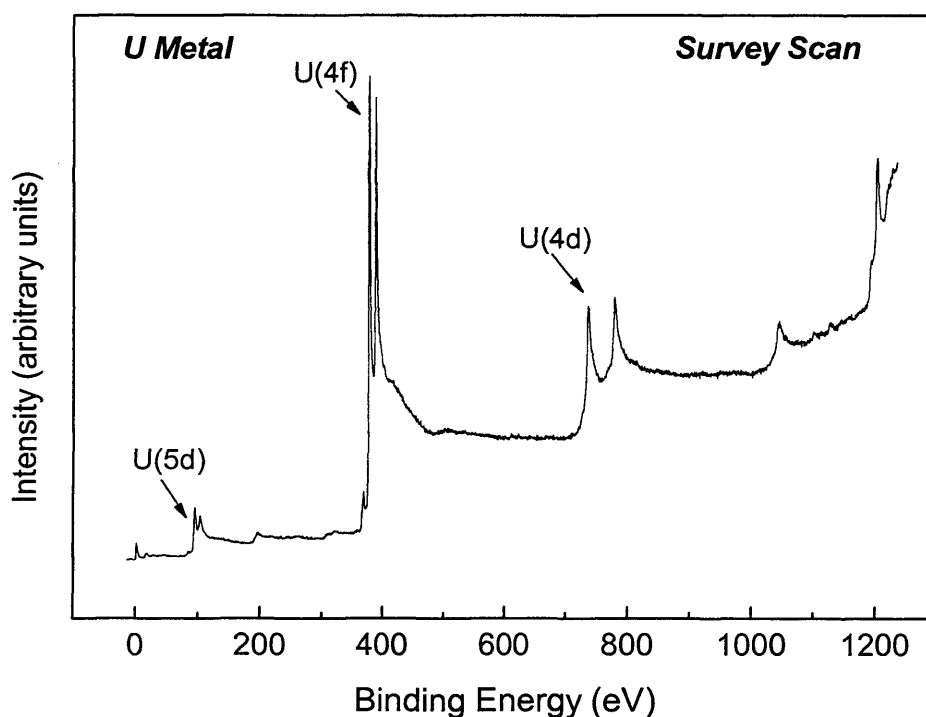


Figure A1.1. A survey scan of uranium showing how the core level electron atomic structure is reflected in the X-ray photoelectron spectra.

By measuring the binding energies of the core level peaks to an accuracy of about 0.1 eV, quantifiable elemental and chemical state information can be derived. An example of the chemical state information that can be generated is shown in figure A1.2, where the Np (4f) core level peak envelope exhibits several components. It is easy to resolve the Np^0 (metal), the Np^{Chem} (surface Np bonded to less than two oxygen atoms) and Np^{4+} (surface Np dioxide, NpO_2). With subsequent curve fitting of this envelope, the relative concentrations of each of the oxidation states can be measured. For all other

elements, similar chemical state information can be gained. Furthermore, for organic systems, the chemical functionality of carbon can be determined. For example differentiation between aldehyde, ketone, ester, halogenated systems and degrees of hybridisation can be achieved.

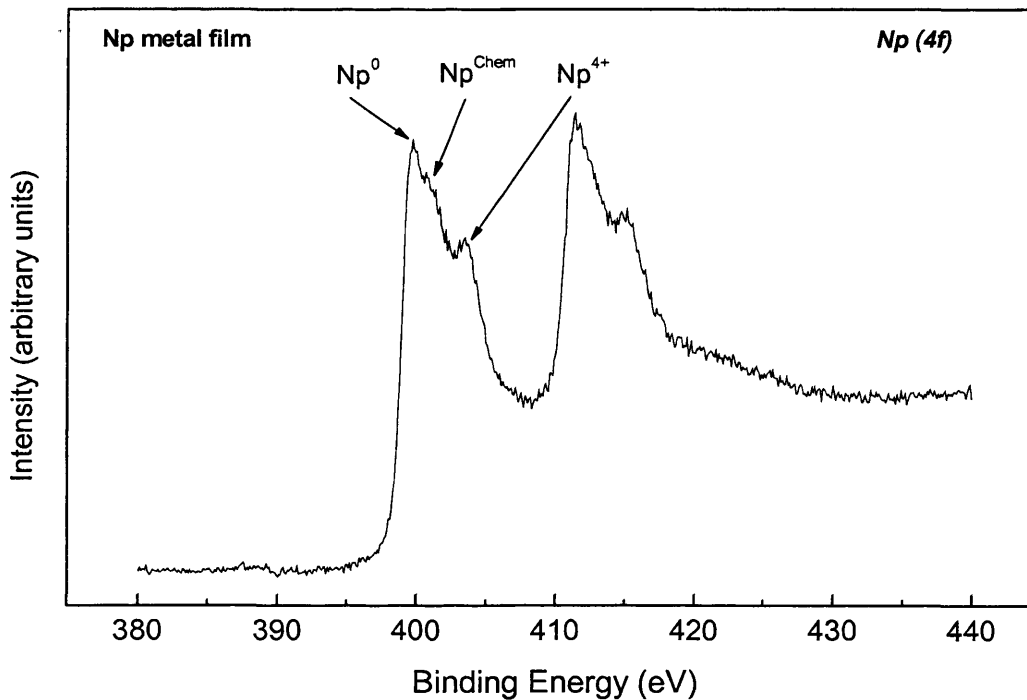


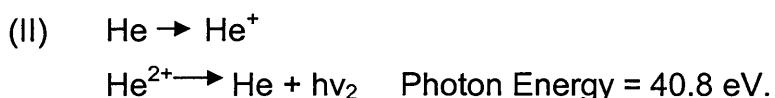
Figure A1.2 Neptunium 4f core level spectrum showing how the Np^{4+} and an intermediate oxidation state can be resolved from the Np^0 metal.

Once a photoelectron has been ejected, atomic relaxation ensues. This can occur by either an X-ray being emitted (X-ray fluorescence) or by an Auger electron being ejected (named after Pierre Auger who discovered the effect in 1923 [1]). The Auger ejection is consequential to the XPS process and is therefore termed X-ray induced Auger electron spectroscopy (X-AES). The use of X-AES in surface electron spectroscopic measurements is limited. However, the use of the more common form of AES, where the initial excitation is by a primary electron beam, gives useful information about surface chemical composition and provides complementary data to that obtained by XPS.

A1.1.2 Ultraviolet Photoelectron Spectroscopy (UPS)

UPS is a widely used technique and Eastman and Cashion [2] were the first to integrate a differentially pumped helium lamp with a UHV chamber, in 1971.

UPS is a variant of photoemission spectroscopy involving the ejection of valence level electrons from atoms resulting from their excitation by an incident ultra-violet photon of energy $h\nu$. The most common photon source consists of an inert gas discharge lamp using helium gas to generate He I (21.2 eV) and He II (40.8 eV) photons. At these excitation energies valence level electrons are ejected from atoms in the very near surface region giving information on the density of states (DOS) at the Fermi edge and molecular orbital occupancy in adsorbates. By accurately measuring the binding energy of the photoemission peaks, surface molecular dissociation can be monitored from a direct observation of molecular orbital populations. By quantifying the DOS at the Fermi edge, a direct measure of the metallic or insulating nature of the material can be gained.



Since valence electrons are involved in chemical bonding, UPS is particularly suited to the study of bonding at surfaces. Also, UPS readily provides measurements of the work function and band structure of the solid, the surface and adsorbed layers.

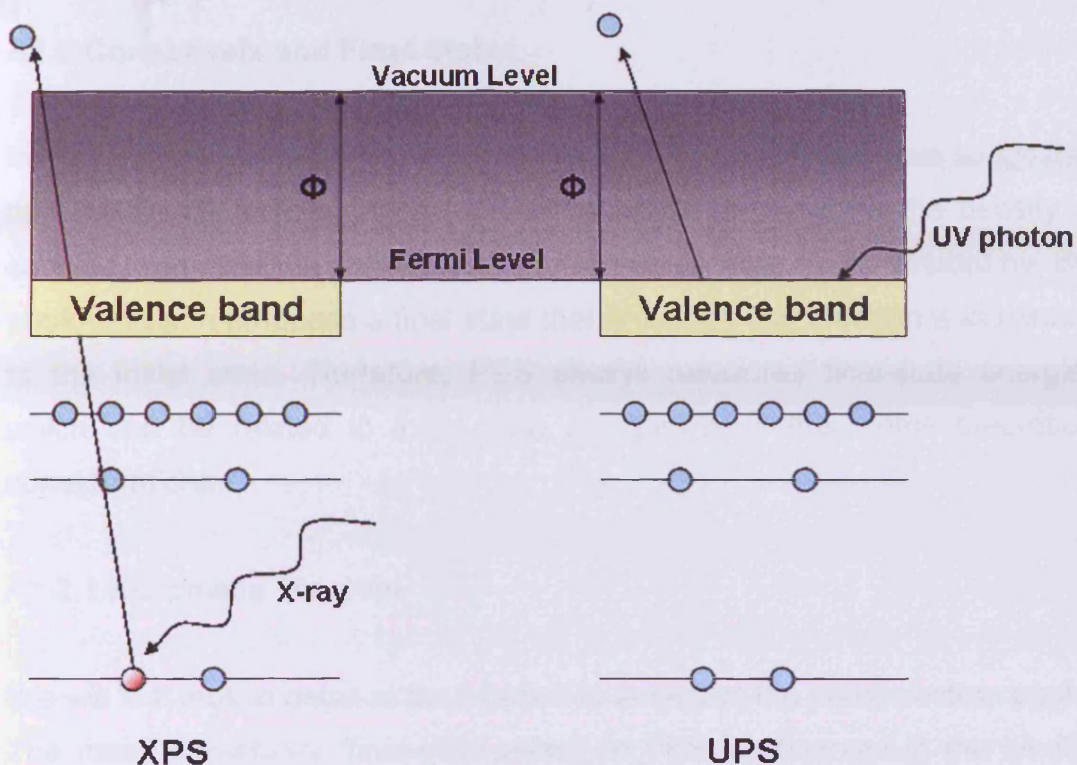


Figure A1.3 A schematic depiction of the atomic level physical processes involved in the electron spectroscopy techniques. The nature of the excitation source and the emitted electrons are shown.

UPS is especially useful in the study of actinides as the 5f photoexcitation cross section is dominating for He II radiation, whereas it is very weak for He I, and this difference helps to identify emission of 5f origin.

Furthermore, the relatively high cross section of O (2p) states for He II excitation makes the He II spectra a very sensitive indicator of any contamination, far superior to the standard monitoring of the O (1s) and C (1s) lines in XPS.

Besides the different cross section, the difference between He I and He II can generally arise due to a different attenuation length, which is about 1.0 nm for He I but only 0.5 nm for He II. Thus, He I spectra normally carry more information about the subsurface region than the He II spectra, which is even more surface sensitive.

A1.2 Core Levels and Final States

In our original very superficial comments about photoemission we suggested that the photoelectron energy spectrum should simply show the density of occupied states in the surface transposed up in energy by an amount $h\nu$. But photoemission produces a final state that is lacking one electron with respect to the initial state. Therefore, PES always measures final-state energies which can be related to initial-state energies only after some theoretical considerations.

A1.2.1 Koopmans Theorem

We will first look in detail at the location in energy of the photoelectron peaks. The most elementary “final-state effect” in PES is observed in the binding energy. The assumption implicit in the description, the photoelectron energy spectrum should simply show the density of occupied states in the surface transposed up in energy by an amount $h\nu$, is that the binding energy ‘seen’ by the photoelectron, E_b , of the state it leaves is the same as it was before the interaction and hence that all other electrons in the system are in the same state as before the photoionisation event. Such a situation reflects Koopman’s theorem and this energy, E_b , is therefore referred to as Koopman’s energy. In this case E_b is referred to the vacuum level, the emergent kinetic energy is indeed given by

$$KE = h\nu - E_b$$

This is only approximately true because it assumes that the PE process does not produce any change in the other orbitals. Stated more exactly, Koopman’s approximation neglects relaxation energies. In order to relate Koopman’s energies to the binding energies actually measured, one has to correct for the relaxation energy. This is the amount of energy necessary for the adjustment of the total system to the hole left in a specific orbital by the photoeffect. When the core hole is created by photoionisation, other electrons relax in energy to lower energy states to screen this hole partially

and so make more energy available to the outgoing photoelectrons. In a solid this relaxation energy consists of two basic contributions: One results from the relaxation of the orbitals on the same atom (intra-atomic relaxation). The other one is due to a charge flow from the crystal onto the ion that carries the hole (extra-atomic relaxation).

A1.2.2 Spin Orbit Coupling, Relative Intensities and Peak Widths

It is clear, from the survey spectra of uranium (figure A1.1), that the core levels have variable intensities and widths and that non-s levels are doublets.

The doublets arise through spin orbit coupling. An electron is a charged particle, its orbit around a nucleus induces a magnetic field whose intensity and direction depend on the electron velocity and on the radius of the orbit, respectively. These can be characterised by an angular momentum, called the orbital angular momentum, which is quantised as the electron can only travel in certain discrete orbitals. The quantum number is l , and l can take values 0, 1, 2, 3, 4, ... The orbiting electron also has a spin, i.e. positive or negative, which also induces a magnetic field; this in turn has a spin momentum, characterised by a spin quantum number s , which can take values $\pm\frac{1}{2}$. The total electronic angular momentum is a combination of the orbital angular and spin momenta, and this combination is in fact simply the vector sum of the two momenta. However, the vector sum can be carried out in two ways, $j-j$ coupling and $L-S$ (Russell-Saunders) coupling.

$j-j$ coupling – the total angular momentum of a single isolated electron is obtained by summing vectorially the individual electron spin and angular momenta. For the particular electron the total angular momentum is then characterised by the quantum number j , where $j = l + s$. Therefore j can take the values $1/2, 3/2, 5/2$, etc. The total angular momentum for the whole atom (J) being the summation for all electrons, where $J = \sum j$. This description is known as $j-j$ coupling. Strictly speaking, $j-j$ coupling is the best description of electronic interaction in elements of high atomic number, i.e. $Z > \sim 75$, but in

fact the nomenclature based on it has been used for spectroscopic features for all parts of the periodic table.

L-S coupling – Vectorial summation is carried out by firstly summing all the individual electronic angular momenta and then all the individual electronic spin momenta. These two total momenta are then characterised by two quantum numbers, the total atomic orbital angular momentum quantum number L , which is equal to $\sum l$, and the total atomic spin quantum number S , which is equal to $\sum s$. Coupling of the two total momenta to give the total atomic angular momentum can then be characterised as before by the quantum number J , which is now, however, equal to $L \pm S$. Hence the name ‘*L-S* coupling’. *L-S* coupling has been found to apply to elements of low atomic number, i.e. $Z < \sim 20$.

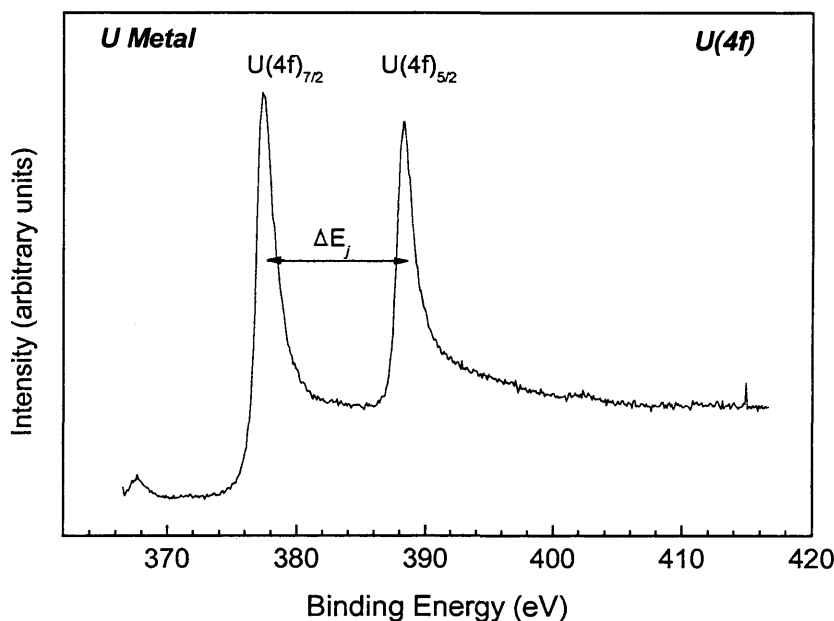


Figure A1.4 *U(4f)* spectrum of clean uranium metal showing *U(4f)_{5/2,7/2}* peaks arising due to spin orbit coupling

The doublets observed in the non-*s* core levels arise through spin-orbit coupling. Two possible states, characterised by the quantum number j ($j = l \pm s$) arise when $l > 0$. The difference in energy of the two states, ΔE_j , reflects the parallel or anti-parallel nature of the spin and orbital angular momentum vectors of the remaining electron. The magnitude of this energy separation is

proportional to the spin-orbit coupling constant which depends on the expectation value ($1/r^3$) for the particular orbital. The separation can be many electron volts. ΔE_j increases as Z increases for a given subshell (constant n, l) or to increase as l decreases for constant n (e.g. for uranium the splitting of $4d > 4f$).

Subshell	j values	Area ratio
S	1/2	-
P	1/2, 3/2	1 : 2
D	3/2, 5/2	2 : 3
f	5/2, 7/2	3 : 4

Table A1.1 Spin-orbit splitting parameters

The relative intensities of the doublet peaks are given by the ratio of their respective degeneracies ($2j + 1$). Thus the area ratios and designations (nl_j) of spin orbit doublets are given in table A1.1.

Relative Intensities – The basic parameter which governs the relative intensities of core level peaks is the photo-emission cross-section, μ . Values of μ have been directly calculated and also derived from X-ray mass absorption coefficients [3]. The cross section is the probability an electron from a particular orbital will be excited at a particular photon energy.

Peak widths - The peak width, defined as the full width at half-maximum (FWHM) ΔE , is a convolution of several contributions:

$$\Delta E = (\Delta E_n^2 + \Delta E_p^2 + \Delta E_a^2)^{1/2}$$

where ΔE_n is the natural or inherent width of the core level, ΔE_p is the width of the photon source (X-ray line) and ΔE_a the analyser resolution, all expressed as FWHM (this assumes that all components have a Gaussian line shape).

There is a contribution to the peak width from the analyser; it is the same for all peaks in the spectrum when the analyser is operated in the constant analyser energy (CAE) mode, but varies across the spectrum when the analyser is operated in the constant retard ratio (CRR) mode (since in this case $\Delta E/E$ is a constant).

The inherent line width of a core level, i.e. the range in KE of the emitted photo-electron, is a direct reflection of uncertainty in the lifetime of the ion state remaining after photoemission. Thus from the uncertainty principle we obtain the line width

$$\Gamma = h / \tau = 4.1 \times 10^{-15} / \tau \text{ eV}$$

with Plank's constant (h) is expressed in electronvolt seconds and the lifetime (τ) expressed in seconds. The narrowest core levels have lifetimes between 10^{-14} and 10^{-15} s whilst the broader core levels have lifetimes close to or even slightly less than 10^{-15} s.

Core hole lifetimes are governed by the processes which follow photoemission, in which the excess energy of the ion is dissipated or decays. One of two mechanisms may be involved: emission of an X-ray photon (fluorescence), or emission of an electron in an Auger process (figure A1.5).

It can be noted that the line widths of the principle light element core levels (1s, 2p) systematically increase with an increase in atomic number. The increase in valence electron density enhances the probability of the relevant Auger process, decreasing the lifetime of the core hole.

A1.2.3 Fate of the Core hole

There are two dominant pathways available for the decay of a core-hole: X-ray fluorescence and the Auger process [4, 5], each mechanism involving the neutralisation of the core hole by an electron from an outer shell (B \rightarrow A), figure A1.5.

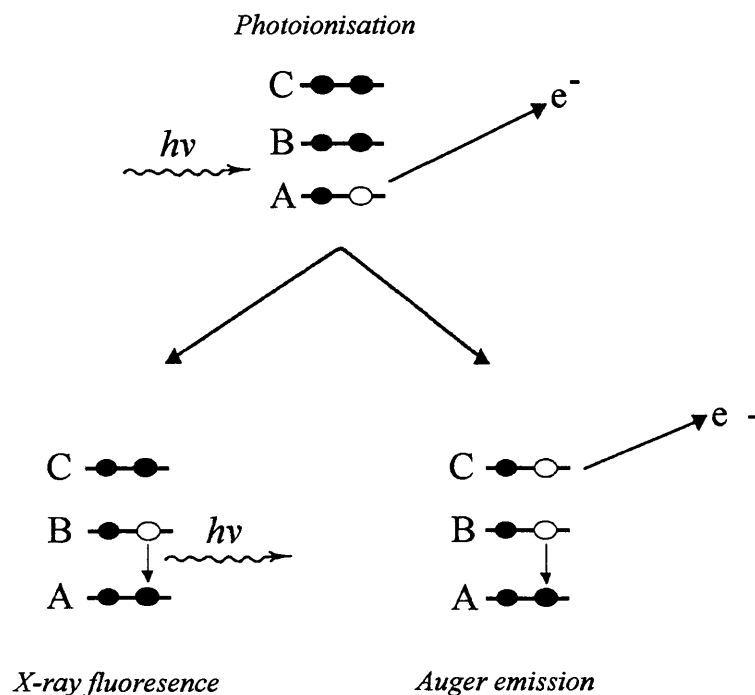


Figure A1.5 Core hole decay via X-ray fluorescence and the Auger process.

X-ray Fluorescence - Transition of the outer electron to the core hole releases energy in the form of an x-ray photon. The energy of the released photon is equal in energy to the difference between energy levels A and B.

Auger Transition - the core hole is occupied by a more energetic electron, with the excess energy being dissipated by ionisation of an outer orbital. This non-radiative mode of decay emits a secondary electron known as the Auger electron, resulting in a doubly ionised system.

These Auger electrons are inevitably analysed along with the photoelectron signal and appear as discrete lines on a spectrum. These often provide us with important complementary information and can be distinguished from photoelectrons by the dependence of their kinetic energy on the incident photon energy. The Auger process is also the basis for another important surface analytical technique AES (Auger Electron Spectroscopy).

A plot (figure A1.6) of the relative yields of the two decay mechanisms as a function of atomic number (z) shows the dominance of Auger decay at low z .

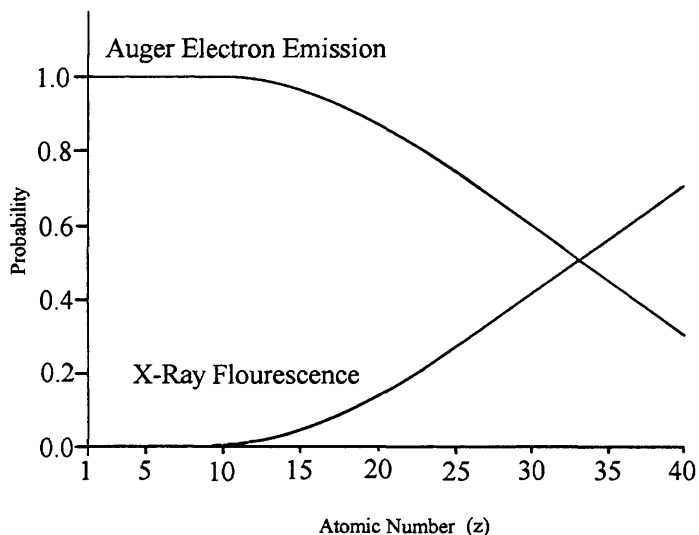


Figure A1.6 Relative yields of X-ray fluorescence and Auger electron emission as a function of atomic number.

A1.2.4. Chemical Shift

In the investigation of molecules and solids, one is not just interested in the absolute binding energy of a particular core level, but also in the change in binding energy between two different chemical forms of the same atom. This energy difference is called the *chemical shift*.

The existence of 'chemical shifts,' associated with different local chemical and electronic environments, is of considerable practical value in XPS. These chemical shifts originate from the sum of two effects; the first of these is the final state effect of relaxation (already discussed). As a metallic environment modifies the energy due to an associated relaxation shift and a further change of nearest neighbours, say from metal to O atoms, can modify this intra-atomic relaxation shift. The second effect is an initial state effect which might be called a true chemical shift; this is the shift in the original binding energy due to the changed electronic environment of the atom. Even without a quantitative description of these effects, valuable work can be performed by using the chemical shifts observed in known systems as a fingerprint. Thus,

extensive tabulations of observed chemical shifts have been compiled, and a common approach to the XPS study of adsorption of species A on solid B is to try first to characterise absolute peak positions of XPS peaks in all known bulk compounds of A and B to provide a reference for the various known chemical shifts to be expected. In this way chemical shifts observed during the adsorption may be related to different stages in the chemical reaction.

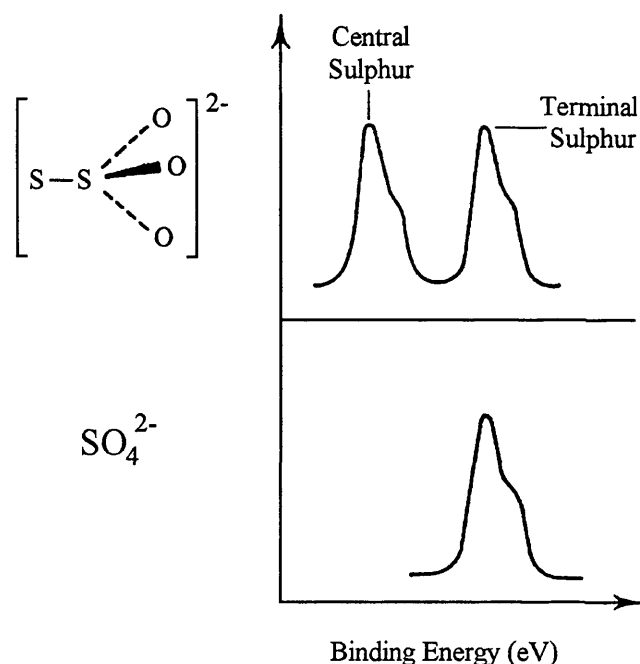


Figure A1.7 S (2p) XPS signals of sodium thiosulphate and sodium sulphate, illustrating the chemical shift [6].

The first observed chemical shift was recorded by Siegbahn [6] for sodium thiosulphate (Figure. A1.7) showing a discrete double peak structure attributed to the chemical states of the sulphur atoms (the central sulphur atom being slightly more electropositive due to the electron-withdrawing oxygen atoms).

A1.2.4.1. Actinides - An alternative view of chemical shifts

Thorium provides the first indication in the actinide series of a possible oddity in the actinide series due to the screening of the photoionisation core hole

involving 5f electrons. The satellite located on the high binding energy side of the Th (4f) peaks can only be explained in terms of final state effects. An explanation in terms of initial state impurities can be ruled out because of the high quality sample preparation and chemical analysis of the surface, e.g. by XPS.

In the final state one has two possibilities for screening: the additional coulomb attraction produced by the core hole (which can be viewed approximately as an additional nuclear charge) can now pull the conduction band so far below E_F that an additional charge can be put into the 5f orbitals leading in a first approximation to a thorium $5f^1$ configuration (figure A1.8). This is essentially the ground state and is very similar to the ground state in Pa metal, to which it corresponds to the $(Z+1)$ -approximation (where Z is the atomic no.) Thus the main line in Th PES always corresponds to the $5f^1$ configuration. However, there is also the possibility that the 5f band, although now below E_F is not filled by a screening electron, and that the screening is instead produced within the 6d7s band. Hence the core level peak intensity is

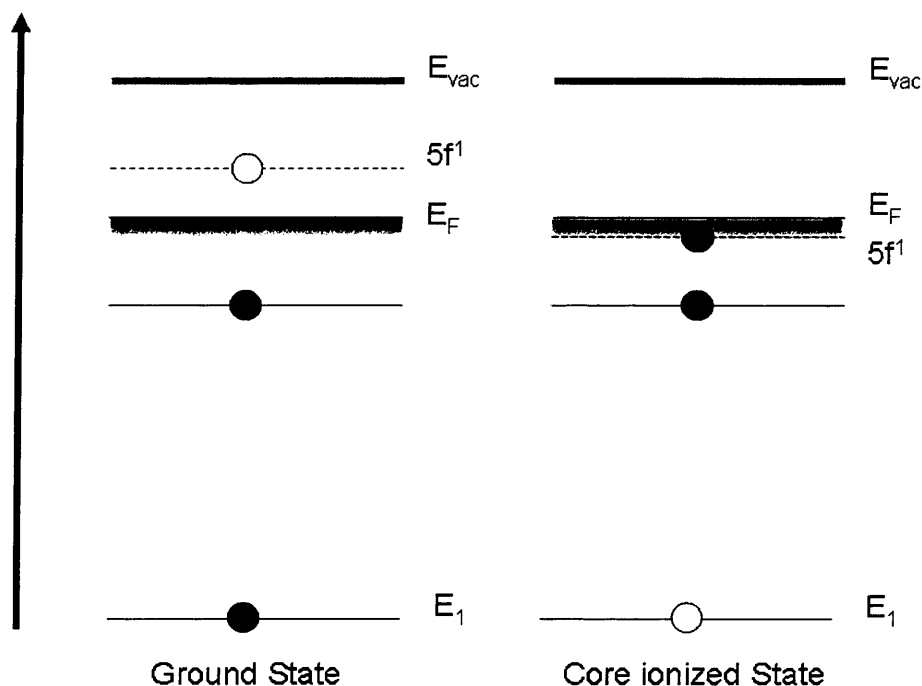


Figure A1.8 Schematic energy level diagram of a thorium metal atom. The previously unoccupied $5f^1$ level is pulled down below the Fermi level in the presence of the core hole, and being filled by hybridization to the conduction band.

assumed to originate from two basic final states, one in which a screening orbital or level becomes occupied by an electron upon core ionization, giving the "well screened" peak, and the other in which the screening level remains empty, giving the "poorly screened" peak. For deep core holes in Th, the best screening level is $5f^1$ which is unoccupied and 3 – 5 eV above E_F [7] but is known to be occupied in Pa. As the $5f$ levels are more extended than the $4f$ they form a true band in Th [7] and are strongly hybridized with other delocalized conduction electrons.

The relative intensity of the well-screened peak increases with increasing strength of coupling between the screening level and the valence bands of the metal. This coupling is described in terms of U_{ac} , the energy by which the screening level is pulled down upon core ionization; W_s , the energy broadening of the screening level; and Δ_+ , the position of the screening level relative to E_F [8]. The coupling is weak when $W_s \ll \Delta_+$ and strong when $W_s > \Delta_+$.

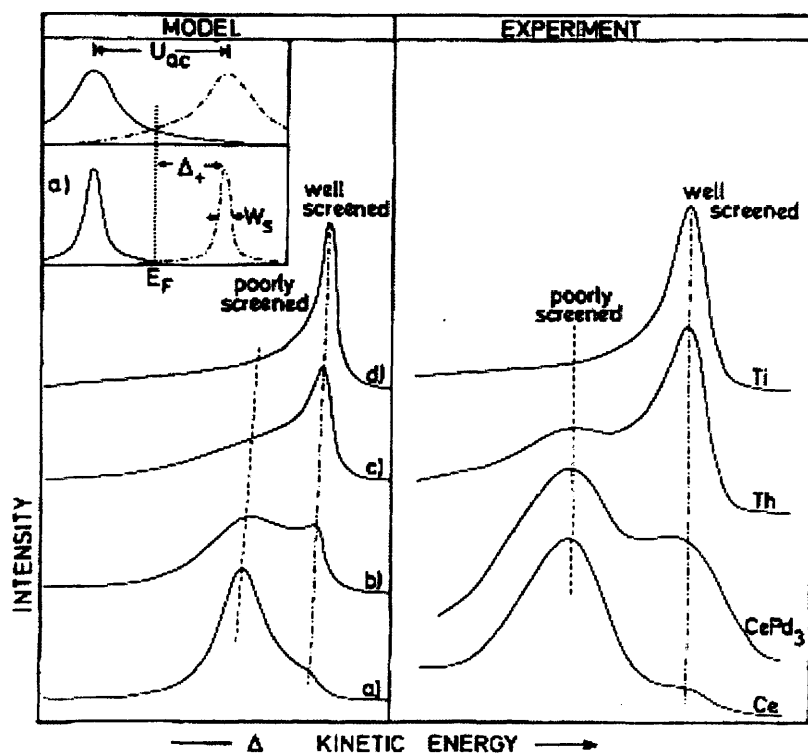


Figure A1.9 Illustration of the Schonhammer-Gunnarsson model of core-hole screening[8]

The Th and CePd₃ cases are typical of intermediate coupling strength. These general shapes are often found in transition-metal oxides such as Fe₂O₃, CoO or CuO, in which the 3d screening level is less strongly coupled than in the pure metals. This gives, in addition to the well-screened peak, a strong poorly screened peak in which a screening electron does not enter the 3d shell. The trend of relative intensities of “well-screened” and “poorly screened” peaks shown in figure A1.9 clearly follows the trends in our preconception of the degree of localization of the orbitals involved in screening. Therefore in relation to the actinides, XPS line shapes could be used to scale the degree of localization of the screening orbitals, i.e. the 5f electrons.

In relation to chemical shifts, these can now be interpreted to some extent not as actual chemical shifts but due to a change in the photoionisation core hole screening processes associated with a change from itinerant to localized 5f electron behaviour. As hybridization of the 5f electrons with the conduction band decreases the 6d7s “poorly screened” peak will begin to dominate as the 5f band does not become occupied with a screening electron and screening is instead produced with the wide 6d7s band. So we see not a shift in peaks but a decrease in the “well screened” and increase in the “poorly screened” peak.

An excellent example of the screening processes observed in actinide systems is americium. The clean metal Am (4f) peak consists of a main peak with a satellite located at 4 eV lower binding energy. Americium is considered to be the first metal in the actinide series to have localised 5f electrons. Therefore we would expect, similar to the lanthanides which have localized 4f electrons, that the screening of the core hole is mainly from the d and s conduction electrons and gives rise to the “poorly screened” peak. The satellite at 4 eV lower binding energy is due to efficient screening from partially hybridised 5f states, the “well screened” peak. Upon oxidation as the 5f electrons within Am become completely localized we see the loss of the “well screened” peak and the slight increase in the “poorly screened” peak. We do not however see any shifts in these peaks. The “shifts” observed in

the photoelectron spectra of actinides upon, for example, oxidation is due to a change in the screening mechanism as the 5f electrons become more localized. A decrease in the “well screened” peak and increase in the “poorly screened” peak gives the impression of chemical “shift” but it is actually due to a change in screening mechanism.

A1.2.5 Surface Sensitivity in XPS.

XPS is limited to surface studies due to the escape depth of the emitted photoelectron. Although X-rays can penetrate to a depth of $>10^4$ Å, the measured photoelectron signal originates from a surface depth not more than ca 50 Å, due to the inelastic scattering of the emitted electrons.

The escape depth or inelastic mean free path (IMFP) of an electron is assigned as the thickness of material that will attenuate an incident flux of electrons by a factor of $1/e$.

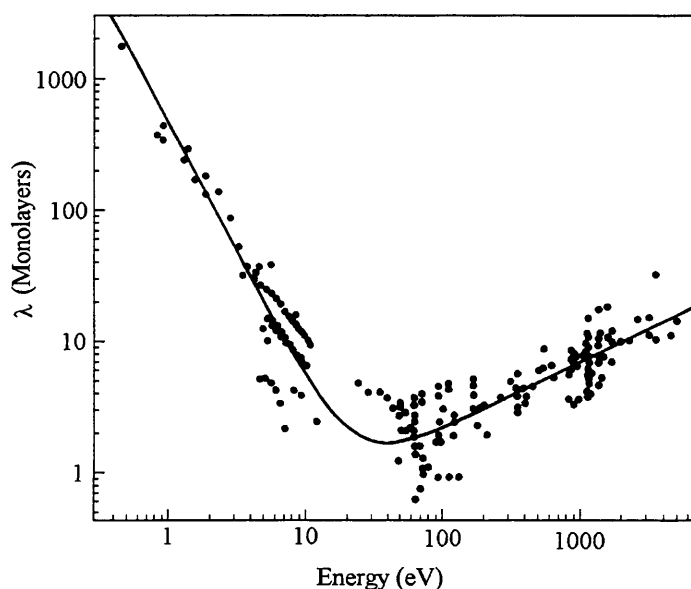


Figure A1.10. Distribution of the inelastic mean free path as a function of photoelectron energy: the universal curve.

The mean free path of the electron from a material is dependent on the photoelectron energy and the substance, this dependence being known as the “universal” curve (Figure A1.10).

Electrons with kinetic energies between 10 - 1500 eV are detected, their escape depths being less than 20 Å, i.e. the surface region. Only photoelectrons that escape the solid without suffering a reduction in energy contribute to the primary photoelectron signal.

A1.2.6 Angle Resolved XPS

For enhanced sensitivity to the outer most atomic layers of the surface, it is possible to vary the collection angle between the analyser direction and the surface. By reducing this angle, photoelectrons collected will have further to travel through the material before reaching the detector. Since the maximum path length of the detected photoelectron must remain constant, only photoelectrons from the outermost layers will escape without losing energy.

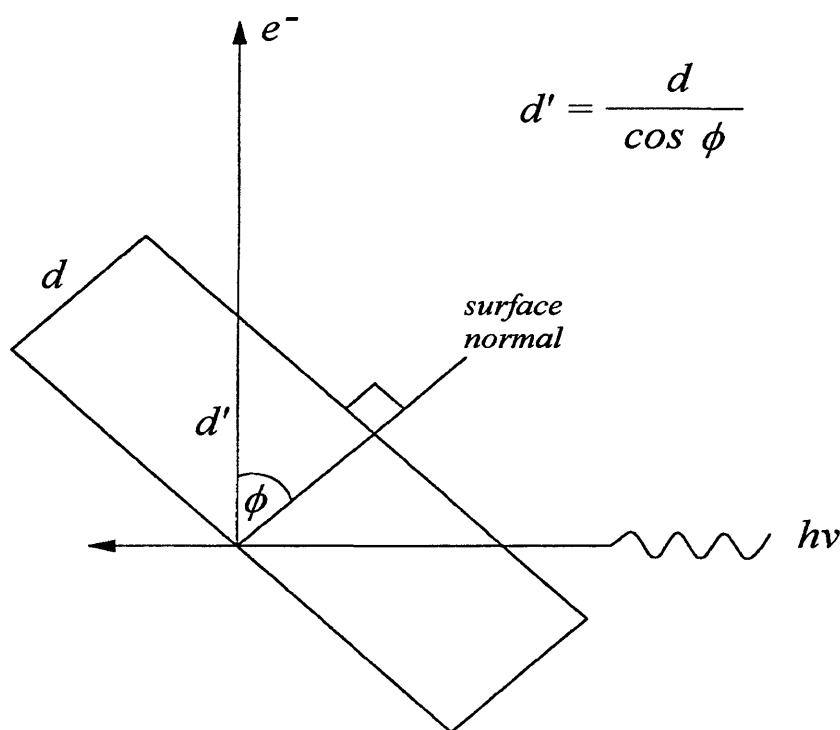


Figure A1.11. Off-normal photoelectron detection angle.

Angle resolved XPS provides a useful tool in the identification of surface contamination. Figure A1.12 shows how angle resolved XPS can yield more information on the surface layers of a Ni sample.

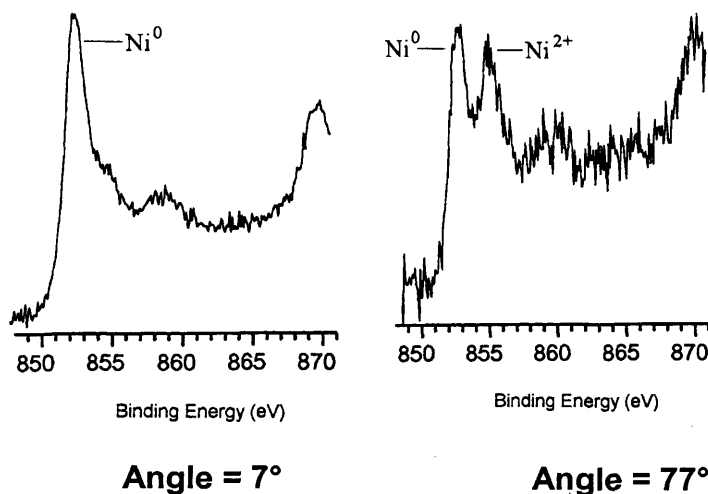


Figure A1.12. Increased surface sensitivity using grazing take-off angle XPS. The Ni (2p) spectra were recorded for the same Na/NiO/Ni(110) surface at different take-off angles [9].

A1.2.7 The Reference Level

For accurate comparisons to be made between experimental binding energies, a definition of a reference level is required. The reference level for the electron binding energy scale of gaseous molecules was conveniently chosen as the vacuum level at infinity. For an electrically conducting sample, the fermi level is used as the reference level. Equalisation of the fermi levels is achieved by charge sharing between the sample, sample probe and the earthed spectrometer only if they are in electrical contact (Figure A1.13).

In the case of insulating materials, XPS measurements will suffer from charging effects arising from electron deficiency at the surface due to the photoionisation process. Furthermore, such materials may also exhibit a binding energy shift due to the so-called 'floating' Fermi edge effect brought about by a lack of electrical equilibrium between the sample and the spectrometer. These problems are particularly frustrating when dealing with real catalytic systems since the majority of these are based on insulating metal oxides. Such effects can be minimised by utilising an electron flood gun to neutralise the resulting positive charge. Alternatively, internal calibrations to a known constant such as adventitious carbon impurities or a deposited thin gold film have also been used.

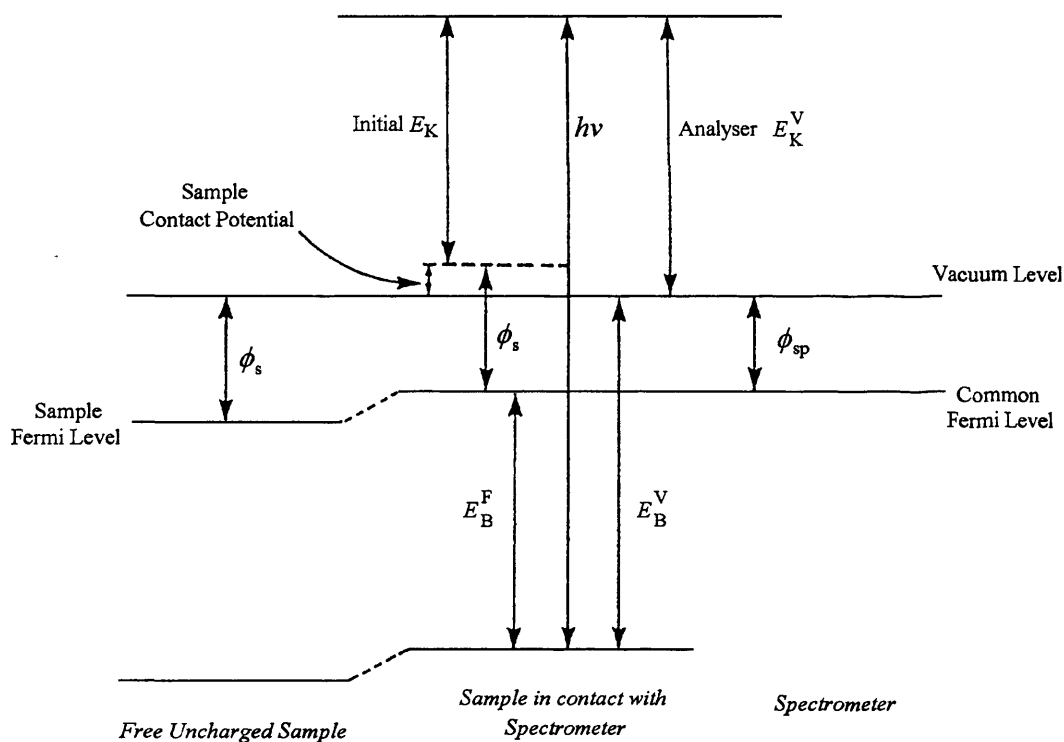


Figure A1.13. The energy level diagram for a conducting sample in contact with the spectrometer [9]

A1.3 Secondary Structure

Before discussing the true secondary structure features in the spectrum it is necessary to identify the sources of spurious low intensity peaks. These arise in two ways. Standard X-ray sources are not monochromatic. Besides the Bremsstrahlung radiation and the principle $K\alpha_{1,2}$ line (see X-ray source in Instrumentation chapter), magnesium and aluminium targets also produce a series of lower intensity lines, referred to as X-ray satellites. The transitions giving rise to $K\alpha_{1,2}$ radiation (an unresolved doublet) are $2p_{3/2,1/2} \rightarrow 1s$. Satellites arise from less probable transitions (e.g. $K\beta$; valence band $\rightarrow 1s$) or transitions in a multiply ionised atom (e.g. $K\alpha_{3,4}$).

X-ray line	Separation from $K\alpha_{1,2}$ (eV) and relative intensity ($K\alpha_{1,2} = 100$)	
	Mg	Al
$K\alpha'$	4.5 (1.0)	5.6 (1.0)
$K\alpha_3$	8.4 (9.2)	9.6 (7.8)
$K\alpha_4$	10.0 (5.1)	11.5 (3.3)
$K\alpha_5$	17.3 (0.8)	19.8 (0.4)
$K\alpha_6$	20.5 (0.5)	23.4 (0.3)
$K\beta$	48.0 (2.0)	70.0 (2.0)

Table A1.2 High energy satellite lines from Mg and Al targets [10]

X-ray ghosts are due to excitations arising from impurity elements in the X-ray source. The most common ghost is Al $K\alpha_{1,2}$ from a Mg $K\alpha$ source. This arises from secondary electrons produced inside the source hitting the thin aluminium window (present to prevent these same electrons hitting the sample). This radiation will therefore produce weak ghost peaks 233.0 eV to higher KE of those excited by the dominant Mg $K\alpha_{1,2}$. Old or damaged targets can give rise to ghost peaks excited by Cu $L\alpha$ radiation, the main line from the exposed copper base of the target. These peaks appear 323.9 eV (556.9 eV) to lower KE of Mg $K\alpha_{1,2}$ (Al $K\alpha_{1,2}$) excited peaks.

A1.3.1 X-ray satellites

Atoms, molecules and solids are many-electron systems. Since the electrons interact with each other via the coulomb and exchange interaction, the emission of one electron after the photoexcitation process can and must lead to excitations in the remaining system. These excitations require energy and therefore lead to signals in the PE spectrum with a smaller kinetic energy (larger binding energy) than the signal corresponding to the ground state of the system after the PE process. This means that the PE spectrum must consist of the "main" line (representing the ground state after photoexcitation) and a number of "extra" (satellite) lines representing excited states.

In solids there is yet another source which gives rise to additional lines in the PE spectrum. Here the photoexcited electron travels a relatively long way through a volume which is occupied by other electrons, and therefore has the possibility of exciting them. This excitation energy must again be supplied from the kinetic energy of the outgoing electron and therefore this photoelectron may be observed with a kinetic energy smaller than otherwise expected. These are usually referred to as shake-up features (when excitation is to a bound state) and shake-off (when excitation is to the continuum).

Shake up processes arise as an outer electron is excited simultaneously with the photo-ionisation event to a higher, unoccupied state. The energy required for this transition is lost by the primary emitted photoelectron, imparting a portion of its kinetic energy for the excitation. The result is a satellite feature to the higher binding energy side of the main peak. These satellite features are associated with an electronic excitation and can therefore yield valuable information about the unoccupied states involved. Shake off processes occur as an outer electron is excited out of the atom resulting in a doubly ionised state and a very broad XPS feature. Shake off processes yield no spectroscopic information and the signals tend to be lost within the background of inelastically scattered electrons.

Of course, there are also electrons which travel through the solid without any loss. These are responsible for the so called no-loss line (or main line), while those experiencing an inelastic collision on their way from the site of the photoexcitation to the surface constitute the "inelastic tail", which generally consists of a featureless part and (broad) discrete peaks.

Thus we see that there are, in principle, two sources of "extra" structure in the PE spectrum (besides the main line), an intrinsic part (created in the photoemission process) and an extrinsic part (created by the photoexcited electron in a solid via interaction with other electrons during its travel to the surface).

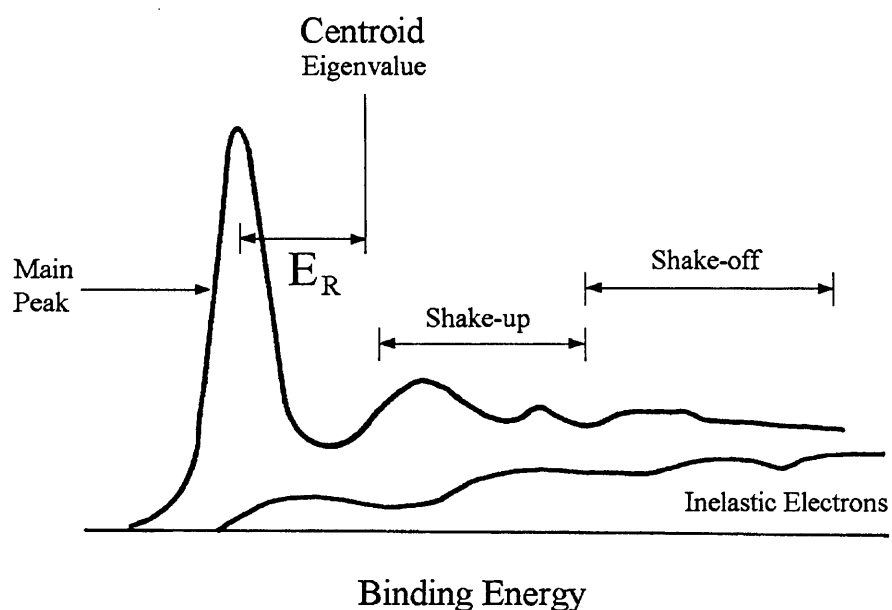


Figure A1.14 Basic elements of an XPS spectrum[9]

A1.3.2 Multiplet splitting

Multiplet splitting of the photoelectron peak occurs where an unpaired valence electron interacts with the unpaired core electron left after photoemission. This results in two final states, which are dependent on the alignment of the spin vector (s) of the electrons, either parallel or anti-parallel, resulting in two peaks in the XP spectrum.

Also known as spin-spin interaction, multiplet splitting is most noticeable for 3s orbitals when unpaired electrons are present in the 3d orbitals, as in the case of Cr (3s). The weak coupling results in the kinetic energy loss suffered by the photoelectron being too small to give any resolved multiplet splitting, instead it is observed as slight core-level asymmetry, or as binding energy shifts.

1.4 References

1. P. Auger, C. R. Acad. Sci. Paris, 1923. **177**. 169.
2. Eastman and Cashion, Physical Review Letters, 1971. **27**. 1520.
3. J.H. Scofield, J. Elec. Spec. Relat. Phenom., 1976. **8**. 129.
4. P. Auger, J. Phys. Radium, 1925. **6**. 205.
5. C. Linsmeier, Vacuum, 1994. **45**. 673.
6. K. Siegbahn, Nova Acta Regiae Sci. Ups. Ser IV, 1967. **20**.
7. Y. Baer and J.K. Lang, Physical Review B, 1980. **21**(6). 2060 - 2062.
8. J.C. Fuggle, M. Campagna, Z. Zolnierrek, R. Lasser, and A. Platau, Phys. Rev. Lett., 1980. **45**. 1597.
9. J.N.O'Shea, PhD Thesis, University of Cardiff, 1999
10. T.A. Carlson, Photoelectron and Auger Spectroscopy. 1976, New York: Plenum.

Appendix 2

Instrumentation

A2.1 Introduction

Uranium and thorium work was undertaken using a Vacuum Generators (VG) ADES 500 spectrometer modified to include high resolution electron energy loss spectroscopy (HREELS) capabilities.

Work performed on neptunium and americium thin films were carried out at the institute for transuranium elements (ITU). There a Leybold-Heraeus LHS-10 spectrometer was used to acquire the data. The spectrometer was modified for work with radioactive materials and included its own in house designed sputter (plasma triode) deposition capabilities.

Contained within this appendix is a brief overview of the instrument in Cardiff. A more in depth look at the system at the ITU can be found at the ITU website [1], although much of the instrumentation and conditions required are applicable to both systems.

A2.2 Requirements for Surface Studies

There are a number of specific requirements that must be achieved for the operation of photoelectron spectrometer. These are outlined below.

A2.2.1 Ultra High Vacuum Requirements

Successful study of metal-adsorbate interactions necessitates the use of ultra high vacuum (UHV), typically considered to be pressures of less ca 10^{-10} mbar. Three reasons dictate the need for a good vacuum:

1. Photoelectrons emitted from the surface towards the analyser should encounter as few molecules as possible. Gas molecules in the

chamber scatter and stop electrons reaching the analyser. A high vacuum ($10^{-5} - 10^{-6}$) will fulfil this.

2. Prevention of electrical discharge. Again a high vacuum is required to prevent electrical discharge between X-ray anode and electron analyser.
3. Although a high vacuum is suffice for points one and two, the need for an atomically clean surface requires UHV.

A spectrometer base pressure of 10^{-6} mbar is sufficient to remove the problem of photoelectrons interacting with gas molecules. It is the requirement of atomically clean surfaces throughout the experimental period that adds more stringent demands on the base pressure. Pressures of 10^{-10} mbar (UHV) are required to avoid contamination build up on the surface.

The rate of impingement (z) of a gas on a surface is governed by the Hertz-Knudsen equation,

$$Z = P / (2M\pi KT)^{1/2} \text{ cm}^{-2}\text{s}^{-1} \quad (2.1)$$

where P = pressure, M = molecular mass, K = Boltzmann constant, T = Temperature (K).

Assuming a sticking probability of unity (i.e. all molecules that strike the surface will stick to it), then a surface consisting of approximately 1.5×10^{15} atoms cm^{-2} at a pressure of 10^{-6} mbar at 300K will be covered with a monolayer of surface contamination in only 4 seconds.

By comparison the same surface for the same gas at 10^{-10} mbar and 300K will not be covered until >8 hours. In practise, the sticking probabilities are seldom close to unity, enabling further time until the surface is contaminated.

A2.2.1.1 Achieving UHV

Base pressures in the system of 10^{-10} mbar are routinely achieved by a combination of rotary, diffusion and sputter-ion pumps. Initial evacuation

('roughing') from atmosphere to $\sim 10^{-2}$ is achieved through oil rotary pumps. The pump itself consists of a wheel with blades on its perimeter lubricated with oil. Rotation of the wheel causes the blades to trap molecules from the vacuum vessel between the wheel and the pump wall and then transports them to an exhaust port of the pump via a one-way valve.

From these rough vacuums, the use of diffusion pumps is required to generate pressures of $\sim 10^{-10}$ mbar. A schematic of a vapour diffusion pump is shown in figure A2.1. A heater at the base of the diffusion pump heats oil to produce a vapour. The choice of oil employed in a diffusion pump is important. The oil must have a high resistance to thermal degradation, a vapour pressure at 298K of 10^{-9} minimum and must not react with the gases passing through the pump to form volatile products. The oil used in our diffusion pumps is a polyphenyl ether oil (Santovac 5, Monsanto Corp.), the vapour pressure of which at 298K is $\sim 4 \times 10^{-10}$ mbar.

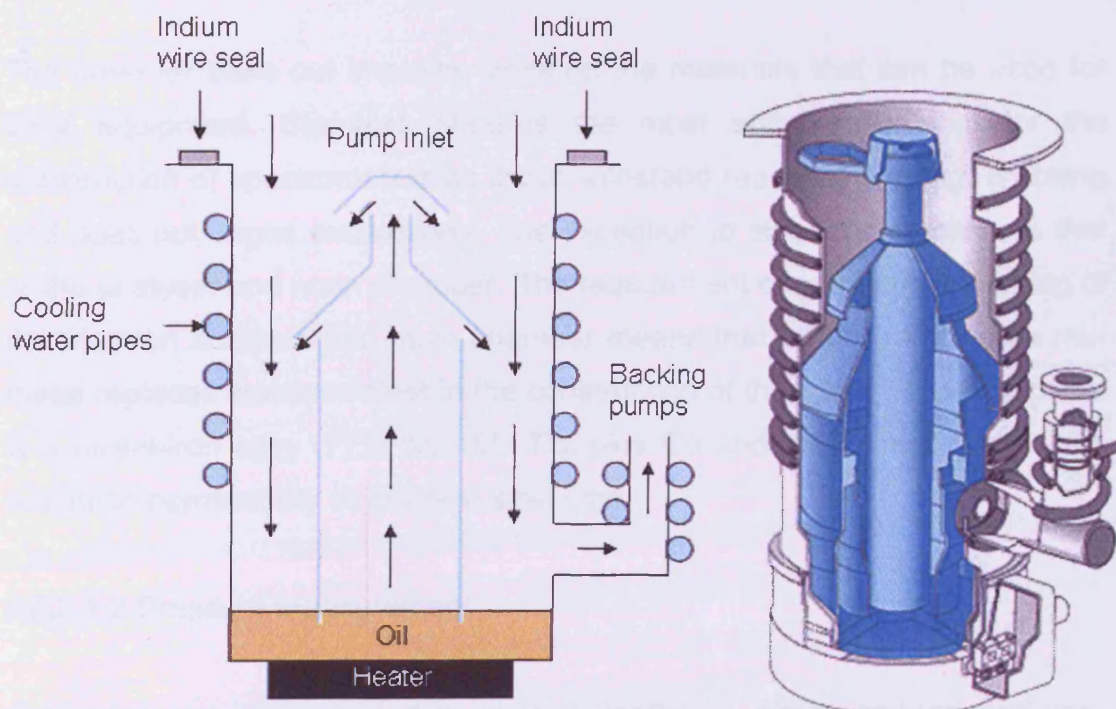


Figure A2.1 Schematic diagram of a vapour diffusion pump

The resulting vapour passes up through the centre of the pump and out through one of several jets. The jets direct the vapour downward with supersonic velocities. Gas molecules entering the pump are struck by the vapour molecules and are swept downwards to be removed by the backing rotary pumps. The oil is then condensed by cooling the body of the pump with water. To avoid oil back streaming into the spectrometer, a liquid nitrogen trap is placed between the pump and the spectrometer.

The sputter-ion pump is employed to differentially pump the x-ray source and to maintain a reasonable vacuum when the system is isolated from the diffusion pump.

To achieve and maintain UHV, the outgassing rate of the spectrometer needs to be minimised. This is achieved by increasing the temperature of the spectrometer to $\sim 180^{\circ}\text{C}$ for a minimum of twelve hours. This is commonly known as 'bake out'. On subsequent cooling the outgassing rate decreases by many orders of magnitude enabling UHV to be achieved.

The need for bake out imposes limits on the materials that can be used for UHV equipment. Stainless steel is the most suitable material for the construction of spectrometers as it can withstand repeated heating, is strong and does not degas excessively. The exception to steel construction, is that of the analyser and main chamber. The requirement of magnetic screening of the electron analyser and main chamber means that an alloy known as mu-metal replaces stainless steel in the construction of these parts. Mu-metal is a nickel-iron alloy (77% Ni, 15% Fe, plus Co and Mo), which has a high magnetic permeability at low field strengths.

A2.2.1.2 Pressure Measurement

Pressures are measured through two methods: pirani gauges and ion-gauges (Bayard-Alpert Gauge). Pirani gauges are employed to measure higher pressures (from $0.5 \cdot 10^{-3}$ mbar). A tungsten filament (incorporated into a wheatstone bridge) within the gauge is heated by a constant voltage

source. Gas present in the system conducts heat away from the filament thus changing its temperature and hence its resistance. The pirani gauge measures the out of balance current produced in the wheatstone bridge as a pressure in nitrogen equivalent mbar. The reliability of the gauge becomes reduced at lower pressures as the heat loss from the filament by radiation becomes large compared to the heat loss by gas conduction.

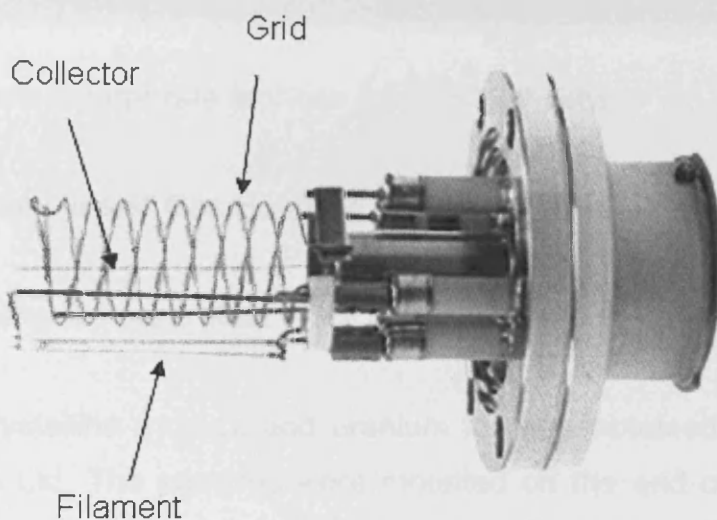


Figure A2.2 A Bayard-Alpert gauge (ion gauge) used for pressure measurement within a UHV system

A Bayard-Alpert ionisation gauge (figure A2.2) is employed to measure pressures in the region of $10^{-3} - 10^{-11}$ mbar. Ion gauges consist of three components; filament, grid (anode) and collector. Application of a current to one of the filaments (typically tungsten or thoria coated iridium) causes the generation of electrons. These electrons are accelerated through a potential of $\sim 150\text{V}$ towards the grid and collide with any molecules within the anode volume, producing positively charged ions. These positive ions are attracted to a negatively charged (with respect to the anode) tungsten collector wire where the current produced is directly proportional to the pressure of the gas molecules in the gas phase.

A2.3 The Spectrometers

Although varied in their application to surface studies, the spectrometers have many similarities, with both instruments consisting of a vacuum system, a dual anode X-ray source, electron energy analyser and a separate pumped gas handling line. Each spectrometer was also equipped with an argon ion gun to clean the metal surfaces and a quadropole mass spectrometer for gas analysis.

Both systems incorporate facilities for XPS and UPS.

A2.3.1. Sample and Gas Handling

A2.3.1.1 Sample Preparation

The polycrystalline thorium and uranium foil was obtained from Goodfellow Cambridge Ltd. The samples were mounted on the end of a sample probe fitted with a resistive heating element and cooling tubes. The sample could be heated to 900K, and cooled to 80K by pumping liquid nitrogen through the tubes. The temperature was measured using a chrome-alumel thermocouple.

The other end of the probe was bolted to a differentially pumped rotary housing, which was bolted to a linear motion drive. This allowed the sample orientation within the spectrometer to be varied as well as providing complete vertical and horizontal movement of the sample.

Neptunium and americium samples were prepared at the ITU using a sputter deposition technique. The plasma triode deposition source (figure A2.3) has been described elsewhere [2]. Typical parameters for neptunium deposition were electron energy 50 – 100 eV, target bias –700 V and 4×10^{-3} mbar Ar.

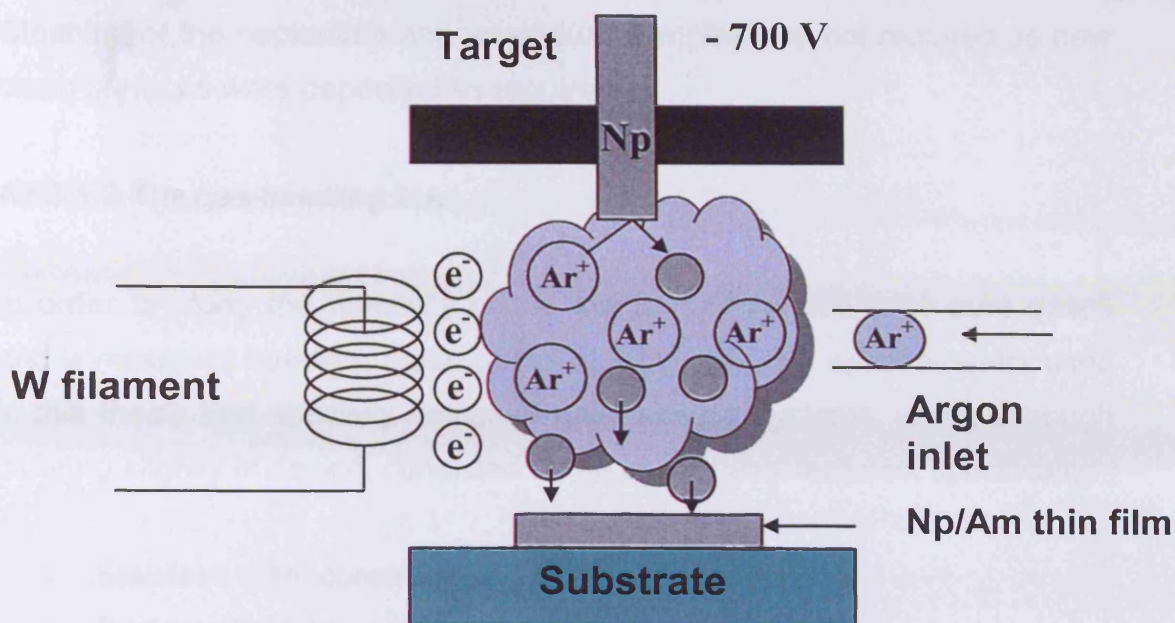


Figure A2.3. Schematic of sputter deposition.

A2.3.1.2 Sample Cleaning

Generating an atomically clean surface was carried out using a Vacuum Generators AGII cold cathode Argon Ion Gun. Argon gas is admitted into the ionisation chamber from an attached cylinder (Argo. LTD, purity 99.999%). A high voltage is applied between the cathode and anode to induce an electrical discharge ionising the Argon to form Ar^+ ions. The Ar^+ ions are focused into a beam, accelerated (2-5 KV) and directed at the surface, sputtering off any adsorbed species. Bombarding is a very destructive technique and for the polycrystalline uranium foil annealing to 450°C was required to reorganise the surface to its original flat state.

For this study, pressures of approximately 10^{-5} mbar Ar with a voltage of 5KV produced a current of $20\mu\text{A cm}^{-2}$. Initial cleaning of the uranium samples required repeated cycles of bombardment and annealing followed by examination of the surface by XPS.

Cleaning of the neptunium and americium samples was not required as new clean surfaces were deposited as required.

A2.3.1.3 The gas-handling line

In order to study the reactivity of the metal-gas interface, ultra-pure gases and a means of handling these gases is required. Both spectrometers used in this thesis had specially designed gas-handling systems, which although differing slightly in design, consisted of the same basic features, specifically:

- Stainless steel construction
- System of rotary and diffusion pumps to attain UHV
- Attachment points for gas vessels isolated from the gas line by a vacuum tap
- Gas mixing chamber
- Leak valves to backfill the preparation chamber

The gas handling line is constructed from stainless steel and consists of a rotary pump, a diffusion pump equipped with a liquid nitrogen trap (capable of achieving base pressures of $<10^{-9}$ mbar), a mixing chamber and two gas-dosing chambers. The chambers are attached to the spectrometer via bakeable leak valves, able to deliver controlled pressures down to 10^{-9} mbar. Gases were admitted from high-pressure cylinders connected directly to the gas line. Gas doses are given in Langmuirs (L), where $1\text{L} = 10^{-6}$ mbar per second.

A2.3.2 Radiation Sources

As discussed in chapter two, photoelectron spectroscopy can be divided into two analytical techniques, XPS and UPS, depending on the ionising source.

A2.3.2.1 The X-ray Source

The spectrometer has a dual X-ray anode source, providing two photon energies for analysis. These are the Al $K\alpha_{1,2}$ and Mg $K\alpha_{1,2}$ lines at 1486.6 eV and 1253.6 eV respectively. Both lines originate from a $2p \rightarrow 1s$ electronic transition; other transitions are possible which can lead to a complete emission spectrum. The advantage of the dual anode system is its ability to switch between sources to resolve any interference, which can occur between the photoelectron and the Auger electron signals. The kinetic energy of the Auger electrons is independent of the photoelectron energy, therefore only the photoelectron signal is affected by switching anodes (photoelectron peaks are seen to shift by 233 eV binding or kinetic energy).

X-rays are produced when high-energy electrons generated by a thoriated iridium filament bombard a target anode of either Al or Mg (figure A2.4). The electrons are accelerated by a potential difference between the filament (kept at near ground potential) and the anode (at a high positive potential)).

A thin aluminium window ($\sim 10\mu\text{m}$) is placed in front of the x-ray source, shielding the sample from stray electrons, heating effects and contamination originating in the source region. The window also blocks out 80% of Bremsstrahlung Radiation - a broad continuous energy background caused by other electronic transitions within the photon source (figure A2.5)

Unmonochromatised x-ray radiation also show satellite lines arising from less probable transitions such as the $K\alpha_{3,4}$ line. This gives rise to additional features in the photoelectron spectrum at approximately 10 eV lower binding energy than the main photoelectron peak (with an intensity 10% that of the $K\alpha_{1,2}$ line) (figure A2.5).

A2.3.2.2 X-ray source: Design

Figure A2.4 shows a schematic of the dual anode X-ray source used within this study. At the tip of the anode are two tapered copper faces – one with a

film of aluminium and the other with a film of magnesium. Either side of each tapered face is a filament at a potential equal to that of Earth, which is used to produce high energy electrons for bombardment.

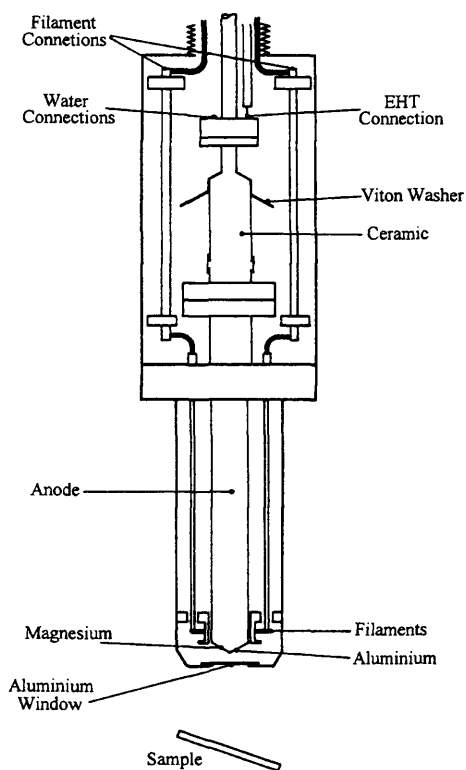


Figure A2.4. Dual anode (Al/Mg $K\alpha$) x-ray photon source

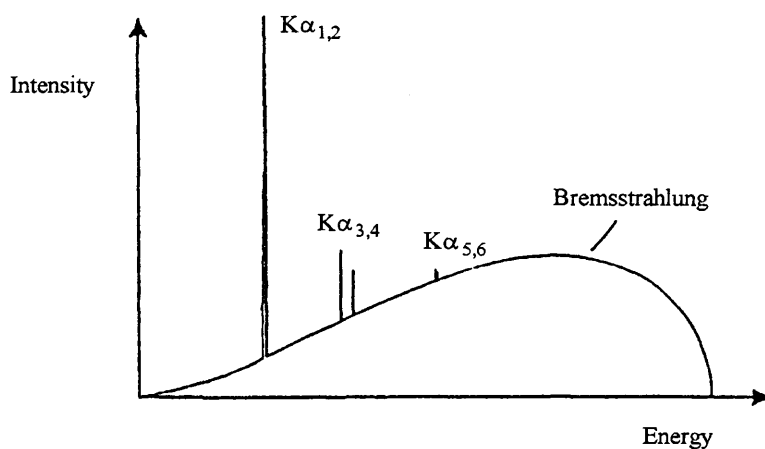


Figure A2.5. X-ray emission spectrum. Principle transitions are superimposed on the rising Bremsstrahlung background.

Application of a high positive potential to the anode (12 – 15 kV) accelerates the electrons to the nearest face causing the ejection of X-ray photons. These photons pass through the aluminium window before impinging on the surface. To minimise the associated rise in temperature, the anode is cooled with a continuous pumped flow of water, typically with a flow rate greater than 3 litre min⁻¹.

A2.3.2.3 Ultra Violet source

Ultraviolet light employed to probe the valence levels is generated via transitions within the gas discharge lamp. For this study, Helium was used with two characteristic discharge lines at 20.2 and 40.8eV, corresponding to the He (I) and He (II) lines respectively. The two lines arise due to transitions from 2p to 1s orbitals within the excited helium atoms (see chapter two). Satellite peaks are seen to form from the He (I) β line, arising from the less probable transition of 3p to 1s, appearing as weak features to the lower binding energy in the photoelectron spectra.

A2.3.3 The Electron Energy Analyser

The measurement of the kinetic energies of the photoelectron by the electron analyser is at the heart of both the XPS and UPS techniques. Two main types of analyser were initially developed, although the concentric hemisphere analyser (CHA) is the preferred choice due to its high resolution. The CHA has two hemispherical surfaces of radii R_1 (inner sphere) and R_2 (outer sphere) positioned concentrically. A potential difference is applied to the surfaces so that R_1 is positive and R_2 is negative. These potentials act producing a region of zero potential equidistant from each hemisphere at radius R_0 , when ideally,

$$R_0 = \frac{R_1 + R_2}{2} \quad (2.2)$$

Electrons entering the analyser encounter an applied retarding potential (V), which decreases the electron energy to a constant fixed energy, known as the analyser pass energy (E_A). Only electrons with this specific pass energy will pass through the analyser without striking either hemisphere surface on the way to the detector. The equation relating pass energy and the applied potential (V) is seen in Equation 2.3.

$$\Delta V = E_P (R_2/R_1 - R_1/R_2) \equiv E_P H \quad (2.3)$$

The term in brackets is the Hemispherical constant. Pass energies are fixed and are typically 20, 50 or 100 eV, depending on the required resolution. A retarding potential (V_R) is applied to the sample to decelerate the photoelectrons, so that: -

$$K.E. = E + eV_R \quad (2.4)$$

Where K.E. = Photoelectron kinetic energy, E = Analyser pass energy, e = electron charge, V_R = retarding potential.

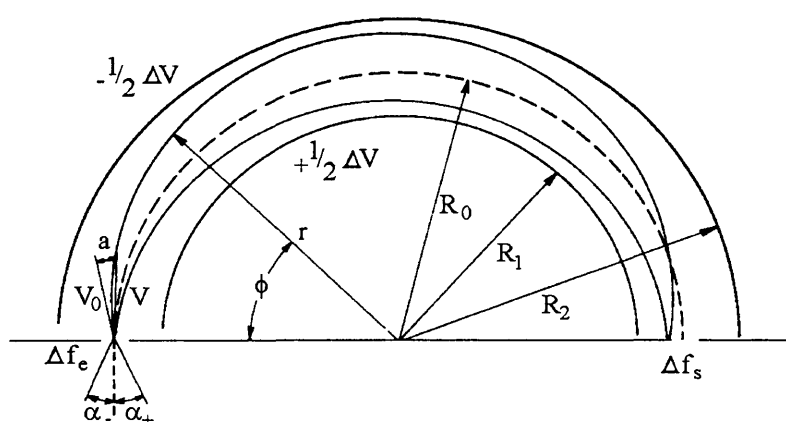


Figure A2.6. Principle of operation of the concentric hemispherical analyser (CHA).

By changing the retarding potential it is possible to vary the kinetic energies of the photoelectrons passing through the analyser to the detector. Normally the retarding potential is linearly ramped so that the electrons of decreasing kinetic energy are analysed.

A2.3.4 The Electron multiplier

Due to the extremely small electron current (10^{-16} to 10^{-13} A) emerging from the analyser, amplification by a channel electron multiplier (channeltron) is required to produce a measurable signal (figure A2.7).

The channeltron consists of a coiled tube of semi conducting glass, coated on the inside with a high secondary electron coefficient material i.e. a material that easily produces electrons when struck by photoelectrons (for example lead oxide).

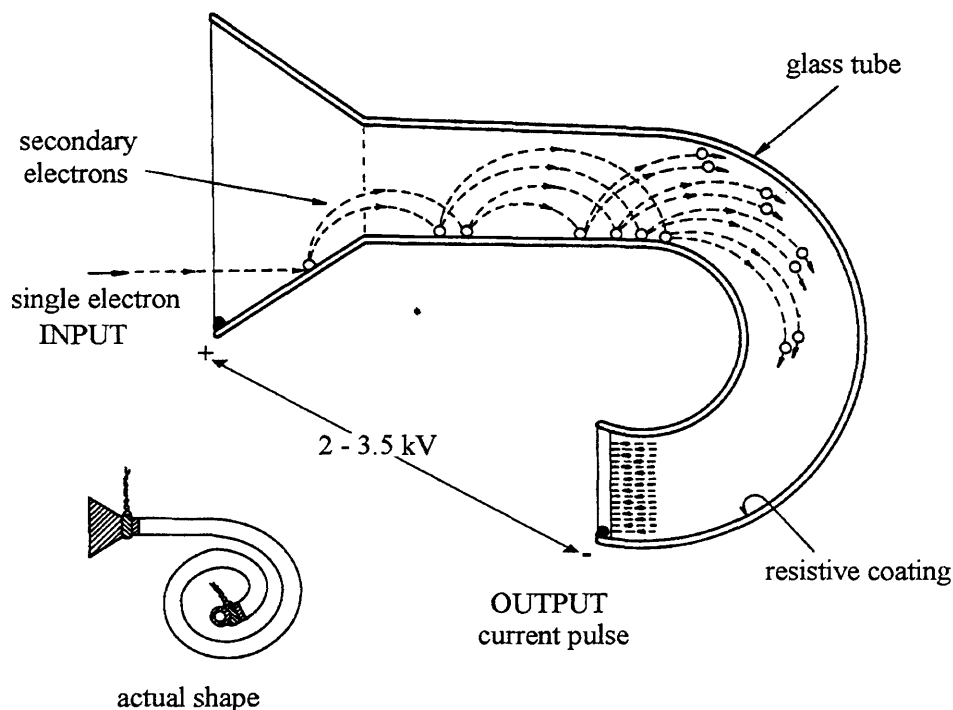


Figure A2.7. The channeltron electron multiplier.

Photoelectrons entering the channeltron via a small entrance cone collide with the interior walls producing several secondary electrons. These electrons are then accelerated along the channeltron via an applied voltage, where they continue to produce more and more secondary electrons resulting in a 10^8 amplification of the original signal.

The multiplier enables a single photoelectron to become a pulse, which is then passed to a discriminator that removes smaller pulses (due to noise) and outputs normalised pulses to a ratemeter and then to a computer for analysis.

A2.4 References

1. <http://itu.jrc.cec.eu.int>, 2005
2. T. Gouder, Journal of Electron Spectroscopy and Related Phenomena, 1999. **101-103**: p. 419-422.

